A HIGHER-ORDER TRANSPORT MODEL FOR PHOTON PROPAGATION AND ITS APPLICATIONS TO OPTICAL TOMOGRAPHY

by

Emine Dilara AYDIN,
B.Sc (Physics), M.Sc. (Nuc. Eng.)

A thesis submitted in fulfilment of the requirement for the degree of
Doctor of Philosophy of the University of London (Ph.D) and the
Diploma of the Imperial College (DIC)

Computational Physics and Geophysics Group
TH Huxley School of Environment, Earth Sciences and Engineering
Imperial College of Science, Technology and Medicine
University of London

October 1999

Abstract

In this thesis, we describe details of a mathematical model for solving the photon propagation problem through densely scattering media. The model numerically calculates the photon intensity within the medium, and the photon current through its surface by solving the linearised one-speed Boltzmann transport equation with a general purpose, finite element-spherical harmonics (FE-P_N) radiation transport method. For the solution of the inverse problem a non-perturbative iterative model named as Reference Cross Section Model is developed. With this model the sensitivity of the detector response is estimated for a reference cross section which is independent from the cross section we wish to reconstruct. Using this model leads to a system of integral equations for the unknown absorption and scattering cross sections. A variational formulation consistent with this equation system is employed to specify the problem in a way that is appropriate for the application of the FE-P_N method.

Although the diffusion approximation is commonly used to calculate the photon migration in biological tissues, it is not capable of dealing with some situations encountered in tissue such as strong discontinuities of optical properties or void-like/transparent regions. The main advantages of the present model apart from the ability of the FE method to handle complex geometries and its computational speed, is the use of full higher-order transport approximation which reduces to the diffusion approximation in its lowest order and the ability of taking into account the anisotropic scattering effects of the medium by choosing the appropriate approximation method for the expansion of the scattering kernel.

The results of benchmark calculations for different geometries and material properties are presented and compared with the Monte Carlo method. Comparisons between diffusion and transport theory are also made for some specific problems. The obtained results show good agreement with Monte Carlo calculation in contrast to the diffusion approximation which becomes inaccurate in certain cases. 2D reconstruction results for the optical properties of cases involving simple geometries and material properties and also complex layered geometries representing human head are presented in order to show the potential of the proposed model.

Acknowledgement

I sincerely wish to thank my supervisors, Prof. A.J.H. Goddard and Dr. C.R.E. de Oliveira, for their supervision, scientific assistance and constant encouragement during the course of this work.

Thanks must also go to Prof. N.C. Roberty, who was visiting professor at the beginning of this project, for his informative discussions and sharing his knowledge on the theoretical aspects of the inverse solution model.

My special thanks are due to Dr. Sotirios Katsimichas, for his valuable advice and assistance that I needed to complete this work.

My appreciations go to my husband, Mr. Murat Aydin, whose help, encourage, support and advice have been very important to my career. I am also deeply in debt to him for all his patience and understanding during our stay in London, creating the necessary conditions for the fulfilment of this work.

I wish to thank Dr. M.A. Byrne, Mr. A.P. Umpleby, Dr. R.A. Price and Dr. C.C. Pain for their assistance, cooperation and advice on many occasions. Also, many thanks to all my colleagues, in particular Dr. S. Mansoorzadeh, Miss. I. bin Hamida, Mr. A. Lal, Miss M. Duglio who have contributed to the success of this work and made my stay at Imperial College a happy experience.

I would like to thank to Consultant Radiologist Dr. A.R. Sever from Maidstone Hospital for sharing his valuable knowledge on Medical Imaging and Dr. F. Nadiri for reading my chapters and making helpful comments.

I also would like to demonstrate my gratitude to my sister, Mrs. Leyla Yeykan, and Dr. Mahmut Aydin, my brother in-law, for their constant support and encouragement through the phone lines.

I want also to acknowledge and thank The Turkish Council of Higher Education and Canakkale Onsekiz Mart University which have supported and granted the presented work.

Contents

Abstract 1

Acknowledgment 2

Table of Contents 3

List of Figures 7

List of Tables 14

Nomenclature 16

1 Introduction 21

1.1 Conventional Medical Imaging Systems 21

1.2 Medical Optical Tomography 30

1.3 Photon Transport Models in Optical Tomography 33

1.3.1 Monte Carlo Method 33

1.3.2 Spherical Harmonics (P_N) Method 35

1.3.3 Diffusion Approximation 36
1.3.4 Finite Element Method 37
1.4 Scope of the Thesis 40

2 Solution of the Photon Transport Equation 43

2.1 Introduction 43
2.2 Photon Propagation and Optical Properties of Tissue 45
2.3 The Boltzmann Transport Equation and the Even-Parity Form 51
2.4 Application of the Variational Method and the Ritz Procedure 59
2.5 The Finite Element-Spherical Harmonics Method 62
2.6 Summary 64

3 Results of Forward Photon Transport Modelling 66

3.1 Introduction 66
3.2 Time-Dependent Cases 67
3.2.1 Comparison of Transport and Diffusion Calculations 67
3.2.2 Comparison between FE-P_N and Monte Carlo Calculations . . 75
3.3 Steady-State Cases 83
3.3.1 Results for Homogeneous Slab Geometry 83
3.3.2 Results for Heterogeneous 2D Geometry 88
3.4 Summary 107

4 A Solution Model for Inverse Photon Scattering Problems **109**

4.1 Introduction 110

4.2 Formulation of the Inverse Problem 114

4.2.1 Photon Transport 114

4.2.2 The Reference Cross Section Model 116

4.3 First- and Second-Order Variational Formulation of The Reference Cross Section Model 121

4.4 Image Reconstruction Algorithm 124

4.5 Summary 125

5 Image Reconstruction Results **127**

5.1 Introduction 127

5.2 Reconstructions from Monte Carlo Data 127

5.3 Reconstruction from FE-P_N-Generated Data 135

5.3.1 Reconstruction Results with Isotropic Scattering 135

5.3.2 Reconstruction Results with Linearly Isotropic (P_1) Scattering 140

5.3.3 Reconstruction Results with Highly Anisotropic Scattering . . 146

5.4 Summary 154

6 Discussion of Results and Conclusions **155**

6.1 General Review of the Thesis 155

6.2 Implementation of Anisotropic Scattering 157

6.3 Forward Solution Results 158

6.3.1 Time-dependence 158

6.3.2 Steady-state 159

6.4 Inverse Solution Results 163

6.5 Recommendations for Future Work 165

Bibliography **167**

A Anisotropic Scattering **192**

A.1 Program PHASEFUN 193

B Definitions of $S_1(\theta)$ and $S_2(\theta)$ for Mie Theory Approximation **205**

C Radiation Transport Code EVENT **207**

C.1 Specification of the Program 207

C.2 Solution Strategies 208

D Legendre Polynomials and Spherical Harmonics **210**

D.1 Legendre Polynomials 210

D.1.1 Associated Legendre Polynomials 212

D.2 Spherical Harmonics 214

E The Tensor Product of Matrices **216**

List of Figures

1.1 The components of radiographic imaging system. Photon A has been absorbed, B and E represent photons that have passed through the patient without interacting while C and D are scattered photons. . . 23

1.2 The CT system co-ordinate geometry. 25

2.1 Attenuation of a collimated photon beam in passage through a slab. . 47

2.2 (a) An arbitrary volume V with surface area S; (b) The position and direction variables of a particle in spherical coordinates. 52

2.3 Definition of the scattering angle θ (a) by a schematic illustration of the collision event; (b) in spherical coordinate system. 55

3.1 Source and detector arrangements used to obtain results of the homogeneous problem. 68

3.2 Examples of typical time profiles of photon current for detectors positioned at 45° degree from the source and detectors positioned at 90°, 135° and 180° degrees from the source. 68

3.3 Comparison of FE-P_N of output current results at 180° for the pure-scattering homogeneous cylinder. 69

3.4 Comparison of FE-P_N solutions for the homogeneous cylinder with absorption. Scattering coefficient is 2.5 mm^{-1} for both calculations. Top: results for $\mu_a = 0.1$ mm^{-1}. Bottom: results for $\mu_a = 0.2$ mm^{-1}. 71

3.5 Absorber and source-detector geometry for the inhomogeneous problem. 72

3.6 Comparison between results of output current modelled with P_7-P_1 approximation and diffusion angular approximation for the inhomogeneous cylinder. 72

3.7 Comparison of output current at 180° for case with centred absorber. Scattering coefficient of the outer region is 2.5 mm^{-1} for both cases. Top: results for $\mu_a = 0.1$ mm^{-1}. Bottom: results for $\mu_a = 0.2$ mm^{-1}. 74

3.8 Comparison of FE-P_7 solutions of output current at 180° for two non-absorbing cases given in Figure 3.3 and Figure 3.6. 75

3.9 The finite element mesh used for the homogeneous problem. 77

3.10 MC and FE-P_N predicted photon leakage at 180° for photons transmitted through a non-absorbing homogeneous cylinder with scattering coefficient $\mu_s = 1$ mm^{-1}. The MC calculation used 4.7×10^8 photons. 77

3.11 Comparison of leakage currents at 180° calculated using both MC and FE-P_N for the homogeneous cylinder shown in Figure 3.9 with an absorption coefficient of 0.1 mm^{-1}. 78

3.12 Simulation geometry with source and detector positions. 79

3.13 FE mesh of the first inhomogeneous test case for MC comparison. . 80

3.14 Comparison of FE-P_N and MC results of photon leakage for inhomogeneous cylinder containing three cylindrical absorbers/scatterers. . 81

3.15 The FE mesh used for the calculation of the second case with one centred cylindrical inhomogeneity. 82

3.16 Comparison of FE-P_N and MC results for photon leakage at 180°, for the inhomogeneous cylinder with one centred cylindrical problem. . . 82

3.17 Geometry of the infinite slab problem. S denotes the source plane and a the slab thickness. 84

3.18 Solutions of photon attenuation through an infinite slab, with an isotropic plane source to show influence of the ratio μ_a/μ'_s on the accuracy of diffusion approximation. 85

3.19 Ratio of the photon fluxes calculated with a P_{25}-transport theory approximation for two different g values and various absorption coefficients (mm^{-1}). Legendre expansion coefficients were obtained from the H-G phase function formula. 86

3.20 Ratio of the photon fluxes calculated with a P_{25}-transport theory approximation for two different g values and various absorption coefficients (mm^{-1}). In this case, SAM phase function formula was used to obtain the Legendre expansion coefficients of the scattering kernel. . 87

3.21 Comparison between the results obtained with the H-G and SAM phase function formulas for various values of absorption coefficient (mm^{-1}). The solid lines are H-G solutions and the dot-dashed lines the SAM solutions. 88

3.22 2D geometry for the steady-state calculation of the layered cylinder problem. 90

3.23 Calculated (log) intensity distribution from the source one using the problem layout shown in Figure 3.22. Result are obtained with P_7 angular approximation with seven coefficients for the scattering kernel. 90

3.24 Sources and detectors configuration used for layered cylindrical problem. 91

3.25 Relative error between FE-P_7 and diffusion solutions calculated at 16 surface detectors and for sources 1-6 for the problem shown in Figure 3.22. 92

3.26 Relative error, in photon current leakage, between FE-P_7 and diffusion solutions at 16 detectors and for sources 7-12 for the problem shown in Figure 3.22. 93

3.27 Relative error, in photon leakage current, at 16 surface detectors and for sources 13-16, between FE-P_7 and diffusion for the problem shown in Figure 3.22. 94

3.28 Mesh layout used for photon diffusion and transport modelling in cylindrical strong absorbing regions and void-like spaces. 95

3.29 Comparison between diffusion and transport theory calculations of the photon intensities in heterogeneous media to investigate influence of μ_a/μ'_s. 96

3.30 Log_{10} of the ratio of the photon intensity, modelled with diffusion and transport theory, near a cylindrical low density region. 98

3.31 Log_{10} of the photon intensity, modelled with diffusion and transport theory, inside the cylindrical low density region shown in Figure 3.28. 99

3.32 Log_{10} of Flux values as calculated by FE-diffusion (top) and transport (bottom) approximations for two-dimensional geometry contains a cylindrical region with almost absorption- and scattering-free optical properties. 100

3.33 Geometry III, used in diffusion and transport simulations of void-like spaces. 101

3.34 The ratio of Log_{10}(photon intensity) calculated with diffusion theory and transport theory near the boundaries of the square void-like region. Results are plotted along an axis passing through the source. 102

3.35 Log_{10} of the ratio of the photon intensity, modelled with diffusion and transport theories, inside a low density square region. 103

3.36 Photon intensity contour maps within the void-like region of problem III, for diffusion theory (top) and transport theory (bottom). 104

3.37 Geometry IV, used for photon diffusion and transport modelling in the CSF layer. 105

3.38 Contoured photon intensity distributions modelled by diffusion theory (top) and transport theory (bottom) for the 2D CSF-layered problem. 106

5.1 Simulation geometry used for the reconstruction of the first inhomogeneous problem with one centred cylindrical region. 128

5.2 The mesh used in the reconstruction of the centred cylinder problem. 129

5.3 Reconstructed images based on MC data obtained from an inhomogeneous cylinder with a centrally located small cylinder. The upper illustration gives the result of μ_a values for the first iteration and the lower shows the result for iteration number 14. 130

5.4 Simulation geometry used to obtain the MC data for the reconstruction. Assumed optical properties of the background and three small cylinders were as follows: Background: μ_a=0.05 mm^{-1} and μ_s=0.45 mm^{-1}, cylinder 1 (green): μ_a=0.09 mm^{-1} and μ_s=0.81 mm^{-1}, cylinder 2 (purple): μ_a=0.12 mm^{-1} and μ_s=1.08 mm^{-1}, cylinder 3 (red): μ_a=0.15 mm^{-1} and μ_s=1.35 mm^{-1}. 131

5.5 Reconstruction of Monte Carlo data of three cylindrical regions within a 20 mm cylinder. The upper illustration shows first iteration results and the lower gives the results for iteration number 12. 133

5.6 Weight functions for absorption coefficient of the problem given in Figure 5.4. The pictures shows the weights from the source 1 to the detectors 2, 3, 4, 5, 6 and 7 for the first iteration. 134

5.7 2D finite element mesh with the absorbing object located at the centre. 136

5.8 Reconstruction of the μ_a image for the problem having a centred absorbing inhomogeneity. 136

5.9 Locations of inhomogeneities for FE-P_N forward solution on 2D circular mesh (represents an infinite cylinder phantom). 138

5.10 Reconstruction of the cylindrical region containing three absorbing objects. The upper illustration shows the result after the first iteration and the lower is for the 10th iteration. 139

5.11 The positioning of the objects used for the reconstruction results given in Figure 5.12. 141

5.12 First two iterations obtained from the absorption coefficient reconstruction process for the problem given in Figure 5.11. 142

5.13 2D circular mesh showing the mesh layout of the problem and the location of the absorbing object. 143

5.14 Results, for 4 iterations, of the reconstruction of the absorption coefficient image for the problem layout given in figure 5.13. 144

5.15 The layered FE mesh used to obtain data for the reconstruction algorithm. The number of nodes is 5919 and the number of triangular mesh elements is 11836. The forward solution took approximately 14 cpu minutes on a Dec Alpha 500/250 workstation. 147

5.16 Absorption coefficient reconstruction of the symmetrical layered cylinder with embedded object. The images show the results for the iteration numbers 2, 4, 5, 6, 7, and 8 respectively. 148

5.17 Mesh and layers/embedded object layout used for the solution of the asymmetrical layered problem. 151

5.18 Absorption coefficient reconstruction results for the asymmetrical layered cylinder for four iterations. The first three images show the results of the first three iterations and the last image is the result of the 7th iteration. The bounding scales give dimensions in *mm*. 152

List of Tables

3.1 Maximum photon leakage rates at 180° for FE-P_N solutions using P_7, P_1 and diffusion approximation for a homogeneous cylindrical region. 70

3.2 Maximum photon leakage rates at 180° for FE-P_N solutions using P_7, P_1 and diffusion approximation for a cylindrical region with centred absorber. 73

3.3 The central coordinates and optical coefficients of 4 cylindrical regions used for the first inhomogeneous case. 80

3.4 Comparative times for the inhomogeneous cylindrical problem given in Figure 3.13. FE-P_N times were obtained for a mesh with 2724 nodes-5446 elements using 60 time steps. 81

3.5 Optical properties of the layers used in the layered cylindrical case, μ_a is the absorption coefficient, μ_s is the scattering coefficient, $\mu_t = \mu_a + \mu_s$, g is the anisotropy factor or the mean cosine of the scattering angle. 89

5.1 Reconstructed absorption coefficient values of the problem given in Figure 5.4. 132

5.2 Side colour scales and reconstructed μ_a values of two illustrations given in Figure 5.10. 140

5.3 Colour scale of reconstruction results given in Figure 5.12. 141

5.4 Side colour scales of 4 iterations given in Figure 5.14. 145

5.5 Optical parameters for the symmetrical layered cylinder. 147

5.6 Colour scales and the corresponding μ_a values of 6 iterations given in Figure 5.16. 149

5.7 Optical parameters used in reconstruction for the asymmetrical layered cylinder. 151

5.8 Side colour scales of Figure 5.18. 153

Nomenclature

Abbreviations

CT	Computed Tomography
SPECT	Single Photon Emission Computed Tomography
PET	Positron Emission Tomography
MRI	Magnetic Resonance Imaging
NIR	Near-Infrared Radiation
UV	Ultraviolet
FE-P_N	Finite Element-Spherical Harmonics
MC	Monte Carlo
P_N	Spherical Harmonics
CSF	Cerebrospinal Fluid
FEM	Finite Element Method
FDM	Finite Difference Method
RCSM	Reference Cross Section Model
EVENT	EVEn parity Neutron Transport
H-G	Henyey-Greenstein
SAM	Simplified Approximate Mie
δ-M	Delta-M Truncation Method
POCS	Projection onto Convex Set
CGD	Conjugate Gradient Descent
SART	Simultaneous Algebraic Reconstruction Technique

Chapter 1

L	X-ray path
$I_\phi(\xi)$	Transmitted intensity

$I_\phi^0(\xi)$	Unattenuated x-ray intensity
$\mu[x, y]$	Linear attenuation coefficient
$\lambda_\phi(\xi)$	Attenuation value or single projection
$\omega_\circ$	Larmor frequency
γ	Gyromagnetic ratio
$H_\circ$	Magnetic field strength

Chapter 2

μ_a	Absorption coefficient
σ_a	Absorption cross section
N	Particle density or atomic number
$\mathbf{r}$	Particle position vector
$\mathbf{\Omega}'$	Initial Photon Direction
$\mathbf{\Omega}$	Direction after photon scattering
$\sigma_s(\mathbf{\Omega}' \rightarrow \mathbf{\Omega})$	Differential scattering cross section
σ_s	Scattering cross section
σ_t	Total cross section
μ_s	Scattering coefficient
μ_t	Total attenuation coefficient
θ	Scattering angle
$f(\mathbf{\Omega}' \rightarrow \mathbf{\Omega})$	Scattering phase function
$\mu_0 \equiv (\cos\theta)$	Cosine of the scattering angle
g	Mean cosine of the scattering angle
$S_1(\theta), S_1(\theta)^*$	Complex amplitude functions
K_S	Normalisation factor
n_p	Anisotropic index
v	Photon characteristic velocity
$\phi(\mathbf{r}, \mathbf{\Omega}, t)$	Angular flux

$S(\mathbf{r}, \mathbf{\Omega}, E, t)$	Source term
σ_{sl}	Scattering expansion coefficient
$P_l(\mu_0)$	Legendre Polynomial of order l
$\delta(\mathbf{\Omega}' - \mathbf{\Omega})$	Dirac δ-function
$\phi^+(\mathbf{r}, \mathbf{\Omega})$	Even-parity flux
$\phi^-(\mathbf{r}, \mathbf{\Omega})$	Odd-parity flux
H	Removal operator
G	Leakage operator
$\phi(\mathbf{r})$	Scalar flux
$\mathbf{J}(\mathbf{r})$	Current vector
$F[\phi^+]$	Quadratic functional
E	Total number of elements, e=1,...,E
N_e	Number of local nodes in element e, j=1,...,N_e
K	Number of spherical harmonics coefficients, k=1,...,M_e
$B_j^e(\mathbf{r})$	Spatial basis functions
$Q_k(\mathbf{r})$	Angular basis functions
ϕ_{jk}^{+e}	Approximate nodal values of scalar flux
$\mathbf{B}^e(\mathbf{r})$	A column-vector of finite element shape functions
$\mathbf{Q}(\mathbf{\Omega})$	A column-vector of normalised spherical harmonics functions
$\mathbf{\Phi}^e$	A column-vector of unknown elements nodal fluxes

Chapter 3

μ_s'	Reduced scattering coefficient, (1-g)μ_s

Chapter 4

V	Volume
∂V	Surface

$\mathbf{n}$	Normal unit vector
F_{ij}^{exp}	Integrated outgoing radiation flux
s	Laplace transform parameter
$R[...]$	Removal operator
ϕ_i	Angular flux for source problem
ϕ_j^*	Adjoint angular flux for detector problem
$R^\circ[...]$	Removal operator for detector problem
N_S	Number of sources
N_D	Number of detectors
W_{ij}	Weight function
δ	A prescribed threshold

To my mum, Nezahat,
and my dad, Mete

Chapter 1

Introduction

Medical imaging may be defined as the visualisation of the inside of the human body without any surgical operation. Medical imaging techniques have become vital tools in recent years for diagnosing a wide range of medical conditions. Apart from diagnosis, medical imaging also serves to assist with planning and monitoring the treatment of malignant diseases [1]. The main objective of all imaging methods is to gather information about the tissue or body under investigation and to display it in such a way that it may be perceived by one or more of the human senses (usually as an image). In most methods, a set of data may be obtained by performing a series of measurements made outside the body. Then, the resultant data set may be supplied to a reconstruction scheme to create the spatial distribution of the optical properties of the selected tissue region with the aid of computer processing.

1.1 Conventional Medical Imaging Systems

Since the discovery of x-rays in 1895 by Wilhelm C. Roentgen [2], a number of powerful techniques have been developed for noninvasive biomedical imaging. Each of these techniques has different advantages and limitations for particular clinical applications.

The first main imaging technique, transmission tomography, depends on the measurement of the x-rays transmitted through the body. Radiography and x-ray computed tomography are both applications of x-ray, transmission-based imaging techniques.

Radiography is a technique of producing images of an opaque object on a photographic film or a fluorescent screen by means of radiation. The photograph produced is called a *radiograph*. Four components of a typical x-ray imaging system and also the formation of a radiographic image are shown in Figure 1.1. Photons are generated by an x-ray tube and enter the body and may be scattered, absorbed or transmitted without interaction. Transmitted photons carry useful information and the image, which is a *projection* of the attenuating properties of all the tissues along the ways of the x-rays, is obtained by using these particular photons. As scattering has harmful effects on the film or screen such as loss of contrast [3], a scatter reduction process (grids) is employed between the body and the image receptor in order to transmit most of the primary radiation but reject most of the scatter [1]. A filtering material, aluminium, is added to the system to filter the low-energy "soft" x-rays from the incident beam [3] because they have low penetration and can cause skin burns without contributing to the image. An extensive introduction into the imaging system, image formation, and the important physical parameters affecting the quality of the image in diagnostic radiology can be found in [1], [4].

Variations in composition and thickness of the tissues through which the x-ray photons have passed appear as contrasts (dark and light areas) on the radiograph. Because x-rays are strongly attenuated by bone but travel easily through soft body tissue, x-ray photographs can reveal the detailed structure of the human skeletal system and are especially invaluable in medical diagnostic procedures leading to the resetting of broken bones. However, conventional x-ray radiography has two main limitations. First, it projects the three-dimensional structure of the body onto a two-dimensional film and produces flat, two-dimensional image. Even through the image reveals an abnormality, it would not indicate the depth of that abnormality within the body. Second, this system is not very effective in differentiating between different types of soft tissue [5],[6]. The contrast between two soft tissue regions, like brain

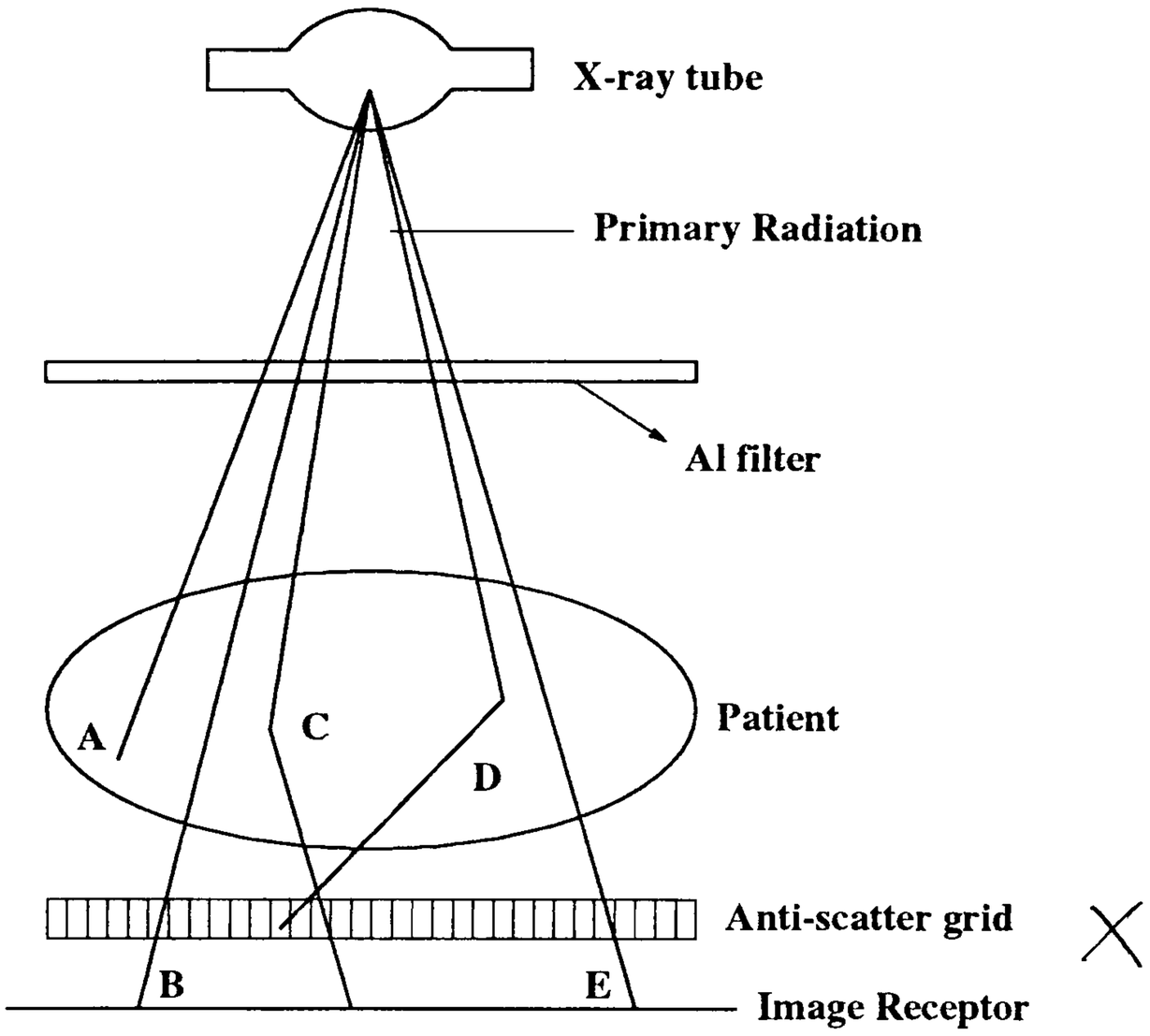


Figure 1.1: The components of radiographic imaging system. Photon A has been absorbed, B and E represent photons that have passed through the patient without interacting while C and D are scattered photons.

and cerebrospinal fluid, may be too small to be discernible in the radiograph, because the linear attenuation coefficients of these structures are so close to each other [4]. Therefore, soft-tissue details, such as the details of brain anatomy, or abnormalities of the liver, pancreas cannot be distinguished by this technique. However, the use of radio-opaque (contrast) materials in certain organs may improve the diagnostic quality to some degree. For example, barium compounds for examination of the digestive tract and intravenous application of iodine compounds for blood vessels examinations (angiography) are employed to generate the visual contrast [1],[6].

In computed tomography (CT), a mathematical reconstruction of selected planes or slices of the human body is made by using a computer. The concept can be summarised as follows: A planar slice of the body is defined and examined (scanned) from multiple angles with a pencil-like x-ray beam. A scintillation detector measures the transmitted radiation, these data are then fed into a computer for analysis by a mathematical algorithm which reconstructs a tomographic image. The most im-

portant feature of CT is its sensitivity in demonstrating a radiographic difference between various soft tissues. For example blood clots, gray matter, white matter, cerebrospinal fluid, and tumours can be distinguished in CT as separate entities [4]. The contrast of the CT picture can be adjusted by employing a windowing control on attenuation coefficients of tissues. This control allows the visual amplification of minor differences in the area of interest [1],[4]. By precisely locating a Tudor, CT also plays an additional role in the field of therapy to indicate the area of the body to be irradiated, and in monitoring the progress of treatment afterwards [6].

Transmission measurements obtained by a CT system consists of line integrals of the absorption coefficient along the straight ray paths connecting the source and detector. Figure 1.2 shows a representative CT system geometry.The (ξ, η) coordinates can be rotated about the origin with respect to the (x,y) coordinates. The physical significance of this is that CT measurements are usually made over a wide range of viewing angles, relative to the body, by physically rotating the measuring system. The transmitted intensity measured along the path L is given by

$$I_\phi(\xi) = I_\phi^0(\xi) exp\left[-\int_L \mu[x,y]d\eta\right], \tag{1.1}$$

where $I_\phi^0(\xi)$ is the incident or unattenuated intensity and $\mu[x,y]$ is the linear attenuation coefficient. From a measurement of both intensities, $I_\phi^0(\xi)$ and $I_\phi(\xi)$, an attenuation value, or a single projection of the cross-section at the angle ϕ is obtained by

$$\lambda_\phi(\xi) = ln[I_\phi^0(\xi)/I_\phi(\xi)] = \int_L \mu[x,y]d\eta. \tag{1.2}$$

A large number of projections can be measured from a set of line integrals obtained by translating source-detector pair across the body at the angles ϕ_1, ϕ_2, ..., ϕ_n. The linear relationship between the function $\mu[x,y]$ and the measured projection data λ_ϕ allows calculation of the density distribution $\mu[x,y]$ of the cross-section within the measurement plane by using one of the reconstruction methods. Therefore the reconstructing problem for a CT imaging system may be defined as the recovery of $\mu[x,y]$ from a set of projections $\lambda_\phi(\xi)$ and the reconstruction methods are generally based on the transformation of line integrals of the attenuation coefficient $\mu[x,y]$ into an image. This can be achieved by using either mathematical transform methods,

which basically rely on Fourier transform theory, or iterative methods. Detailed discussion of these methods is beyond the scope of this work and it can be found, for example, in [7].

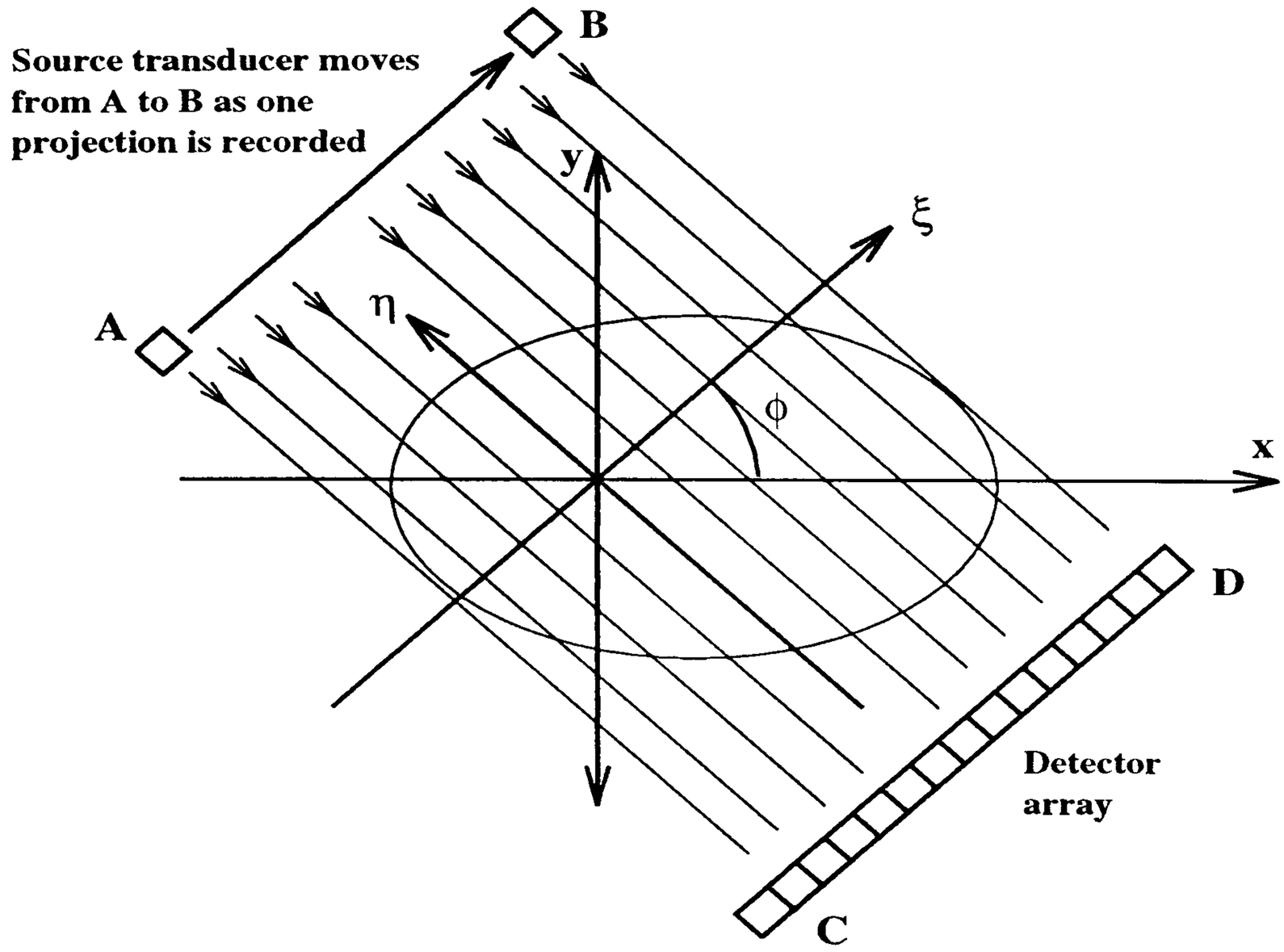


Figure 1.2: The CT system co-ordinate geometry.

The second main imaging technique, Ultrasonic Imaging, is based on the measurement of the reflection of ultrasonic waves transmitted through the body. Ultrasound can be defined as sound of frequency above the bandwidth of human hearing. Ultrasound waves can penetrate and interact with the human body. The single and most important component of an ultrasonic imaging system is the transducer. It is used to transmit the sound waves and also receive the echoes. The transducer must be in close contact with the skin. The tissue interfaces reflect the sound at interfaces between media of different acoustic refractive indices, and the resulting pattern of sound reflection is processed by a computer to produce a photograph or a moving image on a television. The location of the tissue interfaces can be calculated from the elapsed time between the emitting of the pulse and the receiving of the echo, and the velocity of the sound in the transmitting medium [3], [7].

Ultrasonic imaging has gained an important place in diagnostic medicine, because it is not known to have deleterious effect as in x-ray systems and can be used in sensitive regions such as the pregnant abdomen and the eyes [3]. However, health effects of ultrasound may be present, particularly in developing tissues, and cause thermal or structural cellular injury if the method is not used prudently, i.e. with minimum exposure time and acoustic intensity [8].

The third main imaging technique relies on detecting the radioactive emissions from isotopes internally administered and deposited in specific body organs or organ systems. The use of radioisotopes in clinical diagnosis of human diseases has grown rapidly following the development of the cyclotron and of nuclear reactor as methods for producing high specific activity radioactive material [9]. This imaging technique, named nuclear radiology or nuclear medicine, includes such techniques as SPECT and PET which are generally based on the introduction of a radioactive material or radiopharmaceuticals into the human body (usually by injection). This procedure causes the region or organ under study to become an active source, since the body contains very low levels of natural radioactive substances. The radiopharmaceuticals used in nuclear medicine emit gamma rays that can be detected externally by special types of cameras [5]. These cameras work in conjunction with computers used to form images that provide data and information about the area of body being imaged.

Unlike anatomic imaging modalities such as CT and MRI, which are limited by their capacity to asses only structural changes in tissue (e.g. size, shape, density), nuclear medicine studies are capable of producing images that show the chemical functioning of organs and tissue. Although the change in structure or anatomy that occurs with disease can be seen by conventional techniques, biochemical processes are also altered with disease and may occur before there is a change in gross anatomy. For example in Alzheimer's disease, where there is no gross structural abnormality, nuclear medicine is able to show a biochemical change [1]. Therefore, nuclear medicine imaging procedures often identify abnormalities very early in the progression of a disease -long before some medical problems are apparent with other diagnostic tests. This early detection allows a disease to be treated early in its course when there may be a more successful prognosis. The main drawback of these imaging techniques is,

however, the requirement of injection/ingestion/inhalation of radiation emitters into the patient's body.

In early studies of nuclear medicine, a gamma-ray sensitive detector (scintillation or solid-state detectors), which is a combination of a scintillator crystal (NaI) and a photomultiplier tube is used for imaging [10]. The detector is mechanically scanned across the area of interest to obtain the 2D image. A disadvantage of these scanned systems is that only a small portion of the decaying activity is being measured due to their limited field of view for scanning. Therefore, they are unsuitable to study the dynamics of the functioning of an organ because a long time is required to view the area of interest [3]. However, by the development of stationary gamma camera systems, which are made up of multichannel collimators and an array of photomultiplier tubes behind a large sodium iodide scintillating crystal [5], these limitations are now overcome in modern nuclear imaging technology. It is now possible to monitor larger areas at once and make a series of images indicating the distribution of the radioactive material at different time intervals.

In SPECT, single photon emitters, such as Tc-99m that emits a single gamma ray photon of energy 140 keV and has a half-life of about six hours, are used as radioactive isotopes for the reconstruction of their distribution formed inside the body [1]. Similar to nuclear medicine imaging, the detection of these photons in SPECT is done with gamma cameras. Multiple SPECT scans are performed from various angles by using one or more gamma cameras mounted on a computer-controlled rotating gantry. The gantry circles the patient at predetermined increments and by computer methods similar to those used in CT, a 2D image of tracer distribution in multiple organ sections is obtained [7], [11].

Scattering of the gamma ray photons in both the body and the collimator cause serious problems in SPECT image reconstruction. At 140 keV, Compton scattering is the most probable interaction of a gamma ray photon with body tissue [12]. Some photons which experience Compton scattering may be deflected outside the gamma camera's field of view or they may be scattered additional times and eventually get absorbed by the body. In either case, the photons are considered lost to the detection

process [13]. It is possible for a Compton-scattered photon to be scattered into the gamma camera's field of view. Such photons however do not carry directly useful information about the distribution of radiopharmaceutical within the body since they do not indicate from where within the body they originated. As a result, the detection of scattered photons in SPECT leads to loss of image contrast and a technically inaccurate image [1]. Absorption of the photons is another phenomenon that results in a reduction in the number of photons reaching the detector. Therefore, attenuation correction methods are used in SPECT to compensate for absorption effects [7]. Although SPECT imaging resolution is not as high as PET, the practical and economic aspects of SPECT instrumentation make this mode of emission tomography attractive for clinical studies [1].

In PET, positron emitting radioisotopes (for example, C-11, N-13, O-15, or F-18) are used to obtain their distribution inside the body. As a positron annihilates by a collision with a free electron within the body, two coincident gamma ray photons each having an energy of 511 keV and moving in approximately opposite directions are produced [5]. These photons are detected by an array of detectors that surrounds the patient. The PET detector is set up to accept events in which both annihilation photons are detected in coincidence. The detection of these photons serves to identify a line along which the original decay must have occurred. From a large number of such annihilation events, it is possible to reconstruct the original distribution of radioisotopes and to map a two-dimensional image of the area [3].

One of the advantages of PET is added sensitivity which is obtained by naturally collimating the photons through a physical process, without the use of absorbing collimators. Absence of physical collimators increases the sensitivity of PET over SPECT [7]. PET tracers also possess advantages over SPECT tracers because they have a relatively short half-life which reduces the time of exposure to the patient. For example, F-18 has a half-life of under 2 hours and C-11 of only 20 minutes [5]. The main disadvantage of the PET imaging system is the requirement of a large and expensive hospital cyclotron to produce many of the desired positron-emitting elements and the associated radiopharmaceutical laboratory.

PET is powerful in its ability to assess the level of metabolic activity and functioning of various systems of the human body. It is useful clinically in patients with certain conditions affecting the brain and the heart as well as in patients with certain types of cancer. PET scans are used for diagnosing brain tumours and the effect of strokes on the brain, along with various mental illnesses [14]. They are also used in brain research and the mapping of brain functions. In cancer patients, PET scans can evaluate whether or not a particular mass lesion is malignant; anatomic imaging modalities can only detect the presence or absence of the mass. In those diseases that cause abnormalities of blood flow or metabolism, PET can detect these diseases at a time when the anatomic imaging studies are normal [1].

The fourth main imaging technique is Nuclear Magnetic Resonance which generates images of the human body from the magnetic resonance signals produced by the hydrogen nuclei present in water and fat [15]. The technique utilises the fact that nuclei have a spin or magnetic moment which can interact with an applied external magnetic field. In the absence of the magnetic field, the nuclei, for example in tissues with a high water content, are randomly orientated. When they are placed in a strong magnetic field, they can only have two orientations, each with a slightly different energy. In the lower energy state the nuclei align parallel to the magnetic field, while in the higher energy state the nuclei align antiparallel to the field [1],[6]. The interaction between the magnetic force and the angular momentum of the spinning nuclei causes the nuclei to precess around the magnetic field [7]. This precessing occurs at a definite frequency $\omega_\circ$, known as the Larmor frequency, which is proportional to the external magnetic field, and given by

$$\omega_\circ = \gamma H_\circ \tag{1.3}$$

where γ is the gyromagnetic ratio, a property of the nucleus, and $H_\circ$ is the strength of the magnetic field. For a field of 1 Tesla, the resonance frequency of protons is 42.58 MHz [3]. A series of short radio frequency pulses, which are tuned to the Larmor frequency of the proton, is applied to the nuclei in the magnetic field. This causes some of the protons to undergo transitions to the higher energy state. After removal of the pulses, the excited protons return to their equilibrium state by emitting a similar radio frequency called the free induction decay (FID) which is used for image

formation [6].

The components of the NMR imaging systems are a cylindrical magnet capable of generating a uniform magnetic field, a radio frequency receiver coil system to deliver the radio frequency pulses and record the FID signals, another coil system to control the magnetic field gradients and a computer for data collection, image reconstruction and display [7]. A magnetic field gradient, which is a variation in the magnetic field with respect to position, is applied across the body (for example, along one dimension) in addition to the main magnetic field. This causes the nuclei at different spatial locations to experience different magnetic fields [1],[7]. The signal received by the coils is therefore a complex sum of signals produced at different resonant frequencies. Fourier analysis is used to resolve the signal into discrete frequencies, allowing each signal to be assigned to different points in the body [16]. The field gradient can be applied at several angles (between 0 and 359 degree), the NMR spectrum is recorded for each gradient, and sufficient data can be built up to reconstruct the NMR image in a way similar to that in which a CT picture is constructed.

NMR imaging has the important property that it does not employ ionising radiation. Although there is no evidence of any deleterious long-term or short-term effects reported at the exposure levels encountered in current NMR measurements, both patients and staff are exposed to different types of magnetic and electromagnetic field [1]. The large and expensive equipment involved, and the requirement of keeping the patient motionless in order to acquire the data are the main limitations in the use of NMR imaging technique [15],[17].

1.2 Medical Optical Tomography

Optical Tomography is a novel medical imaging technique that tries to reconstruct the spatial distribution of optical properties within the body based on measurements of transmitted near-infrared (NIR) light intensities. NIR light offers the potential for medical diagnostic and functional imaging in biological tissue [18],[19]. Therefore, the use of NIR light for biomedical imaging has received great attention in recent

years and become a fast growing area of research, see [20],[21],[22] and the references therein.

Imaging with NIR light presents several advantages over existing conventional medical imaging modalities. First, the absorption of light by biological tissues is very small in the NIR wavelength range. For example, the absorption coefficient μ_a of biological tissue is typically within the range 0.001-0.01 mm^{-1} [23]. Therefore NIR light can easily penetrate deeply into the tissues and emerge bearing clues about tissues through which it has passed. Because of the small absorption, NIR light is well tolerated in large doses without generating a "cooking" effect (deposition of heat) in tissue. Second, unlike ultraviolet (UV) light, the energy of NIR photons is generally small compared to the that required to break chemical bonds. Therefore it can be safely used in clinical diagnosis without great concern of any ionising or mutagenic effects [24]. Third, display of contrast between soft tissues, which is indistinguishable with the other existing techniques, can be accomplished due to their different optical properties (absorption, scatter, refractive index) at NIR wavelengths [25]. Fourth, the combination of NIR imaging with spectroscopic techniques allows physicians functional information of biological tissues to be obtained. For example, NIR absorption spectroscopy has been used to monitor the oxygenation state of tissue in clinical applications [26]. In addition to these advantages, light-based imaging modality should be inexpensive and portable in comparison to many established techniques such as MRI, CT, and PET [8],[27].

On the other hand, the major disadvantage of using NIR light is that NIR photons, unlike x-rays, do not travel straight through tissue but instead are scattered many times before either exiting the tissue or being absorbed. For example, the scattering coefficient μ_s of biological tissue is on the order of 10 mm^{-1} [28]. In other words, photons are scattered 10 times, on average, per 1 mm travelling distance inside tissue. This multiple scattering of light in biological tissues causes two separate problems that arise in the process of forming an image. First, the distribution of photon pathlengths through the medium does not allow one to directly apply the Beer's law and thus prevents a straightforward characterisation of tissue in terms of absorption or scattering properties. Second, the multiple scattered photons travelling diffusively

through the medium blur images. The image resolution and contrast can severely be degraded by the detection of those multiply scattered light [29].

A variety of experimental techniques have been developed in order to obtain the transmission measurements used for optical imaging of tissues. These may be divided into three categories: continuous-wave [30], time-resolved [31],[32], and intensity modulated systems [33],[34]. These experimental techniques proposed to acquire data suitable for imaging through tissues are reviewed by Hebden et al. [25] and Delpy et al. [26].

It appears that the earliest attempts at optical imaging occurred in the Victorian age when physicians used candlelight to transilluminate the female breast. Then Curling, an English physician, used a flare lattern to transilluminate the scrotum of his patients to screen for tumours in 1843 [8]. Later, in 1929, Dr. Max Cutler reported on the use of light to image the breast [35]. Blurred optical images were obtained due to the effects of light scattering in these early experiments. Over the past two decades efforts to use NIR light to produce images of the inner structures of the human body have continued. These include the imaging of human blood vessels and fluid collection by Beuthan [8], the monitoring of changes in the oxygenation of the brain in the intact cat head by Jöbsis [36], the measurement of human brain blood flow and oxygenation by Edwards et al. [37], the noninvasive detection and classification of breast tissues and tumours using scattering and absorbance properties in an "optical biopsy" system by Chance et al. [38], the imaging of animal bodies and human brain by Benaron [39].

Today, NIR imaging research has been focused on several clinical applications [25], [28]. These include detection of breast tumours, brain hematomas and tumours, prostate tumours and monitoring of tissue oxygenation, metabolic and/or functional states [24]. A good review on clinical applications of optical imaging can be found in [40].

Since objective of this research is the numerical modelling of photon transport in biological tissues, the next section is devoted to the discussion and a review of the literature on the photon migration models.

1.3 Photon Transport Models in Optical Tomography

Optical imaging requires a model for calculating the photon transport through tissues. Models may be divided in two groups: stochastic models that involve following individual photon interactions within the host media, such as Monte Carlo [41], or deterministic models that are based on a partial differential equation, such as the diffusion equation and it is usually combined with finite-difference [42] or finite element [43],[44] methods. The former model is a totally different approach in which the particle transport process is simulated statistically and directly on a computer without referring to any differential equation [45]. All quantities determined by the stochastic methods are averages over the behaviour of many particles. However, in the deterministic approach, these averages, which are exact quantities, are calculated through their balance properties expressed in the differential equation of interest [46].

In the rest of this chapter, the most widely used models for photon transport are presented and their limitations are discussed. As the solution procedure employed in this thesis is based on the Finite Element-Spherical Harmonics methods (FE-P_N), a brief description of spherical harmonics methods is also included. A more detailed explanation of the FE-P_N method is given in Chapter 2.

1.3.1 Monte Carlo Method

In the Monte Carlo (MC) method, the life histories of a significant number of photons are individually tracked from the time of their birth, through their various interactions with the host media till they are either escaped from the the surface or absorbed (or have negligible contribution) within the media. The transport process is simulated by the use of random, statistical sampling method to generate the probability distribution of the expected characteristics of the particles. Therefore a random number generator is generally included in the MC computer codes to produce the sequence of random numbers [47]. The following of a photon begins with the determination

of its point at birth as a source particle. The position and types of interactions that the photon has had are then found. Between interactions, the particle may stream freely till a leakage or capture event that terminates the life history of the photon [48]. A detailed discussion and the procedure for the determination of the parameters through a photon history can be found in Cashwell and Everett [49], Spanier and Gelbard [50] and Goertzel and Kalos [51].

The MC photon simulation method has the advantages of being conceptually simple and handling complex geometries and optical inhomogeneities [52]. The disadvantage of the method is that in order to obtain adequate statistics, it is necessary to track a large number of photon histories which makes the method expensive in computational time [53]. Variance reduction techniques to decrease statistical error in MC simulations have been reviewed by Carter and Cashwell [54].

Many researchers have applied the MC method to tissue optics. Among them, comparisons between diffusion theory and MC simulation were made for a semi-infinite medium representing a typical mammalian soft tissue in the red and near infrared regions of the spectrum by Flock et al. [55]. The optical absorption and scattering coefficients for specimens of normal and diseased human breast tissue were determined using MC simulations for wavelengths in the range 500-1100 nm by Peters et al. [56]. Light transport in tissue was modelled with MC to calculate fluence rates within beef liver, where the optical coefficients of beef liver were determined experimentally on both tissue samples [57]. Various characteristics of photon diffusion process in biological tissues were examined for a semi-infinite homogeneous medium and a homogeneous slab using MC simulation technique [58].The influence of layered-tissue structure on reflectance measurements were investigated with MC method and compared with the experimental results by Hielscher et al. [59]. A fast semi-analytical MC numerical simulation was proposed for time-resolved light-scattering problems by Tinet et al. [60]. Time-dependent and the Laplace-transformed form of the MC solutions were both compared with corresponding finite element transport results for a homogeneous cylinder and a phantom consisting of an infinite cylinder with 3 annular regions [61].

1.3.2 Spherical Harmonics (P_N) Method

The spherical harmonics approximation is a classical method to solve the Boltzmann transport equation [62],[63]. The basic idea of the method is to expand the directional dependence of the photon density or intensity, $\phi(\mathbf{r}, \mathbf{\Omega})$, in the form of a series of spherical harmonics $Y_{lm}(\mathbf{\Omega})$ [47]. These are a complete set of functions in the angular variables that determine the direction of the unit vector $\mathbf{\Omega}$ [64]. Substitution of this representation of the photon intensity, truncated to a finite number of terms N, into the original photon transport equation and employing the orthogonality of spherical harmonics, gives a coupled set of equations named the P_N equations [62]. These equations can then be used as the basis for numerical methods such as finite differences and finite elements for solving the transport equation [45].

The method was first proposed by Jeans [65] for study of radiative transfer in the atmosphere and was modified by Mark [66],[67] to solve neutron transport problems. It has been widely used by researchers for one-dimensional radiative transport problems [68],[69],[70]. The spherical harmonics approximation was extended by Davison [63] to other geometries than slab which lead to high-order moments of the photon intensity. The application of the method to optical imaging problems has been considered by researchers [71],[72],[73]. A P_3 approximation to the transport equation was used by Star [74] and the results of light propagation in a slab geometry were compared with diffusion theory and MC calculations. Recently, Boas et al. [75] employed again the P_3 approximation for an infinite homogeneous media. They determined optical properties of highly absorbing media solving the frequency-domain diffusion equation and transport equation within P_3 approximation.

In this work, a P_N methodology [76],[77], is applied to the solution of optical tomography problem. It is based on a variational formulation for the second-order form of the Boltzmann transport equation. The methodology allows one to go to high-orders of angular approximation for modelling photon angular dependence and scattering phase functions.

1.3.3 Diffusion Approximation

Expansion of the Boltzmann transport equation in spherical harmonics results in a series of linear partial differential equations of increasing order [78]. Since the simplest one is the P_1, or diffusion equation, the diffusion approximation has become a standard approach to model the photon propagation in turbid media [79],[80]. Furthermore, solution for the inverse problems of photon migration in the literature are almost exclusively based on the diffusion theory approximations [81]. As it has been demonstrated by experimental and theoretical work, the diffusion equation is valid under the condition which the absorption coefficient is small compared to the scattering coefficient [82]. At NIR wavelengths (between 600 and 900 nm), this is the case for transillumination of tissue where, typical parameter ranges are μ_a=0.01...0.1 mm^{-1} and μ_s=10...100 mm^{-1}. Therefore, the diffusion theory becomes an appropriate approximation for many biomedical applications [23]. The derivation of the diffusion equation has been given in detail in numerous books, for example [83],[84] and the diffusion equation has been solved for a variety of geometries in tissue optics by Arridge et al. [85].

Although media such as skin, bone, brain matter and breast tissue satisfy the condition given above, there also exist non-scattering clear layers in the body, particularly cerebrospinal fluid (CSF) in the head and blood vessels where the absorption is comparable with the scattering. The effects of those regions were examined by some researchers [86],[87] and these studies showed that the diffusion theory is not good at modelling these situations. Moreover, the problems involving smaller thicknesses of tissue cannot correctly be described by the diffusion approximation because they may not be scatter dominated [43],[61]. The diffusion approximation also breaks down in regions where the optical properties change dramatically from the surrounding region (strong discontinuities), as mostly encountered in tissue [27], and structures near to the boundary [61]. In addition to these limitations, description of an anisotropic source and anisotropic photon scattering cannot directly be taken into account, within this approximation [72],[88].

All these shortcomings of the diffusion approximation have demonstrated that a

more accurate model of photon transport is required. Higher-order approximations to the Boltzmann equation especially need to be employed to describe and analyse photon migration through, for example, the clear regions and blood vessels where the diffusion theory breaks down [89],[27]. In this thesis, the full higher-order transport method, FE-P_N, is employed. The methodology for FE-P_N is adopted from studies involving neutron transport in nuclear materials [90]. Also the main goal of this thesis is to apply this method to the various optical tomography problems to show the potential of the method together with the inadequacy of the diffusion approximation.

1.3.4 Finite Element Method

The theory of the finite element method (FEM) was initially developed for structural mechanics and elasticity in the mid-1950s. Since then, applications of the method have been rapidly extended to the solution of various problems in almost all branches of applied mathematics, engineering and physics [45]. FEM has now become one of the most successful and versatile techniques for most of the areas. The ability of the method to handling complex, irregular geometry and its strong supporting mathematical foundation are the main reasons for its success [45].

In contrast to the finite difference method (FDM) that is usually based on differential formulations, the FEM is based on integral formulations. The basic idea of FEM is to subdivide the problem domain into a finite number of subregions called *elements*. Within an element, the solution is approximated by local piece-wise polynomial trial functions (shape functions). All these small elements are then assembled together. Provided that the boundary conditions of the problem are satisfied, a unique solution can be obtained to the overall system of linear algebraic equations with a large, sparsely-populated stiffness matrix. Two basic approaches for generating FEM formulations are used: weighted residuals and variational methods.

Weighted Residual Methods

The weighted residuals is a technique that involves two steps: the first step is to assume an approximate or trial solution which satisfies the governing differential equation and boundary conditions. Substitution of this approximate solution into the differential equation leads to an error called the residual. For exact solution, the residual should be zero at all points of the solution domain. The objective of the method is the minimisation of this residual to obtain an accurate solution to the original equation [91],[92]. The choice of weighting to obtain the residual is arbitrary, but the most popular methods are referred to as point collocation, subdomain collocation, least squares and Galerkin.

Weighted residual technique for neutron transport was first suggested in the early 1970's [93]. The method was used subsequently by Martin [94] to solve the first-order Boltzmann equation for both steady state and time dependent neutron transport problems. Later, the solution of the second-order even-parity form of the transport equation using a weighted residual technique was obtained by Fletcher[95]. The technique has been discussed in detail in Crandall [96], Zienkiewicz [97], Collatz [98], and Fletcher [99].

Recently, Arridge et al. applied Galerkin formulation to solve the diffusion equation for modelling photon transport in tissue [44]. Later, the application of FEM to the inverse problem was extended by Schweiger et al. [88].

Variational Methods

The analysis of many physical problems frequently requires the determination of a function which is the solution of a differential equation governing the behaviour of the system under consideration. In some circumstances, however, the physical problem can also be formulated in a variational form and then an alternative solution approach may be adopted, which consists of determining the function that makes a certain integral statement (or functional) stationary [97]. The variational formulation

of a problem often has advantages over the differential formulation as a means for obtaining an approximate solution. It is easier to deal with the functional, since the functional has lower-order derivatives than the differential operator [101]. Often it is possible to have many different variational formulations that correspond to the same problem [102]. If the problem possesses two variational formulation, it is possible to find upper and lower bounds on the functional by minimising one functional and maximising another functional of a different form [64]. Moreover, the use of variational methods, from a purely mathematical point of view, is useful as it sometimes proves the existence of a solution [64]. A variational form can be derived from a differential equation by using one of the standard approaches such as the Euler-Lagrange approach, method of bi-linear functionals or least-squares methods [97].

In the classical Euler-Lagrange approach, a functional is developed for a given partial differential equation, which gives the original equation as its Euler-Lagrange equation on its first variation [47]. In order to develop such functional, the partial differential equation has to be self-adjoint [45] and of even-order [100]. Thus to apply this method in neutron transport, one has to use even-parity or odd-parity second-order transport equation, because the term $\mathbf{\Omega} \cdot \nabla\phi$ in the Boltzmann equation is not self-adjoint [45]. A comprehensive treatment of this theory is given by Kaplan and Davis [102] and detailed accounts of this approach can be found in [94], [103].

The objective of the method of bi-linear functionals is the development of a bi-linear functional on the basis of second-order even and odd parity equations and the properties of leakage and removal operators [47]. Ackroyd employed the method to derive a maximum principle for even-parity transport equation [104]. The method was used for the study of various one-dimensional slab geometry problems [105] and extended to two-dimensional problems by Ackroyd and Grenfell [106]. The variational bounds on local integral quantities were determined and linear anisotropic problems were also studied with this method [107]. The bi-linear functionals method, based upon the extension of Vladimirov's principle [108], was applied by de Oliveira [76] to multi-dimensional and multi-group (energy) cases for the general case of anisotropic scattering.

In the standard least-squares approach, an approximate solution is inserted into the original differential equation and then the sum of the squares of the residual, or error, at each point in the problem domain is required to be minimised [91]. A generalised least-squares method was given by Ackroyd for neutron transport problems [109],[110]. The method was used to generate variational principles for both first- and second-order forms of the transport equation and for both continuous and discontinuous trial function across the interfaces of elements [100],[111]. The method was also employed by Ackroyd in order to develop well-behaved weighted-residual approaches [112]. Various slab geometry problems were solved employing a least-squares principle with the help of discontinuous finite elements. Ackroyd and Nanneh [113] showed that this approach can be employed to determine the upper and lower bounds on some of the global characteristics of a system.

1.4 Scope of the Thesis

This thesis is concerned with the solution of Optical Tomography problems in highly scattering and low absorbing media. The linearised one-speed Boltzmann transport equation, which describes the migration of monoenergetic photons through a random media, is solved for this purpose by using the Finite Element-Spherical Harmonics method. The two themes of the thesis are: (i) the description and applications of the FE-P_N forward model to solve photon propagation problems within a densely scattering media with high-order transport approximations, and (ii) the derivation and applications of the non-perturbative iterative reconstruction model based on the transport equation for the solution of inverse scattering imaging problems.

In the next chapter the use of the particle transport equation for the propagation of light in tissues is explained and the basic definitions of two phenomena (absorption and scattering), which occur when light interacts with tissues is briefly given. The one-speed Boltzmann transport equation with the appropriate initial and boundary conditions is introduced along with its second-order, even-parity form. Variational methods, in particular the Ritz procedure is described. Finally, the FE-P_N method,

employed in this thesis as a tool to solve the Boltzmann transport equation, is presented.

Chapter 3 contains results of the FE-P_N forward model for various one-dimensional slab and two-dimensional geometry test cases. In the first part of the chapter, time-dependent results are given. FE-P_N forward model results obtained with diffusion approximation and higher-order angular approximations are compared for simple homogeneous and inhomogeneous media to show the limitation of the diffusion theory when absorption is increased. Comparisons are also made between the FE-P_N model and an independent MC model for isotropic and also non-isotropic problems to demonstrates the validity and accuracy of the present model. In the second part of the chapter, solutions of time-independent form of the transport equation are presented to examine limitations of the diffusion approximation in various 1D and 2D cases of realistic situations, e.g. large and optically dense media representing the brain.

The Reference Cross Section Model (RSCM) is introduced in Chapter 4 for the solution of inverse scattering problem. First- and second-order forms of the model are given enabling the formulation of the inverse problem as a system of integral equations used in iterative reconstruction algorithm. The image reconstruction algorithm is described as a final section of the chapter.

Results of the reconstruction algorithm are given in Chapter 5. This chapter demonstrates the performance and capabilities of the reconstruction procedure by applying the algorithm to FE-P_N and MC data. Images of various test cases for the recovery of the absorption coefficient are presented.

Finally, a discussion of the results obtained and proposals for further development are presented in Chapter 6. In the appendices, some auxiliary information are covered. Appendix A is particularly important, as it outlines and lists the program that has been developed to calculate the expansion coefficients of Legendre polynomial for the scattering kernel. The definitions of parameters appearing in the Mie scattering phase function formulae are given in appendix B and in appendix C, a brief specification of the FE-P_N radiation transport code EVENT and the solution strategies implemented in EVENT are introduced. In appendix D, properties of Legendre polynomials and

spherical harmonics are given and in the last appendix, the definition of direct product of matrices and its properties are introduced.

Chapter 2

Solution of the Photon Transport Equation

This chapter is concerned with the theoretical background of the Finite Element-Spherical Harmonics forward model employed to solve the problem of light propagation in biological tissues. The chapter begins with a brief introduction to forward problems, then describes light transport phenomena in biological media, and then defines the basic optical properties of tissue for the migration of light, e.g. the absorption and scattering parameters and the scattering phase function. The second-order even-parity form of the Boltzmann transport equation for photons for the general case of anisotropic scattering is derived and the even-parity equation is formulated in a variational form by defining a quadratic functional. The Ritz procedure for deriving the Finite Element-Spherical Harmonics as a system of linear equations is then described.

2.1 Introduction

Having a computable and reliable model to describe photon transport in tissue is essential in the medical application of optical radiation. Problems involving light propagation may be expressed in terms of two different classes: *forward* and *inverse*

problems. Forward problems are crucial in optical imaging studies because, initially, forward results are employed for the solution of inverse imaging problems. The present chapter focuses on the forward solution procedure that have been employed in this thesis. The description and details of the inverse problem are given in Chapter 4.

A forward problem can be defined as the determination of the distribution of photons, inside a host medium, from the given detailed description of geometry, source, and detector characteristics, using known optical properties. Forward problems form the most common class of transport problems and have applications in nuclear reactor theory, plasma physics, and gas dynamics as well as in radiation transport [45]. Solutions to forward problems in photon transport, in general, can be obtained by using conventional numerical techniques, which have been developed to solve neutron transport problems in nuclear engineering, such as the discrete ordinates or integral transport methods. A comprehensive review of forward solution methods can be found in Sanchez and McCormick [114].

Because different physical principles are involved, forward problems vary among fields of application. For example, forward problems in x-ray computed tomography differ from those in optical tomography because x rays and optical radiation interact with biomedical tissues in different ways. The most common forward solution methods for calculating light transport through tissue were given in section 1.3. The solution method described in this thesis is a variational Finite Element-Spherical Harmonics approach, where the spatial and angular variables are expanded using finite elements and spherical harmonics, respectively. This solution procedure is implemented in EVENT (EVEn-parity Neutron Transport), a general purpose radiation transport code, for the solution of the second-order even-parity form of the photon transport equation with anisotropic scattering and sources. This chapter is concerned with the theoretical basis of the FE-P_N method together with the outlines of the solution procedure employed in the radiation transport code EVENT.

2.2 Photon Propagation and Optical Properties of Tissue

The propagation of light in tissue is a question of growing concern in many medical applications such as disease diagnosis and medical imaging using optical techniques [24],[115]. The interaction of light and tissue is, fundamentally, described by the wave equation of classical electrodynamics (Maxwell equations) [116],[117]. Although this is physically a realistic model, the use of Maxwell's equations has not yet found application in tissue optics because of its complexity arising from inhomogeneity of biological tissue and the lack of detailed information about tissue dielectric properties [52]. Instead, the preferred approach, and the one which we follow in this study, is called transport theory, also called radiative transport theory. The relationship between electromagnetic theory (Maxwell's equations) and radiative transport theory has been examined in detail by Fante [118] and de Boer [119]. In radiative transport theory, the wave properties of the light such as interference are ignored and the flow of energy through a medium containing random scattering and absorbing particles is considered [68],[116],[120]. The basic differential equation is the equation of transfer or its equivalent, the linearised Boltzmann particle transport equation used in the kinetic theory of gases and in neutron transport theory [52]. In this study, we employ the Boltzmann transport equation to describe the transport of photons since it is quite similar in form to that of the transport equation characterising radiative transfer [45].

From the viewpoint of transport theory, light propagation in biological tissues is due to the transport of individual photons and it is governed by the scattering and absorption of photons by the tissue [24]. When a single particle within the medium (e.g. a hemoglobin molecule or a cell constituent) is illuminated by a beam of photons, two phenomena may mainly occur: absorption and scattering. In absorption, a photon from the incident beam is absorbed by the particle and in scattering the photon collides with the particle and is scattered in a new direction [4],[45]. When photons are absorbed, they are completely removed from the beam and this results in a reduction in the intensity of the incident beam. Tissue optical properties are, therefore, characterised typically by the absorption coefficient μ_a, the scattering coef-

ficient μ_s, and the angular scattering probability distribution or phase function [121]. The definitions of those quantities are given briefly in the following subsections.

Absorption

Suppose a collimated beam of photons strikes perpendicularly a specified area of purely absorbing homogeneous medium of arbitrary thickness as indicated schematically in Figure 2.1. If a slab of infinitesimal thickness dx that is parallel to the surface is considered, the fraction of the photons falling on this thin layer can be written as

$$-\frac{dI}{I} = \mu_a dx, \tag{2.1}$$

where -dI is the decrease in the photons per unit area as the result of passing through the thickness dx of target material and $\mu_a[\mathrm{mm}^{-1}]$ is a material constant called the *absorption coefficient*. If this equation is solved for an incident beam intensity of I_0 at x=0, the intensity after a thickness x of the material or an exponential attenuation of the incident beam of the following form is obtained

$$I_x = I_0 exp(-\mu_a x). \tag{2.2}$$

The absorption coefficient can be expressed as the product of the atomic number or particle density [atoms or nuclei/mm^3] in the target material and the microscopic *absorption cross section* σ_a [mm^2]:

$$\mu_a = N\sigma_a. \tag{2.3}$$

If the medium has a homogeneous mixture of different absorbing compounds, then the absorption coefficient characterising the mixture is a linear superposition of the single contributions which themselves may vary with position, time, and energy:

$$\mu_a(\mathbf{r}, E, t) = \sum_i \mu_a^i(\mathbf{r}, E, t) = \sum_i N^i(\mathbf{r}, t)\sigma_a^i(E). \tag{2.4}$$

The inverse of the absorption coefficient represents the *absorption mean free path* λ [mm] which gives the average total (or scalar) distance (pathlength) between two successive absorption events.

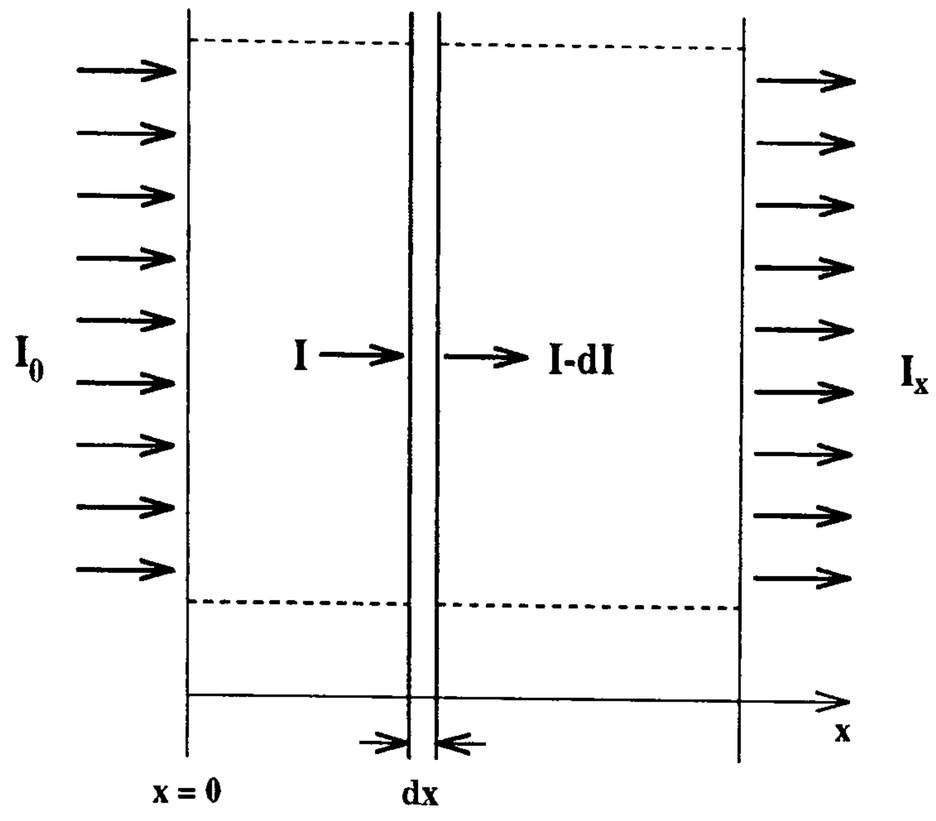


Figure 2.1: Attenuation of a collimated photon beam in passage through a slab.

Scattering

Scattering describes the effect where part of the incoming photons is scattered into other directions and therefore reduces the amount of photons in the original direction. The optical coefficients for soft tissues, (e.g. brain, liver, lung, skin) in the NIR range of wavelengths, 600-1300 nm, are $\mu_a \sim$ 0.01-1 mm^{-1} and $\mu_s \sim$ 10-100 mm^{-1}[120]. Therefore, the propagation of light in biological tissues, with typical mean free scattering pathlengths (distance between scattering events) of the order of 10^{-1} mm and with a source-detector separation of 1 mm or above, is characterised by multiple scattering events [17].

To understand the process involved in multiple scattering events, it is essential to investigate single scattering mechanisms. Scattering in optically thick media can be characterised by the scattering coefficient μ_s which is the probability per infinitesimal path length that a photon will be scattered by the tissue [52]. In order to include the angular dependence of photons emerging from collision, another parameter, called *differential scattering cross section* $\sigma_s(\mathbf{\Omega}' \rightarrow \mathbf{\Omega})$, is defined. This parameter is the probability that a photon moving initially in a direction $\mathbf{\Omega}'$ is scattered to a new direction $\mathbf{\Omega}$ [116],[117].

$$\sigma_s = \int_{4\pi} d\mathbf{\Omega}' \sigma_s(\mathbf{\Omega}' \rightarrow \mathbf{\Omega}). \tag{2.5}$$

The sum of the scattering and absorption cross section is called the *total* or *attenuation cross section* σ_t, and it gives the attenuation of the incident photon beam intensity due to absorption and scattering [83]:

$$\sigma_t = \sigma_a + \sigma_s, \tag{2.6}$$

In a similar manner the *scattering* and the *total attenuation coefficients* (mm^{-1}) can be written as the product of the particle density and the corresponding cross section:

$$\mu_s = N\sigma_s, \qquad \mu_t = \mu_s + \mu_a = N\sigma_t, \tag{2.7}$$

and if a medium consists of a mixture of scattering compounds or a homogeneous mixture of different nuclides, the total scattering and attenuation coefficients characterising the mixture are given by

$$\mu_s(\mathbf{r}, E, t) = \sum_i \mu_s^i(\mathbf{r}, E, t) = \sum_i N^i(\mathbf{r}, t)\sigma_s^i(E), \tag{2.8}$$

$$\mu_t(\mathbf{r}, E, t) = \sum_i \mu_t^i(\mathbf{r}, E, t) = \sum_i N^i(\mathbf{r}, t)\sigma_t^i(E). \tag{2.9}$$

A normalised form of the differential scattering cross section, called *the phase function*, is often used instead of $\sigma_s(\mathbf{\Omega}' \to \mathbf{\Omega})$. The phase function describes the angular distribution for a single scattering event [115]. It is a dimensionless probability density function for scattering from direction $\mathbf{\Omega}'$ to direction $\mathbf{\Omega}$ defined by [45]

$$f(\mathbf{\Omega}' \to \mathbf{\Omega}) = \frac{\sigma_s(\mathbf{\Omega}' \to \mathbf{\Omega})}{\sigma_s}, \tag{2.10}$$

with a normalisation condition

$$\int_{4\pi} d\mathbf{\Omega} f(\mathbf{\Omega}' \to \mathbf{\Omega}) = 1. \tag{2.11}$$

In most situations, the detailed description of the scattering phase function is not required or the form of the phase function is not known. In these cases, it may be adequate to characterise the phase function by a single parameter denoted by g, the average cosine of the scattering angle θ. Assuming scattering is independent of the incident photon direction ($\mathbf{\Omega}'$) and the scattered photon direction ($\mathbf{\Omega}$) and the phase

function is a function of the absolute value of the angle (θ) spanned by the two vectors $\mathbf{\Omega}'$ and $\mathbf{\Omega}$ [52], i.e.,

$$f(\mathbf{\Omega}' \rightarrow \mathbf{\Omega}) = f(\mathbf{\Omega}' \cdot \mathbf{\Omega}) = f(\cos\theta), \tag{2.12}$$

the mean cosine of the scattering angle is described by

$$g = \frac{\int_{4\pi} d\mathbf{\Omega}(\mathbf{\Omega}' \cdot \mathbf{\Omega}) f(\mathbf{\Omega}' \cdot \mathbf{\Omega})}{\int_{4\pi} d\mathbf{\Omega} f(\mathbf{\Omega}' \cdot \mathbf{\Omega})} = \langle \cos\theta \rangle . \tag{2.13}$$

This parameter is sometimes termed the anisotropy factor g corresponding to -1, 0, and 1 and describes highly backward, isotropic, and forward scattering, respectively. In biological media, scattering is typically highly forward-directed (anisotropic) with typical anisotropy factors g=0.9 for visible wavelengths [52],[115].

The use of diffusion theory for modelling NIR light propagation in tissues requires the scattering and absorption coefficients and the mean cosine of the scattering angle, g, rather than the detailed form of the scattering phase function. Monte Carlo and the radiative transfer theory (or transfer theory), however, require knowledge of absorption and scattering coefficients, and the phase function [122]. As the work described in this thesis requires solutions to the Boltzmann transport equation, it is necessary to adopt a scattering phase function formula. Therefore, a program has been developed during this work which is capable of calculating the scattering phase function values and the Legendre expansion coefficients for scattering kernel in the transport equation using three different formulae (see appendix A); Mie theory, Henyey-Greenstein (H-G) and Simplified Approximate Mie (SAM) Scattering Phase Function. It is the subject of the following parts to introduce these phase function formulae briefly.

The process of light scattering in tissues involves the laws of electromagnetic interaction, which are best represented by Maxwell's equations. Mie was the first physicist who established a theory to calculate the scattering phase function for spherically symmetric spheres, based on Maxwell's equation [123]. A detailed discussion of the theory can be found in one of the standard textbooks on this topic (e.g.,Kerker [124]). We adopted the Bohren and Huffmann Mie scattering code published in the appendix of Bohren and Huffman light scattering book [117]. The following parameters need

to be known in order to describe the Mie scattering problem: radius of the spherical particles (a), index of refraction of the sphere (m), index of refraction of the medium (real) (M) and wavelength in a vacuum (λ). The Mie scattering phase function formula is given as [125]

$$f_{MIE}(\cos\theta) = \frac{S_1(\theta)S_1^*(\theta) + S_2(\theta)S_2^*(\theta)}{2\pi \int_0^\pi [S_1(\theta)S_1^*(\theta) + S_2(\theta)S_2^*(\theta)] \sin\mu d\mu} \tag{2.14}$$

where $S_1(\theta)$ and $S_2(\theta)$ are two complex amplitude functions defined in appendix B and $S_1^*(\theta)$ and $S_2^*(\theta)$ are their complex conjugates, while $\mu = \cos\theta$, θ being the angle between the incident and scattered directions. As the Mie theory requires detailed information about the medium and the scatterers, its use is complicated and impractical in most cases.

Most researchers in biological optics fields use a formula proposed by Henyey-Greenstein in an astronomical paper [126] as the universal phase function. This is due to the simplicity of this formula as containing only one free parameter. It is defined as [127]

$$f_{HG}(\cos\theta) = \frac{(1-g^2)}{4\pi(1+g^2-2g\cos\theta)^{3/2}} \tag{2.15}$$

where θ is the scattering angle and g is the mean cosine of the scattering angle. Although the H-G formula is the most widely adopted one, it has been pointed out in the literature that this formula shows significant discrepancy in biomedical applications compared with the solutions from Maxwell's equations for the same mean cosine of the scattering angle [128]. A reasonably good agreement between Mie and H-G formula exists only for a mean cosine less than 0.8 [127] and the H-G formula shows big errors at forward scattering when compared with results from Mie theory [122].

In this work, we employed, for the first time, a new scattering phase function formula to describe the scattering profile (angular distribution). The formula, SAM, demonstrates much better agreement with Mie theory than the H-G phase function for biomedical media (with the mean cosine of scattering angles g>0.8). The SAM scattering phase function formula was proposed by Liu [122] as

$$f_{SAM}(\cos\theta) = K_S(1+\cos\theta)^{n_p} \tag{2.16}$$

where n_p is an independent parameter and K_S is the normalisation factor. n_p is a so-called "anisotropic index" given by

$$n_p = \frac{2g}{1-g} \tag{2.17}$$

where g is the mean cosine of the scattering angle. The anisotropic index n_p is limited to non-negative even integers. The larger n_p is, the stronger the forward scattering. Because n_p is the power of $(1 + \cos\theta)$ in the SAM phase function formula, it also specifies the number of Legendre expansion coefficients for the associated g value. For example, for an average cosine of 0.9, the value of n_p is equal to 18. This means that 18 coefficients can be obtained using SAM phase function formula for g=0.9. The normalisation factor, K_S, is

$$K_S = \frac{(n_p+1)}{2^{(n_p+2)}\pi} \tag{2.18}$$

Substituting the normalisation factor in equation (2.16), the SAM scattering phase function formula takes the following form

$$f(\cos\theta) = \frac{(n_p+1)}{2^{(n_p+2)}\pi}(1+\cos\theta)^{n_p} \tag{2.19}$$

2.3 The Boltzmann Transport Equation and the Even-Parity Form

The particle transport equation used in reactor core calculations and radiation shieldings, as well as radiative transfer analysis of stellar or planetary atmospheres, is younger (less than 40 years old) and simpler (being in a linearised form) than the original non-linear *Boltzmann equation* developed for the transport of molecules in a dilute gas. The fundamentals of modelling such transport phenomena can be found in several monographs [62],[63],[129], [130],[131]. In the present work, as mentioned earlier, the propagation of NIR light will be analysed in the same manner as is neutron transport and, accordingly, the linear Boltzmann transport equation is considered. The transport equation describes a transport process by determining the distribution of photons in a host medium, taking account of the motion of the photons and their interaction with the medium. For the flow of monoenergetic photons in a given

volume V (Figure 2.2a) the one-speed linear Boltzmann transport equation can be written as:

$$\frac{1}{v}\frac{\partial\phi}{\partial t} + \mathbf{\Omega}\cdot\nabla\phi(\mathbf{r},\mathbf{\Omega},t) + \sigma_t(\mathbf{r})\phi(\mathbf{r},\mathbf{\Omega},t) = \int_{4\pi} d\mathbf{\Omega}'\sigma_s(\mathbf{r},\mathbf{\Omega}'\rightarrow\mathbf{\Omega})\phi(\mathbf{r},\mathbf{\Omega}',t) + S(\mathbf{r},\mathbf{\Omega},t). \tag{2.20}$$

where $\mathbf{r}$ is the position vector of a particle or photon moving along the direction given by the unit direction vector $\mathbf{\Omega}$ at time t (Figure 2.2b) and $\phi(\mathbf{r},\mathbf{\Omega},t)$ is the particle angular flux or photon intensity; v is the photon characteristic velocity; $\sigma_t(\mathbf{r})$ is the total or removal position-dependent macroscopic cross section (absorption+scattering); $\sigma_s(\mathbf{r};\mathbf{\Omega}'\rightarrow\mathbf{\Omega})$ is the differential macroscopic scattering cross section and $S(\mathbf{r},\mathbf{\Omega},t)$ is the source term.

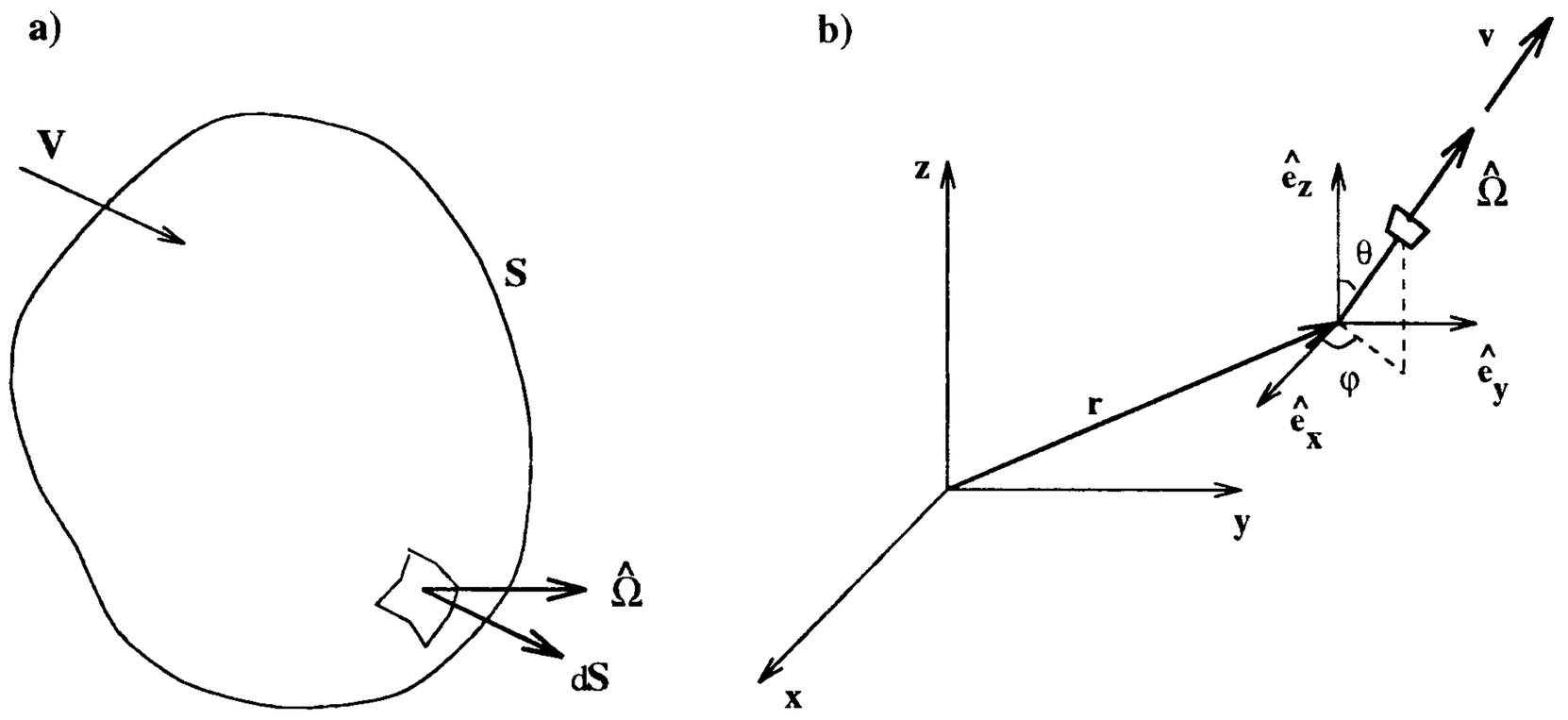


Figure 2.2: (a) An arbitrary volume V with surface area S; (b) The position and direction variables of a particle in spherical coordinates.

Although we are dealing with photons in this study, because of the standard procedure used in the literature for the derivation of the second-order form of the transport equation, we will use the same terminology as used in neutron transport theory. Therefore, instead of using, e.g. photon and intensity, we will use particle and angular flux in the rest of this chapter.

Equation (2.20) is a statement of particle conservation and gives the time rate of change of the number of particles by a balance relation between the various mecha-

nisms by which particles can be gained or lost from the volume element considered. Each term in this equation posses a clear physical significance and can be described in terms of one of those gain or loss mechanisms. As the first term on the left represents the time rate change, the second and third terms represent the number of photons leaving the volume V due to streaming through the surface S and collisions in V, whilst the terms on the right of the equation represent the number of particles arising due to scattering from other directions and sources, respectively [90].

In order to complete the mathematical description of particle transport, the initial (at t=0) and boundary conditions must be defined. The initial condition can be chosen to specify the initial value of the angular flux for all positions and directions:

$$\phi(\mathbf{r}, \mathbf{\Omega}, 0) = \phi_0(\mathbf{r}, \mathbf{\Omega}) \tag{2.21}$$

Boundary conditions can be a bare or vacuum surface, a reflecting and periodic conditions, internal interfaces, and others [45],[132] as depending on the particular problem of interest. In this study, two types of boundary conditions are considered on the external boundaries of the problem domain: the bare surface (or vacuum) condition and surface source condition. The first condition means that no particles are entering the body from the outside [47], i.e:

$$\phi(\mathbf{r_s}, \mathbf{\Omega}, t) = 0 \qquad \mathbf{\Omega} \cdot \mathbf{n} < 0, \ \textit{for all } \mathbf{r_s} \textit{ on } S, \tag{2.22}$$

where, $\mathbf{r_s}$ is a point on the surface S and $\mathbf{n}$ is the outward normal to the surface S. For the surface source boundary condition, an incoming angular flux $T(\mathbf{r}, \mathbf{\Omega}, t)$ is considered at surface S [47],[133], i.e.

$$\phi(\mathbf{r_s}, \mathbf{\Omega}, t) = T(\mathbf{r_s}, \mathbf{\Omega}, t), \qquad \mathbf{\Omega} \cdot \mathbf{n} < 0, \ \textit{for all } \mathbf{r_s} \textit{ on } S. \tag{2.23}$$

The Boltzmann transport equation is known as "integro–differential" since it contains both derivatives in space and angle as well as integrals over angle. It is a linear equation in the unknown dependent variable $\phi(\mathbf{r}, \mathbf{\Omega}, t)$. However, the complexity of the transport equation as having seven independent variables ($\mathbf{r} = x, y, z; \mathbf{\Omega} = \theta, \varphi; E; t$) in its general form either limits its utility to extremely simple situations (one dimension) or requires the use of numerical schemes to generate a solution [83]. An elegant

and powerful numerical technique that has been applied to transport problems is the calculus of variations. The characterisation of a physical problem by a variational principle is useful for the derivation of practical approximation procedures. The variational principle has been discussed widely on the literature as a point of departure for the application of the finite element method to neutron transport problems [134],[135],[136], [137],[138],[139]. Details of the variational principles associated with the solution of neutron transport problems, using the finite element approximations, can be found in Ackroyd [140].

Several alternative variational principles may be used to derive finite element discretisations of the transport equation. Two principles exist which are based on the second-order, self-adjoint forms of the transport equation in terms of either the even- or the odd-parity components of the angular flux. The use of these two principles for finite element approximations permits reduction of the angular domain of the problem to one-half of that which would be required if the angular flux was retained as the dependent variable [76],[141].

In the present study, the second-order even-parity form of the transport equation is used. Here a brief derivation of this form of the transport equation is presented. In this derivation, only the steady-state form of the Boltzmann transport equation is considered. The one-speed, steady-state form of the transport equation can be written as

$$\mathbf{\Omega} \cdot \nabla \phi(\mathbf{r}, \mathbf{\Omega}) + \sigma_t(\mathbf{r})\phi(\mathbf{r}, \mathbf{\Omega}) = \int_{4\pi} d\mathbf{\Omega}' \sigma_s(\mathbf{r}, \mathbf{\Omega}' \rightarrow \mathbf{\Omega})\phi(\mathbf{r}, \mathbf{\Omega}') + S(\mathbf{r}, \mathbf{\Omega}). \quad (2.24)$$

Time discretisation schemes that are implemented in the radiation transport code EVENT for the solution of time-dependent Boltzmann transport equation, equation (2.20), are briefly given in appendix C.

Expansion of the Scattering Kernel

In most practical applications, it can be assumed that the scattering collisions have rotational symmetry [83]. This means that the differential scattering cross section $\sigma_s(\mathbf{r}, \mathbf{\Omega}' \rightarrow \mathbf{\Omega})$ does not depend on the incident and scattered particle direction, but

only on the change in particle direction (see Figure 2.3). This is most conveniently expressed in terms of the dependence upon the cosine of the angle, the so-called *scattering angle* θ, between the two directions ($\mu_0 \equiv \cos\theta$). In the general form, it can be written as the dot product between the unit direction vectors ($\mu_0 = \mathbf{\Omega}' \cdot \mathbf{\Omega}$). Thus the differential scattering cross section takes the following form:

$$\sigma_s(\mathbf{r}, \mathbf{\Omega}' \to \mathbf{\Omega}) = \sigma_s(\mathbf{r}, \mathbf{\Omega}' \cdot \mathbf{\Omega}) = \sigma_s(\mathbf{r}, \mu_0). \tag{2.25}$$

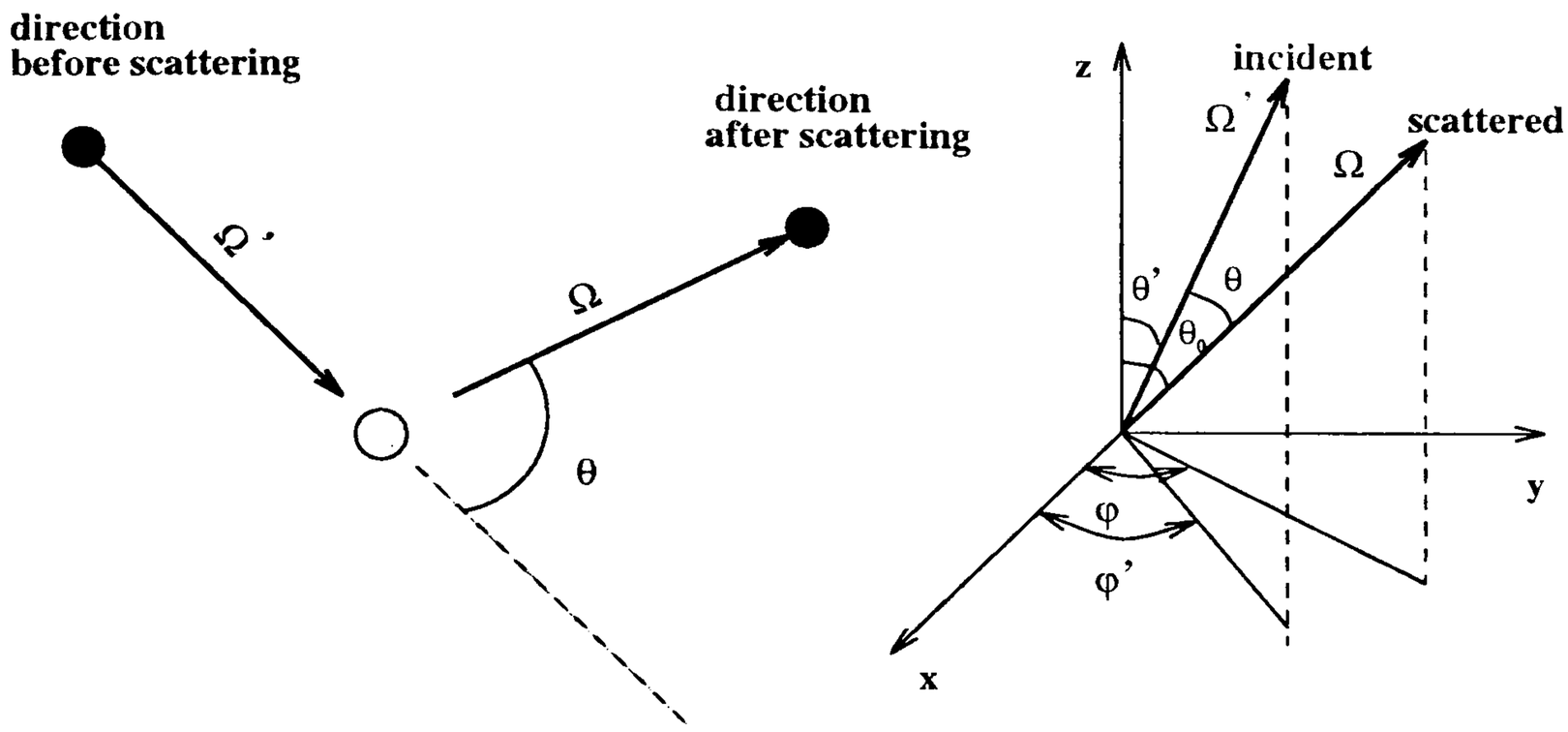


Figure 2.3: Definition of the scattering angle θ (a) by a schematic illustration of the collision event; (b) in spherical coordinate system.

Consequently, $\sigma_s(\mathbf{r}, \mu_0)$ may be expanded as the sum of a series of Legendre polynomials (for properties of Legendre polynomials see appendix D) [45],[103], i.e.,

$$\sigma_s(\mathbf{r}, \mu_0) = \sum_{l=0}^{\infty} \frac{2l+1}{4\pi} \sigma_{sl}(r) P_l(\mu_0), \tag{2.26}$$

where $P_l(\mu_0)$ is the Legendre Polynomial of order l and σ_{sl} is the scattering coefficient given by the orthogonality of Legendre Polynomials as

$$\sigma_{sl}(r) = 2\pi \int_{-1}^{+1} d\mu_0 \sigma_s(\mathbf{r}, \mu_0) P_l(\mu_0), \tag{2.27}$$

with the normalisation condition

$$\sigma_{s0}(r) = 2\pi \int_{-1}^{+1} d\mu_0 \sigma_s(\mu_0) = 1. \tag{2.28}$$

Further expressing the angular Dirac δ-function $\delta(\mathbf{\Omega}' - \mathbf{\Omega})$ in terms of a series of Legendre Polynomials [132], the second term on the left hand side of equation (2.24) can be written as follows:

$$\begin{aligned}\sigma_t(\mathbf{r})\phi(\mathbf{r},\mathbf{\Omega}) &= \sigma_t(\mathbf{r})\int_{4\pi} d\mathbf{\Omega}'\phi(\mathbf{r},\mathbf{\Omega}')\delta(\mathbf{\Omega}'-\mathbf{\Omega}) \\ &= \sigma_t(\mathbf{r})\sum_{l=0}^{\infty}\left(\frac{2l+1}{4\pi}\right)\int_{4\pi} d\mathbf{\Omega}' P_l(\mu_0)\phi(\mathbf{r},\mathbf{\Omega}'). \qquad (2.29)\end{aligned}$$

Substituting those expansions obtained for both the scattering kernel and angular Dirac δ-function into equation (2.24), the one-speed, steady-state Boltzmann transport equation takes the following form

$$\mathbf{\Omega}\cdot\nabla\phi(\mathbf{r},\mathbf{\Omega}) + \sum_{l=0}^{\infty}\left(\frac{2l+1}{4\pi}\right)\sigma_l(\mathbf{r})\int_{4\pi} d\mathbf{\Omega}'\phi(\mathbf{r},\mathbf{\Omega}')P_l(\mu_0) = S(\mathbf{r},\mathbf{\Omega}), \qquad (2.30)$$

where

$$\sigma_l(\mathbf{r}) = \sigma_t(\mathbf{r}) - \sigma_{sl}(\mathbf{r}). \qquad (2.31)$$

This equation is known not to be self-adjoint [45],[142]. Although associated variational principles exist for the mono-energetic integro-differential Boltzmann equation, these are not extremum principles, which means that if a variational principle is used for the derivation of numerical approximations to equation (2.30), it will not necessarily yield the best solution [45],[90]. However, equation (2.30) can be cast into a self-adjoint form (or second-order form) in order to formulate the problem in terms of the extremum variational principles [45], [90],[140].

Even-Parity Form of the Transport Equation

The steady-state, one-speed linear transport equation, equation (2.30), is the starting point for the derivation of the second-order forms. Since equation (2.30) is valid for all unit vectors $\mathbf{\Omega}$, then it is also valid for photons travelling along the opposite direction to $\mathbf{\Omega}$ [102], viz,

$$-\mathbf{\Omega}\cdot\nabla\phi(\mathbf{r},-\mathbf{\Omega}) + \sum_{l=0}^{\infty}\left(\frac{2l+1}{4\pi}\right)\sigma_l(\mathbf{r})\int_{4\pi} d\mathbf{\Omega}'\phi(\mathbf{r},\mathbf{\Omega}')P_l(-\mu_0) = S(\mathbf{r},-\mathbf{\Omega}). \qquad (2.32)$$

Introducing the following definitions for the even and odd (angular) quantities as

$$\phi^{+}(\mathbf{r},\mathbf{\Omega}) = \frac{1}{2}[\phi(\mathbf{r},\mathbf{\Omega}) + \phi(\mathbf{r},-\mathbf{\Omega})], \tag{2.33}$$

$$\phi^{-}(\mathbf{r},\mathbf{\Omega}) = \frac{1}{2}[\phi(\mathbf{r},\mathbf{\Omega}) - \phi(\mathbf{r},-\mathbf{\Omega})], \tag{2.34}$$

$$S^{+}(\mathbf{r},\mathbf{\Omega}) = \frac{1}{2}[S(\mathbf{r},\mathbf{\Omega}) + S(\mathbf{r},-\mathbf{\Omega})], \qquad S^{-}(\mathbf{r},\mathbf{\Omega}) = \frac{1}{2}[S(\mathbf{r},\mathbf{\Omega}) - S(\mathbf{r},-\mathbf{\Omega})]. \tag{2.35}$$

and using the identity

$$P_l(-\mu_0) = (-1)^l P_l(\mu_0),$$

it is possible to identify equations (2.30) and (2.32) as two coupled equations for the even- and odd-parity fluxes. In the above definitions, $\phi^{+}(\mathbf{r},\mathbf{\Omega})$ represents the even-parity flux and is an even function of $\mathbf{\Omega}$ ($\phi^{+}(\mathbf{r},\mathbf{\Omega}) = \phi^{+}(\mathbf{r},-\mathbf{\Omega})$). $\phi^{-}(\mathbf{r},\mathbf{\Omega})$ represents the odd-parity flux and is an odd function of $\mathbf{\Omega}$ [133]. By adding and subtracting those two equations, equations (2.30) and (2.32), the original Boltzmann transport equation is split into two equations [45],[102] as

$$\mathbf{\Omega}\cdot\nabla\phi^{-}(\mathbf{r},\mathbf{\Omega}) + \sum_{l\ even}\left(\frac{2l+1}{4\pi}\right)\sigma_l(\mathbf{r})\int_{4\pi} d\mathbf{\Omega}'\phi^{+}(\mathbf{r},\mathbf{\Omega}')P_l(\mu_0) = S^{+}(\mathbf{r},\mathbf{\Omega}), \tag{2.36}$$

and

$$\mathbf{\Omega}\cdot\nabla\phi^{+}(\mathbf{r},\mathbf{\Omega}) + \sum_{l\ odd}\left(\frac{2l+1}{4\pi}\right)\sigma_l(\mathbf{r})\int_{4\pi} d\mathbf{\Omega}'\phi^{-}(\mathbf{r},\mathbf{\Omega}')P_l(\mu_0) = S^{-}(\mathbf{r},\mathbf{\Omega}). \tag{2.37}$$

Equations (2.36) and (2.37) are a pair of coupled first-order differential equations known as mixed parity or canonical form for the even- and odd-parity components of the angular flux. From these equations, it is possible to derive the second-order self-adjoint forms of the transport equation for the even-parity flux $\phi^{+}(\mathbf{r},\mathbf{\Omega})$ or the odd-parity flux $\phi^{-}(\mathbf{r},\mathbf{\Omega})$.

Solving equation (2.37) for the odd-parity flux we obtain

$$\phi^{-}(\mathbf{r},\mathbf{\Omega}) = \sum_{l\ odd}\left(\frac{2l+1}{4\pi}\right)\left(\frac{1}{\sigma_l}\right)\int_{4\pi} d\mathbf{\Omega}' P_l(\mu_0)[S^{-} - \mathbf{\Omega}'\cdot\nabla\phi^{+}]. \tag{2.38}$$

Substituting this expression into equation (2.36) results in the second-order transport equation for the even-parity flux as

$$-\sum_{l\ odd}\left(\frac{2l+1}{4\pi}\right)\left(\frac{1}{\sigma_l}\right)\mathbf{\Omega}\cdot\nabla\int_{4\pi}d\mathbf{\Omega}'P_l(\mu_0)\ \mathbf{\Omega}'\cdot\nabla\phi^+$$

$$+\sum_{l\ even}\left(\frac{2l+1}{4\pi}\right)\sigma_l(\mathbf{r})\int_{4\pi}d\mathbf{\Omega}'P_l(\mu_0)\phi^+(\mathbf{r},\mathbf{\Omega}')$$

$$=S^+-\sum_{l\ odd}\left(\frac{2l+1}{4\pi}\right)\left(\frac{1}{\sigma_l}\right)\mathbf{\Omega}\cdot\nabla\int_{4\pi}d\mathbf{\Omega}'P_l(\mu_0)\ S^-, \tag{2.39}$$

or, in an operator notation

$$-\mathbf{\Omega}\cdot\nabla G\mathbf{\Omega}\cdot\nabla\phi^+ + H\phi^+ = S^+ - \mathbf{\Omega}\cdot\nabla GS^- \tag{2.40}$$

where H and G, which are termed removal and leakage operators respectively, are linear, self-adjoint and positive definite operators [102], defined as

$$Gf(\mathbf{r},\mathbf{\Omega})=\sum_{l\ odd}\left(\frac{2l+1}{4\pi}\right)\left(\frac{1}{\sigma_l}\right)\int_{4\pi}d\mathbf{\Omega}'P_l(\mu_0)f(\mathbf{r},\mathbf{\Omega}'), \tag{2.41}$$

and

$$Hf(\mathbf{r},\mathbf{\Omega})=\sum_{l\ even}\left(\frac{2l+1}{4\pi}\right)\sigma_l\int_{4\pi}d\mathbf{\Omega}'P_l(\mu_0)f(\mathbf{r},\mathbf{\Omega}'). \tag{2.42}$$

The boundary conditions associated with the even-parity transport equation take the following forms [64],[90],[102]. The vacuum condition becomes

$$\phi^+(\mathbf{r},\mathbf{\Omega})+G[S^-(\mathbf{r},\mathbf{\Omega})-\mathbf{\Omega}\cdot\nabla\phi^+(\mathbf{r},\mathbf{\Omega})]=0, \qquad \mathbf{\Omega}\cdot\mathbf{n}<0,\ \ \mathbf{r}\in S, \tag{2.43}$$

and

$$\phi^+(\mathbf{r},\mathbf{\Omega})-G[S^-(\mathbf{r},\mathbf{\Omega})-\mathbf{\Omega}\cdot\nabla\phi^+(\mathbf{r},\mathbf{\Omega})]=0, \qquad \mathbf{\Omega}\cdot\mathbf{n}>0,\ \ \mathbf{r}\in S, \tag{2.44}$$

while the surface source condition is

$$\phi^+(\mathbf{r},\mathbf{\Omega})+G[S^-(\mathbf{r},\mathbf{\Omega})-\mathbf{\Omega}\cdot\nabla\phi^+(\mathbf{r},\mathbf{\Omega})]=T(\mathbf{r},\mathbf{\Omega}), \qquad \mathbf{\Omega}\cdot\mathbf{n}<0,\ \ \mathbf{r}\in S, \tag{2.45}$$

and

$$\phi^+(\mathbf{r},\mathbf{\Omega})-G[S^-(\mathbf{r},\mathbf{\Omega})-\mathbf{\Omega}\cdot\nabla\phi^+(\mathbf{r},\mathbf{\Omega})]=T(\mathbf{r},\mathbf{\Omega}), \qquad \mathbf{\Omega}\cdot\mathbf{n}>0,\ \ \mathbf{r}\in S. \tag{2.46}$$

The even-parity form of the transport equation offers several attractive features. The even-parity component of the angular flux is non-negative and the even-parity equation is self-adjoint for monoenergetic problems [135]. Most importantly, the odd P_N approximations can only be derived from even-parity variational principle and they are in general preferred to even P_N approximations [90].

The scalar flux distribution, which is often the quantity of interest, can be obtained directly from the solution of the even-parity equation. Angular integration of the odd-parity component leads more naturally to the current distribution, but as the current can be written in terms of the even-parity flux and then obtained by solving the even-parity equation, both scalar flux and current distribution may be obtained [141]. Thus, the definitions of the scalar flux and the current vector are given as

$$\phi(\mathbf{r}) = \int_{4\pi} d\mathbf{\Omega}\phi(\mathbf{r},\mathbf{\Omega}) = \int_{4\pi} d\mathbf{\Omega}\phi^{+}(\mathbf{r},\mathbf{\Omega}), \tag{2.47}$$

and

$$\mathbf{J}(\mathbf{r}) = \int_{4\pi} d\mathbf{\Omega}\mathbf{\Omega}\phi(\mathbf{r},\mathbf{\Omega}) = \int_{4\pi} d\mathbf{\Omega}\mathbf{\Omega}\phi^{-}(\mathbf{r},\mathbf{\Omega}). \tag{2.48}$$

However, combining equations (2.38) and (2.48) yield the current in terms of the even-parity flux as [90],[141]

$$\mathbf{J}(\mathbf{r}) = \int_{4\pi} d\mathbf{\Omega}\mathbf{\Omega}G[S^{-} - \mathbf{\Omega}'\cdot\nabla\phi^{+}]. \tag{2.49}$$

2.4 Application of the Variational Method and the Ritz Procedure

In what follows, a variational principle is employed as a point of departure for the application of finite element methods to transport problems. To formulate finite element methods variationally, the second-order even-parity equation is considered and cast in a variational form by seeking a functional, $F[\phi^{+}]$, that will yield equation (2.40) and its associated boundary conditions as Euler-Lagrange equations. As can be seen

from the works of Vladimirov [108], Kaplan and Davis [102] and Ackroyd [104], indefinite number of variational principles may be associated to the even-parity problem. One is a self-adjoint minimum principle, with the related quadratic functional being defined [90],[140] as

$$F[\phi^+] = F[\phi^+, \phi^+] - 2F_S[\phi^+], \tag{2.50}$$

with

$$F[\phi_1^+, \phi_2^+] = (\mathbf{\Omega} \cdot \nabla\phi_1^+, G\mathbf{\Omega} \cdot \nabla\phi_2^+) + (\phi_1^+, H\phi_2^+) + \left\langle \phi_1^+, \phi_2^+ \right\rangle, \tag{2.51}$$

and

$$F_S[\phi_1^+] = (\phi_1^+, S^+) + (\mathbf{\Omega} \cdot \nabla\phi_1^+, GS^-) + \left\langle \phi_1^+, T \right\rangle, \tag{2.52}$$

where T is the specified flux for the boundary condition, (.,.) and $< .,. >$ are the angular integrations, which are here written in inner-product form, defined [90],[142] as

$$(f, g) = \int_V dV \int_{4\pi} d\mathbf{\Omega} f(\mathbf{r}, \mathbf{\Omega}) g(\mathbf{r}, \mathbf{\Omega}), \tag{2.53}$$

and

$$\langle f, g \rangle = \int_{\partial V_S} dS \int_{4\pi} d\mathbf{\Omega} \mid \mathbf{\Omega} \cdot \mathbf{n} \mid f(\mathbf{r}, \mathbf{\Omega}) g(\mathbf{r}, \mathbf{\Omega}). \tag{2.54}$$

Having defined the variational functional as shown above, it is possible to find a solution to the second-order even-parity transport equation (2.40), with its appropriate boundary conditions, because solving equation (2.40) is the same as finding a function that minimises the quadratic functional $F[\phi^+]$ of equation (2.50). Requiring this functional to be stationary with respect to variations in ϕ^+, which can be expressed as

$$\delta F[\phi^+] = 0, \tag{2.55}$$

yields an Euler-Lagrange equation that is just the second-order even-parity equation and corresponds to the minimum value of the functional [141]. This requirement that the first variation of $F[\phi^+]$ vanishes forms the basis of the Ritz numerical method.

Approximate solutions to the problem can thus be generated via the Ritz procedure [91],[143]. To use this procedure, the spatial domain V of $F[\phi^+]$ is first divided into E non-overlapping continuous sub-domains or elements connected together at N nodal points and the even-parity flux within each element is approximated by a piecewise linear interpolation or trial function as

$$\phi^+(\mathbf{r},\mathbf{\Omega}) = \sum_{i=1}^{N_e} B_i^e(\mathbf{r},\mathbf{\Omega})\phi_i^{+e}, \tag{2.56}$$

where N_e is the number of nodes in element e, $B_i^e(\mathbf{r},\mathbf{\Omega})$ is an interpolating spatial shape function, which is zero outside of element and unity at node i, and ϕ_i^{+e} is just the approximate scalar flux value at node i of element e. It is convenient to denote equation (2.56) as the scalar product

$$\phi^+(\mathbf{r},\mathbf{\Omega}) = \mathbf{B}^T\mathbf{\Phi}, \tag{2.57}$$

where $\mathbf{B}^T$ is a row-vector of finite element shape functions and $\mathbf{\Phi}$ is a column-vector of unknown element nodal fluxes for the even-parity component, respectively. Substituting this expression into the functional of equation (2.50) results in the following reduced functional [90]

$$F[\phi^+] = \mathbf{\Phi}^T\mathbf{A}\mathbf{\Phi} - 2\mathbf{\Phi}^T\mathbf{S}, \tag{2.58}$$

where $\mathbf{A} \equiv F[\mathbf{B},\mathbf{B}^T]$ is a $N \times N$ matrix and $\mathbf{S} \equiv F_S[\mathbf{B}]$ is a $N \times 1$ column vector. Using the requirement given by equation (2.55) leads to a set of simultaneous linear equations suitable for solution on a digital computer, which can be represented symbolically by the matrix equation

$$\mathbf{A}\mathbf{\Phi} = \mathbf{S}, \tag{2.59}$$

where $\mathbf{A}$ is simply the coefficient matrix obtained from the spatial operators and the boundary conditions, $\mathbf{\Phi}$ is the vector of unknown even-parity fluxes, and $\mathbf{S}$ is the source vector. Because the operators involved are self-adjoint, the coefficient matrix $\mathbf{A}$ is a symmetric and also banded matrix providing an advantage in solving the system of equations (2.59) such as the minimisation of computer memory requirements [135].

2.5 The Finite Element-Spherical Harmonics Method

In FE-P_N approach, the spatial dependence of the angular flux is expanded using finite elements and the angular dependence is expanded using spherical harmonics. Employing normalised spherical harmonics, the trial function for the even-parity flux $\phi^+(\mathbf{r},\mathbf{\Omega})$ is

$$\phi^+(\mathbf{r},\mathbf{\Omega}) = \sum_{k=1}^{M} Q_k(\mathbf{\Omega})\phi_k^+(\mathbf{r}) = \mathbf{Q^T}(\mathbf{\Omega})\mathbf{\Phi}(\mathbf{r}), \tag{2.60}$$

where $Q_k(\mathbf{\Omega})$ are the set of angular basis functions chosen to be the even terms of the spherical harmonics expansion as

$$Q_{k(lm)} = \sqrt{\frac{(2l+1)}{4\pi}(2-\delta_{m,0})\frac{(l-m)!}{(l+m)!}}\; P_l^m(\mu)\left\{\begin{array}{l}\cos(m\chi)\\ \\ \sin(m\chi)\end{array}\right\}, \tag{2.61}$$

for l even and $m = 0, 1, ..., l$. The expansion is truncated at $l = N-1$ and substituted into the even-parity transport equation, which results in a set of coupled equations called the P_N equations.

As has been described in the previous section, the spatial dependence of the even-parity flux in the expansion (2.60) above is approximated using finite element trial functions. Therefore, the domain is subdivided into a number of regions, or elements, and the angular moments $\phi_k^+(\mathbf{r})$ are approximated using the basis functions $B_j^e(\mathbf{r})$ and nodal values ϕ_{jk}^{+e} as

$$\phi_k^{+e}(\mathbf{r}) = \sum_{j=1}^{N_e} B_j^e(\mathbf{r})\phi_{jk}^{+e} = \mathbf{B}^{eT}\mathbf{\Phi}_k^e, \tag{2.62}$$

for all moments k. To construct the trial function for the angular moments, covering the whole domain, the contributions of the angular moments from all elements are simply added as follows

$$\phi_k^+(\mathbf{r}) = \sum_{e=1}^{E} \phi_k^{+e}(\mathbf{r}). \tag{2.63}$$

Using (2.62) and (2.63) the trial function given by (2.60) takes the following form

$$\phi^+(\mathbf{r},\mathbf{\Omega}) = \sum_{e=1}^{E}\sum_{j=1}^{N_e}\sum_{k=1}^{M} B_j^e(\mathbf{r})Q_k(\mathbf{\Omega})\phi_{jk}^{+e}, \tag{2.64}$$

where E is the total number of elements, N_e is the number of local nodes in element e and M is the number of spherical harmonics coefficients or moments. Or, (2.64) can be rewritten in a more compact tensor notation as

$$\phi^+(\mathbf{r},\mathbf{\Omega}) = \sum_{e=1}^{E} \mathbf{B}^{eT}(\mathbf{r}) \otimes \mathbf{Q}^T(\mathbf{\Omega})\mathbf{\Phi}^e, \tag{2.65}$$

where $\otimes$ denotes the direct or tensor product (see appendix E) of vectors $\mathbf{B}^e$ and $\mathbf{Q}$, and $\mathbf{\Phi}^e$ is a $(MN_e \times 1)$ column-vector of unknown element nodal fluxes, $\mathbf{B}^e(\mathbf{r})$ is a $(N_e \times 1)$ column-vector of finite element shape functions, and $\mathbf{Q}(\mathbf{\Omega})$ is a $(M \times 1)$ column-vector of normalised spherical harmonics functions. The functional described by (2.50) can now be written as

$$F[\mathbf{\Phi}(\mathbf{r})] = \sum_{e=1}^{E} F^e[\mathbf{\Phi}(\mathbf{r})] = \sum_{e=1}^{E} F^e[\mathbf{\Phi}(\mathbf{r}), \mathbf{\Phi}(\mathbf{r})] - 2F_S^e[\mathbf{\Phi}(\mathbf{r})], \tag{2.66}$$

with the element superscript denoting that the spatial integrations extend over the volume of the element. Inserting the trial function (2.65) into the element functionals F^e and F_S^e, the discretised or reduced functional can be obtained as

$$F[\mathbf{\Phi}] = \sum_{e=1}^{E} \mathbf{\Phi}^{eT}\mathbf{A}^e\mathbf{\Phi}^e - 2\mathbf{\Phi}^{eT}\mathbf{S}^e, \tag{2.67}$$

where $\mathbf{A}^e$ is a symmetric, partitioned $MN_e \times MN_e$ matrix defined by

$$\begin{aligned} \mathbf{A}^e &\equiv (\mathbf{\Omega}\cdot\nabla\mathbf{B}^{eT} \otimes \mathbf{Q}^T, G\mathbf{\Omega}\cdot\nabla\mathbf{B}^{eT} \otimes \mathbf{Q}^T) + (\mathbf{B}^{eT} \otimes \mathbf{Q}^T, H\mathbf{B}^{eT} \otimes \mathbf{Q}^T) \\ &+ \left\langle \mathbf{B}^{eT} \otimes \mathbf{Q}^T, \mathbf{B}^{eT} \otimes \mathbf{Q}^T \right\rangle, \end{aligned} \tag{2.68}$$

and $\mathbf{S}^e$ is a partitioned $MN_e \times 1$ column vector given by

$$\mathbf{S}^e \equiv (\mathbf{B}^{eT} \otimes \mathbf{Q}^T, S^+) + (\mathbf{\Omega}\cdot\nabla\mathbf{B}^{eT} \otimes \mathbf{Q}^T, G\mathbf{\Omega}\cdot\nabla S^-) \tag{2.69}$$

The nodal moments of the flux can be written, by the use of nodal compatibility, as a $MN \times 1$ column-vector, and the discretised functional takes the form

$$F[\mathbf{\Phi}] = \mathbf{\Phi}^T\mathbf{A}\mathbf{\Phi} - 2\mathbf{\Phi}^T\mathbf{S}, \tag{2.70}$$

where $\mathbf{A}$ is the global $MN \times MN$ matrix (N being the total number of nodes in the spatial domain) and $\mathbf{S}$ the global $MN \times 1$ source vector:

$$\mathbf{A} \equiv \sum_{e=1}^{E} \mathbf{A}^e, \qquad \mathbf{S} \equiv \sum_{e=1}^{E} \mathbf{S}^e.$$

Although the summation over the elements is here symbolic, because the local and global quantities have different dimensions, it simply means adding the local coefficients into their proper locations in the global matrix and vector. By requiring $F[\Phi]$ of equation (2.70) to be stationary, that is the first variation of the reduced functional to vanish with respect to each component of Φ

$$\frac{\partial F[\Phi]}{\partial \Phi} = 0, \tag{2.71}$$

a system of linear equations is obtained and can be written in a matrix form as

$$\mathbf{A}\Phi = \mathbf{S}. \tag{2.72}$$

The formulation described above has been developed to its most general form and has been implemented in the finite-element program EVENT [144], [145]. A brief description of the program's present capabilities are given in appendix C and a general information about the solution strategies that are employed for the equation system (2.72) can be found in [145].

2.6 Summary

In the first part of this chapter, a short introduction to the forward problem in optical imaging was given, and the use of particle transport equation for modelling of light migration in tissue was discussed. The definitions of two phenomena, absorption and scattering, which characterise the propagation of light in biological tissues were briefly given. As scattering in biological tissues is generally strongly forward-peaked, the relevant parameters to specify this kind of scattering, e.g. the scattering phase function and the mean cosine of the scattering angle, were also explained.

The main emphasis of this chapter was to provide a theoretical background to the FE-P_N method used in this study for numerical solution of the particle transport equation. The one-speed Boltzmann transport equation was presented in its general form. Then, expansion of the scattering kernel in terms of Legendre polynomials to treat the case of anisotropic scattering, and the procedure applied to the transport

equation for obtaining the even-parity form were presented. A self-adjoint variational principle for the even-parity form of the transport equation and the Ritz numerical solution procedure for generating approximate solutions to the problem were introduced. Finally, the formulation of the FE-P_N method, which has the same outlines as the Ritz procedure but differs in the choice of the trial functions to approximate the even-parity flux, was presented.

Chapter 3

Results of Forward Photon Transport Modelling

3.1 Introduction

In Chapters 2 and 4, the theoretical and numerical implementation of Finite Element-Spherical Harmonics (FE-P_N) method for the solution of both forward and inverse problems were presented. However, the practical suitability of the method may not be best appreciated unless it is applied to various test cases. In this chapter, the results for selected case studies are presented to demonstrate the effectiveness of the forward solution formulation.

Descriptions of the case studies (relative to NIR light applications) and the results are divided in two categories. The first concerns time-dependent solutions of the Boltzmann transport equation for various geometries. Comparisons have been made between FE-P_N solutions using different angular approximations, for two different simple geometries, in order to show the limitation of the diffusion approximation in presence of absorption. Since it is also important, when testing a numerical method, to demonstrate its accuracy, time-dependent results for four different problem geometries are compared here with an independent Monte Carlo model.

Although other researchers have applied MC modelling to determine the limits of diffusion theory [146],[147],[148], these simulations have normally been limited to small tissue volumes. To compute the photon propagation in large and optically dense volumes, such as the breast and brain, MC simulations are less applicable because the computation times easily exceed several weeks or month. FE-P_N formulation of the transport equation used in this study is an alternative method to (fastly) and accurately calculate the light distribution in highly scattering media. The second category of tests and results involve assessing the limits of the diffusion approximation by solving the time-independent Boltzmann transport equation. In this section, comparisons between diffusion and transport theory solutions have been made for various homogeneous and heterogeneous cases where diffusion theory is expected not to be valid.

3.2 Time-Dependent Cases

In this section, time-dependent 2D results obtained with the FE-P_N radiation transport model are presented for simple homogeneous and inhomogeneous media. FE-transport and diffusion calculations are compared in order to show the influence of increasing absorption on the results. In a second part, the validity of the FE-P_N method is tested in comparison with a MC model. In all cases of this section, numerical test phantoms consisting of an infinite cylinder are considered.

3.2.1 Comparison of Transport and Diffusion Calculations

Homogeneous Cylinder with No Absorption

We have considered a homogeneous non-absorbing cylinder with a radius of 15 mm, with the scattering property of $\mu_s = 2.5\ \mathrm{mm}^{-1}$ and an anisotropy factor of g=0.5. An isotropic source located at the position (x =20 mm,y =0 mm, 0°), as shown in Figure 3.1, was pulsed for a duration of 2 picoseconds. For the construction of the finite

element mesh 3522 nodes and 7042 linear triangular elements were used. Figure 3.2 shows output photon current obtained with a P_7 angular approximation for various detector positions.

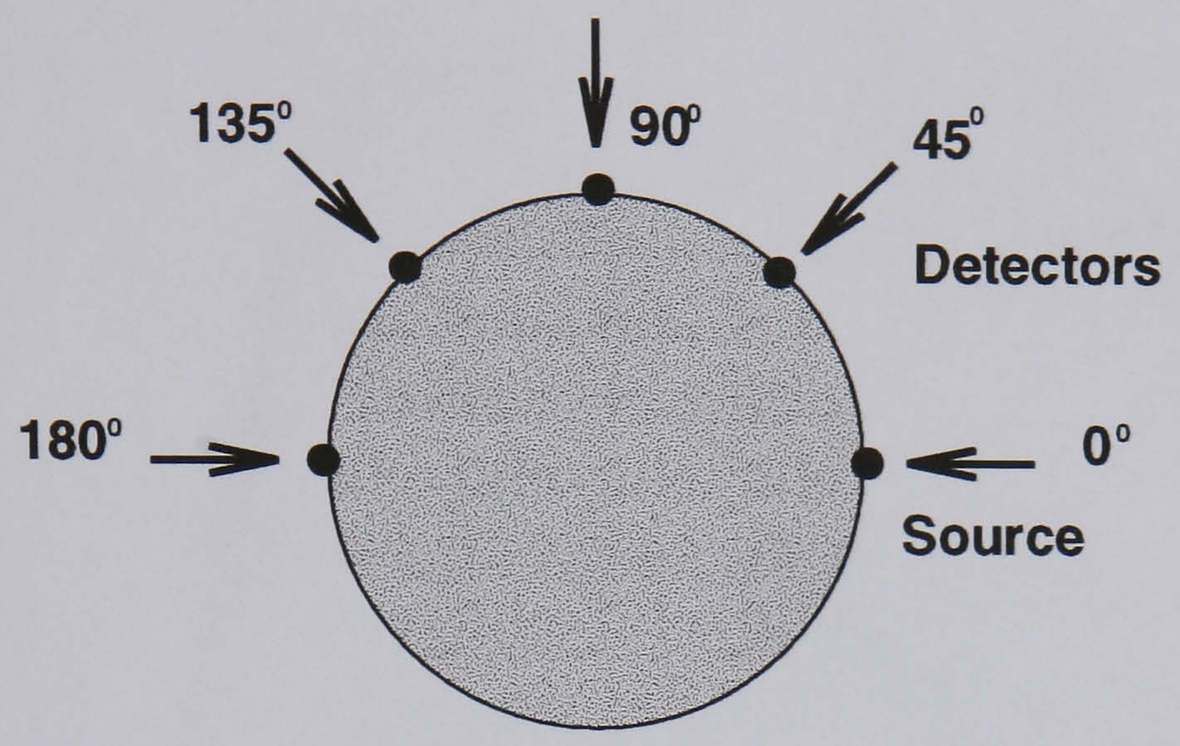


Figure 3.1: Source and detector arrangements used to obtain results of the homogeneous problem.

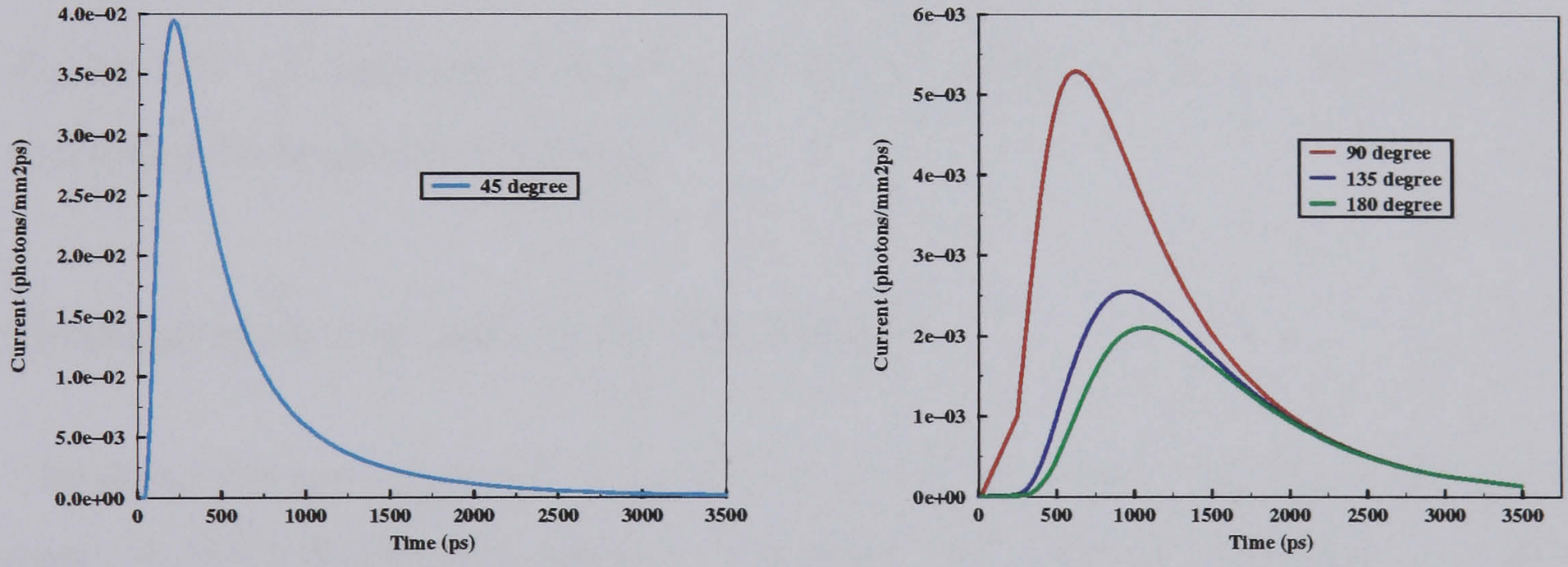


Figure 3.2: Examples of typical time profiles of photon current for detectors positioned at 45° degree from the source and detectors positioned at 90°, 135° and 180° degrees from the source.

Figure 3.3 shows time variation of photon current obtained with diffusion, P_1 and P_7 angular approximations for the detector located at 180° from the source. As the diffusion approximation holds for highly scattering media with the criteria $\mu_a \ll \mu_s$, the results show an excellent agreement among the P_N solutions and diffusion theory, and confirm the validity of the diffusion approximation to treat this case.

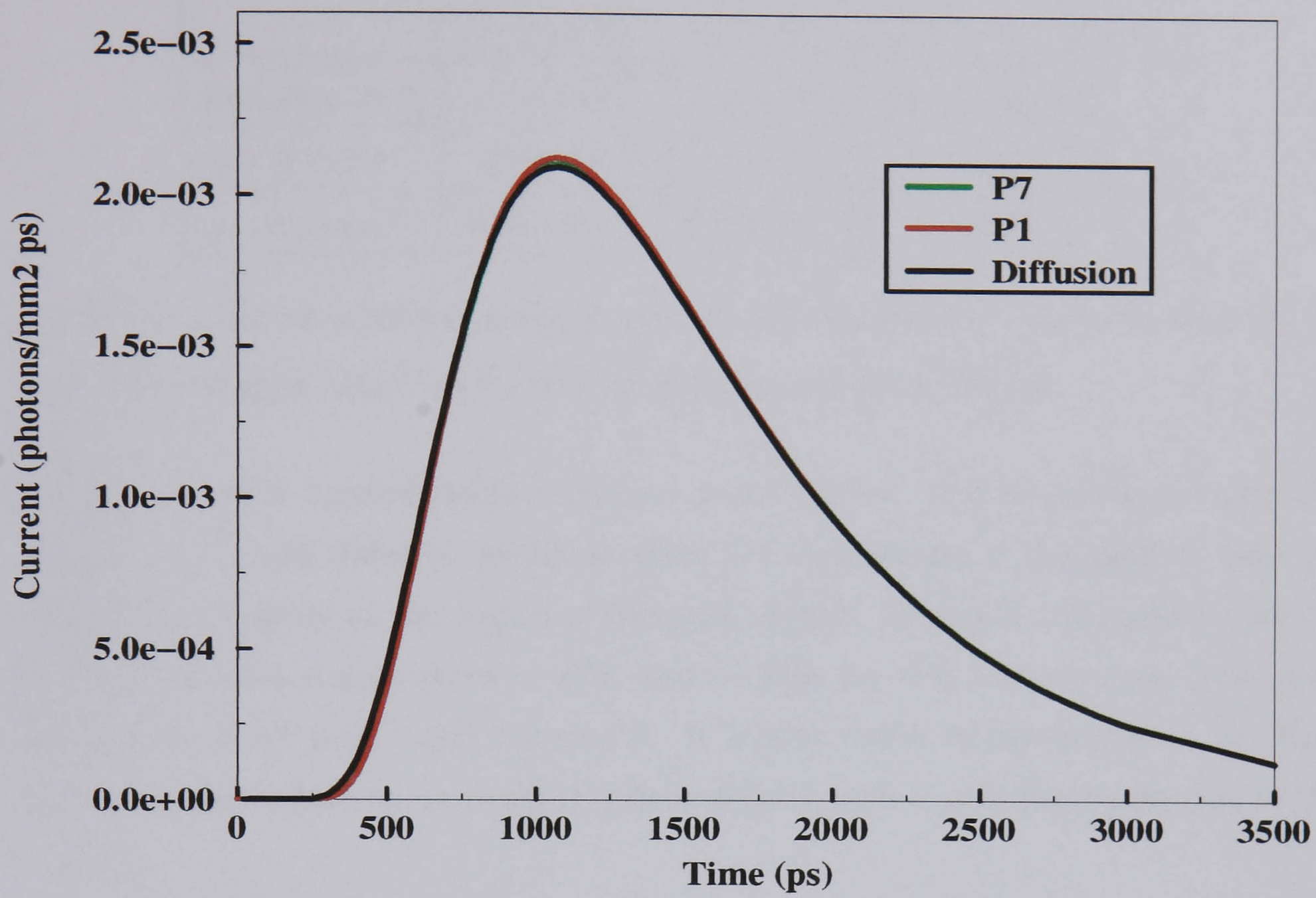


Figure 3.3: Comparison of FE-P_N of output current results at 180° for the pure-scattering homogeneous cylinder.

Homogeneous Cylinder with Absorption

The above homogeneous cylinder with the same source-detector configurations is used again in the following two cases to investigate the effect of absorption on the solutions. FE-P_N calculations were carried out with two different homogeneous absorption properties. In the first, optical properties of $\mu_s = 2.5$ mm^{-1} and $\mu_a = 0.1$ mm^{-1} were employed, while in the second the absorption coefficient was increased to 0.2 mm^{-1}. Table 3.1 shows the maximum values of output currents obtained at the detector opposite to the source (180°) for the three angular approximations. Time-dependent results using diffusion, P_1 and P_7 approximations are plotted in Figure 3.4 separately for two different absorption coefficients.

It can be seen from the figure (or the table) that the differences between FE-

Cylinders	Values (photons/mm^{2}ps)		
	P_7 Approx.	P_1 Approx.	Diffusion Approx.
Non-absorbing	2.105×10^{-3}	2.124×10^{-3}	2.095×10^{-3}
μ_a= 0.1 mm^{-1}	9.983×10^{-9}	7.909×10^{-9}	7.294×10^{-9}
μ_a=0.2 mm^{-1}	4.760×10^{-12}	2.287×10^{-12}	1.979×10^{-12}

Table 3.1: Maximum photon leakage rates at 180° for FE-P_N solutions using P_7, P_1 and diffusion approximation for a homogeneous cylindrical region.

P_N and diffusion approximations become more marked with increasing absorption. While FE-P_N and diffusion solutions show the same trend, a discrepancy between them occurs mainly at the region of the peak values. Maximum differences between P_7 and diffusion results were $\sim$ 27% and $\sim$ 58% for this homogeneous case with absorption of 0.1 mm^{-1} and 0.2 mm^{-1}. It is also worth mentioning that the time for those peak values to be reached differs slightly with increasing absorption in the medium.

Inhomogeneous Cylinder with No Absorption

A non-absorbing cylinder of 15 mm radius with a small cylindrical region located at the centre is considered in further investigating the influence of increased absorption inside the outer cylindrical region. The small absorbing region had a diameter of 3 mm and was purely absorbing with $\mu_a = 0.3$ mm^{-1}. The outer cylinder had the same scattering coefficient $\mu_s = 2.5$ mm^{-1} and the same anisotropy factor of g=0.5 as in the homogeneous case. Figure 3.5 illustrates the geometry and source-detector configurations. The source was pulsed for 2 picoseconds. The mesh used to solve this problem consisted of 7496 triangular elements and 3749 nodes. In Figure 3.6, the FE-P_N results obtained with P_7, P_1 and diffusion angular approximations are presented. As it can be seen from the figure that there are slightly greater differences between the angular approximations compared to the homogeneous case due to the effect of small absorber located at the centre.

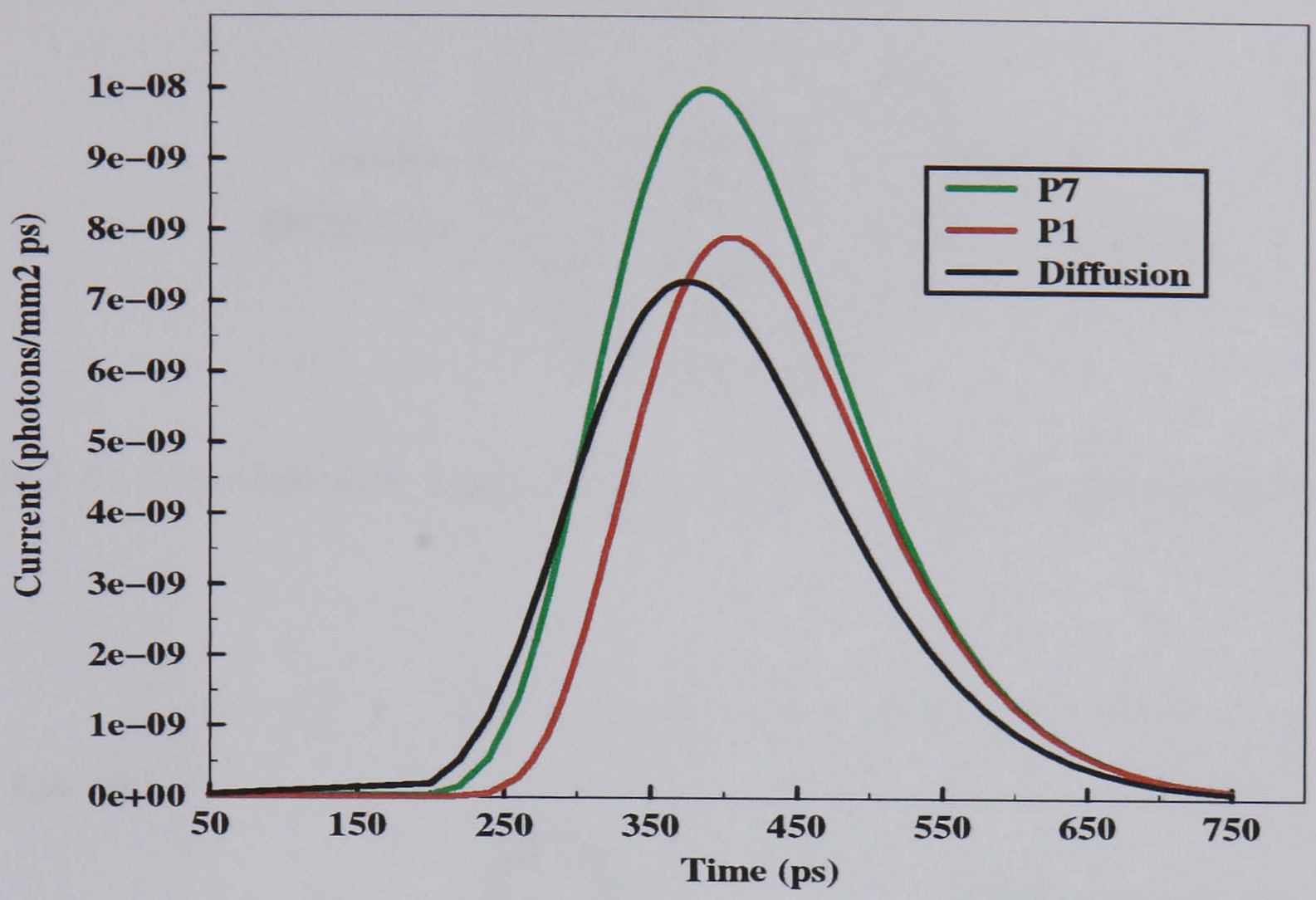


Figure 3.4: Comparison of FE-P_N solutions for the homogeneous cylinder with absorption. Scattering coefficient is 2.5 mm^{-1} for both calculations. Top: results for $\mu_a = 0.1$ mm^{-1}. Bottom: results for $\mu_a = 0.2$ mm^{-1}.

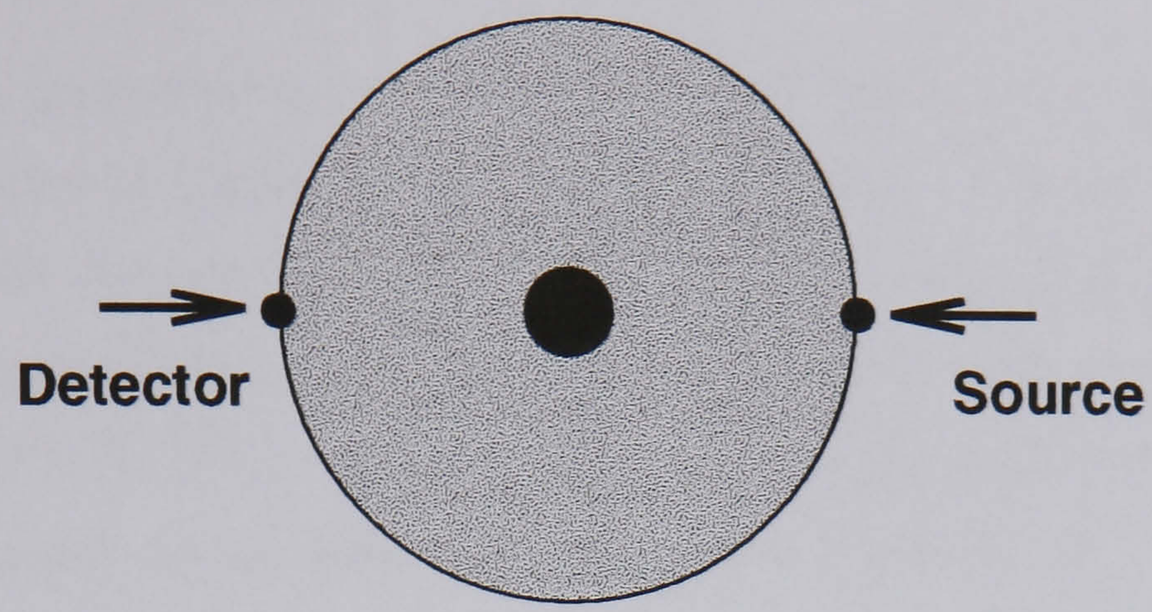


Figure 3.5: Absorber and source-detector geometry for the inhomogeneous problem.

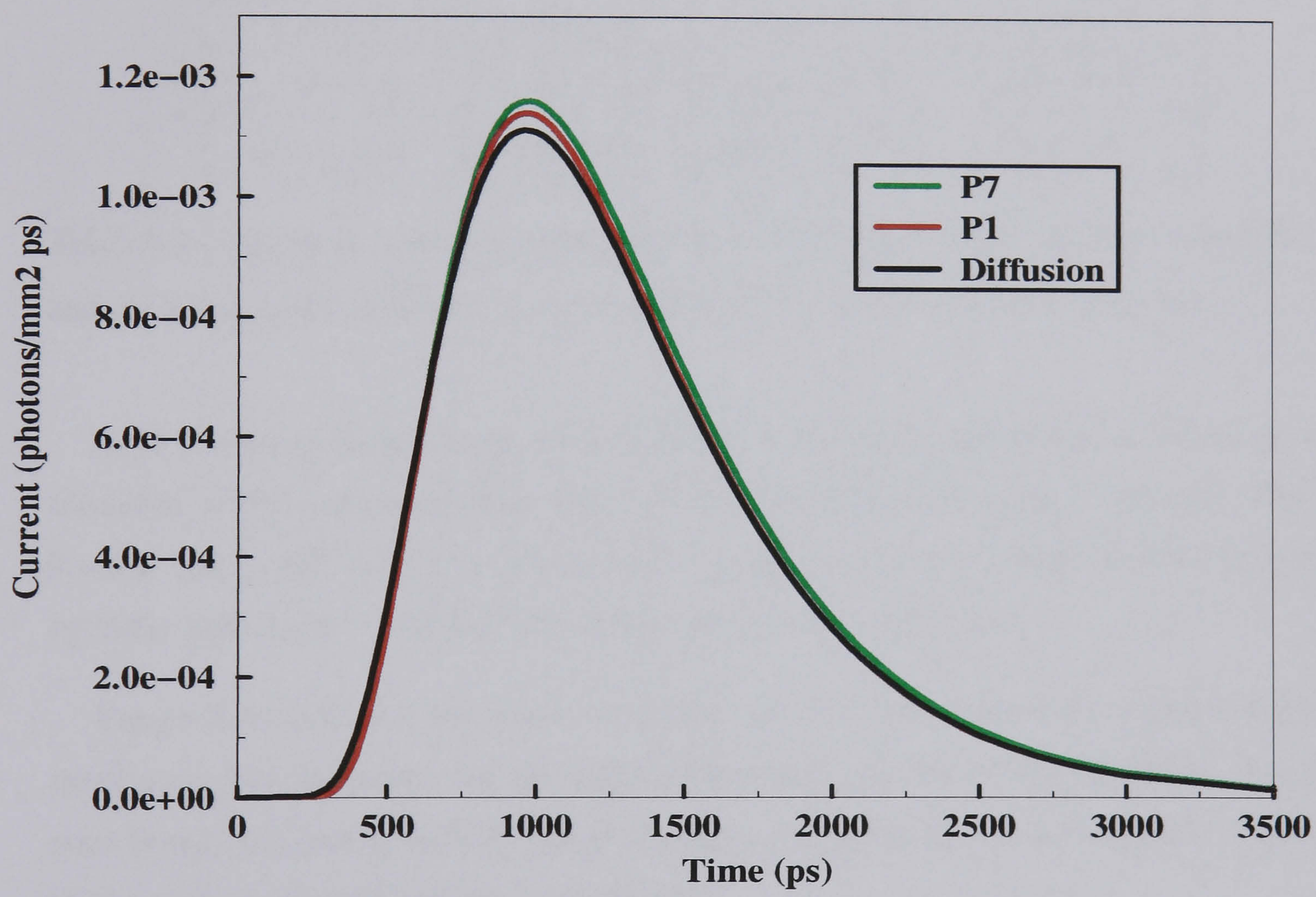


Figure 3.6: Comparison between results of output current modelled with P_7-P_1 approximation and diffusion angular approximation for the inhomogeneous cylinder.

Inhomogeneous Cylinder with Absorption

As in the previous section, the influence on photon output current of increased absorption in the main outer cylinder is investigated. The same source-detector configu-

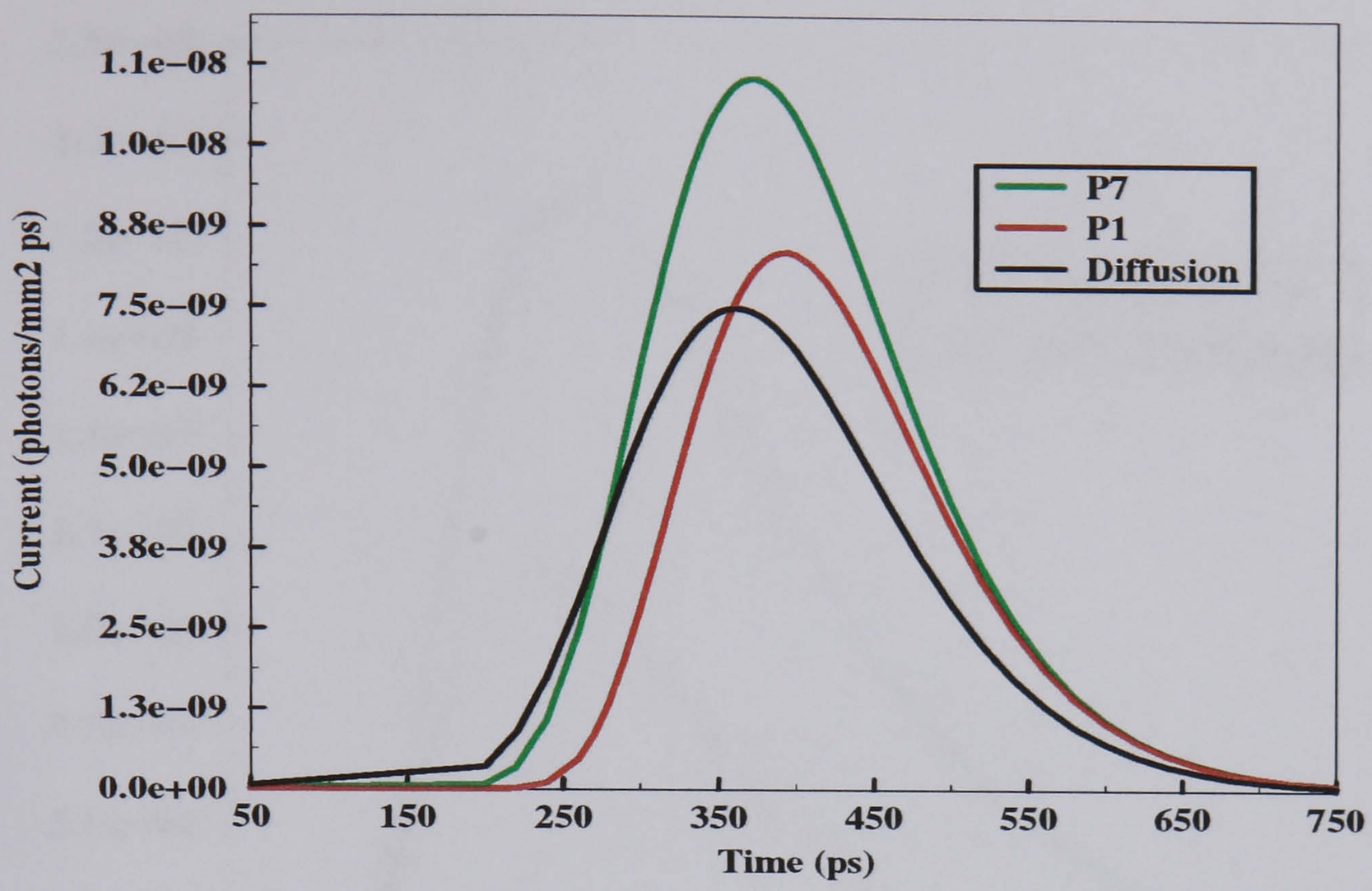
rations, problem geometry were used as in the non-absorbing problem. Two different values of absorption coefficient, $\mu_a = 0.1\ \text{mm}^{-1}$ and $\mu_a = 0.2\ \text{mm}^{-1}$ were added in the outer region. The time-dependent FE-P_N solutions were obtained with P_7, P_1 and the diffusion angular approximations. Results obtained with increased absorption are plotted in Figure 3.7. The maximum values of each particular solution performed for the three inhomogeneous problems are also given in Table 3.2.

Cylinders	Values (photons/mm^{2}ps)		
	P_7 Approx.	P_1 Approx.	Diffusion Approx.
Non-absorbing	1.1585×10^{-3}	1.138×10^{-3}	1.111×10^{-3}
μ_a= 0.1 mm^{-1}	1.104×10^{-8}	8.354×10^{-9}	7.495×10^{-9}
μ_a=0.2 mm^{-1}	9.043×10^{-12}	4.062×10^{-12}	3.351×10^{-12}

Table 3.2: Maximum photon leakage rates at 180° for FE-P_N solutions using P_7, P_1 and diffusion approximation for a cylindrical region with centred absorber.

As it can be seen that larger discrepancies between P_7 and diffusion solutions were observed in this inhomogeneous case in comparison to the homogeneous one. The difference was $\sim 32\%$ with the addition of 0.1 mm^{-1} absorption into the inhomogeneous cylinder and it was $\sim 63\%$ for the absorption value of 0.2 mm^{-1}.

Figure 3.8 compares the FE-P_N results obtained above with P_7 angular approximation for two, homogeneous and inhomogeneous, non-absorbing problems. It can be seen that in the presence of a central absorbing inhomogeneity, a significant reduction in the output photon current was observed.



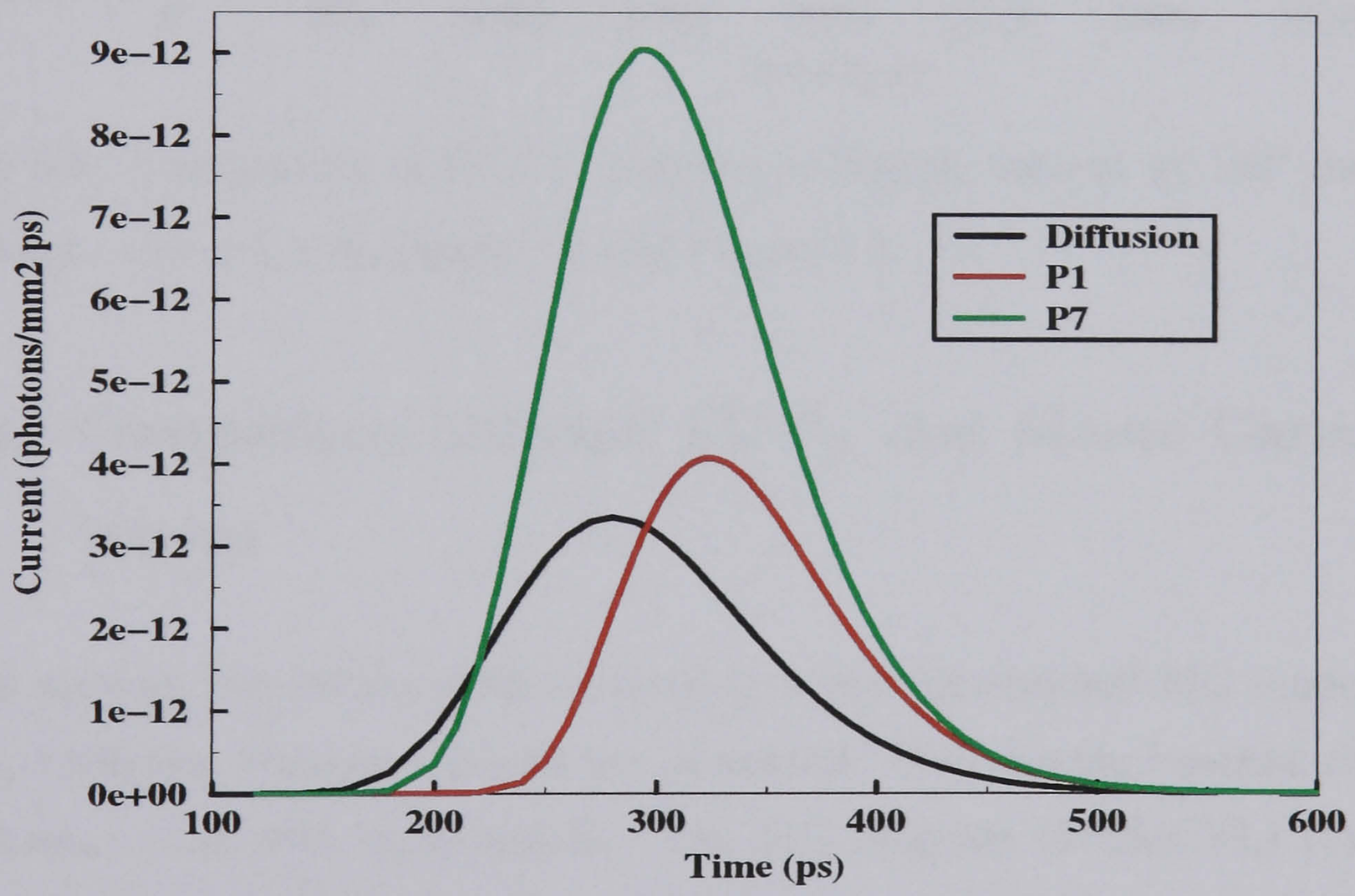


Figure 3.7: Comparison of output current at 180° for case with centred absorber. Scattering coefficient of the outer region is 2.5 mm^{-1} for both cases. Top: results for $\mu_a = 0.1$ mm^{-1}. Bottom: results for $\mu_a = 0.2$ mm^{-1}.

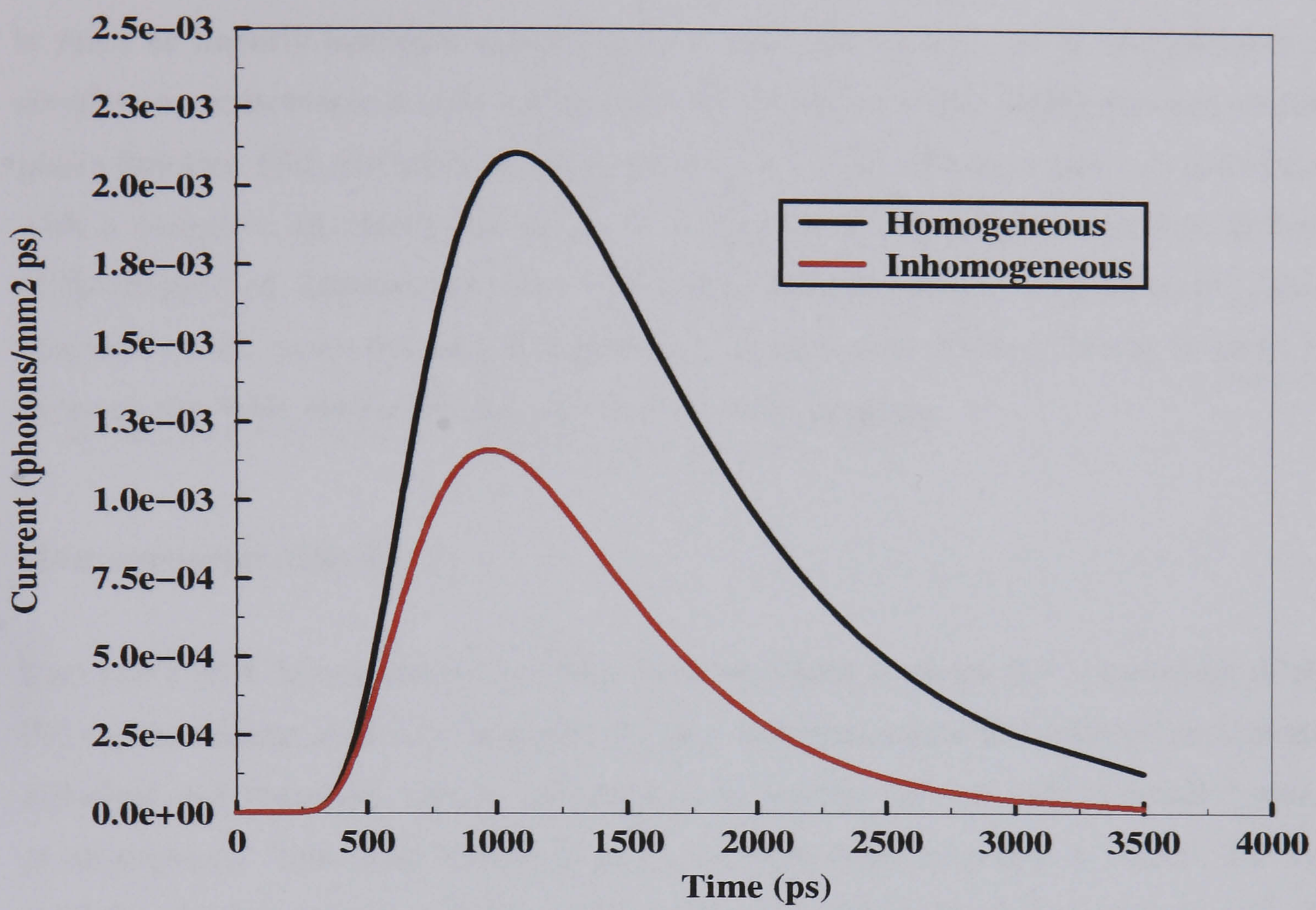


Figure 3.8: Comparison of FE-P_7 solutions of output current at 180° for two non-absorbing cases given in Figure 3.3 and Figure 3.6.

3.2.2 Comparison between FE-P_N and Monte Carlo Calculations

In this section, the results from comparing a two-dimensional MC model with the FE-P_N radiation transport model are presented. Four simple benchmark problems have been solved with both models. The MC program (MCMCYL) [149] used in this study can calculate transport of photons in an infinite cylinder with internal cylindrical regions. It uses light sources and detectors placed on the surface of a cylinder. The light source, which is normally incident on the surface of the cylinder, is assumed to be half-isotropic meaning that it is uniform in angular intensity over all directions into the cylinder. All cases of this section were run on a Dec Alpha 500/250 workstation.

The MC modelling can yield simulation results for a medium having isotropic (g is zero) or linearly isotropic scattering (g is taken to be 0.5). It is also possible to simulate an anisotropic scattering by entering the values of the highly forward-peaked phase function (the variation of g being from 0.5 to 1.0). Those values are calculated with a program, as mentioned earlier (see Appendix A), using the analytical form of the Simplified Approximate Mie scattering phase function. In all following cases, the radii of the outer cylindrical regions are chosen as 6, 10 and 20 mm in order to decrease the time needed to run the Monte Carlo program.

Homogeneous Cases

Two cases with homogeneous cylinder were modelled to check the correctness of the FE-P_N modelling used in this work and also to demonstrate the differences between diffusion and transport theory calculations of output current with a small amount of absorption. The same source-detector configuration as given in Figure 3.5 was used for the homogeneous cases. The source was pulsed for 2 picoseconds and the transmittance leakage currents were plotted for a detector positioned at the opposite side, 180° from the source. The mesh used for the FE-P_N calculation shown in Figure 3.9 and consisted of 2243 nodes and 4484 triangular elements. Linearly isotropic or P_1 scattering with g=0.5 was considered. Due to resource restrictions for the MC calculations, the MC and corresponding FE-P_N simulations were performed for a radius of 6 mm.

It can be seen from Figure 3.10 that the results obtained with the MC model are in reasonable agreement with FE-P_N for the P_{15} or P_3 approximations. As diffusion theory is valid under conditions in which $\mu_a \ll \mu_s$ [88], it was expected for this case that diffusion theory result agreed with the MC and transport solutions. However, even the medium is non-absorbing, the substantial discrepancy between the diffusion theory result and transport or MC is apparent. This must be due to the small problem radius, where the detector is very close to the source, causing the diffusion theory fail to describe the propagation of photons through the medium. For the transport solutions P_3 and P_{15}, we observe that there is no difference between them.

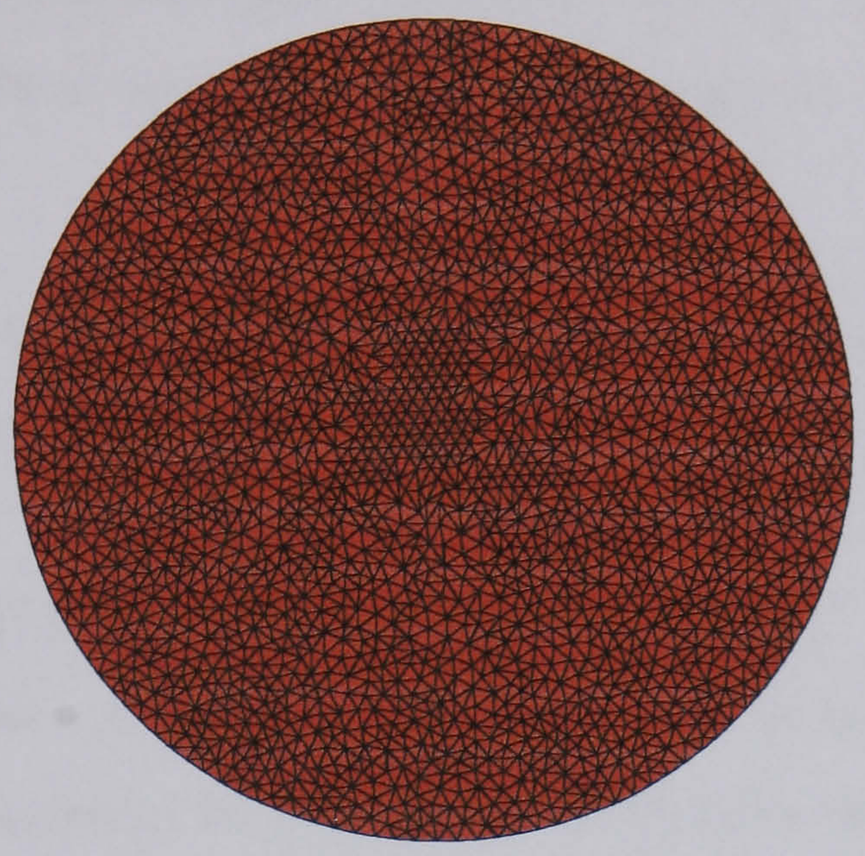


Figure 3.9: The finite element mesh used for the homogeneous problem.

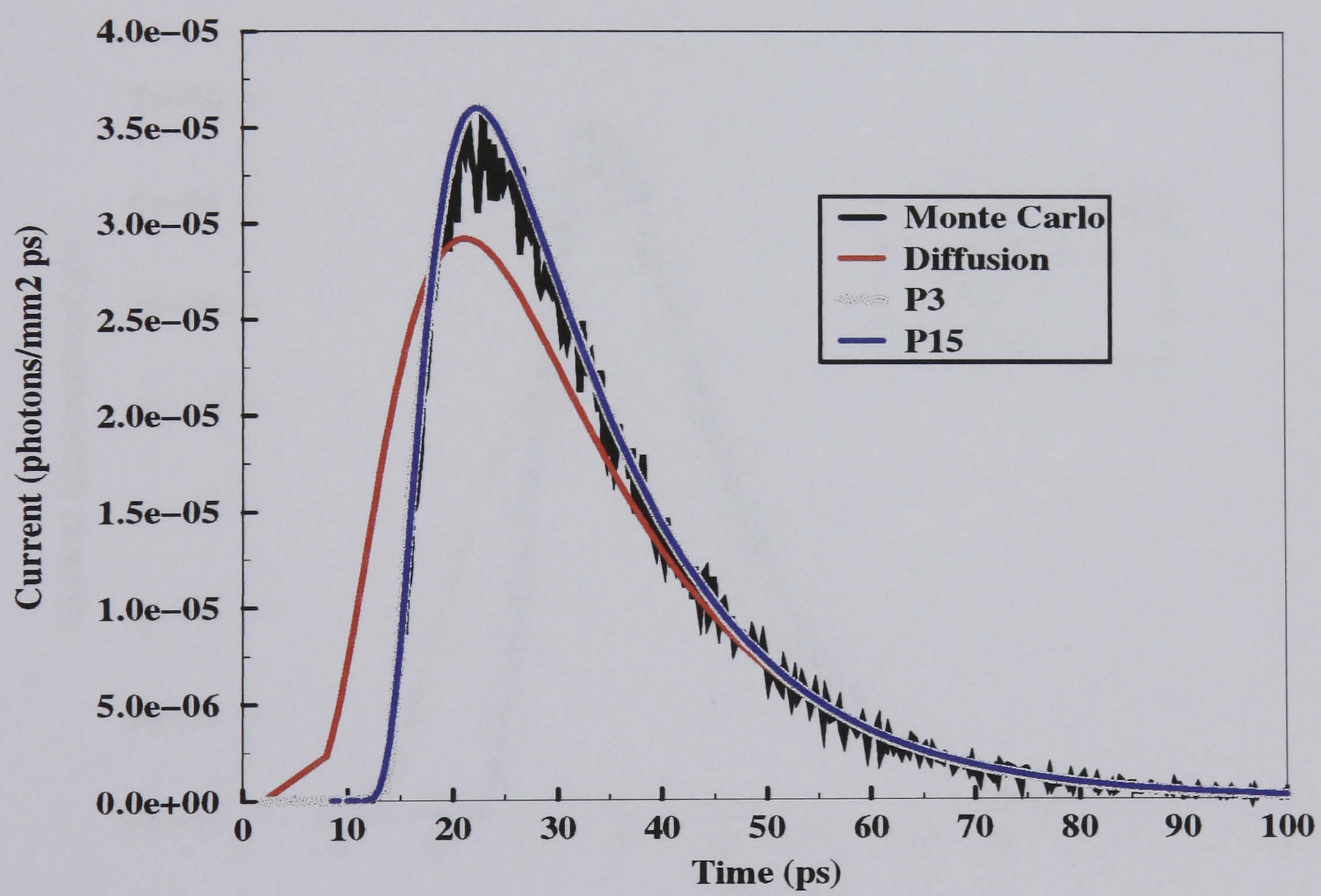


Figure 3.10: MC and FE-P_N predicted photon leakage at 180° for photons transmitted through a non-absorbing homogeneous cylinder with scattering coefficient $\mu_s = 1$ mm^{-1}. The MC calculation used 4.7×10^8 photons.

As the solution with P_{15} angular approximation normally takes longer time than the solution with P_3 approximation, it would be advantageous to use only the P_3 result for comparison.

Figure 3.11 shows the modelled results for the same homogeneous cylinder as above, but with 0.1 mm^{-1} absorption. For the result of MC calculation 5.1×10^8 photon histories were performed. Satisfactory agreement is again seen between the results produced with the FE-P_N approximations and with MC. It can be seen that the difference between diffusion theory and FE-P_N or MC is increased significantly with the addition of a small amount of absorption. Diffusion theory fails to describe the photon migration through the cylinder and overestimate the absorption, even the ratio of μ_a/μ_s is equal to 1/10.

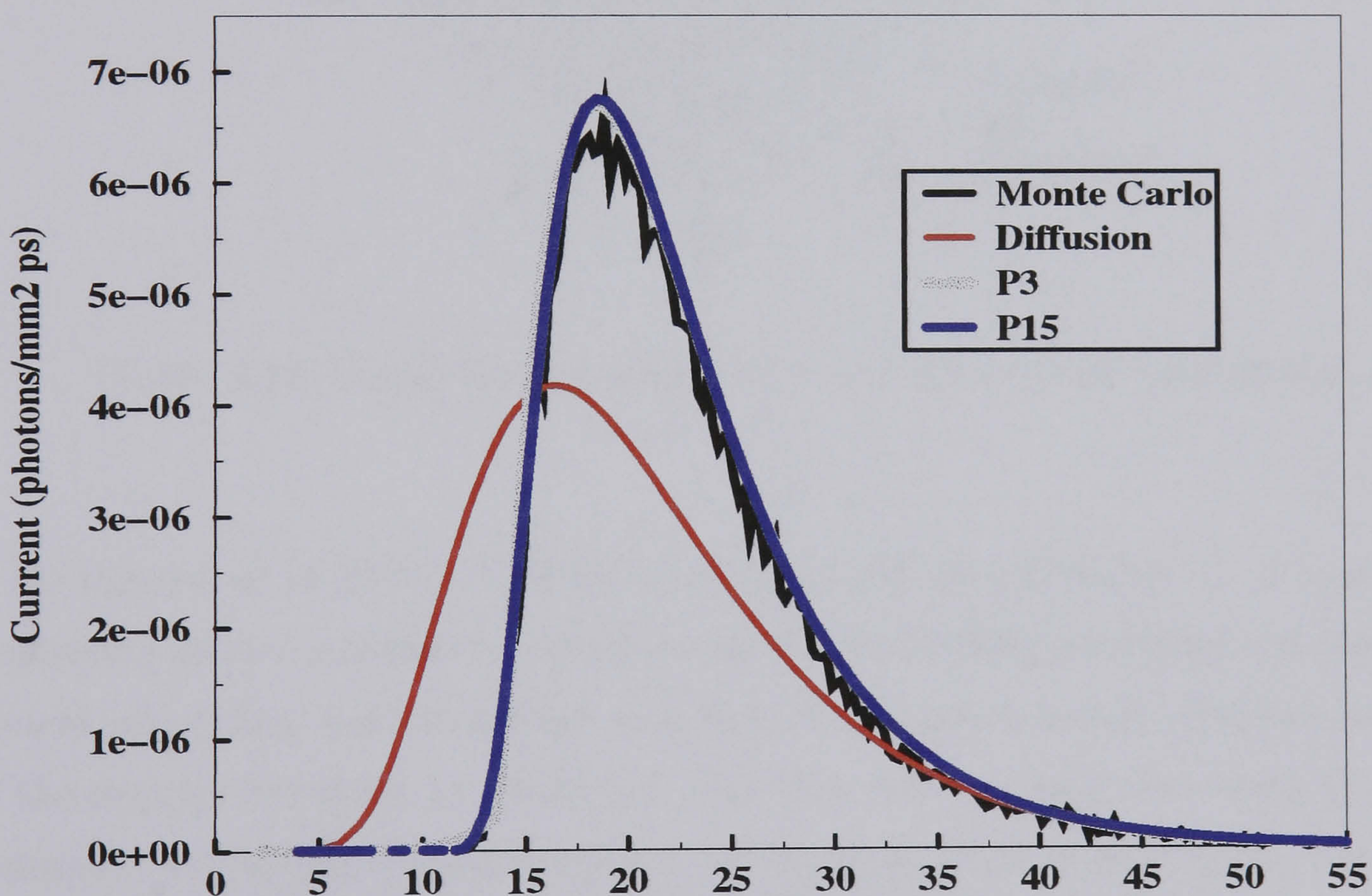


Figure 3.11: Comparison of leakage currents at 180° calculated using both MC and FE-P_N for the homogeneous cylinder shown in Figure 3.9 with an absorption coefficient of 0.1 mm^{-1}.

Inhomogeneous Cases

In two cases of this subsection, the MC calculations were performed using 8 sources and detectors located at 8 coincident and equidistant points around the external boundary, as shown in Figure 3.12. However, the MC results used in this section for comparison with FE-P_N solutions obtained from the detector 5 due to the source 1 located opposite. The results of MC with 8 sources and detectors will be used in Chapter 5 as data supplied into the reconstruction algorithm.

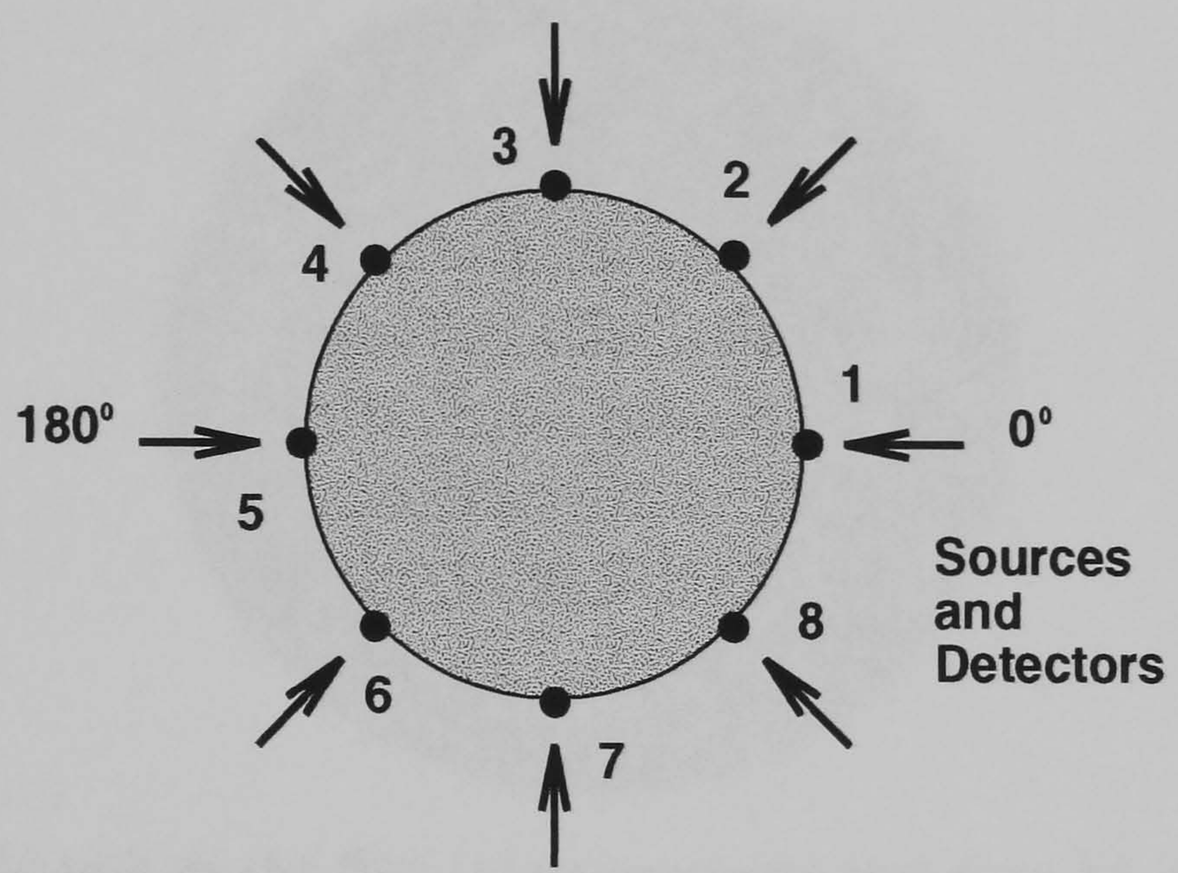


Figure 3.12: Simulation geometry with source and detector positions.

As illustrated in Figure 3.13 inhomogeneous cylindrical region of 10 mm radius, containing three 1 mm radius cylindrical regions of differing scattering and absorption optical properties, was considered as a first inhomogeneous case. Optical properties of the regions are given in Table 3.3. For this case isotropic scattering (g=0) was assumed. In the MC calculation 5.0×10^9 incident photons were used. For FE-P_N solution, an isotropic source was pulsed for 1 picosecond at t=0. The 2D finite element mesh given in Figure 3.13 consisted of 2724 nodes and 5446 triangular elements.

The time evolution of the leakage current was recorded by a modelled detector located at the 180° from the source. In Figure 3.14 the solutions for MC, diffusion, P_9 and P_{15} approximations are presented and the computing time requirements for this problem are listed in Table 3.4 . As can be seen from the figure that good agreement

Cylinders	(x,y) coordinates (mm)	$\mu_a(mm^{-1})$	$\mu_s(mm^{-1})$
Background	(0,0)	0.05	0.45
Cylinder 1	(-6,2)	0.09	0.81
Cylinder 2	(5,5)	0.12	1.08
Cylinder 3	(-3,-2)	0.15	1.35

Table 3.3: The central coordinates and optical coefficients of 4 cylindrical regions used for the first inhomogeneous case.

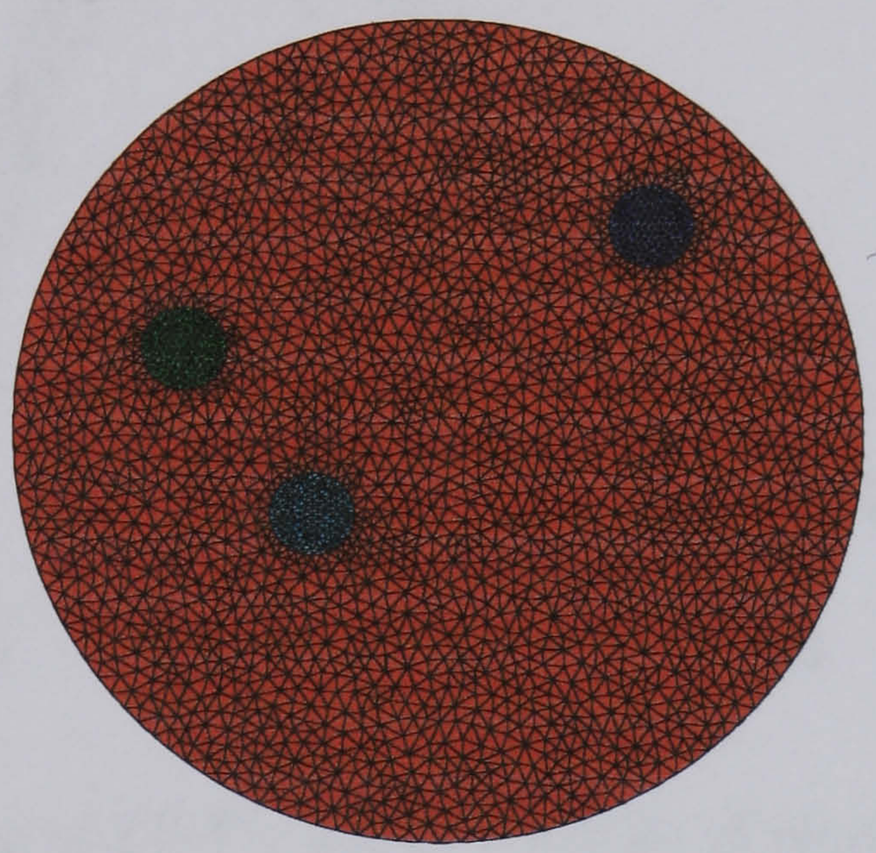


Figure 3.13: FE mesh of the first inhomogeneous test case for MC comparison.

was again obtained between the FE-P_{15} approximation and the MC solution while significantly different time variations were predicted for diffusion theory. As P_9 and P_{15} produced the same result, it is also worth noting that the use of only P_9 angular approximation for modelling the problem was advantageous due to the long time requirement for the P_{15} approximation.

The above inhomogeneous cylinder was modelled with MC and FE-P_N for the case of only one small cylinder located at the centre. The large cylinder had the same absorption and scattering properties given as Background in Table 3.3 and the central cylinder had the optical properties of Cylinder 2 from the same table. The revised mesh distribution was 4876 triangular elements consisting of 2439 nodes as shown in Figure 3.15. 5.0×10^9 photons were used in the MC simulation. The results obtained by two models are given in Figure 3.16. Again MC appeared to agree well with

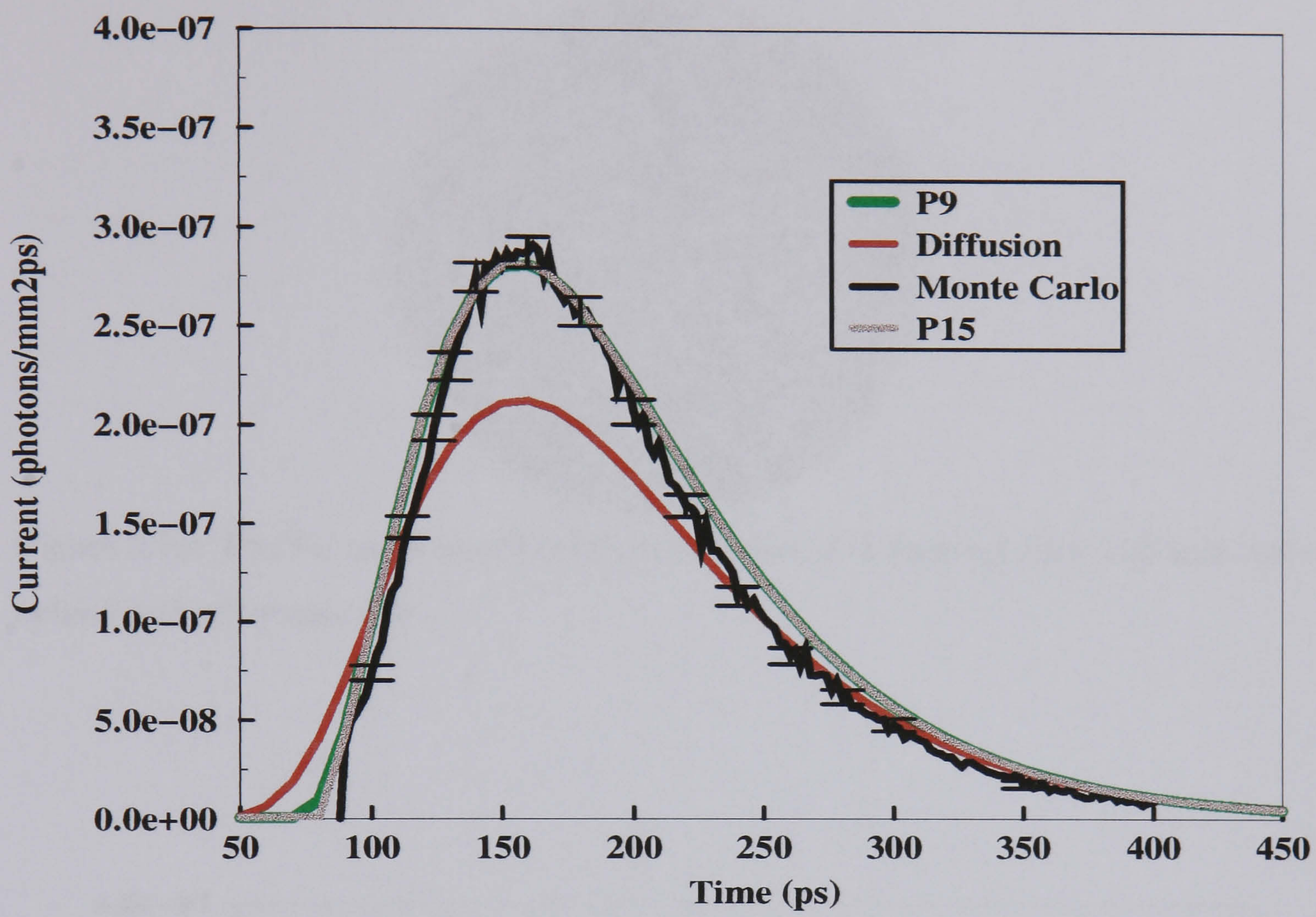


Figure 3.14: Comparison of FE-P_N and MC results of photon leakage for inhomogeneous cylinder containing three cylindrical absorbers/scatterers.

Methods	CPU times in minutes
MC (5×10^9 photons)	2505.72
FE-P_{15}	500.11
FE-P_9	294.32
FE-P_0(Diffusion)	6.40

Table 3.4: Comparative times for the inhomogeneous cylindrical problem given in Figure 3.13. FE-P_N times were obtained for a mesh with 2724 nodes-5446 elements using 60 time steps.

the FEM (P_{15} or P_9 approximations). On the other hand, diffusion theory showed significant discrepancies with transport and MC solutions.



Figure 3.15: The FE mesh used for the calculation of the second case with one centred cylindrical inhomogeneity.

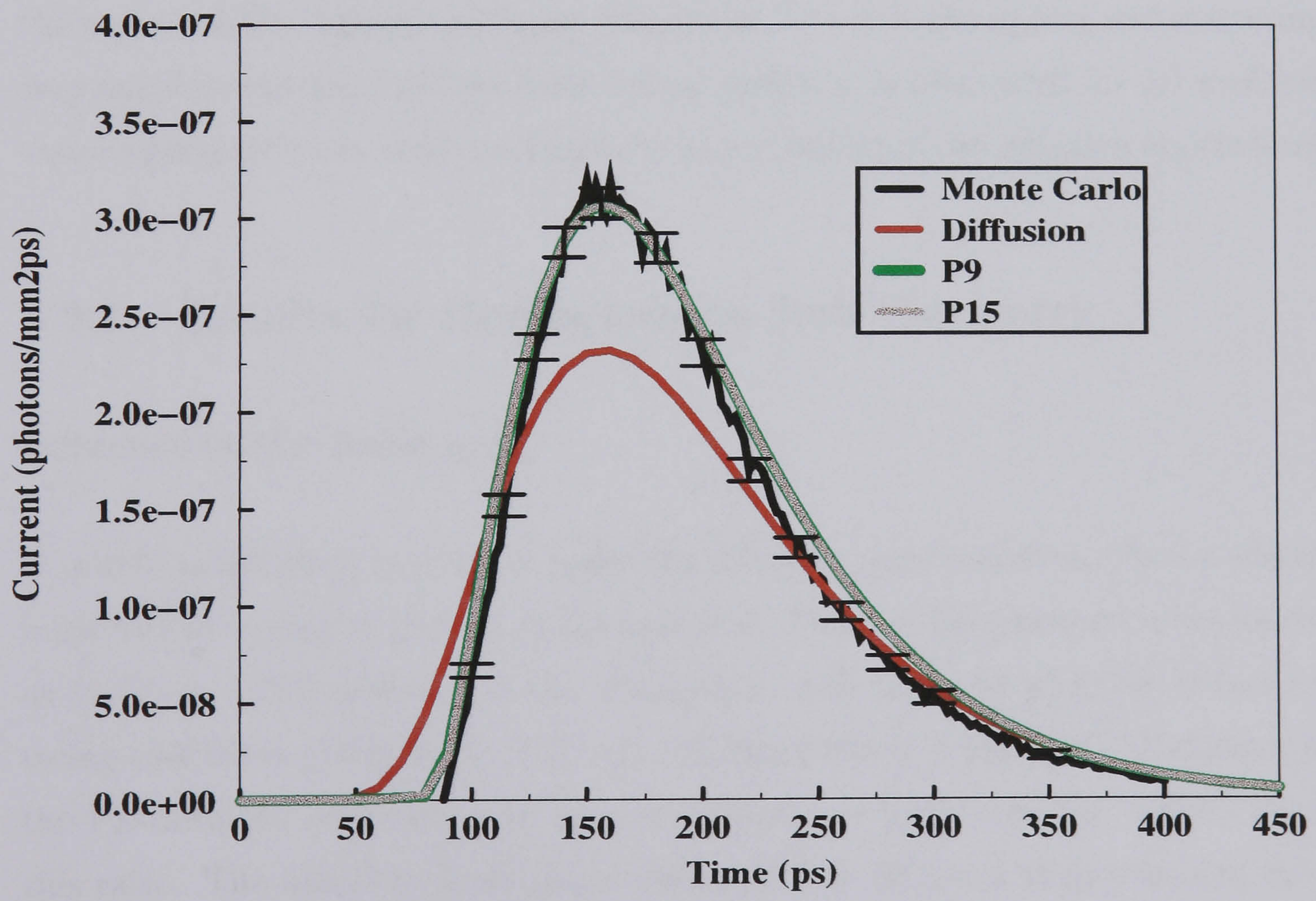


Figure 3.16: Comparison of FE-P_N and MC results for photon leakage at 180°, for the inhomogeneous cylinder with one centred cylindrical problem.

3.3 Steady-State Cases

In this section, investigations are carried out on the limitations of the diffusion approximation to the time-independent form of the Boltzmann transport equation for photon propagation in homogeneous and heterogeneous media. Results are presented in four categories. The first concerns the comparison of FE-diffusion and transport calculations in 1D and 2D geometries where the influence of the ratio of absorption to reduced scattering coefficient, (μ_a/μ'_s), on the accuracy of the diffusion approximation is quantified. The second study investigates the effect of the anisotropy factor g in modelling the propagation of light in homogeneous 1D tissue-like media. The third concerns the comparison between diffusion and transport calculations in a layered cylindrical geometry which can be seen as a very simplistic approximation of a human head. The last study investigates the influence of boundaries between two materials with different optical properties, to show how good diffusion theory can model transition zones between materials. In this category, the propagation of light through void-like regions and layers (channels), in which absorption and scattering are very small compared with the surrounding medium, is illustrated for 2D problems of various geometries, in order to demonstrate the failure of the diffusion approximation.

3.3.1 Results for Homogeneous Slab Geometry

Influence of the Ratio μ_a/μ'_s

It is well known that, in order to apply the diffusion approximation, photon scattering must be the dominant process in the material. This can be expressed mathematically as $\mu_a/\mu'_s \ll 1$ [87] where μ_a is the absorption coefficient and μ'_s is the reduced scattering coefficient given by $\mu'_s = (1\text{-}g)\mu_s$. In this section, a series of calculations using the FE-diffusion and transport approximations are performed for various values of this ratio. The aim is to investigate when and how diffusion theory fails in the case that (μ_a/μ'_s) approaches 1.

As sketched in Figure 3.17, an infinite slab of width 9 mm was considered. An

isotropic plane source was located at $x = 0$ and vacuum boundary condition was applied at the outer surface. In all calculations the reduced scattering coefficient was $\mu_s' = 10\ \text{mm}^{-1}$ and the anisotropy factor g was taken equal to zero (assuming isotropic scattering only). To obtain μ_a/μ_s' ratios ranging from 1/10 to 1/2, the absorption coefficient was varied from $\mu_a = 0.1\ \text{mm}^{-1}$ to $5.0\ \text{mm}^{-1}$. For the transport theory solutions, a P_{25} angular approximation was employed. A mesh consisting of 101 nodes and 102 quadratic elements was used for calculations.

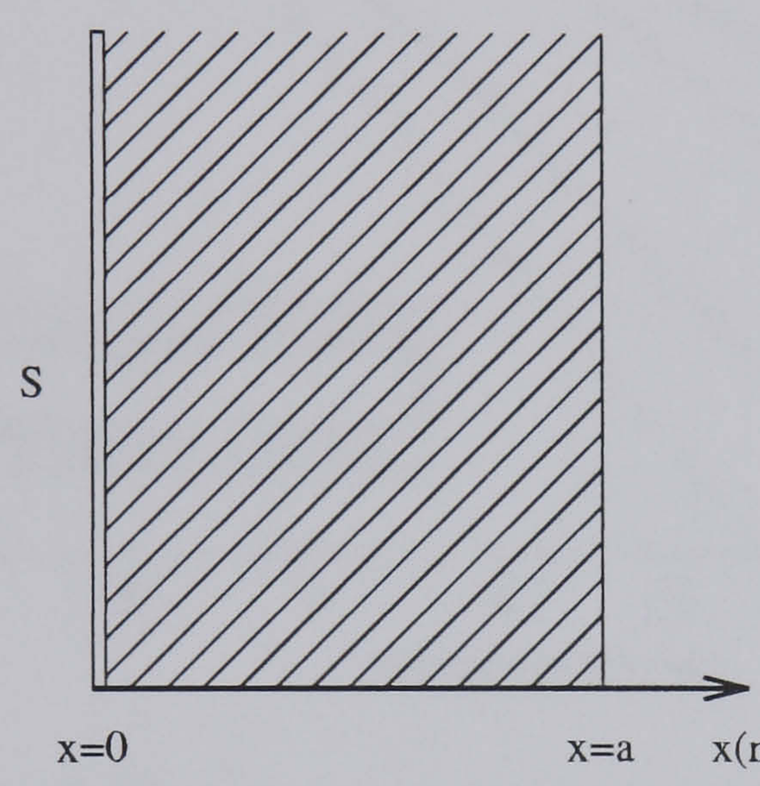


Figure 3.17: Geometry of the infinite slab problem. S denotes the source plane and a the slab thickness.

Figure 3.18 shows the calculated results of photon intensity for four different absorption coefficients using diffusion and transport theory. Diffusion and transport theory produced similar result when the ratio of μ_a/μ_s' was equal to 1/100; when absorption was very small. When the absorption was increased, diffusion theory more and more underestimated the photon intensity or in other words overestimated the absorption in the medium. It was also clear that the difference between two theories increased with increasing distance from the source. For example, diffusion theory underestimated the photon intensity at a distance of 8.5 mm^{-1} by over five orders of magnitude for an absorption coefficient of $\mu_a = 2.5\ \text{mm}^{-1}$.

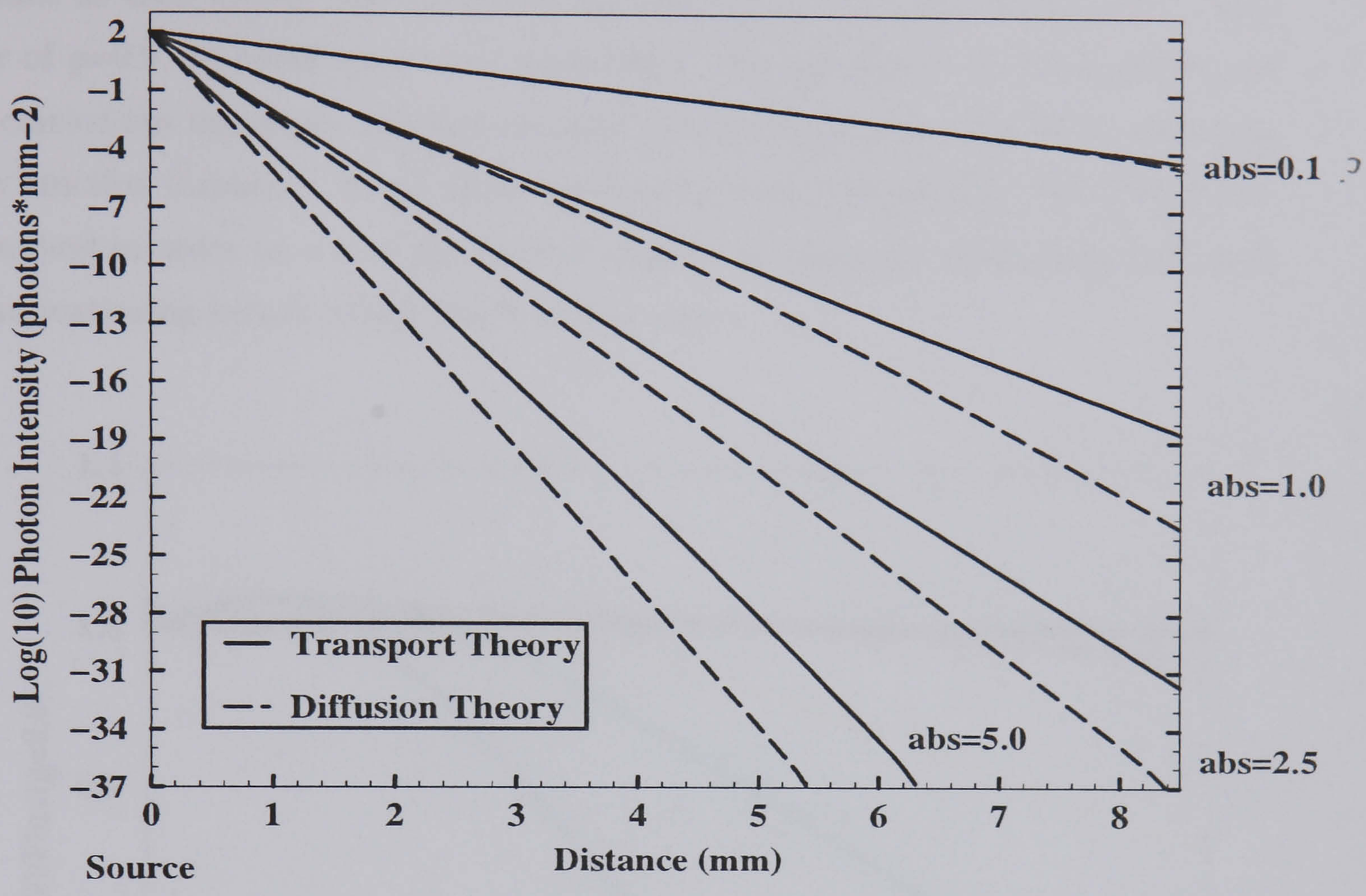


Figure 3.18: Solutions of photon attenuation through an infinite slab, with an isotropic plane source to show influence of the ratio μ_a/μ'_s on the accuracy of diffusion approximation.

Influence of g

In the following examples, the effects of high g values (highly forward-peaked scattering) on the propagation of photons in simulated tissue are studied again using the same infinite slab geometry. We compared transport calculations of media with the same reduced scattering coefficients, $\mu'_s = (1\text{-}g)\mu_s$, but varying g values. Since in diffusion theory only the parameter μ'_s appears but not g, all media with the same μ'_s will give the same results. We will show that this is not the case when transport calculations are performed.

Flux distributions for two medium with $\mu_s = 10.0\ \text{mm}^{-1}$, $g = 0.9$ ($\Rightarrow \mu'_s = 1\ \text{mm}^{-1}$) and $\mu_s = 1.0\ \text{mm}^{-1}$, $g = 0.0$ ($\Rightarrow \mu'_s = 1\ \text{mm}^{-1}$) were calculated for various values of

the absorption coefficient μ_a. Source and boundary conditions, and the mesh, were the same as used above. For transport calculations in the media having anisotropy factor of g=0.9, 18 coefficients were calculated. The calculation of those coefficients were carried out using two different formula: Henyey-Greenstein and SAM scattering phase function formulas. Then, those coefficients were truncated by the delta-M (δ-M) method in order to obtain the desired number of Legendre expansion coefficients for the scattering kernel, which was 9 in this case.

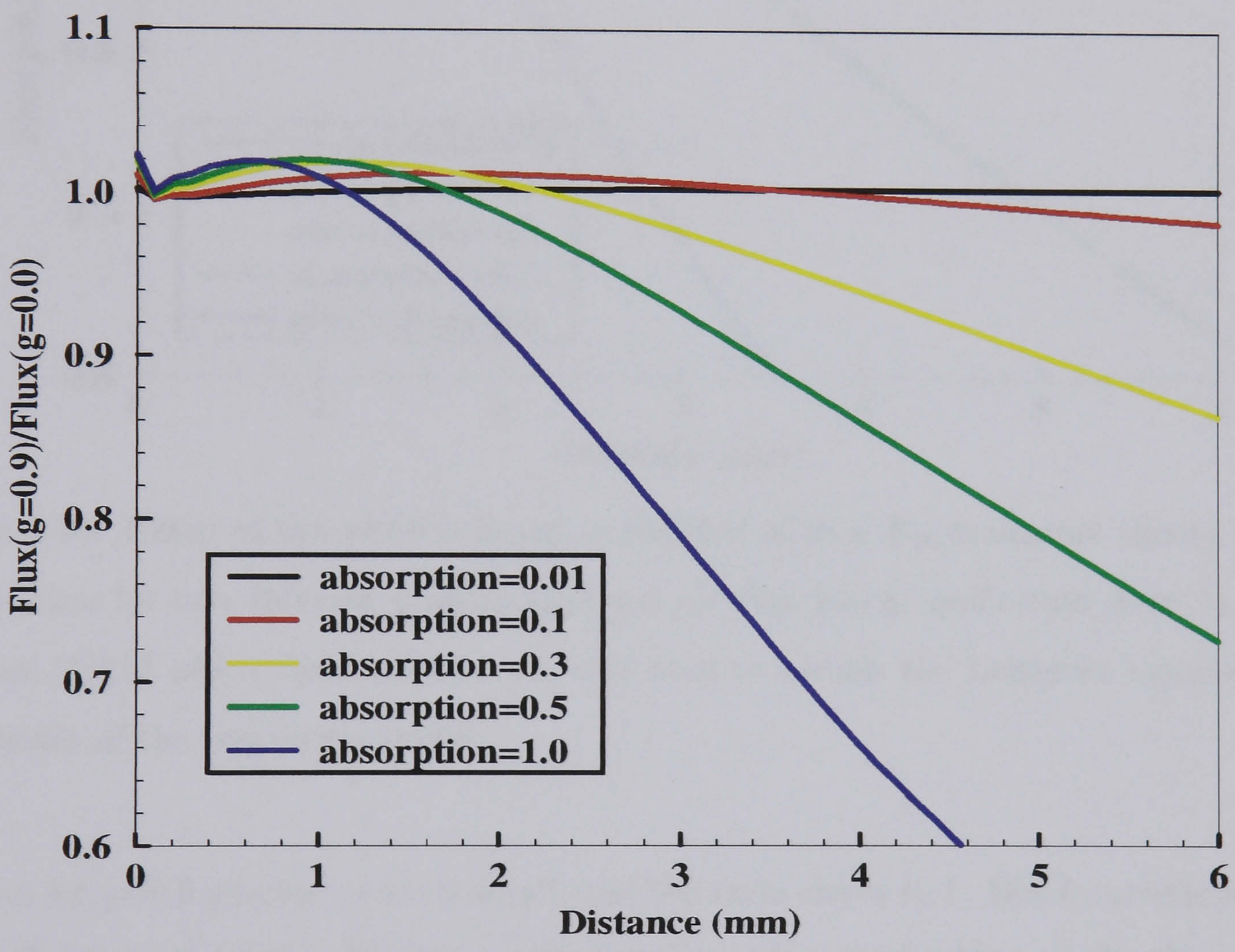


Figure 3.19: Ratio of the photon fluxes calculated with a P_{25}-transport theory approximation for two different g values and various absorption coefficients (mm^{-1}). Legendre expansion coefficients were obtained from the H-G phase function formula.

Figures 3.19 and 3.20 show the ratio of the photon flux distributions calculated using the above two phase functions formulas. It can be seen that, for small values of absorption coefficient ($\mu_a = 0.01$ mm^{-1} and $\mu_a = 0.1$ mm$^{-1} \ll \mu_s' = 1$ mm^{-1}), which means that the diffusion approximation is valid, the difference in photon distribution

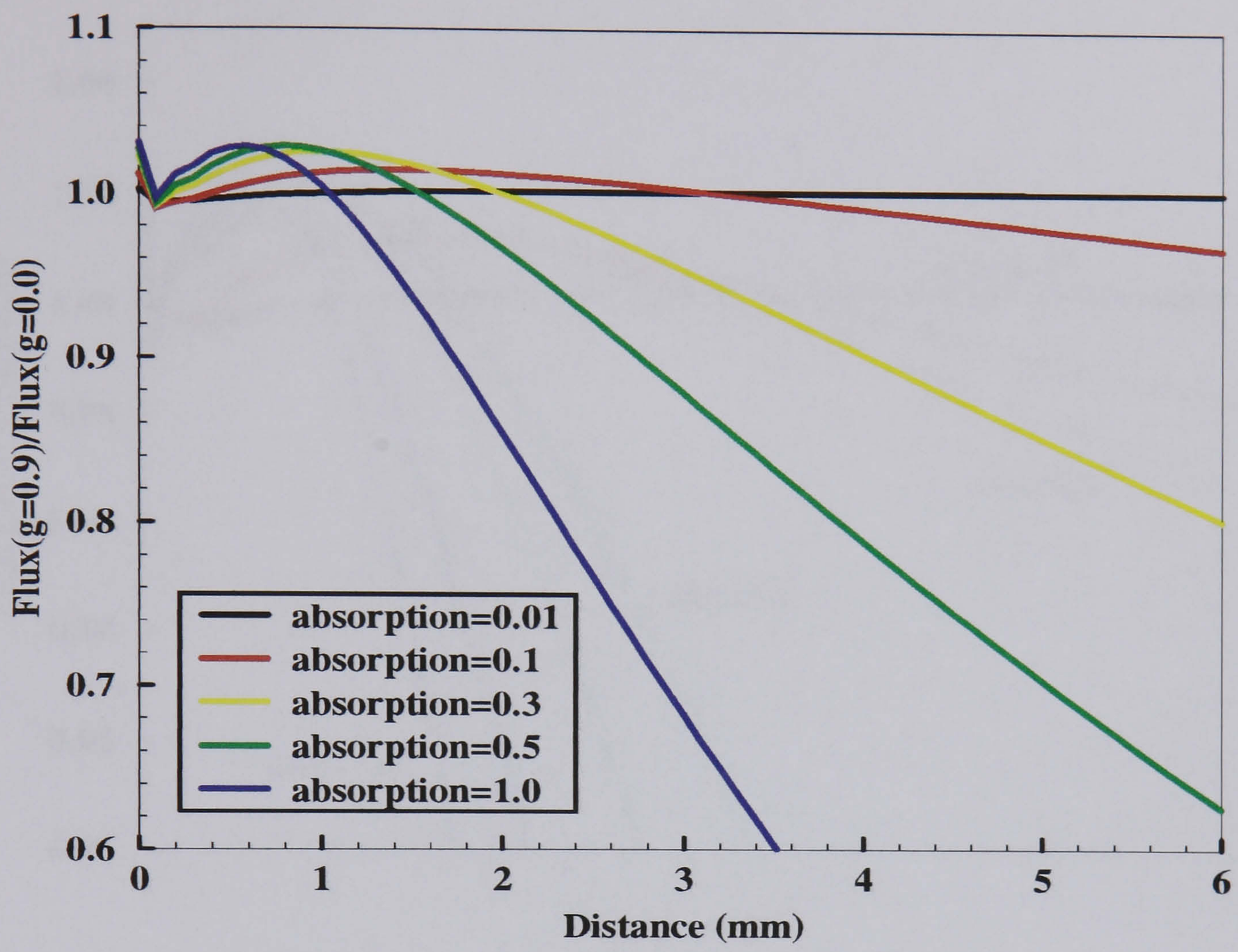


Figure 3.20: Ratio of the photon fluxes calculated with a P_{25}-transport theory approximation for two different g values and various absorption coefficients (mm^{-1}). In this case, SAM phase function formula was used to obtain the Legendre expansion coefficients of the scattering kernel.

between for g=0.9 and for g=0.0 is small, and the ratio closes to 1. But for coefficients $\mu_a = 0.3$, 0.5, and 1.0 the diffusion approximation is less applicable and the choice of g is important. In both figures, use of the larger g value leads an initial small increase in the photon intensities up to 0.5-1 mfp from the source forward by a substantial decrease further from the source plane.

The ratio of the photon flux distributions calculated using the H-G and the SAM phase function formulas, already shown in Figures 3.19 and 3.20, separately, are plotted together in Figure 3.21. For small absorptions both give closely similar results. However, when the absorption coefficient is increased higher values are obtained with the SAM formula than with the H-G formula, close to the source and larger decreases

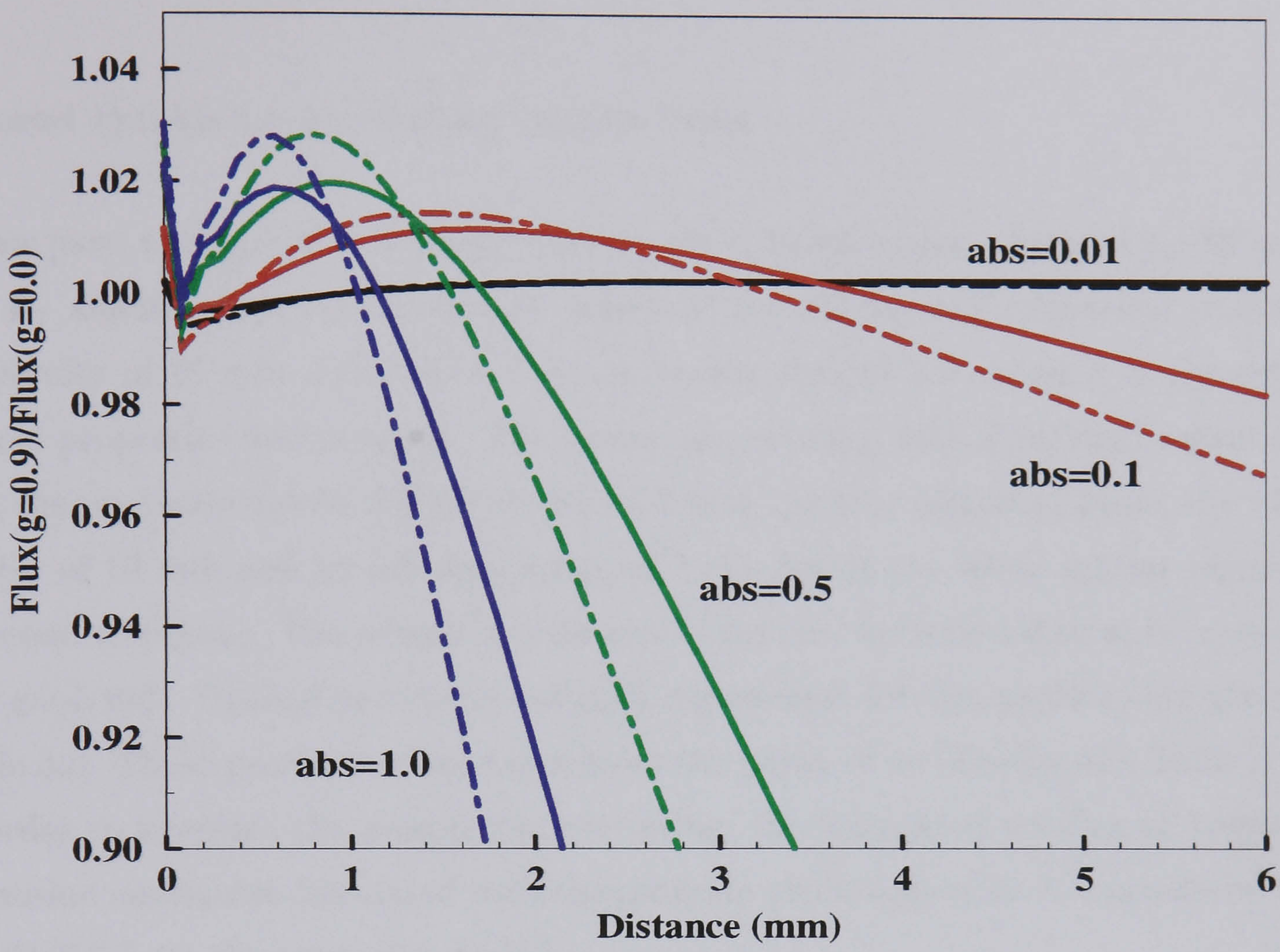


Figure 3.21: Comparison between the results obtained with the H-G and SAM phase function formulas for various values of absorption coefficient (mm^{-1}). The solid lines are H-G solutions and the dot-dashed lines the SAM solutions.

missing?

are observed far from the source.

3.3.2 Results for Heterogeneous 2D Geometry

In this section, the limits of the diffusion approximation are analysed in 2D heterogeneous media. Four different geometries are considered for transport and diffusion theory calculations. The aim is to investigate the propagation of photons in a layered cylinder resembling a human head and the effects on the distribution of light caused by both strong absorbing and void-like heterogeneities and layers (channels) in which absorption and scattering are very small compared with the surrounding medium. It was shown that diffusion theory fails to accurately describe the propagation of

photons in layered geometry and also in both highly absorbing and void-like regions.

Layered cylinder representing human head

In this part, a comparison between the forward solution results obtained by diffusion and P_7 angular approximations are presented for 2D layered cylindrical problem. A cylinder of 20 mm radius with 5 layers having various scattering and absorption optical properties was adopted. The layers are, starting with skin/skull region of 5 mm, the cerebrospinal fluid (CSF) region of 2 mm, the grey matter of 3 mm, the white matter of 10 mm and an inhomogeneity of 2 mm inside the white matter region to represent a tumour. The central coordinates of the tumour were taken to be x=4 mm and y=-5 mm. Optical parameters of each region used for this problem are given in Table 3.5. Those parameters are taken from the paper of de Oliveira and Tahir [150]. In order to simulate the anisotropic scattering, the associated number of Legendre expansion coefficient calculated with the program given Appendix A was entered into the EVENT for the scattering kernel.

Regions	Radius (mm)	$\mu_t(mm^{-1})$	$\mu_a(mm^{-1})$	$\mu_s(mm^{-1})$	g
Skin/skull	20	18.775	0.025	18.75	0.92
CSF	17	1.005	0.005	1.00	0.0
Grey matter	15	50.04	0.04	50.00	0.92
White matter	10	90.015	0.015	90.00	0.9
Inhomogeneity	2	90.1	0.1	90.00	0.9

Table 3.5: Optical properties of the layers used in the layered cylindrical case, μ_a is the absorption coefficient, μ_s is the scattering coefficient, $\mu_t = \mu_a + \mu_s$, g is the anisotropy factor or the mean cosine of the scattering angle.

The positioning of the layers is shown in Figure 3.22 and the log plots of steady-state intensity distribution obtained with EVENT for the source one and detector 9 (see Figure 3.24) is given in Figure 3.23. FE mesh consisted of 10493 nodes and 20984 elements.

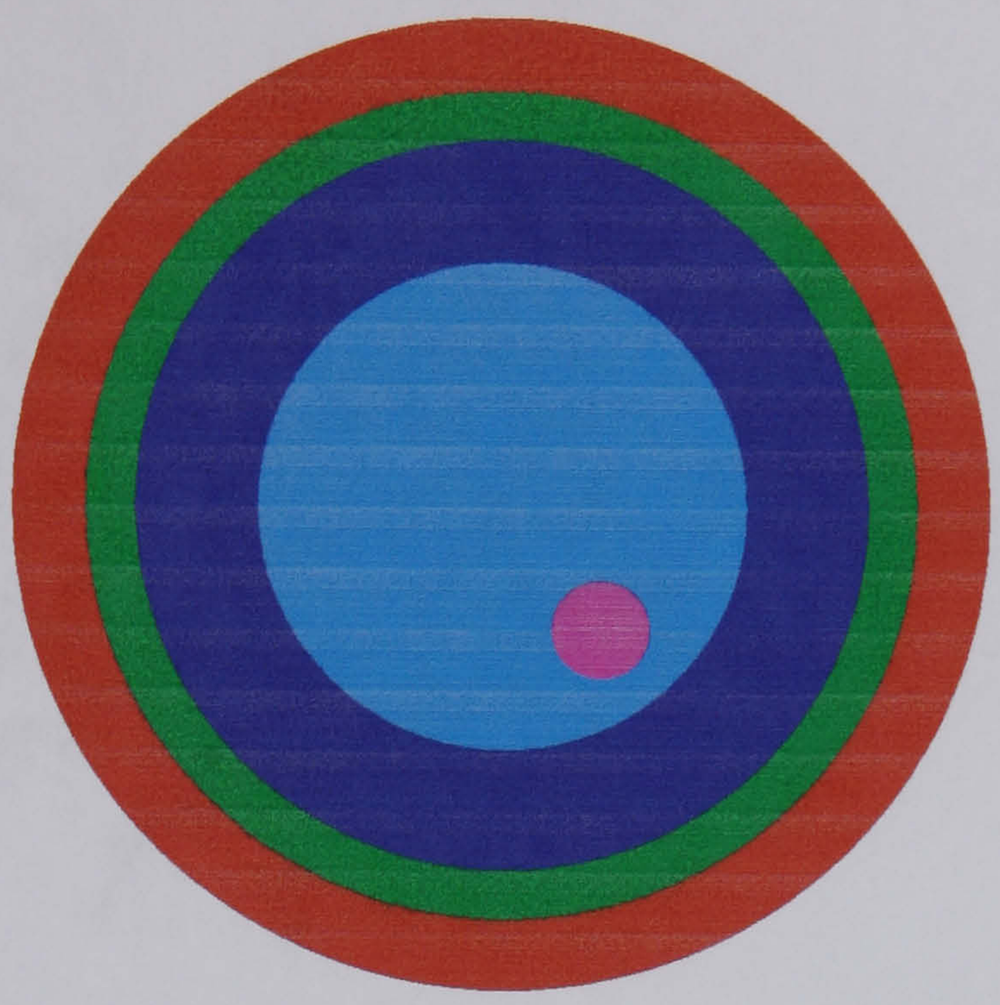


Figure 3.22: 2D geometry for the steady-state calculation of the layered cylinder problem.

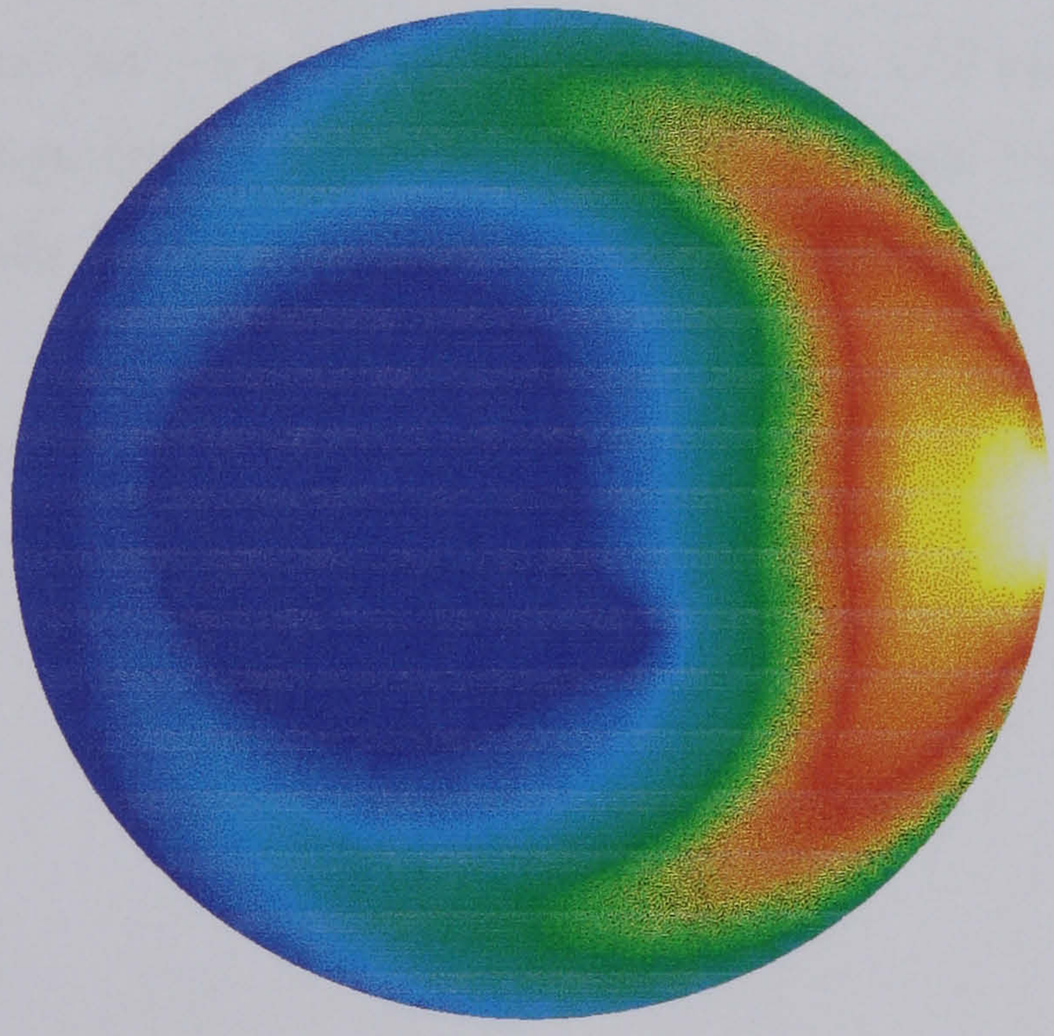


Figure 3.23: Calculated (log) intensity distribution from the source one using the problem layout shown in Figure 3.22. Result are obtained with P_7 angular approximation with seven coefficients for the scattering kernel.

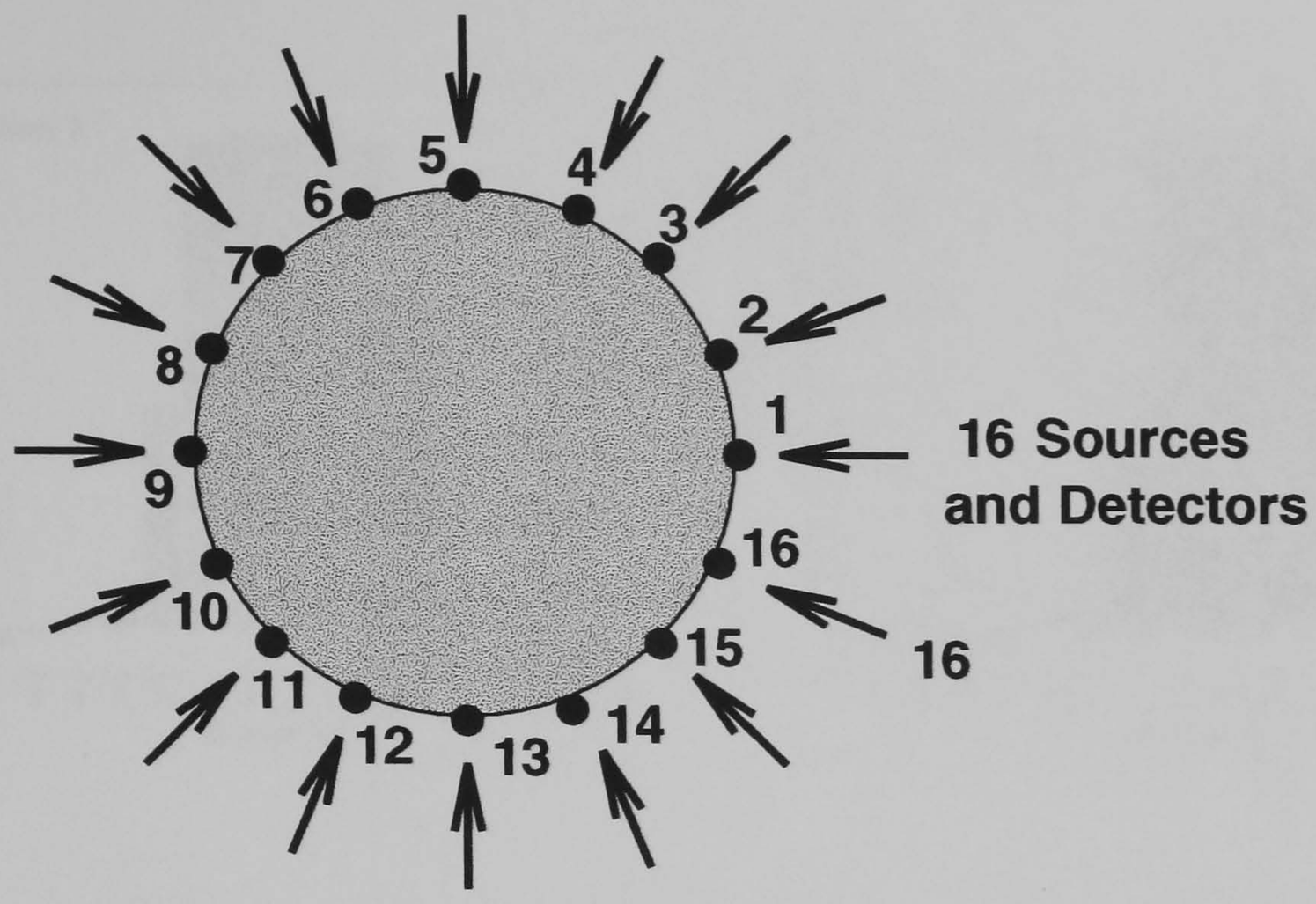
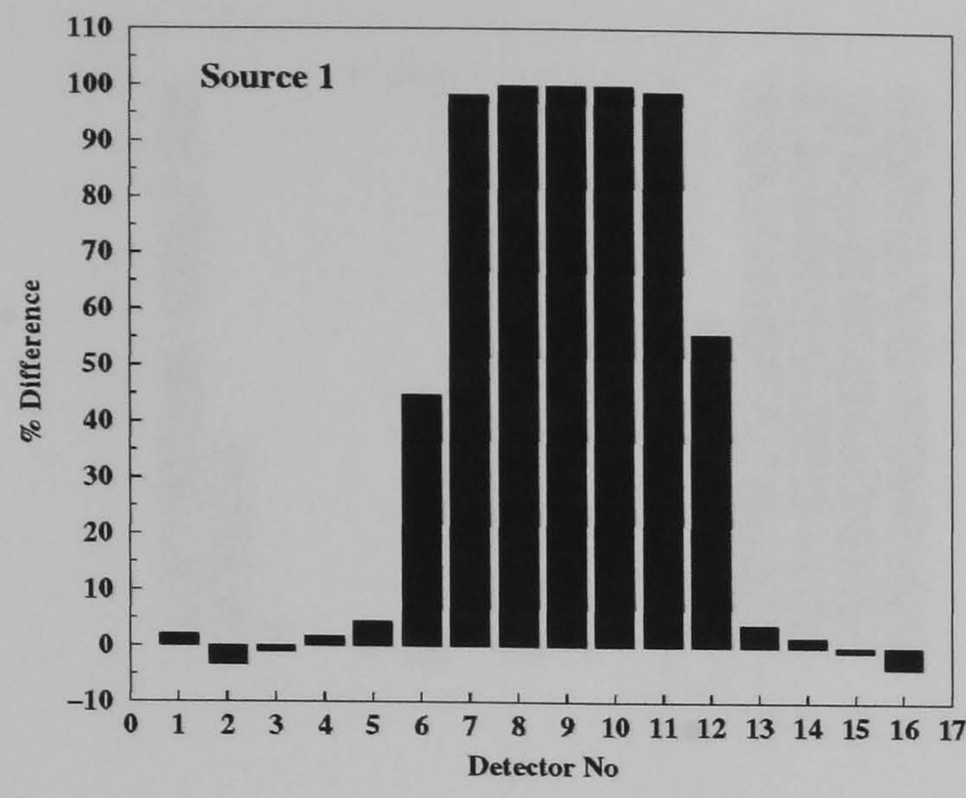
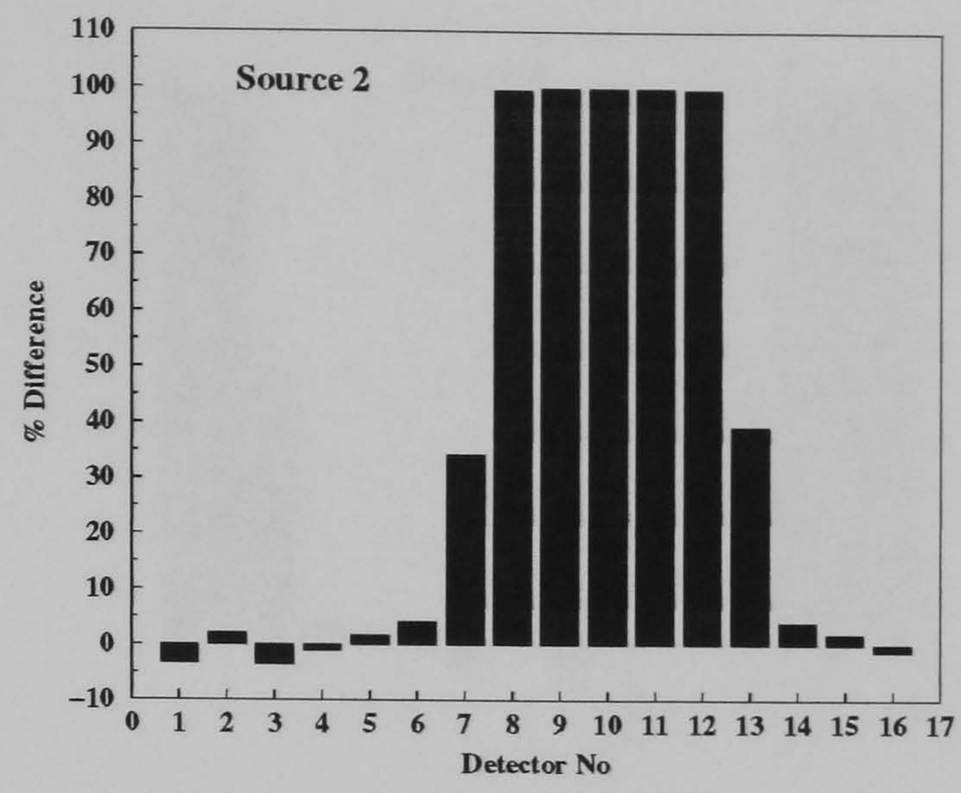
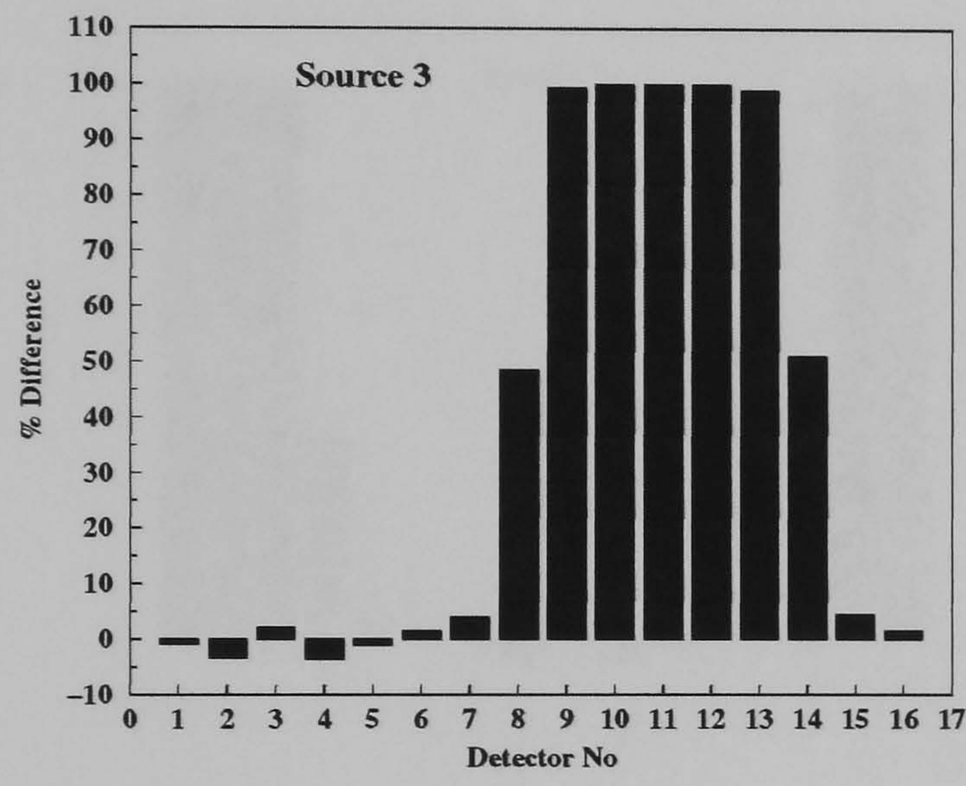


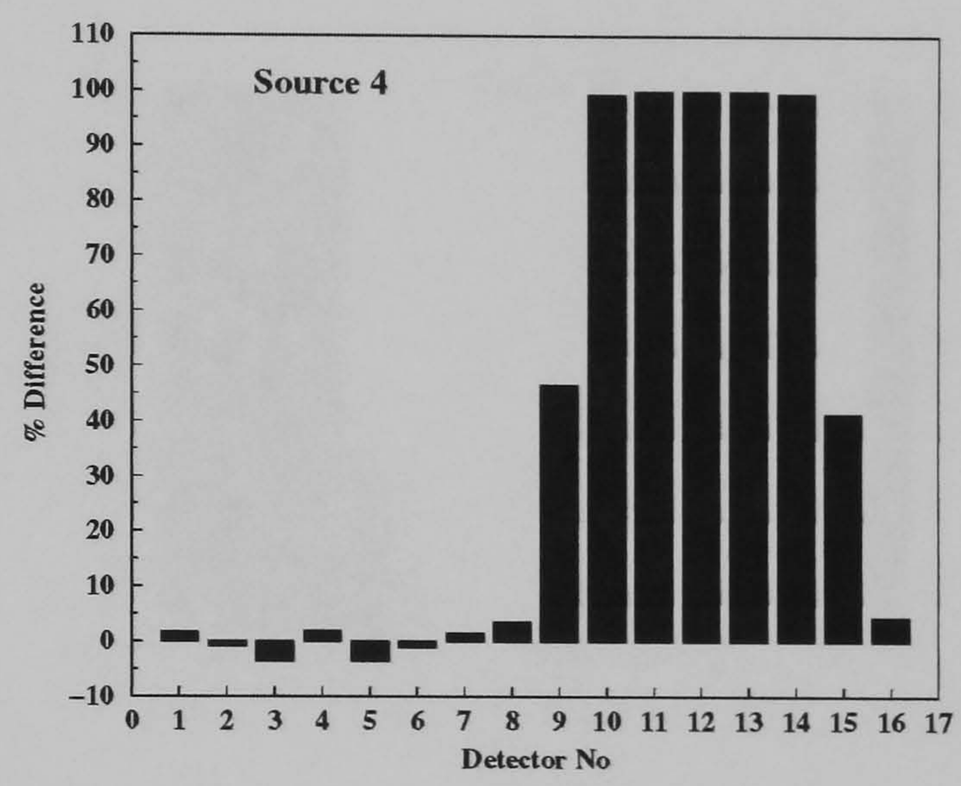
Figure 3.24: Sources and detectors configuration used for layered cylindrical problem.

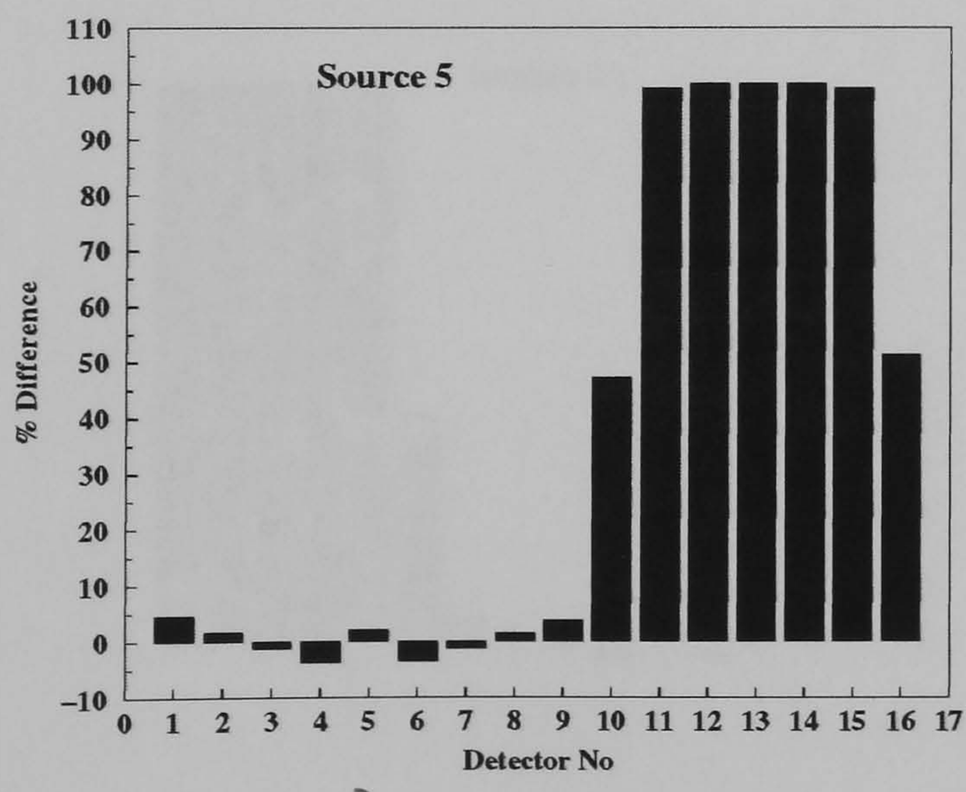
The percentage difference between diffusion and P_7 solutions measured at 16 detectors, using 16 isotropic sources are given in Figures 3.25, 3.26 and 3.27. It can be seen that, in all figures, large discrepancies (up to 100 %) between the two approximations are observed, especially at the detectors far from the sources.











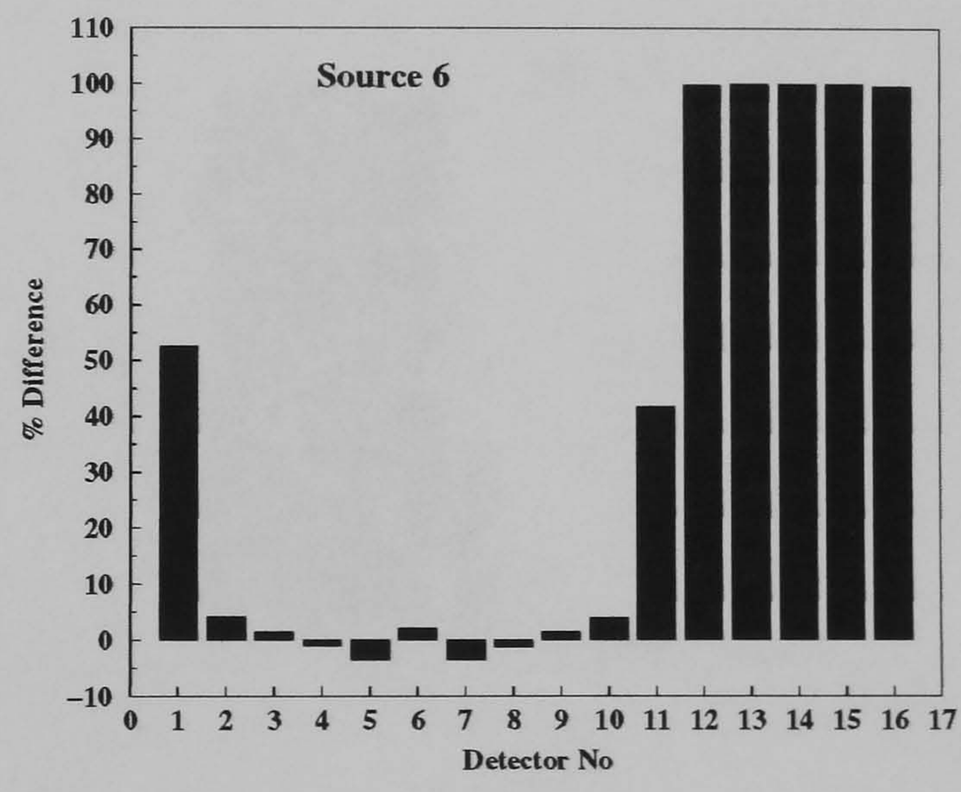


Figure 3.25: Relative error between FE-P_7 and diffusion solutions calculated at 16 surface detectors and for sources 1-6 for the problem shown in Figure 3.22.

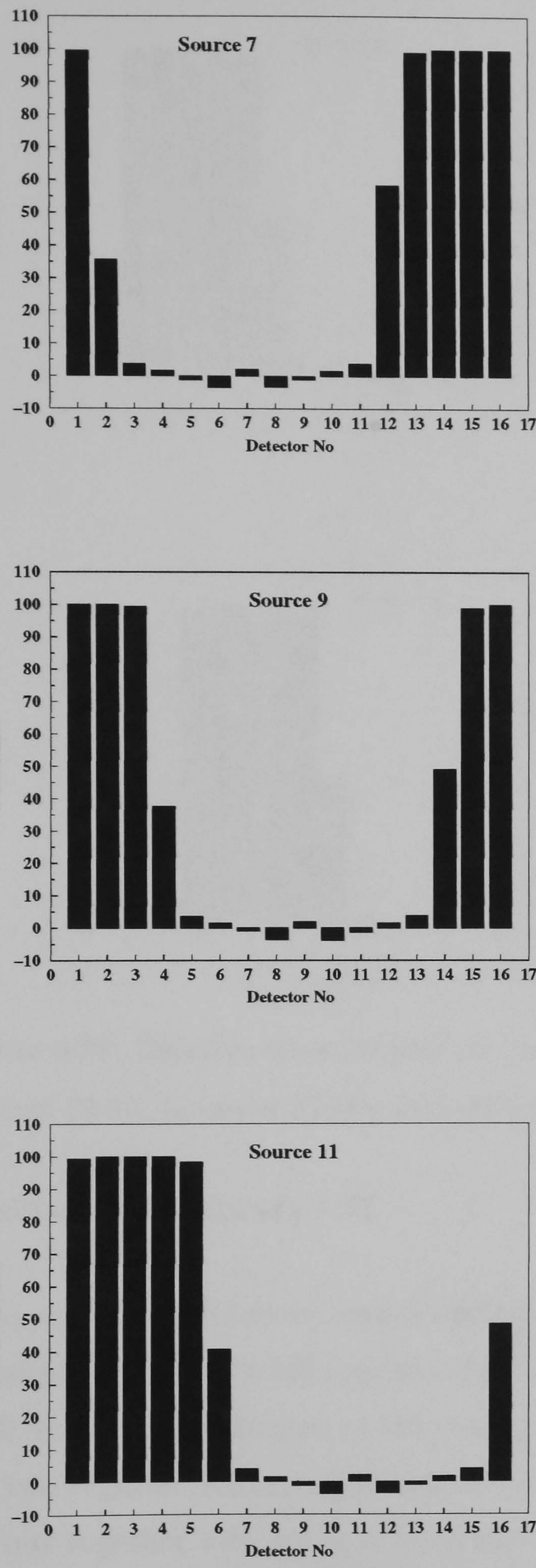


Figure 3.26: Relative error, in photon current leakage, between FE-P_7 and diffusion solutions at 16 detectors and for sources 7-12 for the problem shown in Figure 3.22.

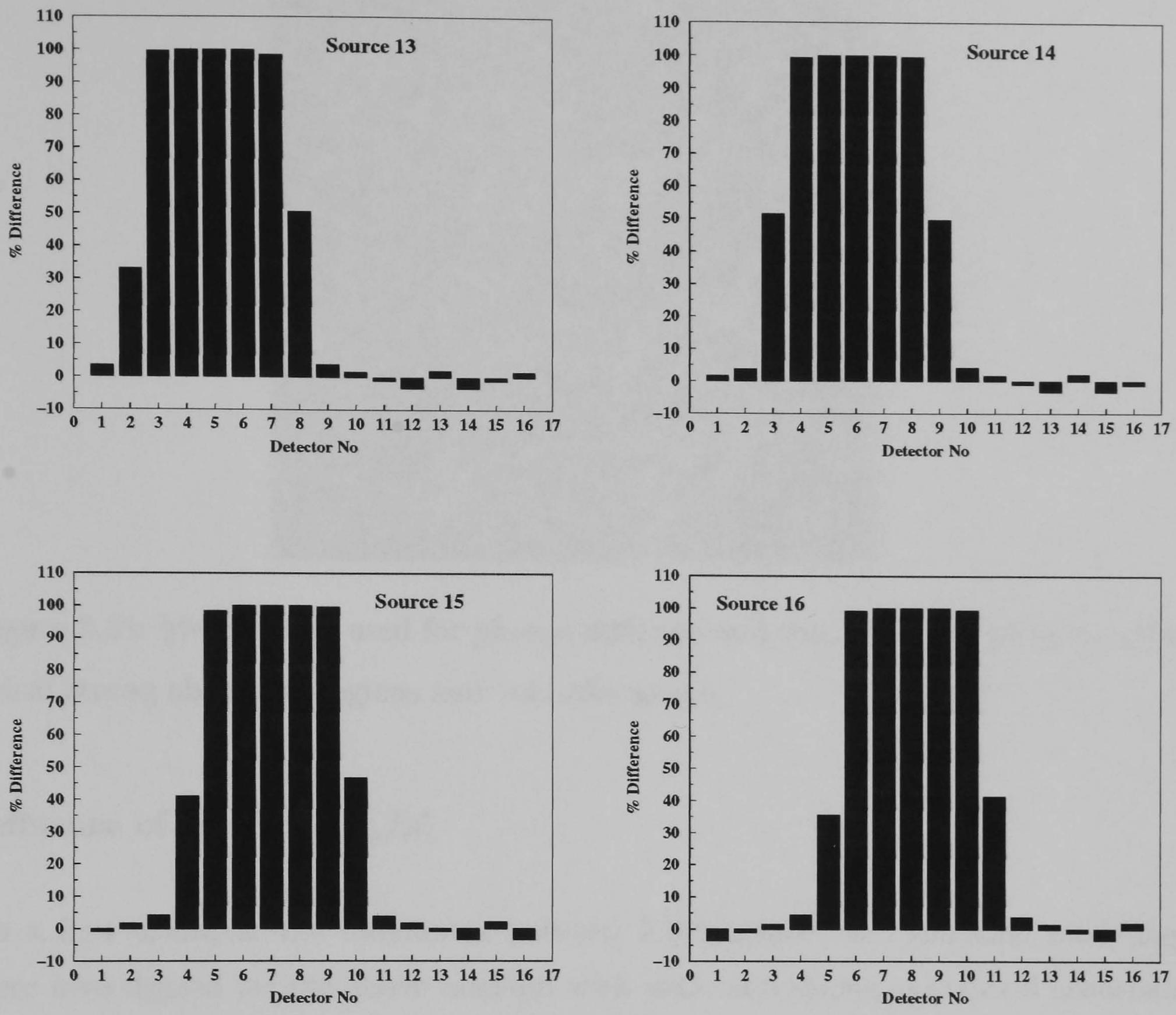


Figure 3.27: Relative error, in photon leakage current, at 16 surface detectors and for sources 13-16, between FE-P_7 and diffusion for the problem shown in Figure 3.22.

Simulation Geometry - II

The geometry adopted for various diffusion and transport simulations is as follows. A two dimensional 100×100 mm box (but infinite in the z direction), enclosed a cylinder of 20 mm diameter located at the centre. Various optical properties were assumed for the two regions. An isotropic source was positioned at the centre of the left side of the box together with vacuum boundary conditions on the four sides of the box. The photon intensities were plotted on a line passing through the centre of the cylinder. A mesh consisting of 3642 nodes and 7282 linear triangular elements, as illustrated in Figure 3.28, was employed in all problems.

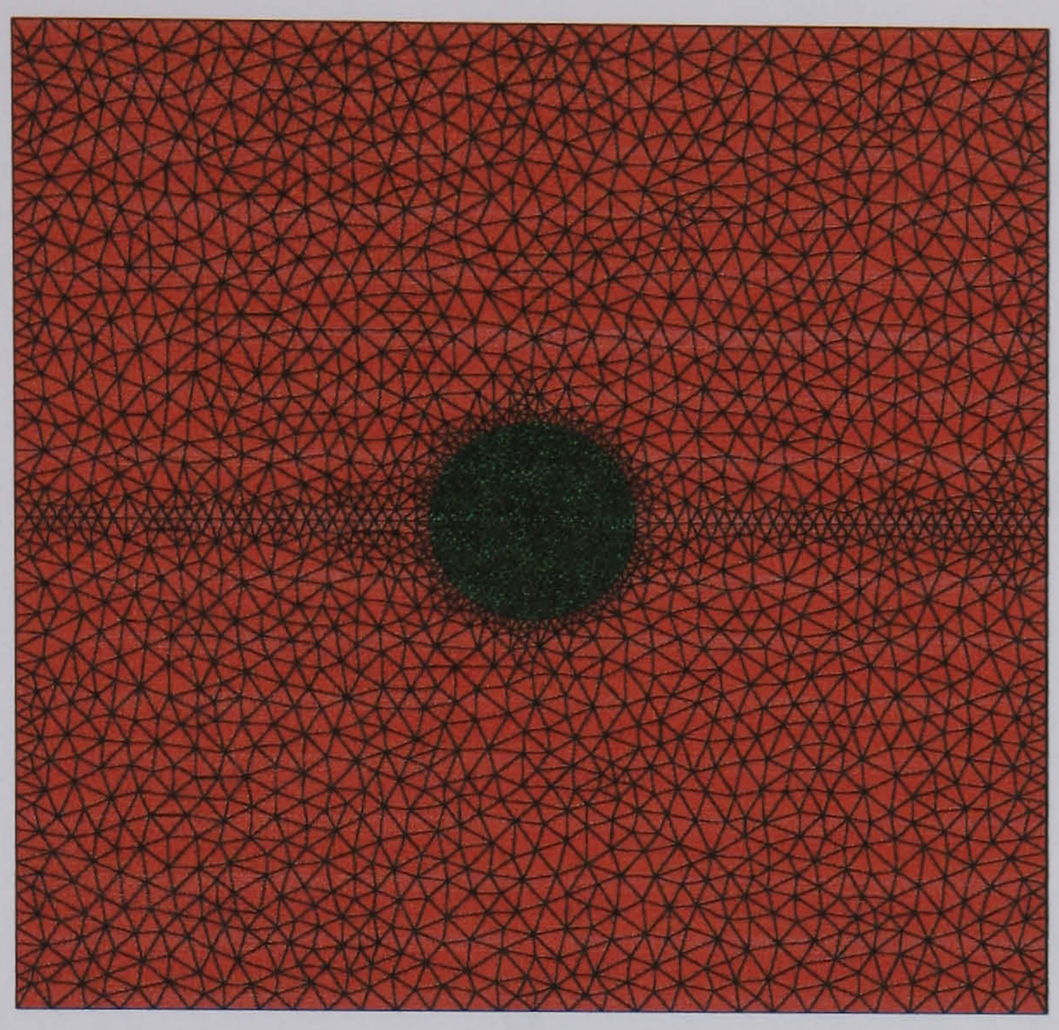


Figure 3.28: Mesh layout used for photon diffusion and transport modelling in cylindrical strong absorbing regions and void-like spaces.

Influence of the Ratio μ_a/μ'_s

As a first example, the differences between FE-transport and diffusion modelling were investigated for the above medium with weak and strong cylindrical absorbers at the centre to simulate a photon transport environment that may be encountered in blood vessels or haematoma. In the near-infrared wavelength region, blood has an absorption coefficient μ_a that is comparable with the reduced scattering coefficient μ'_s [151],[152]. Because the criteria, $\mu_a \ll \mu'_s$, for the validity of the diffusion theory is violated, diffusion calculations may be expected to disagree with transport calculations in these regions. The P_{25} angular approximation was used in the transport calculations described below.

To study the simulated influence of blood-filled heterogeneities, the calculation of photon intensities were performed for two situations. The box had an absorption coefficient of 0.01 mm^{-1} and a scattering coefficient of 1.0 mm^{-1} in both cases. g was assumed zero so that the reduced scattering coefficient, μ'_s, was also equal to 1.0 mm^{-1}. In the first case, the cylindrical region had a ten times higher absorption coefficient, $\mu_a = 0.1$ mm^{-1}, than the background medium and, in the second case the

absorption coefficient equalled μ_s', $\mu_a = 1.0\ \text{mm}^{-1}$. The scattering coefficient and the reduced scattering coefficient of the cylinder equalled the background value, $\mu_s = \mu_s'$ $= 1.0\ \text{mm}^{-1}$ in both situations.

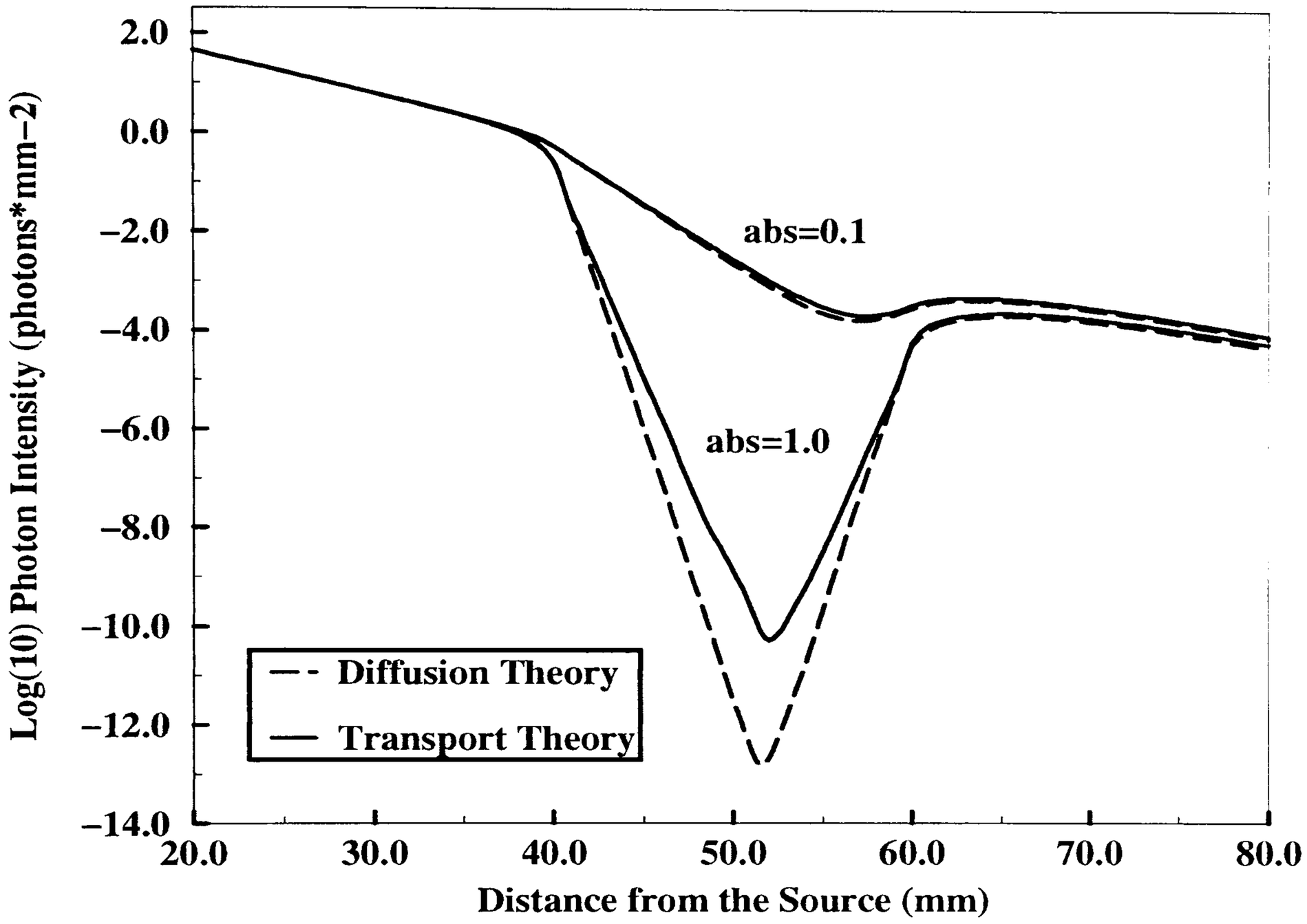


Figure 3.29: Comparison between diffusion and transport theory calculations of the photon intensities in heterogeneous media to investigate influence of μ_a/μ_s'.

Results are shown in Figure 3.29 in logarithmic scale. In the first case, transport and diffusion theory modelling agree well throughout the medium. However, in the second case, large differences between transport and diffusion modelling can be seen inside the cylinder while outside this region the two models agree well. For this latter case, diffusion theory overestimates the photon intensity in the inhomogeneity by more than two orders of magnitude. These results of an overestimation of absorption in regions where the ratio μ_a/μ_s' approaches 1 are in agreement with the findings for the homogeneous infinite slab case. From the result we can say that diffusion theory fails to model photon propagation inside of blood vessels or organs with a high blood

perfusion, such as liver. Therefore, higher-order angular approximations have to be considered in order to calculate the migration of photons accurately through these regions.

Influence of Void-like Regions

In this section, investigations are reported on the effect of boundaries of two media with different optical properties. The same geometry as used above, with a cylinder inside a box is retained. The optical properties of two regions are chosen in order to ensure that the diffusion approximation holds according to one criteria, which means $\mu_a/\mu_s' \ll 1$, everywhere in the medium. However, the cylinder is assigned lower absorption and scattering coefficients than the surrounding medium in order to simulate the absorption and scattering free regions that may be encountered in the ventricles of the brain, which are filled with the cerebrospinal fluid (CSF) [151].

To model this case, the following optical properties are used: The absorption coefficient of the box was 0.005 mm^{-1} and the scattering coefficient 0.5 mm^{-1}. Anisotropy factor g is assumed zero, and so the reduced scattering coefficient was equal to the scattering coefficient inside the box. Within the cylinder, the absorption and scattering coefficients were $\mu_a = 0.0001$ mm^{-1}, $\mu_s = 0.01$ mm^{-1}. The cylinder reduced scattering coefficient was again equal to the scattering coefficient because g was also assumed zero. An isotropic source was located at the left side of the box 50 mm from the centre of the cylinder and photon intensities evaluated along the line passing through the centre of the cylinder. The P_{25} angular approximation was employed for the transport calculations.

Figure 3.30 shows the ratio of the photon intensities calculated with diffusion theory and transport theory. The location of the cylinder is marked in the figure. While diffusion theory is applicable in the background medium significant difference between two theories occurs near the boundary of the cylindrical region. Photons flow from the left to right in Figure 3.30 and diffusion theory fails to represent the angular distribution of photons leaking from the first surface and being affected from the second.

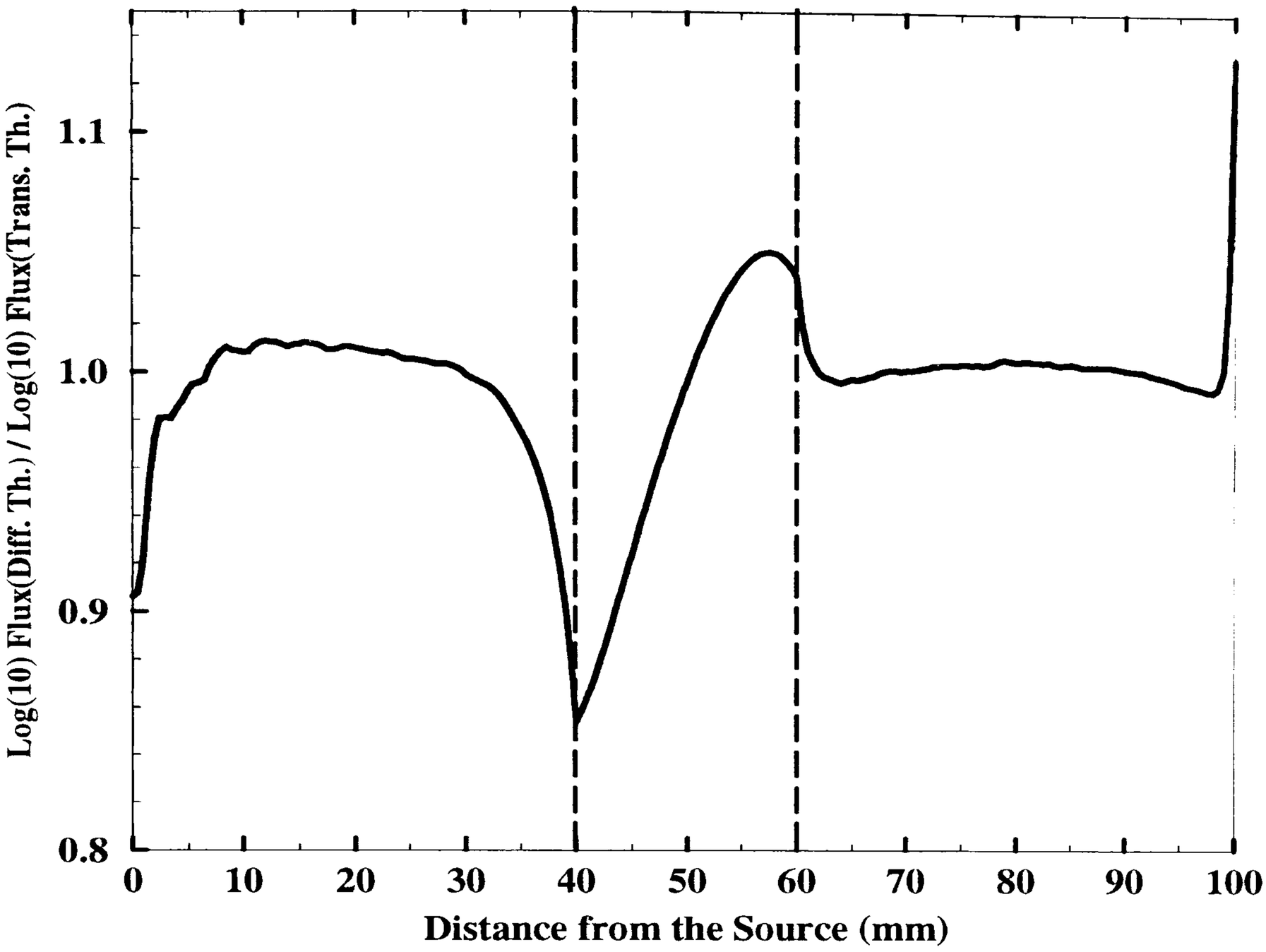


Figure 3.30: Log_{10} of the ratio of the photon intensity, modelled with diffusion and transport theory, near a cylindrical low density region.

Figure 3.31 shows the photon intensities in the above problem. Diffusion theory predict an almost constant intensity inside the low cross section medium. Just before the circular region, transport theory predicts an intensity higher than diffusion theory and a smaller intensity just behind. We have noted that these differences arise due to the ability of transport theory to model photon angular distributions.

In Figure 3.32, contour maps of photon intensity are shown for diffusion and transport theory predictions. In both figures, an area 40×40 mm centred in the middle of the 20 mm diameter cylindrical inhomogeneity are shown. The diffusion results show an almost constant intensity throughout the inhomogeneity, whereas transport results show a circular decrease in photon intensity, which is expected because of the geometrical effects inside the void region [151].

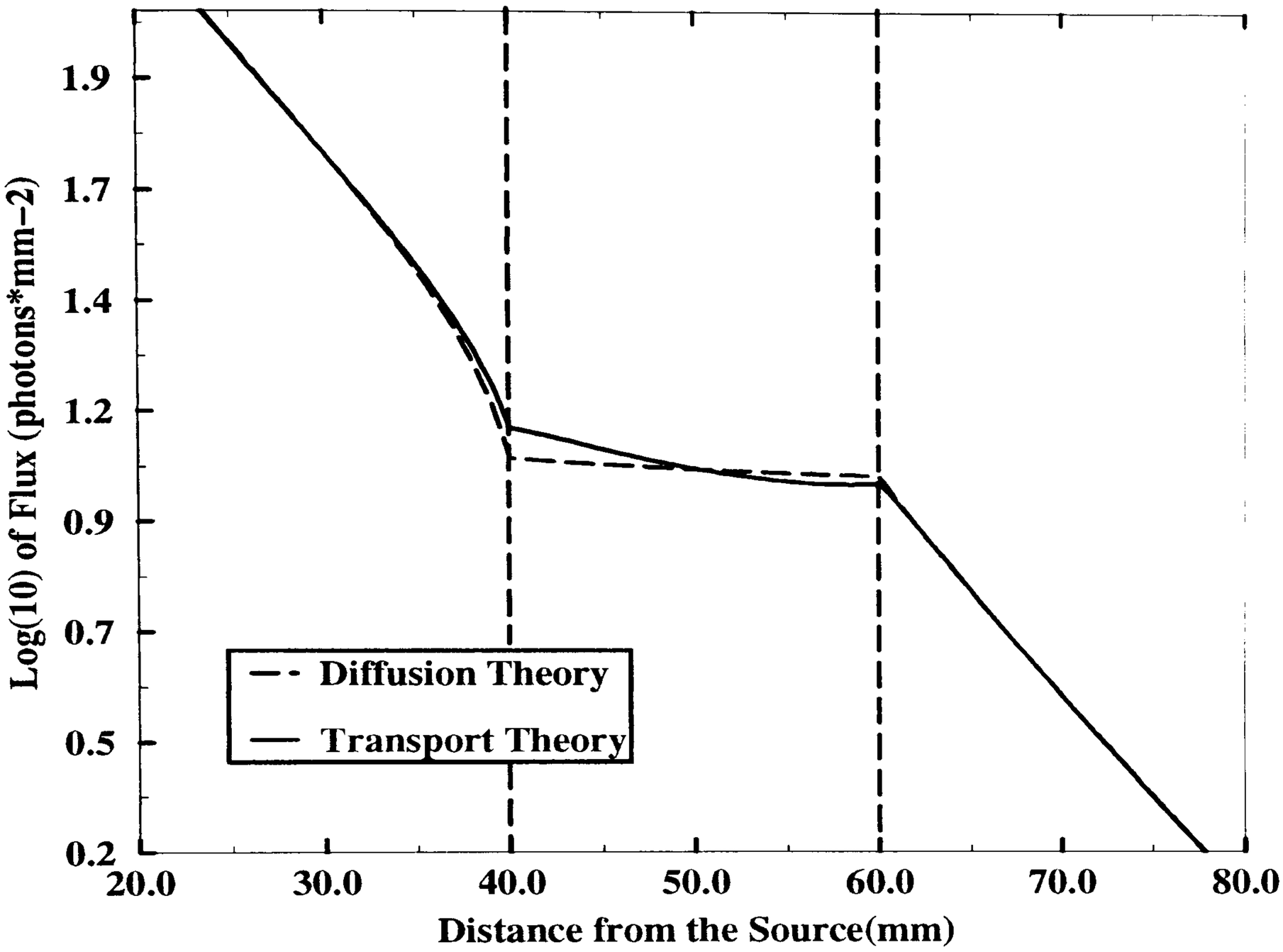


Figure 3.31: Log_{10} of the photon intensity, modelled with diffusion and transport theory, inside the cylindrical low density region shown in Figure 3.28.

Simulation Geometry III - a second void-like problem

As a second geometry for investigating steady-state 2D modelling of heterogeneous medium, a 120×120 mm square region enclosing smaller square region of 40×40 mm is considered. The geometry is shown in Figure 3.33. The 'real' geometry modelled by EVENT is that of two infinite square prisms, the outer having an infinite time source centrally along one face. The same optical properties are assumed for both the large and small squares as were used in the previous case. An isotropic source is located at (x=0 mm,y=60 mm) and the vacuum boundary conditions apply at the problem periphery. The finite element mesh of the problem consisted of 10790 linear triangular elements and 5396 nodes.

Diffusion and transport theory modelling were performed to investigate intensity

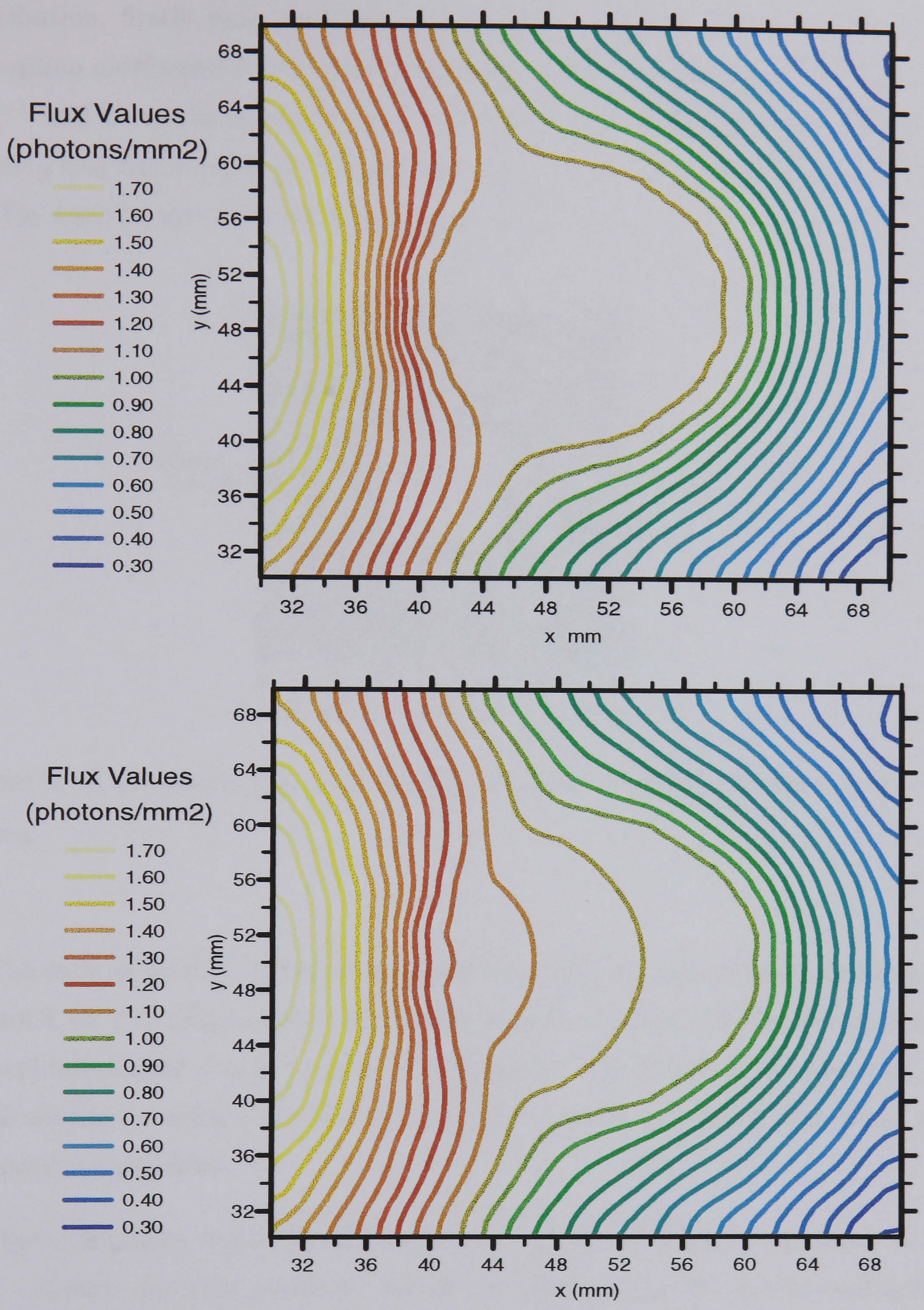


Figure 3.32: Log_{10} of Flux values as calculated by FE-diffusion (top) and transport (bottom) approximations for two-dimensional geometry contains a cylindrical region with almost absorption- and scattering-free optical properties.

distribution, firstly near the boundaries of the problem. Reduced scattering and absorption coefficients for the background region were $\mu_s' = 0.5$ mm^{-1} and $\mu_a = 0.005$ mm^{-1}, and for the inner square $\mu_s' = 0.01$ mm^{-1}, $\mu_a = 0.0001$ mm^{-1}. The anisotropy factor g was again taken to be zero in both regions. For the transport calculation, the P_{25} angular approximation was again adopted.

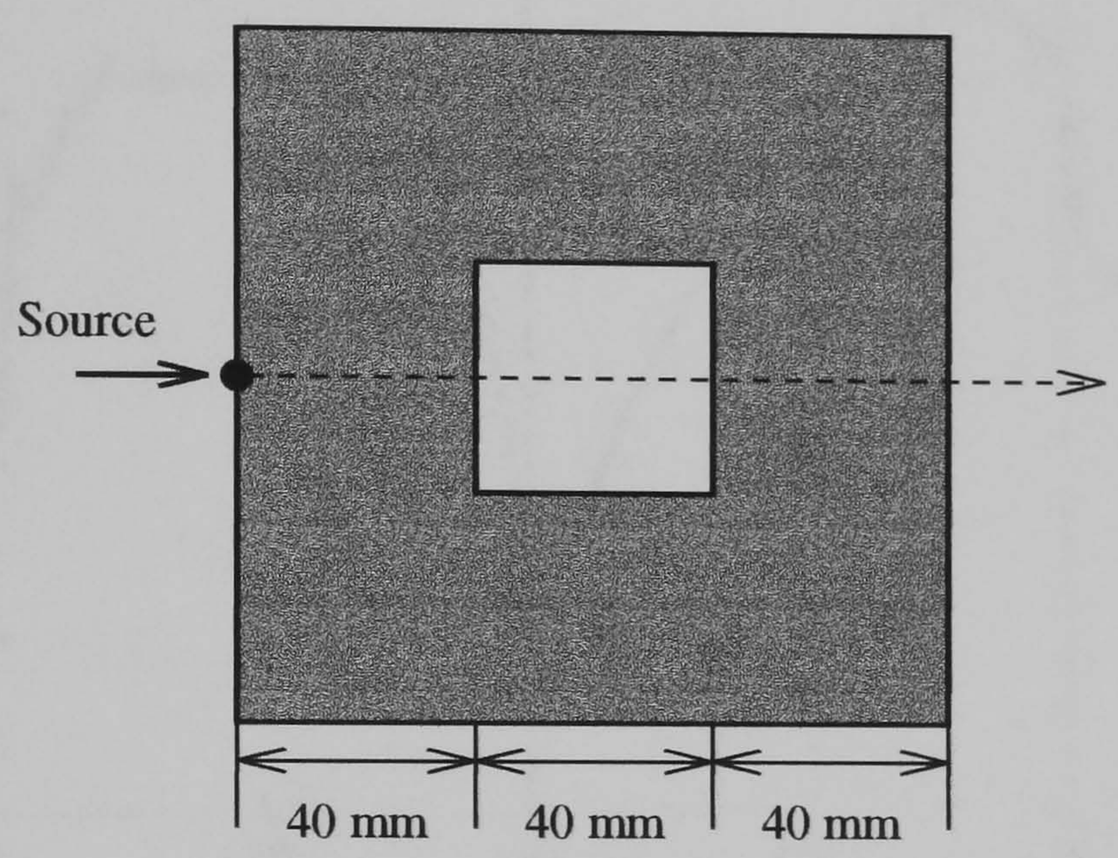


Figure 3.33: Geometry III, used in diffusion and transport simulations of void-like spaces.

The ratio of photon intensity modelled using the two approximations are given in Figure 3.34. The shape of the distribution is similar to that obtained for the geometry of a cylinder inside a square region. The magnitude and form of the boundary effects (with photons flowing from left to right) are in close agreement with those seen in the previous problem.

Photon intensity results for diffusion and transport are plotted separately in Figure 3.35. Results for this geometry match the findings for the media containing the cylindrical void-like region. Again, inside the inner square region, diffusion theory predicts an almost constant photon intensity, while transport theory yields photon distribution having a sleeper form within the void-like region.

Figure 3.36 shows Log_{10} of the photon intensity plotted as contours in a plane that contains the source. The region shown is the void-like region alone. Differences

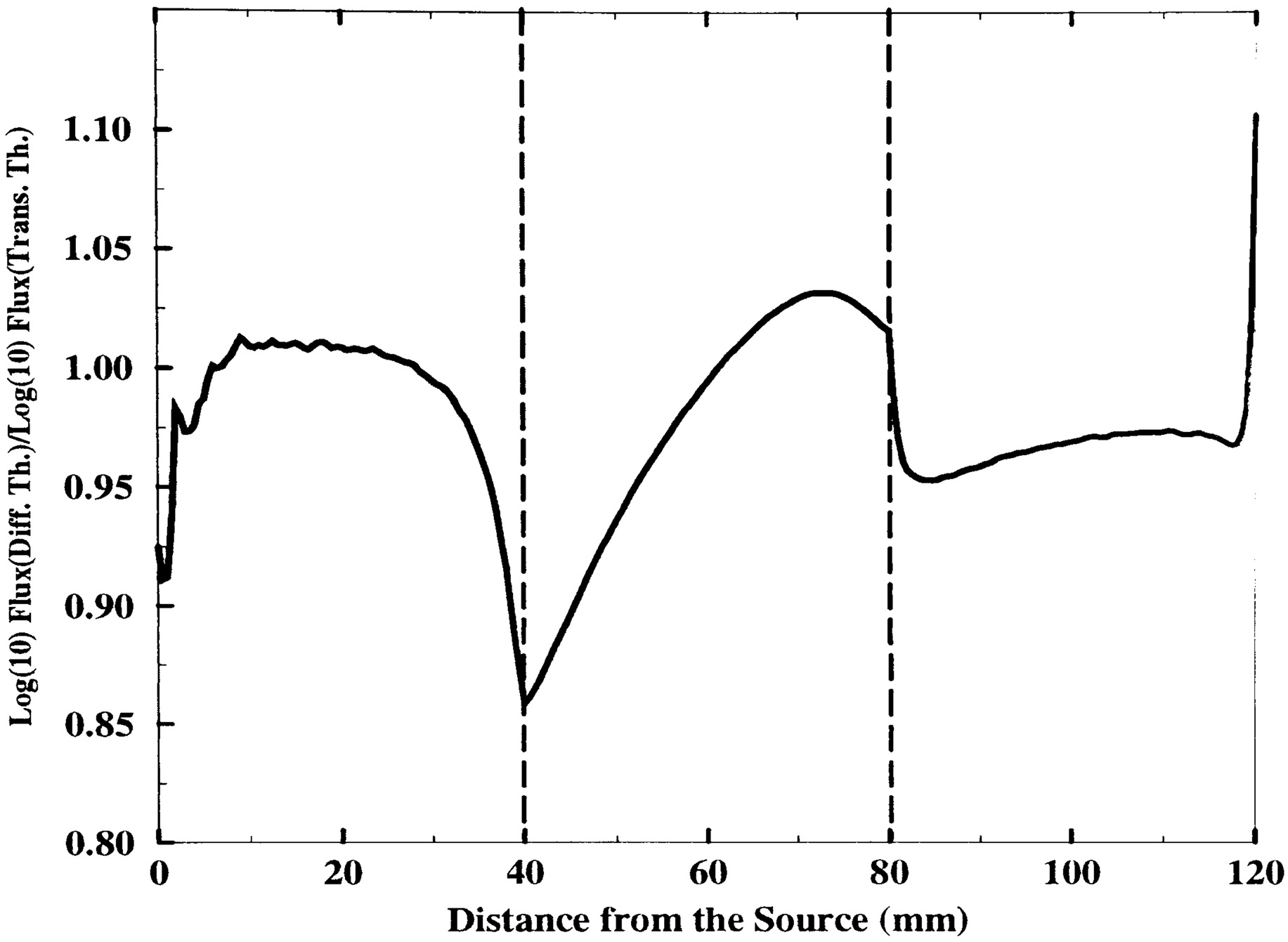


Figure 3.34: The ratio of Log_{10}(photon intensity) calculated with diffusion theory and transport theory near the boundaries of the square void-like region. Results are plotted along an axis passing through the source.

between diffusion and transport theory reflect those seen in Figure 3.35. As before, diffusion theory predicts an almost constant photon intensity throughout the void, whereas transport theory results in a decrease in intensity across the void, which is expected due to the geometrical effects [153]. It has been observed that diffusion theory fails to accurately model the propagation of light within regions with very low scattering and absorption coefficients, such as the void-like ventricles in the brain. However, transport theory can handle these kind of structures.

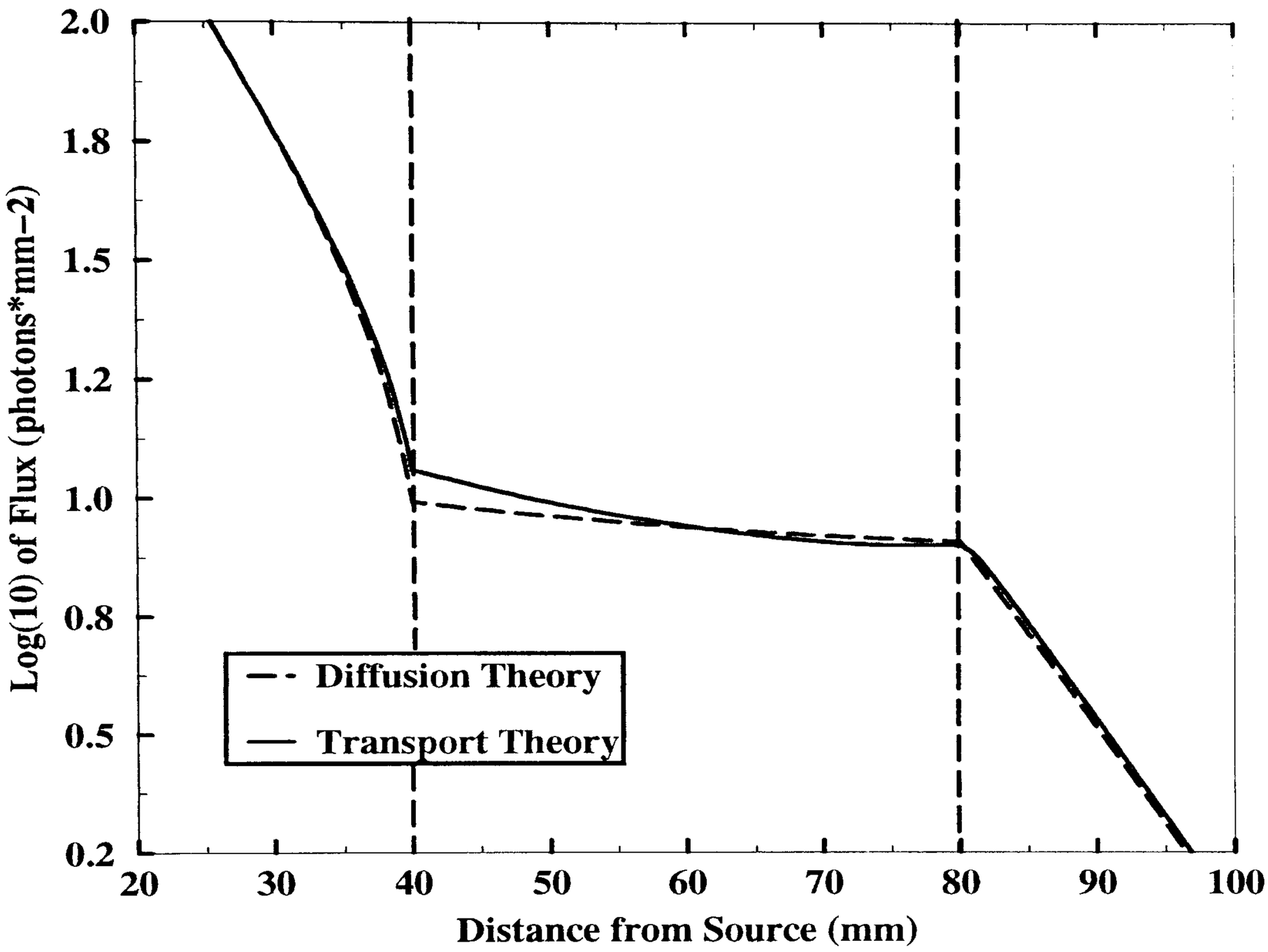


Figure 3.35: Log_{10} of the ratio of the photon intensity, modelled with diffusion and transport theories, inside a low density square region.

Simulation Geometry - IV

A clear layer of cerebrospinal fluid (CSF), the subarachnoid space, forms a boundary between the outside tissues (skull and scalp) and the brain [86],[153]. As the brain is embedded in such a photon absorption and scattering-free fluid, the third example of this section is chosen to simulate this situation very approximately. A 100×100 mm square with $\mu_a = 0.005$ mm^{-1} and $\mu_s' = 0.5$ mm^{-1} is considered. This fluid is represented by a 4 mm thick void-like structure with $\mu_a = 0.0001$ mm^{-1} and $\mu_s' = 0.01$ mm^{-1}, which surrounds an 76×76 mm inner square as shown in Figure 3.37. As before, when we speak of a 'square', 2D EVENT modelling implies an infinite prism of square cross section.

An isotropic source positioned at the centre of the left side of the box was employed

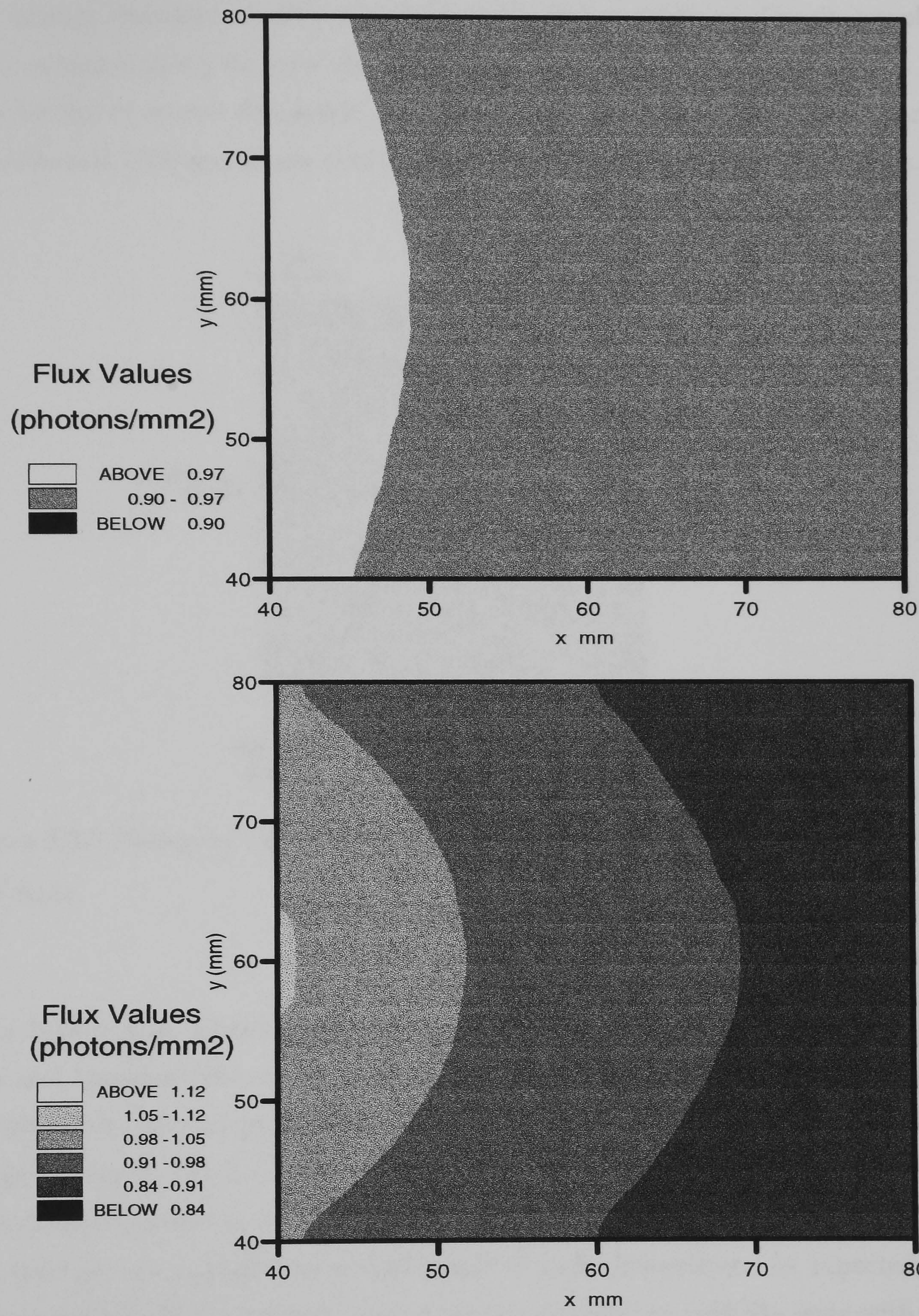


Figure 3.36: Photon intensity contour maps within the void-like region of problem III, for diffusion theory (top) and transport theory (bottom).

and vacuum boundary conditions applied on the outer boundaries. Results are plotted along an axis passing through the source. The P_{25} angular approximation was again used for the transport simulation. A FE mesh consisting of 10598 linear triangular elements and 5300 nodes was used in both diffusion and transport simulations.

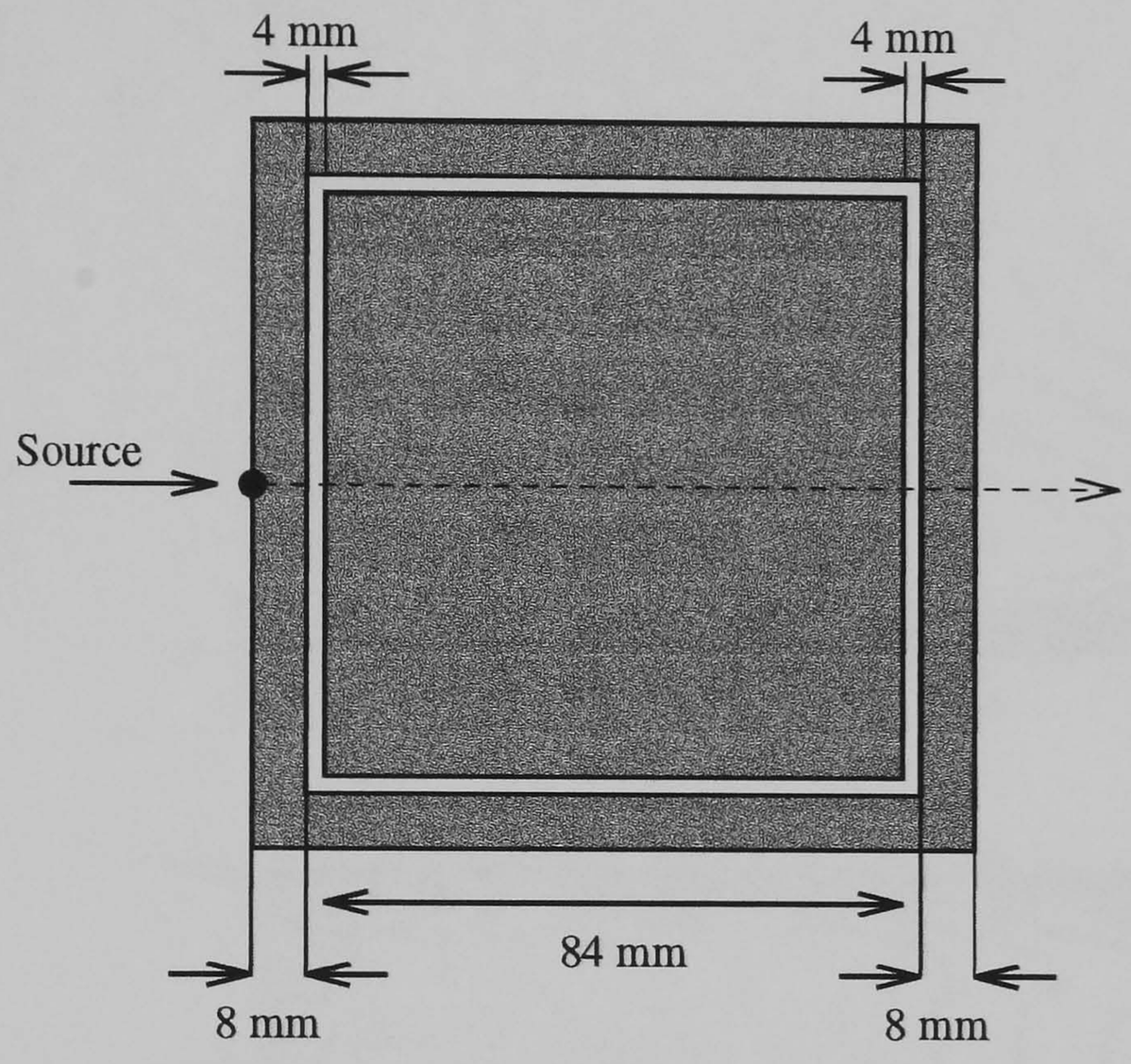


Figure 3.37: Geometry IV, used for photon diffusion and transport modelling in the CSF layer.

In Figure 3.38, contour maps of Log_{10}(photon intensities) calculated with diffusion and transport theory are shown separately. The failure of diffusion theory in modelling the photon propagation in void-like layers is also apparent in this case. Large differences can be observed between two theories. Diffusion theory predicts a light-channelling within the almost clear layer that surrounds the inner core, whereas transport theory calculations do not result in such channelling. As expected, large decrease in the photon intensity can be observed inside the void-like layer with transport theory caused by geometrical effects. This result confirms the finding of Firbank et al. [86], who showed that diffusion theory predicts erroneous backreflections from a turbid media when a clear subsurface layer is introduced.

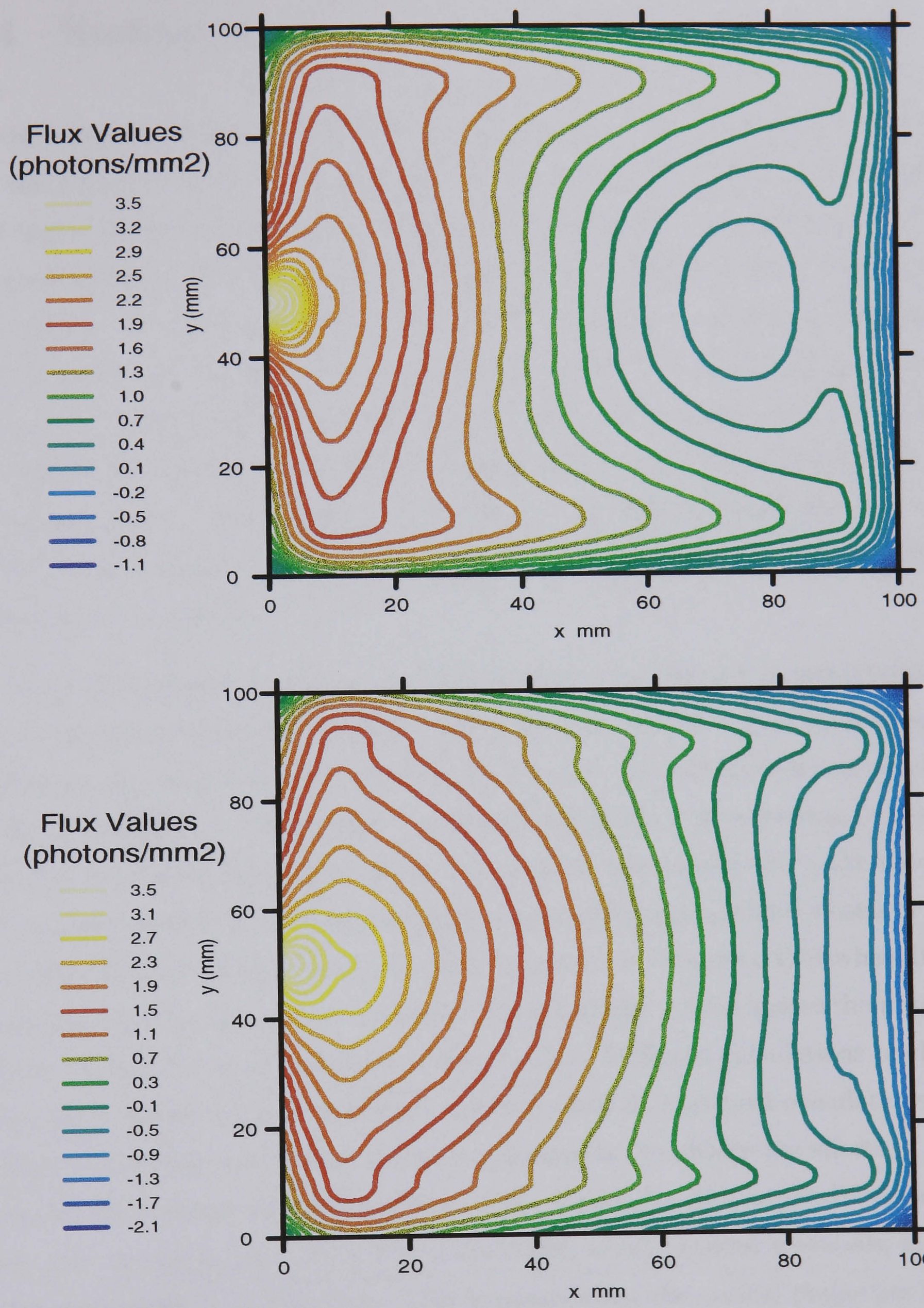


Figure 3.38: Contoured photon intensity distributions modelled by diffusion theory (top) and transport theory (bottom) for the 2D CSF-layered problem.

3.4 Summary

In this chapter, numerical results obtained by the FE-P_N method were presented for the solution of forward problems. Firstly the FE-P_N solutions with diffusion and higher-order angular approximations were compared in homogeneous and inhomogeneous cases in order to show the breakdown of diffusion theory in presence of absorption. Good agreements were obtained between P_7, P_1 angular approximations and diffusion with no absorption cases. However, when a small amount absorption was incorporated, significantly different variations, which become more marked with increase in absorption, were predicted in output current by diffusion than by P_7 angular approximation. Also in this part, the FE-P_N method was validated by comparing it with results of a MC model in simple geometries consisting of objects embedded in a homogeneous cylinder.

In the second part of this chapter, the limits of the diffusion approximation were investigated for various homogeneous and heterogeneous test cases. It was shown that differences between transport and diffusion photon intensity calculations occur especially in two regions: regions that are almost absorption and scattering free, such as the CSF filled ventricles or the subarachnoid space and regions where the absorption is comparable to the scattering coefficient, such as hematoma, blood vessels or organs with high blood perfusion. For homogeneous regions, we observed that when diffusion approximation ($\mu_a/\mu_s' \ll 1$) is violated, diffusion theory overestimates the absorption effects, or in other words underestimates the flux. Diffusion calculations predict, for this case, a larger decrease in photon intensity than do transport calculations. As in homogeneous regions, diffusion theory overestimates the absorption effects of heterogeneities that contain a material with $\mu_a \sim \mu_s'$. It was also shown that diffusion theory may give an inaccurate description of transition zones between materials, even if it is valid everywhere in the medium. This happens when the optical properties changes dramatically across material boundaries. Furthermore, it was observed that diffusion theory fails to accurately describe the light propagation in regions with very low scattering and absorption coefficients, as found especially in the brain. If these almost scattering- and absorption-free regions form a tunnel-like structure, diffusion theory

predicts a channelling of light, while transport theory suggest a decrease in photon intensity even within these tunnels due to geometrical light attenuation.

Chapter 4

A Solution Model for Inverse Photon Scattering Problems

This chapter presents details of a new approach developed to solve inverse imaging problems. It begins with an introduction to the inverse photon scattering problem and summarises inverse solution methods that have appeared in the literature. The linearised one-speed Boltzmann transport equation, with the appropriate boundary conditions for tomographic studies, is considered first, followed by its Laplace transformed form. The Reference Cross Section Model, which allows formulation of the inverse problem as a system of linear equations for the unknown absorption and scattering coefficients, is then introduced. First- and second-order variational formulations of this equation system are then given in order to specify the problem in a form that is suitable for the application of the FE-P_N method. Finally, the non-perturbative iterative image reconstruction algorithm for the recovery of the absorption and scattering coefficients is explained.

4.1 Introduction

The second and more difficult class of research into the modelling of photon transport in tissue is the *inverse problem* which involves the recovery of the parameters of the media under investigation. The inverse problem may be stated as the use of the given distribution, such as a set of measurements and error estimates, together with only a *limited* set of parameters describing the medium and the experiment, in deriving the remaining parameters of the tissue through which the photons have propagated [154]. Inverse problems are encountered in fields such as astrophysics in order to infer properties of stars and nuclear medicine to determine, for example, if a tumour is present.

In the main medical imaging techniques used, such as CT and SPECT (which employ gamma rays), scattering is normally neglected and the path of the detected photon is taken as a straight line between the chosen source-detector pair. This type of reconstruction problems can be formulated directly from the particle transport equation as a system of linear equations in the limit of negligible scattering [116]. Therefore, they are relatively easily solvable numerically. However, in the case of strongly scattering environments, such as Near-Infrared Optical Tomography, the progressive influence of scattering with distance makes the reconstruction problem remarkably complex and non-linear. Solution involves not only the calculation of optical properties, but also of the intensity and direction of the scattered photons inside the medium, due to the contribution of scattered photons which add to the net flux. A consequence of the additional term is that there is not a generally applicable direct method for the solution of highly scattering inverse problems [155]. A solution can only be obtained by employing the results of a forward solution model for photons transport. Theoretical details of common tomographic modalities, with and without scattering, and alternative solution procedures of the appropriate inverse problems can be found in Roberty and Oliveira [156]. General discussions on the image reconstruction algorithms employed by several authors are given by Arridge [78] and Arridge and Hebden [157].

A variety of studies have been performed in recent years aimed at developing a

reconstruction algorithm for problems involving the propagation of photons through scattering and absorbing media. As a result, several inverse solution methods have been developed to date for imaging problems in heterogeneous media including back-projection methods, nonlinear optimisation methods solved using Newton iterative methods and based on the diffusion equation, and perturbation methods [78].

Gratton *et al.* employed a weighted back-projection algorithm, which is similar in principle to that used in computerised tomography, to obtain approximate spatial maps of absorption and scattering coefficients [158], [159]. Although various back-projection methods have been postulated and demonstrated by Benaron *et al.* [160], it has not been demonstrated that these formulation may be used to solve the inverse problem [161].

The concept of the nonlinear approach is to choose a solution by minimising the least-squares functional at the surface between the measured data, obtained via the detection system, and the estimated value obtained through the solution of the forward problem with trial cross sections. The inverse problem can then be solved using standard numerical techniques for non-linear least-squares such as the Levenberg-Marquardt method [162]. This approach was employed by Arridge *et al.* who used FEM for the forward model and adopted a modified Newton-Raphson scheme to progress iteratively towards the minimisation of a least-squared error-norm [163],[164]. Levenberg-Marquardt conditioning, together with Tikhonov and Philips-Twomey regularisation, were also employed for controlling the stability of the solution. Another method, similar to that developed by Arridge and which casts image formation as a nonlinear optimisation problem, was applied by Jiang *et al.* to frequency-domain data [165]. They used an FEM routine for processing the optical data into images of absorption and scattering coefficients. Their reconstruction method works to minimise both the least-squares difference between the measured data and the calculated data from a 2-dimensional FEM of the diffusion equation, as well as minimising the total variation of the image. This minimisation is performed by a Levenberg-Marquardt algorithm. Details of the finite element algorithm and the reconstruction method can be found in references [166],[167],[168], [169].

Another commonly used method for the solution of inverse problems in optical

diffusion tomography is perturbation theory, which involves solving a system of linear equations derived from the transport theory [41]. In this method one seeks to solve a linear perturbation equation of the form $\Delta\mathbf{I} = \mathbf{W}\Delta\mathbf{x}$, where $\Delta\mathbf{I}$ and Δx are, respectively, the changes in detector readings and interior optical properties of the target medium with respect to a reference medium, and $\mathbf{W}$ is the weight matrix whose elements are the constant of proportionality relating a small perturbation at one particular site in the interior to the corresponding change in the signal received by a specific detector. Measurements of both the target and the reference are performed (or estimates are computed), and the differences between corresponding detector readings for the two are the input for the image-recovery algorithm. The use of perturbation methods requires specification of some type of reference medium whose properties are believed to differ as little as possible from those of the target medium. To solve the linear perturbation equation, several iterative algorithms have been developed, including POCS (projection onto convex set) [170],[171],[172], CGD (conjugate gradient descent)[173],[174], SART (simultaneous algebraic reconstruction technique) [175],[176], a multi-grid reconstruction algorithm [155], [177] and PE (a progressive expansion algorithm)[155],[178].

The perturbation approach and the algorithms mentioned above have been employed in a number of studies for reconstruction of images. Schlereth *et al.* have formulated image reconstruction as a learning problem in a neural net structure [179] and this method, taken from suggestions by Singer *et al.* and Grünbaum *et al.*, provides great flexibility in modelling the forward problem by yielding accurate and numerically stable results when having a good initial estimate of the structure of the target medium. The method employed by Singer *et al.*[180] and Grünbaum *et al.*[181] is a general mathematical model derived from the discretisation of the transport equation in both the spatial and angular domains. The application of the method to arbitrarily shaped objects is possible and it permits iterative estimation of both the absorption and scattering coefficients of a target medium. Graber *et al.* presented a theoretical model of photon propagation in a scattering medium, in which algebraic formulae were derived for detector-reading perturbations (ΔI) produced by one or two localised perturbations in the macroscopic absorption cross section ($\Delta\mu_a$)[182], [183]. They have investigated the effects of the certain factors related

to physical measurement and computational complexity together with the effects of the imaging algorithm chosen on the quality of images and computational efficiency [184],[185],[186],[187],[188]. Arridge *et al.* used a method [85],[189] similar to the perturbation model described above for reconstruction of cylindrical media by employing the diffusion approximation to the transport equation to derive closed-form solutions for the scattered field and its gradient.

In this chapter, the fundamental basis of a new approach, which has been derived by N.C. Roberty [190] and implemented numerically by de Oliveira [191] to obtain the solution of the so-called forward and adjoint (source-detector) problems by the use of a higher-order spherical harmonic approximation with finite element method, is given. The application of the FE-P_N method to the solution of the one-speed linear Boltzmann transport equation considerably reduces the computational effort and gives fast-accurate solutions to the transport problems in both diffusive and non-diffusive situations. Having such accurate and fast solutions of the forward problem is of great importance for the reconstruction problems and makes the iterative reconstruction algorithm a practical and feasible tool.

The method directly uses the Boltzmann transport equation for the problem of cross section parameter identification without making any simplification in the physical formulation. Writing the transport equation for both source problem formulated by the use of the unknown-trial cross sections, and detector problem devised by using the known-reference cross sections, and taking the difference between these two problems, it is possible to obtain a system of integral equations named as the non-reciprocal equation system or inverse Boltzmann equation [190]. A variational formulation consistent with the non-reciprocal integral system of equation is used to specify the problem in the appropriate way for the application of FE-P_N method. The resultant non-linear equation is solved by Newton-secant linearisation method to determine the cross sections followed by the application of projection on convex set. The methodology outlined above is a viable one for computational implementation of the reconstruction problem of the absorption and scattering cross sections in highly scattering media.

4.2 Formulation of the Inverse Problem

4.2.1 Photon Transport

In this model, an optical imaging system, designed to image a volume V bounded by a surface ∂V, is considered for the formulation of the inverse problem. The volume V contains the medium whose optical properties are unknown. The system consists of sources and detectors placed at the boundary of the volume. The detectors can differ in position as well as orientation and the sources and detectors can be placed at the same positions. The propagation of photons within the volume V can be described by the linearised one-speed Boltzmann transport equation as

$$\begin{aligned} \frac{1}{v}\frac{\partial\phi(\mathbf{r},\mathbf{\Omega},t)}{\partial t} + \mathbf{\Omega}\cdot\nabla\phi(\mathbf{r},\mathbf{\Omega},t) + \sigma(\mathbf{r})\phi(\mathbf{r},\mathbf{\Omega},t) &= \int_{4\pi} d\mathbf{\Omega}'\sigma_s(\mathbf{r},\mathbf{\Omega}\cdot\mathbf{\Omega}')\phi(\mathbf{r},\mathbf{\Omega}',t) \\ &+ S(\mathbf{r},\mathbf{\Omega},t), \end{aligned} \tag{4.1}$$

Two boundary conditions, a prescribed incoming flux and a measure of the outgoing flux, accompany the transport equation in describing the angular flux $\phi(\mathbf{r},\mathbf{\Omega},t)$ [156]:

$$(i) \qquad \phi(\mathbf{r},\mathbf{\Omega},t) = \phi_{in}(\mathbf{r},\mathbf{\Omega},t), \qquad \mathbf{\Omega}\cdot\mathbf{n} < 0, \quad \mathbf{r}\in\partial V, \tag{4.2}$$

$$(ii) \qquad \phi(\mathbf{r},\mathbf{\Omega},t) = \phi_{out}(\mathbf{r},\mathbf{\Omega},t), \qquad \mathbf{\Omega}\cdot\mathbf{n} > 0, \quad \mathbf{r}\in\partial V, \tag{4.3}$$

where $\mathbf{n}$ is the outward normal to the surface ∂V. The incoming flux in (i) can be simulated by placing a source at the boundary of the body. The estimated outgoing flux, ϕ_{out}, in the boundary condition (ii) can be obtained by positioning detectors on the surface of the body. This second condition generally appears in the adjoint formulation in the context of direct problems and is related with the importance and the reaction rate field [156].

In the experimental measurements, a laser light source is used to generate ultra-short light pulses for the required picoseconds duration. Time behaviour of the source can thus be represented by a Dirac-delta distribution [190]. The response of the detectors, for time windows of finite width, is some quantity derived from the temporal distribution of the measured signal over all time points lying within the specified

windows, such as the photon fluxes at different time intervals for each source-detector pair. For a typical photon source positioned at i and emitting photons in direction $\mathbf{\Omega}_i$ at time t_i, the incoming flux $\phi_{in}(\mathbf{r}, \mathbf{\Omega}, t)$ can be taken as:

$$\phi_{in}(\mathbf{r}, \mathbf{\Omega}, t) = S_i \delta(\mathbf{r} - \mathbf{r}_i) \frac{1}{2\pi} \delta(\mathbf{\Omega} \cdot \mathbf{\Omega}_i - 1) \delta(t - t_i), \quad \mathbf{r} \in \partial V, \ \mathbf{\Omega} \cdot \mathbf{n} < 0, \ t > 0, \tag{4.4}$$

where S_i is the photon beam intensity and the triple Dirac-delta product represents the mathematical representation of the localisation, direction of collimation and duration of the pulse, respectively. The integrated outgoing radiation flux can be combined from the detectors located at the position $\mathbf{r}_j$ as follows [72]:

$$F_{ij}^{exp}(t) = \eta_j \int_{\partial V} \delta(\mathbf{r} - \mathbf{r}_j) ds \int_{\mathbf{\Omega} \cdot \mathbf{n} > 0} d\mathbf{\Omega} \mid \mathbf{\Omega} \cdot \mathbf{n} \mid \phi_i(\mathbf{r}, \mathbf{\Omega}, t), \tag{4.5}$$

where η_j is the efficiency of detector j and $F_{ij}^{exp}(t)$ is the experimental temporal measurement of the outgoing intensity field, due to the photon source at position $\mathbf{r}_i$. Alternatively it can be seen as the response of the detector to the particle density produced by a surface source placed at $\mathbf{r}_i$. Equations (4.4) and (4.5) are the additional boundary conditions used as data for studies involving the reconstruction of cross section distributions [190].

Solution of the one-speed, transient, Boltzmann equation when a pulsed source is located at the boundary is computationally expensive. To avoid this difficulty by reducing time dependent transport equation to an equation which formally resembles the stationary equation, it is convenient to apply the Laplace transform. Applying the Laplace transform to equation (4.1) and using the expanded form of the scattering kernel in terms of Legendre Polynomials, equation (2.29), the stationary transport equation for a source-free medium is obtained as follows:

$$\begin{aligned} \mathbf{\Omega}.\nabla\tilde{\phi}(\mathbf{r}, \mathbf{\Omega}, s) \ &+ \ \left(\sigma(\mathbf{r}) + \frac{s}{v}\right) \tilde{\phi}(\mathbf{r}, \mathbf{\Omega}, s) \\ &- \ \sum_{l=0}^{\infty} \left(\frac{2l+1}{4\pi}\right) \sigma_{sl}(\mathbf{r}) \int_{4\pi} d\mathbf{\Omega}' P_l(\mathbf{\Omega} \cdot \mathbf{\Omega}') \tilde{\phi}(\mathbf{r}, \mathbf{\Omega}', s) = 0, \end{aligned} \tag{4.6}$$

where s is the Laplace Transform parameter. The term added to the total cross section arises from the transformation of the time transient term and it is called the

equivalent absorption cross section. If the removal operator is defined as [190]

$$R_s[\tilde{\phi}] = \left(\sigma(\mathbf{r}) + \frac{s}{v}\right)\tilde{\phi}(\mathbf{r},\mathbf{\Omega},s) - \sum_{l=0}^{\infty}\left(\frac{2l+1}{4\pi}\right)\sigma_{sl}(\mathbf{r})\int_{4\pi} d\mathbf{\Omega}' P_l(\mathbf{\Omega}\cdot\mathbf{\Omega}')\tilde{\phi}(\mathbf{r},\mathbf{\Omega}',s), \tag{4.7}$$

then equation (4.6) takes the following form:

$$\mathbf{\Omega}\cdot\nabla\phi(\mathbf{r},\mathbf{\Omega}) + R[\phi(\mathbf{r},\mathbf{\Omega})] = 0, \tag{4.8}$$

where the Laplace transform parameter s is omitted for simplicity.

4.2.2 The Reference Cross Section Model

In order to formulate the inverse problem as a system of linear equations a non- perturbative iterative model has been developed, and employed, in which the sensitivity of the detector response is estimated for a reference cross section that is independent from the cross section investigating for reconstruction. This model, which is similar to the perturbation approach [155], involves the use of two optical imaging systems, the first being the unknown (real) medium and the second the known (reference) medium, referred to source and detector problems respectively. Therefore the first step is to write equation (4.8) for the source problem for a photon starting from an isotropic surface source located at position i by using the trial cross sections (σ_a, σ_s) that are the real values desired to be reconstructed in the removal operator as follows:

$$\mathbf{\Omega}\cdot\nabla\phi_i(\mathbf{r},\mathbf{\Omega}) + R[\phi_i(\mathbf{r},\mathbf{\Omega})] = 0 \tag{4.9}$$

with the Laplace transformed form of the boundary condition, equation (4.4),

$$\phi_i(\mathbf{r},\mathbf{\Omega}) = S_i\delta(\mathbf{r}-\mathbf{r}_i), \qquad \mathbf{\Omega}\cdot\mathbf{n} < 0, \quad \mathbf{r}\in\partial V, \quad i = 1,...,N_S, \tag{4.10}$$

where N_S is the number of sources employed in the system.

In order to formulate the detector problem, it is assumed that some sort of prior information about the cross sections of the medium are known and those cross section fields will have the following notation in the rest of the derivation:

$$\sigma^{\circ}(\mathbf{r}), \quad \sigma^{\circ}_{sl}, \qquad\qquad l \geq 0.$$

To construct the detector problem, the adjoint transport equation is considered and can be written with the appropriate boundary condition on outward directions for detectors located at j as:

$$-\mathbf{\Omega}.\nabla\phi_j^*(\mathbf{r},\mathbf{\Omega}) + R^\circ[\phi_j^*(\mathbf{r},\mathbf{\Omega})] = 0, \tag{4.11}$$

$$\phi_j^*(\mathbf{r},\mathbf{\Omega}) = S_j\delta(\mathbf{r}-\mathbf{r}_j), \qquad \mathbf{\Omega}\cdot\mathbf{n} > 0, \quad \mathbf{r}\in\partial V, \quad j=1,...,N_D, \tag{4.12}$$

where $S_j(=\eta_j)$ is the detector efficiency, N_D is the number of detectors used in the system and $\phi_j^*(\mathbf{r},\mathbf{\Omega})$ is the adjoint angular flux ($\phi_j^*(\mathbf{r},\mathbf{\Omega}) = \phi_j(\mathbf{r},-\mathbf{\Omega})$). For the general analysis that follows, the solutions are discussed in Hilbert space where the real inner product, the inner product for the characterisation of the boundary and also the inner products characterising incoming ($\mathbf{\Omega}\cdot\mathbf{n} < 0$) and outgoing ($\mathbf{\Omega}\cdot\mathbf{n} > 0$) directions are defined as follows [45],[190]:

$$(\phi_i,\phi_j^*) = \int_V dV \int_{4\pi} d\mathbf{\Omega}\ \ \phi_i(\mathbf{r},\mathbf{\Omega})\phi_j^*(\mathbf{r},\mathbf{\Omega}), \tag{4.13}$$

$$\left\langle\phi_i,\phi_j^*\right\rangle = \int_{\partial V} ds \int_{4\pi} d\mathbf{\Omega}\ \mathbf{\Omega}\cdot\mathbf{n}\ \phi_i(\mathbf{r},\mathbf{\Omega})\phi_j^*(\mathbf{r},\mathbf{\Omega}), \tag{4.14}$$

$$\left\langle\phi_i,\phi_j^*\right\rangle_\pm = \int_{\partial V} ds \int_{(\mathbf{\Omega}\cdot\mathbf{n}\gtrless 0)} d\mathbf{\Omega}\ |\ \mathbf{\Omega}\cdot\mathbf{n}\ |\ \phi_i(\mathbf{r},\mathbf{\Omega})\phi_j^*(\mathbf{r},\mathbf{\Omega}). \tag{4.15}$$

In order to find a relation between the source and detector problems, equation (4.9) is multiplied by $\phi_j^*(\mathbf{r},\mathbf{\Omega})$ and equation (4.11) by $\phi_i(\mathbf{r},\mathbf{\Omega})$; the resulting equations are subtracted and the difference is integrated over all variables [132]. By using this procedure together with the definition given by equation (4.13), the following equation is obtained for the relation between sources and detectors as:

$$\Big[(\mathbf{\Omega}\cdot\nabla\phi_i,\phi_j^*) + (\mathbf{\Omega}\cdot\nabla\phi_j^*,\phi_i)\Big] + \Big[(R[\phi_i],\phi_j^*) - (R^\circ[\phi_i],\phi_j^*)\Big] = 0. \tag{4.16}$$

To include the boundary conditions, equation (4.16) is manipulated into a form by combining the two gradient terms in the first square brackets. Since the gradient operator ∇ involves derivatives with respect to position coordinates only, it is permissible to write [132]

$$\mathbf{\Omega}\cdot\nabla\phi_i = \nabla\cdot\mathbf{\Omega}\,\phi_i, \qquad \mathbf{\Omega}\cdot\nabla\phi_j^* = \nabla\cdot\mathbf{\Omega}\,\phi_j^*,$$

and by substituting these into the equation (4.16), the sum of two terms is obtained as

$$\begin{aligned}(\mathbf{\Omega}\cdot\nabla\phi_i,\phi_j^*)+(\mathbf{\Omega}\cdot\nabla\phi_j^*,\phi_i) &= (\nabla\cdot\mathbf{\Omega}\,\phi_i,\phi_j^*)\\ &= \int_V dV\int_{4\pi} d\mathbf{\Omega}\,\nabla\cdot\mathbf{\Omega}\,\phi_i(\mathbf{r},\mathbf{\Omega})\phi_j^*(\mathbf{r},\mathbf{\Omega}).\end{aligned} \tag{4.17}$$

The volume integral in the above equation can be converted to a surface integral by using the divergence theorem and the result is the inner product, $\langle\phi_i,\phi_j^*\rangle$, given by equation (4.14). Using equation (4.15) in the following identity

$$\langle\phi_i,\phi_j^*\rangle = \langle\phi_i,\phi_j^*\rangle_+ - \langle\phi_i,\phi_j^*\rangle_-\,, \tag{4.18}$$

the introduction of the boundary conditions, equations (4.10) and (4.12) respectively, into equation (4.17) is achieved as follows:

$$\begin{aligned}(\mathbf{\Omega}\cdot\nabla\phi_i,\phi_j^*) \;+\; (\mathbf{\Omega}\cdot\nabla\phi_j^*,\phi_i) = \langle\phi_i,\phi_j^*\rangle &= \langle\phi_i,\phi_j^*\rangle_+ - \langle\phi_i,\phi_j^*\rangle_-\\ &= S_i\int_{\partial V}\delta(\mathbf{r}-\mathbf{r}_i)ds\int_{\mathbf{\Omega}\cdot\mathbf{n}<0} d\mathbf{\Omega}\mid\mathbf{\Omega}\cdot\mathbf{n}\mid\phi_j^*(\mathbf{r},\mathbf{\Omega})\\ &- \eta_j\int_{\partial V}\delta(\mathbf{r}-\mathbf{r}_j)ds\int_{\mathbf{\Omega}\cdot\mathbf{n}>0} d\mathbf{\Omega}\mid\mathbf{\Omega}\cdot\mathbf{n}\mid\phi_i(\mathbf{r},\mathbf{\Omega}).\end{aligned} \tag{4.19}$$

Another form of equation (4.16) , which is a system of integral equations called the non-reciprocal integral equation [190] for the number of sources and detectors used in the system, is recovered by replacing the equivalent expression derived for the sum of the two gradient terms in the first square brackets, thus:

$$\begin{aligned}(R[\phi_i],\phi_j^*)-(R^\circ[\phi_i],\phi_j^*) &= S_i\int_{\partial V}\delta(\mathbf{r}-\mathbf{r}_i)ds\int_{\mathbf{\Omega}\cdot\mathbf{n}<0} d\mathbf{\Omega}\mid\mathbf{\Omega}\cdot\mathbf{n}\mid\phi_j^*(\mathbf{r},\mathbf{\Omega})\\ &- \eta_j\int_{\partial V}\delta(\mathbf{r}-\mathbf{r}_j)ds\int_{\mathbf{\Omega}\cdot\mathbf{n}>0} d\mathbf{\Omega}\mid\mathbf{\Omega}\cdot\mathbf{n}\mid\phi_i(\mathbf{r},\mathbf{\Omega})\end{aligned} \tag{4.20}$$

The right hand side of this equation can be interpreted physically as the difference between the detector response corrected by the detector efficiency η_j to the point

source located at r_i, (or simply detector measurements) and the boundary source term corrected by the importance of the source to the detector located at r_j (or the source importance)[132], [190]. If the following expression is defined using equation (4.5) and the adjoint flux $\phi_j^{\circ *}(\mathbf{r}, \mathbf{\Omega})$ calculated with reference cross section fields as

$$f_{diff}^{\circ} = F_{ji}^{\circ} - F_{ij}^{exp}, \tag{4.21}$$

where

$$F_{ji}^{\circ} = S_i \int_{\partial V} \delta(\mathbf{r} - \mathbf{r}_i) ds \int_{\mathbf{\Omega}\cdot\mathbf{n}<0} d\mathbf{\Omega} \mid \mathbf{\Omega} \cdot \mathbf{n} \mid \phi_j^{\circ *}(\mathbf{r}, \mathbf{\Omega}), \tag{4.22}$$

equation (4.20) becomes a non-linear system of integral equations having the unknown cross section parameters, (σ_a, σ_s), together with the angular flux, $\phi_i(\mathbf{r}, \mathbf{\Omega})$, and it can be rewritten as follows:

$$\begin{aligned} (R[\phi_i], \phi_j^{\circ *}) - (R^{\circ}[\phi_i], \phi_j^{\circ *}) &= F_{ji}^{\circ} - F_{ij}^{exp} \\ &= f_{diff}^{\circ}, \qquad i = 1, N_S;\ j = 1, N_D;\ i \neq j. \end{aligned} \tag{4.23}$$

This equation basically gives the difference of two cross section problems formulated with the reference ($R^{\circ}[..]$) and trial ($R[..]$) removal operators. It relates this difference to the experimental measurements (F_{ij}^{exp}) and the numerical solution of the detector problem employing the prior information for the reference cross section fields (F_{ji}°). Using the expression for the Dirac-delta function expanded in terms of a series of Legendre polynomials given by equation (2.29) the following form of equation (4.23) can be obtained:

$$\begin{aligned} \sum_{l=0}^{\infty} \frac{2l+1}{4\pi} \int_V dV[(\sigma - \sigma_{sl}) \quad - \quad (\sigma^{\circ} - \sigma_{sl}^{\circ})] \int_{4\pi} d\mathbf{\Omega} \int_{4\pi} \mathbf{d\Omega'} P_l(\mathbf{\Omega} \cdot \mathbf{\Omega'}) \phi_i(\mathbf{r}, \mathbf{\Omega'}) \phi_j^{\circ *}(\mathbf{r}, \mathbf{\Omega}) \\ = \quad F_{ji}^{\circ} - F_{ij}^{exp} = f_{diff}^{\circ}. \end{aligned} \tag{4.24}$$

By considering the definition of the scattering phase function $f(\mathbf{r}, \mathbf{\Omega} \cdot \mathbf{\Omega'})$ as

$$f(\mathbf{r}, \mathbf{\Omega} \cdot \mathbf{\Omega'}) = \frac{\sigma_s(\mathbf{r}, \mathbf{\Omega} \cdot \mathbf{\Omega'})}{\int_{4\pi} d\mathbf{\Omega'} \sigma_s(\mathbf{r}, \mathbf{\Omega} \cdot \mathbf{\Omega'})} = \frac{\sigma_s(\mathbf{r}, \mathbf{\Omega} \cdot \mathbf{\Omega'})}{\sigma_s(\mathbf{r})}, \tag{4.25}$$

another form may also be obtained such that:

$$\int_V dV[\sigma_a(\mathbf{r}) + \sigma_s(\mathbf{r}) - \sigma_a^{\circ}(\mathbf{r}) + \sigma_s^{\circ}(\mathbf{r})] \int_{4\pi} d\mathbf{\Omega} \phi_i(\mathbf{r}, \mathbf{\Omega}) \phi_j^{\circ *}(\mathbf{r}, \mathbf{\Omega})$$

$$- \int_V dV[\sigma_s(\mathbf{r}) - \sigma_s^\circ(\mathbf{r})] \int_{4\pi} d\mathbf{\Omega} \int_{4\pi} d\mathbf{\Omega}' f(\mathbf{r}, \mathbf{\Omega} \cdot \mathbf{\Omega}') \phi_i(\mathbf{r}, \mathbf{\Omega}') \phi_j^{\circ *}(\mathbf{r}, \mathbf{\Omega})$$

$$= F_{ji}^\circ - F_{ij}^{exp} = f_{diff}^\circ \tag{4.26}$$

Writing the integral equation in this form provides explicit separation of the total cross section, the scattering cross section and the scattering phase function. This is helpful for the studies involving only the reconstruction of absorption and scattering cross sections by guessing the scattering phase function for the whole problem.

A definition important in the propagation of radiation through a random media is that of weight functions. The idea of weights or importance functions is commonly used in the control of nuclear reactors [192]. The un-normalised probability that photon, originating from the pulsed source at $\mathbf{r}_i \in \partial V$, reaching the neighbourhood of the position $\mathbf{r}$ with direction $\mathbf{\Omega}$ is

$$\phi_i(\mathbf{r}, \mathbf{\Omega}) dV d\mathbf{\Omega},$$

and the un-normalised probability of a photon localised in the neighbourhood of $\mathbf{r}$ with direction near $\mathbf{\Omega}$ reaching the detector located at $\mathbf{r}_j \in \partial V$ following the reverse path is

$$\phi_j^*(\mathbf{r}, \mathbf{\Omega}) dV d\mathbf{\Omega}.$$

By a combination of the two probabilities, a weight function can be produced for a given source-detector configuration as

$$dV \int_{4\pi} \phi_i(\mathbf{r}, \mathbf{\Omega}) \phi_j^*(\mathbf{r}, \mathbf{\Omega}) d\mathbf{\Omega} = W_{ij} dV. \tag{4.27}$$

Here we consider the steady-state case only. As these weight fields are related with the optical path travelled by the photon in scattering condition, W_{ij} maps un-normalised densities of probabilities for photon propagation through the medium.

Using the weight function definition above, the integral equations (4.24) and (4.26) can be written as

$$F_{ji}^\circ - F_{ij}^{exp} = \sum_{l=0}^{\infty} \frac{2l+1}{4\pi} \int_V dV W_{lij}^\circ(\mathbf{r}) [\sigma(\mathbf{r}) - \sigma_{sl}(\mathbf{r}) - \sigma^\circ(\mathbf{r}) + \sigma_{sl}^\circ(\mathbf{r})], \tag{4.28}$$

$$F_{ji}^{\circ} - F_{ij}^{exp} = \int_V dV W_{ij}^{\circ}(\mathbf{r})[\sigma_a(\mathbf{r}) - \sigma_a^{\circ}(\mathbf{r})] + \int_V dV\{W_{ij}^{\circ}(\mathbf{r}) - W_{fij}^{\circ}(\mathbf{r})\}[\sigma_s(\mathbf{r}) - \sigma_s^{\circ}(\mathbf{r})], \tag{4.29}$$

where W_{ij}, W_{fij} and W_{lij} are the weight functions defined for absorption and scattering separately as follows:

$$W_{ij}^{\circ}(\mathbf{r}) = \int_{4\pi} d\mathbf{\Omega}\phi_i(\mathbf{r},\mathbf{\Omega})\phi_j^{\circ *}(\mathbf{r},\mathbf{\Omega}), \tag{4.30}$$

$$W_{fij}^{\circ}(\mathbf{r}) = \int_{4\pi} d\mathbf{\Omega} \int_{4\pi} d\mathbf{\Omega}' f(\mathbf{\Omega}\cdot\mathbf{\Omega}')\phi_i(\mathbf{r},\mathbf{\Omega}')\phi_j^{\circ *}(\mathbf{r},\mathbf{\Omega}), \qquad or \tag{4.31}$$

$$W_{lij}^{\circ}(\mathbf{r}) = \int_{4\pi} d\mathbf{\Omega} \int_{4\pi} d\mathbf{\Omega}' P_l(\mathbf{\Omega}\cdot\mathbf{\Omega}')\phi_i(\mathbf{r},\mathbf{\Omega}')\phi_j^{\circ *}(\mathbf{r},\mathbf{\Omega}). \tag{4.32}$$

These weight function definitions will be used in the derivations that follow.

4.3 First- and Second-Order Variational Formulation of The Reference Cross Section Model

For the derivation of the first- and second-order forms of the reference cross section model, the following definitions separate the angular fluxes of source and detector problems and also the scattering kernel in equations (4.9) and (4.11) into their even and odd components:

$$\begin{aligned}\phi_i^{+}(\mathbf{r},\mathbf{\Omega}) &= \frac{1}{2}[\phi_i(\mathbf{r},\mathbf{\Omega}) + \phi_i^{*}(\mathbf{r},\mathbf{\Omega})],\\ \phi_i^{-}(\mathbf{r},\mathbf{\Omega}) &= \frac{1}{2}[\phi_i(\mathbf{r},\mathbf{\Omega}) - \phi_i^{*}(\mathbf{r},\mathbf{\Omega})],\end{aligned} \tag{4.33}$$

$$\begin{aligned}\phi_j^{+}(\mathbf{r},\mathbf{\Omega}) &= \frac{1}{2}[\phi_j(\mathbf{r},\mathbf{\Omega}) + \phi_j^{*}(\mathbf{r},\mathbf{\Omega})],\\ \phi_j^{-}(\mathbf{r},\mathbf{\Omega}) &= \frac{1}{2}[\phi_j(\mathbf{r},\mathbf{\Omega}) - \phi_j^{*}(\mathbf{r},\mathbf{\Omega})],\end{aligned} \tag{4.34}$$

$$\begin{aligned}\sigma_s^{+}(\mathbf{r},\mathbf{\Omega}\cdot\mathbf{\Omega}') &= \frac{1}{2}[\sigma_s(\mathbf{r},\mathbf{\Omega}\cdot\mathbf{\Omega}') + \sigma_s(\mathbf{r},-\mathbf{\Omega}\cdot\mathbf{\Omega}')],\\ \sigma_s^{-}(\mathbf{r},\mathbf{\Omega}\cdot\mathbf{\Omega}') &= \frac{1}{2}[\sigma_s(\mathbf{r},\mathbf{\Omega}\cdot\mathbf{\Omega}') - \sigma_s(\mathbf{r},-\mathbf{\Omega}\cdot\mathbf{\Omega}')].\end{aligned} \tag{4.35}$$

Inserting the equivalent expressions of $\phi_i(\mathbf{r},\mathbf{\Omega}')$ and $\phi_j^*(\mathbf{r},\mathbf{\Omega})$ in terms of ϕ_i^+ - ϕ_i^- and ϕ_j^+ - ϕ_j^- into equation (4.32) results in the new form of the weight function as

$$W_{lij}(\mathbf{r}) = \int_{4\pi} d\mathbf{\Omega} \int_{4\pi} d\mathbf{\Omega}' P_l(\mathbf{\Omega}\cdot\mathbf{\Omega}') \left[\phi_i^+(\mathbf{\Omega})\phi_j^+(\mathbf{\Omega}) - \phi_i^-(\mathbf{\Omega})\phi_j^-(\mathbf{\Omega})\right]. \qquad (4.36)$$

The separation of the even and odd components for the weight function is carried out as follows

$$W_{lij} = \left\{ \begin{array}{ll} W_{lij}^+ = \int_{4\pi} d\mathbf{\Omega} \int_{4\pi} d\mathbf{\Omega}' P_l(\mathbf{\Omega}\cdot\mathbf{\Omega}')\phi_i^+(\mathbf{\Omega})\phi_j^+(\mathbf{\Omega}) & if\ l\ even \\ \\ W_{lij}^- = -\int_{4\pi} d\mathbf{\Omega} \int_{4\pi} d\mathbf{\Omega}' P_l(\mathbf{\Omega}\cdot\mathbf{\Omega}')\phi_i^-(\mathbf{\Omega})\phi_j^-(\mathbf{\Omega}) & if\ l\ odd \end{array} \right\}, \qquad (4.37)$$

and it can be rewritten as:

$$W_{lij}(\mathbf{r}) = W_{lij}^+ - W_{lij}^-. \qquad (4.38)$$

Employing this form of the weight function in equation (4.28) yields the first- order form of the reference cross section model:

$$F_{ji}^\circ - F_{ij}^{exp} = \int_V dV \int_{4\pi} d\mathbf{\Omega} \left\{\phi_j^+(\mathbf{r},\mathbf{\Omega})\triangle R[\phi_i^+(\mathbf{r},\mathbf{\Omega})] - \phi_j^-(\mathbf{r},\mathbf{\Omega})\triangle R[\phi_i^-(\mathbf{r},\mathbf{\Omega})]\right\} \qquad (4.39)$$

where the operator for the difference is defined as

$$\begin{aligned} \triangle R[\phi(\mathbf{r},\mathbf{\Omega})] &= R[\phi(\mathbf{r},\mathbf{\Omega})] - R^\circ[\phi(\mathbf{r},\mathbf{\Omega})] \\ &= \sum_{l=0}^{\infty}\left(\frac{2l+1}{4\pi}\right)[\sigma - \sigma_{sl} - \sigma^\circ + \sigma_{sl}^\circ]\int_{4\pi} d\mathbf{\Omega}' P_l(\mathbf{\Omega}\cdot\mathbf{\Omega}')\phi(\mathbf{r},\mathbf{\Omega}'), \end{aligned} \qquad (4.40)$$

with

$$\triangle R[\phi^+(\mathbf{r},\mathbf{\Omega})] \implies \text{l is even} \quad \text{and} \quad \triangle R[\phi^-(\mathbf{r},\mathbf{\Omega})] \implies \text{l is odd.}$$

Applying the same procedure, given in section (2.3) while deriving the even-parity form of the transport equation, to the equations of source and detector problems respectively, equations (4.9) and (4.11), yields a pair of coupled first-order differential equations for the even- and odd-parity fluxes.

$$\mathbf{\Omega}\cdot\nabla\phi_i^-(\mathbf{r},\mathbf{\Omega}) + R^+[\phi_i^+(\mathbf{r},\mathbf{\Omega})] = 0,$$

$$\mathbf{\Omega} \cdot \nabla \phi_i^+(\mathbf{r}, \mathbf{\Omega}) + R^-[\phi_i^-(\mathbf{r}, \mathbf{\Omega})] = 0, \tag{4.41}$$

and

$$\mathbf{\Omega} \cdot \nabla \phi_j^-(\mathbf{r}, \mathbf{\Omega}) + R^{\circ +}[\phi_j^+(\mathbf{r}, \mathbf{\Omega})] = 0,$$

$$\mathbf{\Omega} \cdot \nabla \phi_j^+(\mathbf{r}, \mathbf{\Omega}) + R^{\circ -}[\phi_j^-(\mathbf{r}, \mathbf{\Omega})] = 0. \tag{4.42}$$

Recovering the odd-parity components $\phi_i^-(\mathbf{r}, \mathbf{\Omega})$ and $\phi_j^-(\mathbf{r}, \mathbf{\Omega})$ from the first-order equations in terms of $\mathbf{\Omega} \cdot \nabla \phi_i^+(\mathbf{r}, \mathbf{\Omega})$ and $\mathbf{\Omega} \cdot \nabla \phi_j^+(r, \mathbf{\Omega})$ as

$$\phi_i^-(\mathbf{r}, \mathbf{\Omega}) = -(R^-)^{-1}[\mathbf{\Omega} \cdot \nabla \phi_i^+(\mathbf{r}, \mathbf{\Omega})], \qquad \phi_j^-(\mathbf{r}, \mathbf{\Omega}) = -(R^{\circ -})^{-1}[\mathbf{\Omega} \cdot \nabla \phi_j^+(\mathbf{r}, \mathbf{\Omega})], \tag{4.43}$$

and substituting in equation (4.39), the second-order even-form of the reference cross section model is obtained such that:

$$\int_V dV \int_{4\pi} d\mathbf{\Omega} \left\{ \triangle (R^-)^{-1}[\mathbf{\Omega} \cdot \nabla \phi_i^+(\mathbf{r}, \mathbf{\Omega})]\, \mathbf{\Omega} \cdot \nabla \phi_j^+(\mathbf{r}, \mathbf{\Omega}) - \triangle R[\phi_i^+(\mathbf{r}, \mathbf{\Omega})]\, \phi_j^+(\mathbf{r}, \mathbf{\Omega}) \right\}$$

$$= F_{ji}^{\circ} - F_{ij}^{exp} \tag{4.44}$$

where the right hand side of this equation is

$$F_{ji}^{\circ} - F_{ij}^{exp} = \int_{4\pi} d\mathbf{\Omega} \mid \mathbf{\Omega} \cdot \mathbf{n} \mid \phi_i^+(\mathbf{r}_j, \mathbf{\Omega}) - S_i \int_{4\pi} d\mathbf{\Omega} \mid \mathbf{\Omega} \cdot \mathbf{n} \mid \phi_j^+(\mathbf{r}_i, \mathbf{\Omega}), \tag{4.45}$$

and $(R)^{-1}$ is called as the leakage operator and the difference $\triangle (R^-)^{-1}$ is given by

$$\triangle (R^-)^{-1}[\circ] = \sum_{l=odd}^{\infty} \left(\frac{2l+1}{4\pi} \right) \left[\frac{1}{\sigma - \sigma_{sl}} - \frac{1}{\sigma^{\circ} - \sigma_{sl}^{\circ}} \right] \int_{4\pi} d\mathbf{\Omega}' P_l(\mathbf{\Omega} \cdot \mathbf{\Omega}')[\circ]. \tag{4.46}$$

The boundary condition takes the following form

$$\phi_i^+(\mathbf{r}, \mathbf{\Omega}) \; - \; (R^-)^{-1}[\mathbf{\Omega} \cdot \nabla \phi_i^+(\mathbf{r}, \mathbf{\Omega})] = \phi_{in}(\mathbf{r}, \mathbf{\Omega}), \qquad \mathbf{r} \in \partial V, \;\; \mathbf{\Omega} \cdot \mathbf{n} \; < \; 0,$$

$$\phi_i^+(\mathbf{r}, \mathbf{\Omega}) \; + \; (R^-)^{-1}[\mathbf{\Omega} \cdot \nabla \phi_i^+(\mathbf{r}, \mathbf{\Omega})] = \phi_{in}(\mathbf{r}, -\mathbf{\Omega}), \qquad \mathbf{r} \in \partial V, \;\; \mathbf{\Omega} \cdot \mathbf{n} \; > \; 0. \tag{4.47}$$

For the solution of this equation to obtain the even-parity flux, a self-adjoint minimum principle is used and the associated variational functional can be written as

$$F[\phi_i^+] = (\mathbf{\Omega} \cdot \nabla \phi_i^+, (R^-)^{-1} \mathbf{\Omega} \cdot \nabla \phi_i^+) + (\phi_i^+, R^+[\phi_i^+]) + \left\langle \phi_i^+, \phi_i^+ \right\rangle - 2 \left\langle \phi_i^+, \phi_s \right\rangle, \tag{4.48}$$

where (.,.) and $\langle .,. \rangle$ are the angular integration given by equations (4.28)-(4.29) and ϕ_s is the isotropic source term in the boundary

$$\phi_s(\mathbf{r},\mathbf{\Omega}) = \left\{ \begin{array}{ll} \phi_{in}(\mathbf{r},\mathbf{\Omega}) & if \;\; \mathbf{\Omega}\cdot\mathbf{n} < 0, \\ \\ \phi_{in}(\mathbf{r},-\mathbf{\Omega}) & if \;\; \mathbf{\Omega}\cdot\mathbf{n} > 0, \end{array} \right\}.$$

Minimising this functional by taking the first variation with respect to the even-parity flux ϕ_i^+ equal to zero as

$$\delta F[\phi_i^+;\delta\phi_i^+] = 0 \tag{4.49}$$

results in equation (4.44) and the associated boundary conditions equation (4.47). This procedure leads to the desired set of simultaneous equations suitable for solution on a digital computer.

4.4 Image Reconstruction Algorithm

In the algorithm, equation (4.28) is used for the recovery of the real cross section fields $[\sigma(r),\ \sigma_{sl}(r)]$ and can be represented in a concise, matrix form as

$$\mathbf{W_{lij}}\ \triangle\sigma = \mathbf{F^{\circ}_{ji}} - \mathbf{F^{exp}_{ij}} = \mathbf{f^{\circ}_{diff}}. \tag{4.50}$$

Starting with a good initial estimate of the reference medium (σ_a°,σ_s°) and taking the experimental measurements F_{ij}^{exp} as the given data for the real medium, the following steps are employed to solve the inverse problem:

(1) In the reference medium, calculation of $\phi_i^{+\circ}(r,\mathbf{\Omega})$ from the expression given by equation (4.36) and the weight function from the equation

$$W^{\circ}_{lij}(r) = \int_{4\pi} d\mathbf{\Omega} \int_{4\pi} d\mathbf{\Omega}' P_l(\mathbf{\Omega}\cdot\mathbf{\Omega}') \left[\phi_i^{+\circ}(r,\mathbf{\Omega})\phi_j^{+\circ}(r,\mathbf{\Omega}) - \phi_i^{-\circ}(r,\mathbf{\Omega})\phi_j^{-\circ}(r,\mathbf{\Omega})\right] \tag{4.51}$$

and substituting the value of $\phi_i^{-\circ}$ obtained as

$$\phi_i^{-\circ}(r,\ \mathbf{\Omega}) = \frac{1}{\sigma^{\circ}(r) - \sigma^{\circ}_{sl}(r)}\ \mathbf{\Omega}\cdot\nabla\phi_i^{+\circ}(r,\mathbf{\Omega}). \tag{4.52}$$

(2) Solution of the inverse problem to determine the difference f°_{diff} between the real and reference cross sections fields as follows

$$[(\sigma - \sigma_{sl}) - (\sigma^{\circ} - \sigma^{\circ}_{sl})] = f^{\circ}_{diff} = F^{\circ}_{ji} - F^{exp}_{ij}/W^{\circ}_{lij}, \tag{4.53}$$

and then updating the real medium by the trial cross section fields (σ^k_a,σ^k_s);

(3) Determination of $\phi^{+\circ}_i(r, \mathbf{\Omega})$ by the new trial cross sections, the weight function from

$$W^k_{lij}(r) = \int_{4\pi} d\mathbf{\Omega} \int_{4\pi} d\mathbf{\Omega}' P_l(\mathbf{\Omega} \cdot \mathbf{\Omega}') \left[\phi^{+k}_i(r, \mathbf{\Omega})\phi^{+\circ}_j(r, \mathbf{\Omega}) - \phi^{-k}_i(r, \mathbf{\Omega})\phi^{-\circ}_j(r, \mathbf{\Omega})\right] \tag{4.54}$$

with the value of $\phi^{-k}_i(r,\ \mathbf{\Omega})$ as

$$\phi^{-k}_i(r,\ \mathbf{\Omega}) = \frac{1}{\sigma^k(r) - \sigma^k_{sl}(r)}\ \mathbf{\Omega} \cdot \nabla \phi^{+k}_i(r, \mathbf{\Omega}), \tag{4.55}$$

and something about F^k_{ij}, solution of the inverse problem to calculate the difference f^k_{diff} between the trial and reference cross section fields as follows:

$$\left[(\sigma^k - \sigma^k_{sl}) - (\sigma^{\circ} - \sigma^{\circ}_{sl})\right] = f^k_{diff} = F^{\circ}_{ji} - F^k_{ij}/W^k_{lij}, \tag{4.56}$$

(4) Checking the convergence criterion as

$$\left(f^k_{diff} - f^{\circ}_{diff}\right)^2 < \delta \tag{4.57}$$

where δ is a prescribed threshold. If results are convergent, display the first trial cross section fields (σ^k_a,σ^k_s). If the convergence criterion is not satisfied, restart from the third step as in updating values of the cross sections.

4.5 Summary

In this chapter, the fundamental basis of a new mathematical model developed for the solution of the problem of imaging the interior of dense scattering media by employing the Boltzmann transport equation was presented and an iterative reconstruction algorithm for the solution of a system of linear equations of the form $\mathbf{W} \triangle \sigma = \mathbf{f}$

was outlined. Firstly, the definition of inverse problem was given together with the commonly used solution methods encountered in optical tomographic image reconstruction. The Boltzmann transport equation with the appropriate boundary conditions considered for tomographic studies and the Laplace transformed form of this equation were next presented. The Reference Cross Section Model (RCSM) based on the transport equation and used to obtain a system of integral equations named as the inverse Boltzmann equation was then introduced. A variational formulation consistent with this equation system was next presented for the implementation of the numerical solution through the FE-P_N method. The iterative image reconstruction algorithm employed for the reconstruction of images in this study was finally discussed.

Chapter 5

Image Reconstruction Results

5.1 Introduction

In this chapter, we present reconstruction results involving the recovery of absorption coefficient in various optically heterogeneous media. The finite-element-based reconstruction algorithm, based on the Boltzmann transport equation, was used for reconstruction of images. The solution model and reconstruction algorithm have been discussed in Chapter 4. Images were reconstructed using both the Monte Carlo data and data obtained from the Finite Element-Spherical Harmonics forward model. The aim was to demonstrate the performance and capabilities of the reconstruction approach in detecting inhomogeneities within the modelled objects.

5.2 Reconstructions from Monte Carlo Data

As a test of employing MC data, the results plotted in Figures 3.14 and 3.16 have been used again in reconstructing images of the two simply structured inhomogeneous cases of Section 3.2.2. The problem geometry for the first case was repeated in Figure 5.1. The centred inhomogeneity was 2 mm in diameter with coefficients μ_a=0.12 mm^{-1}

and μ_s=1.08 mm^{-1}. The outer cylinder was 20 mm in diameter and had coefficients μ_a=0.05 mm^{-1} and μ_s=0.45 mm^{-1}. The mean cosine of the scattering angle, g, was taken equal to 0 (assuming isotropic scattering). The MC data had been obtained using 8 sources, which are pulsed for 1 picosecond, and 8 detectors for 5.0×10^9 incident photon histories.

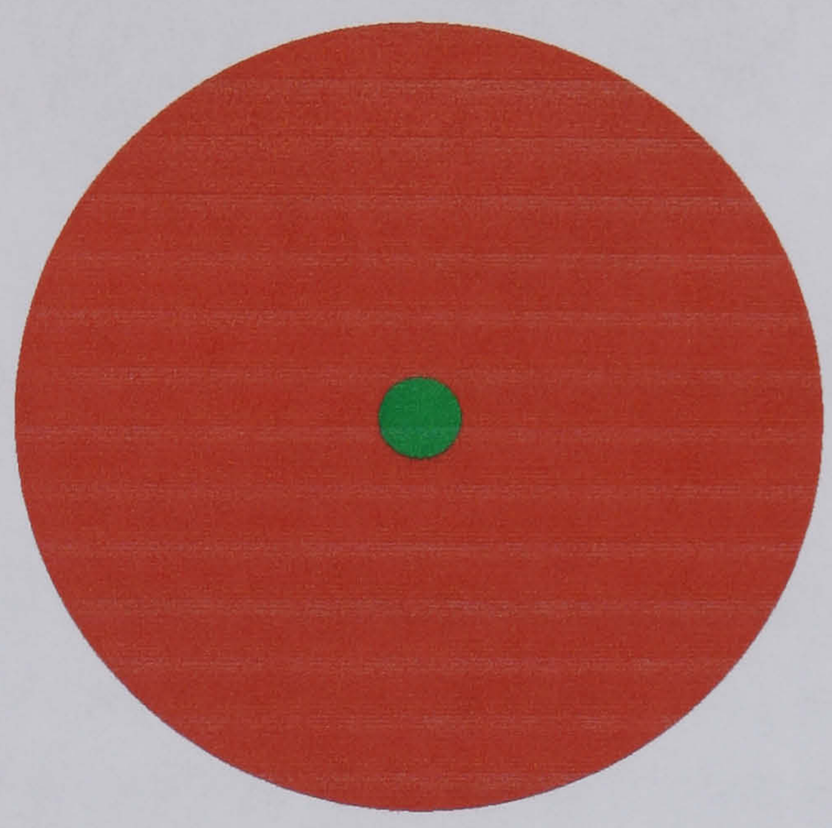


Figure 5.1: Simulation geometry used for the reconstruction of the first inhomogeneous problem with one centred cylindrical region.

In order to use the MC results as input data to the reconstruction algorithm, the Laplace transform was applied for obtaining equivalent steady-state solutions. As mentioned before, the application of the Laplace transform offers an important resource savings and provides a feasible way to deal with overdetermination arising from transient measurements [190]. The Laplace transform parameters s plays an important role on the choice of better reconstruction. When s<0, the problem becomes scattering dominated and the importance in reconstruction is given to scattered photons. When s>0 is chosen, the problem becomes more absorbing and the importance is for less-scattered photons. So, having the Laplace transformed data allows data to be evaluated to different values of s in order to emphasise the relative importance of absorption and scattering [190].

A mesh shown in Figure 5.2, and consisting of 2285 nodes and 4568 linear triangular elements was used in this reconstruction. The Laplace transform parameter s was

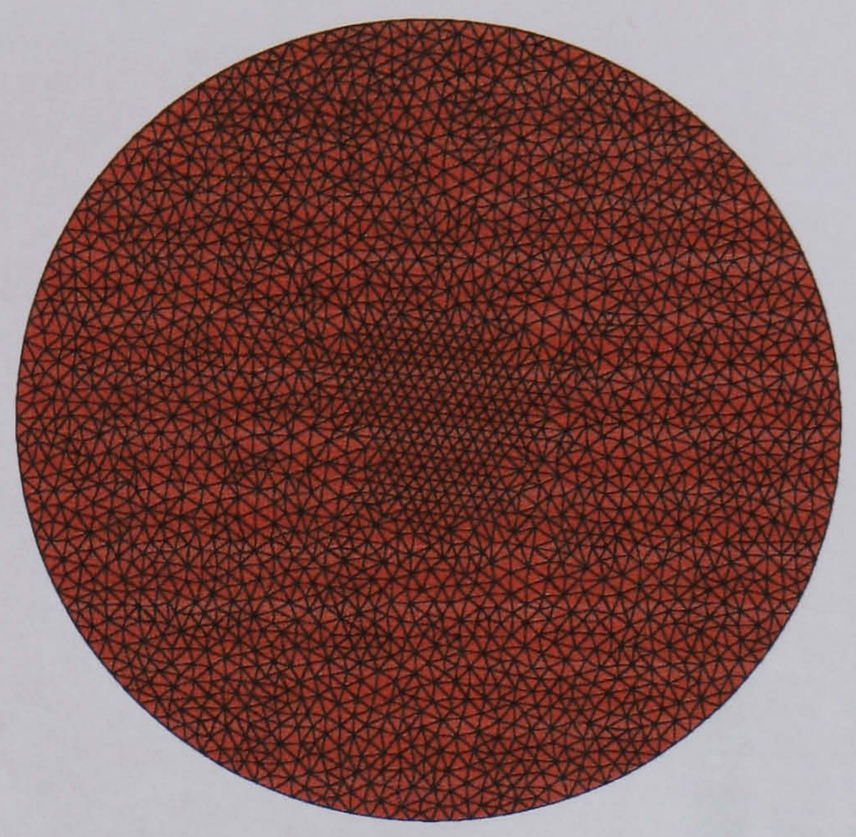


Figure 5.2: The mesh used in the reconstruction of the centred cylinder problem.

chosen as 0.0226 and the Laplace transformed results associated to this value were taken and entered to the reconstruction algorithm. The corresponding value of s/v =0.1, which was called the equivalent absorption cross section in Chapter 4, was added to the absorption coefficient of the cylinder shown in Figure 5.2. The iteration process was started with the following values for the cylindrical region: $\mu_a = 0.15$ mm^{-1} and $\mu_s = 0.45$ mm^{-1}.

The reconstruction algorithm can be used with different grid resolutions, such as a 16x16 x-y grid, a 24x24 x-y grid or 32x32 x-y grid. In this problem, the images were reconstructed at a 32x32 resolution. A P_5 angular approximation was used for the inverse solution. Reconstruction time took approximately 13 cpu minutes for 14 iterations on a Dec Alpha 500/250.

Figure 5.3 shows the reconstruction distributions of absorption coefficient μ_a (reconstructed from the Laplace transformed MC data) for the first and last (14) steps of iteration respectively. The side colour scale represents the reconstructed μ_a (mm^{-1}) values and the bounding scales give dimensions in mm. The illustration shows that the inhomogeneity is detected even in the first iteration and as the number of iteration increases, the inhomogeneity is more clearly identified against the background medium. The absorption coefficient values obtained by the reconstruction algorithm for both regions, the outer cylinder and inhomogeneity, are found as follows: In the

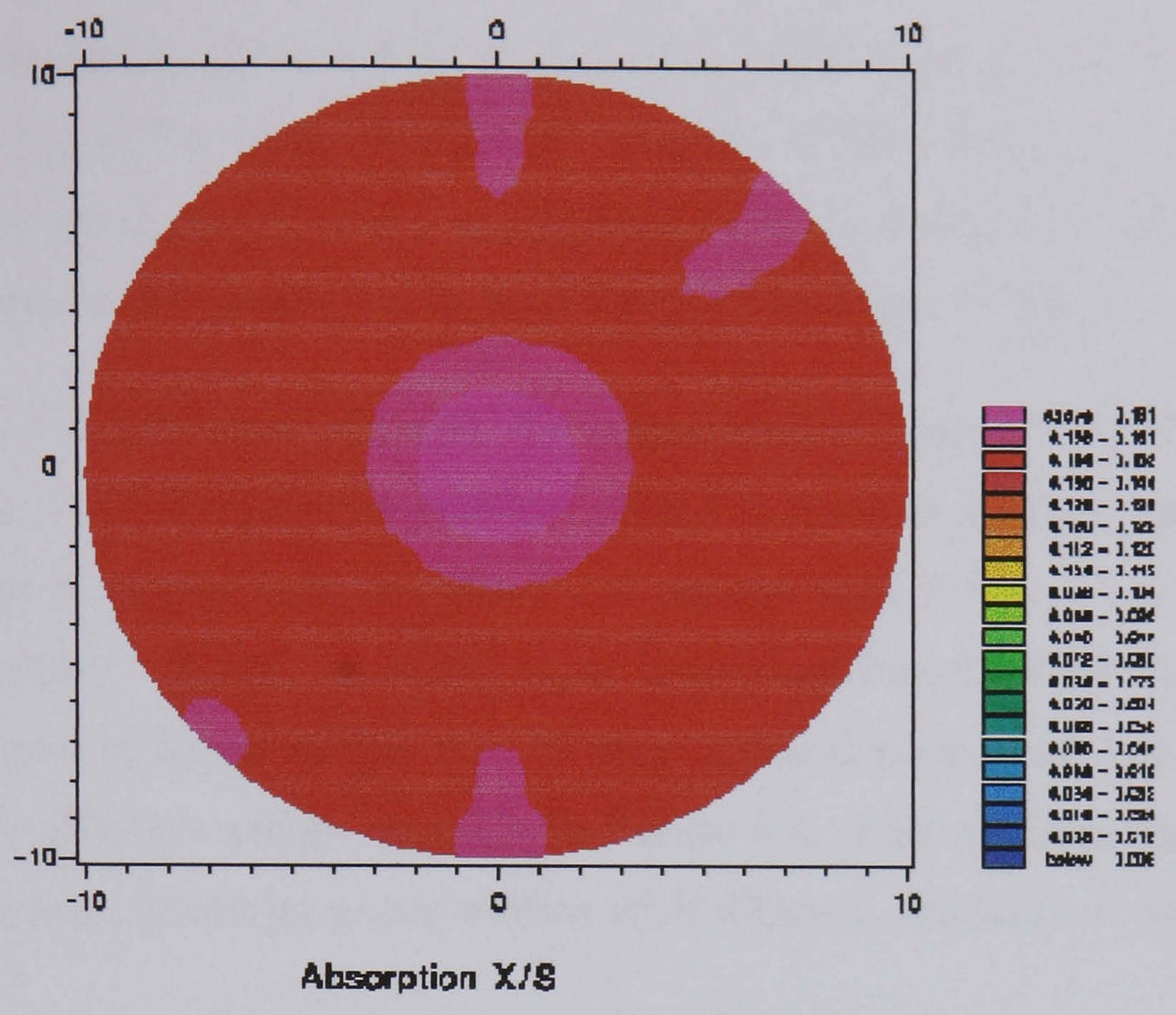


Figure 5.3: Reconstructed images based on MC data obtained from an inhomogeneous cylinder with a centrally located small cylinder. The upper illustration gives the result of μ_a values for the first iteration and the lower shows the result for iteration number 14.

first iteration, μ_a^{bac}= 0.136 - 0.153 mm^{-1}, μ_a^{inh}= 0.153 - 0.161 mm^{-1} and in the last iteration, μ_a^{bac}= 0.09 - 0.197 mm^{-1}, μ_a^{inh}= 0.269 - 0.358 mm^{-1}. Although the inhomogeneity is found, those results show that the absorption value of the small centred cylinder is overestimated in both the first and last iterations.

The second case selected for reconstruction using the MC generated data was the first inhomogeneous problem solved in Section 3.2.2 of Chapter 3. The problem consisted of four infinite cylindrical regions with different absorption and scattering properties. The radius of the three individual inhomogeneities was set to 1 mm and the outer cylinder radius was 10 mm. Optical properties and the positioning of the small cylinders are given again in Figure 5.4. This problem differs from the first one in having 2 more inhomogeneities with different absorption coefficients.

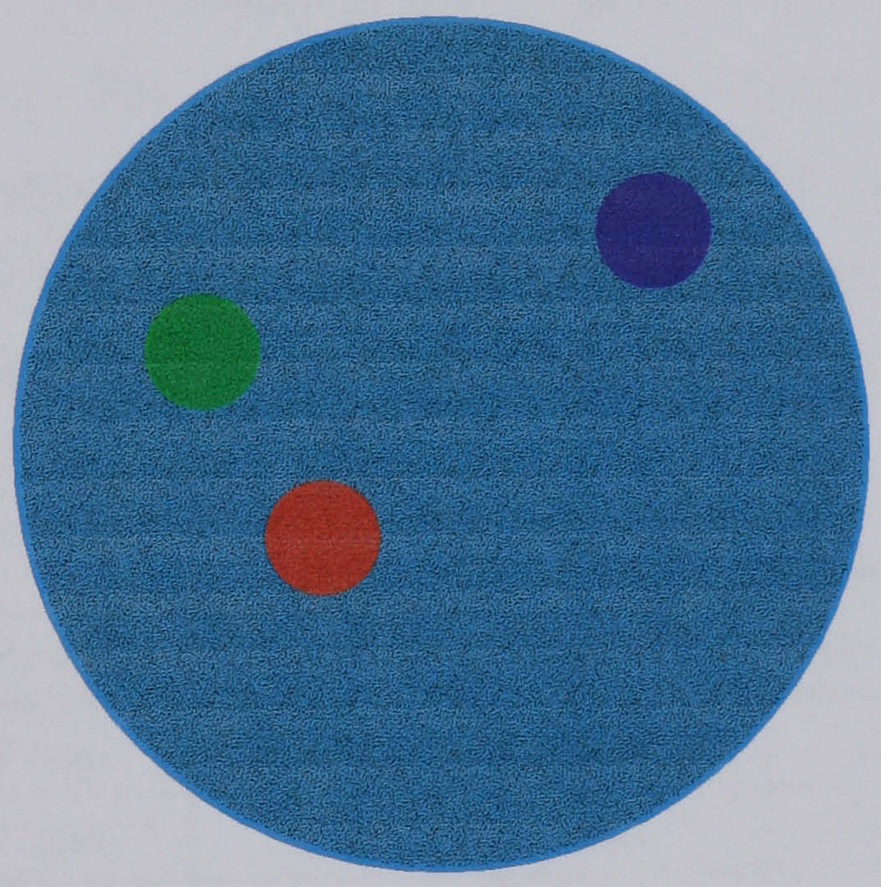


Figure 5.4: Simulation geometry used to obtain the MC data for the reconstruction. Assumed optical properties of the background and three small cylinders were as follows: Background: μ_a=0.05 mm^{-1} and μ_s=0.45 mm^{-1}, cylinder 1 (green): μ_a=0.09 mm^{-1} and μ_s=0.81 mm^{-1}, cylinder 2 (purple): μ_a=0.12 mm^{-1} and μ_s=1.08 mm^{-1}, cylinder 3 (red): μ_a=0.15 mm^{-1} and μ_s=1.35 mm^{-1}.

MC time-dependent data were generated for all 64 combinations of 8 source and 8 detector positions, equally spaced on the surface as shown in Figure 3.11, by using 5.0×10^9 photon histories. All sources were pulsed for 1 picosecond. Isotropic scat-

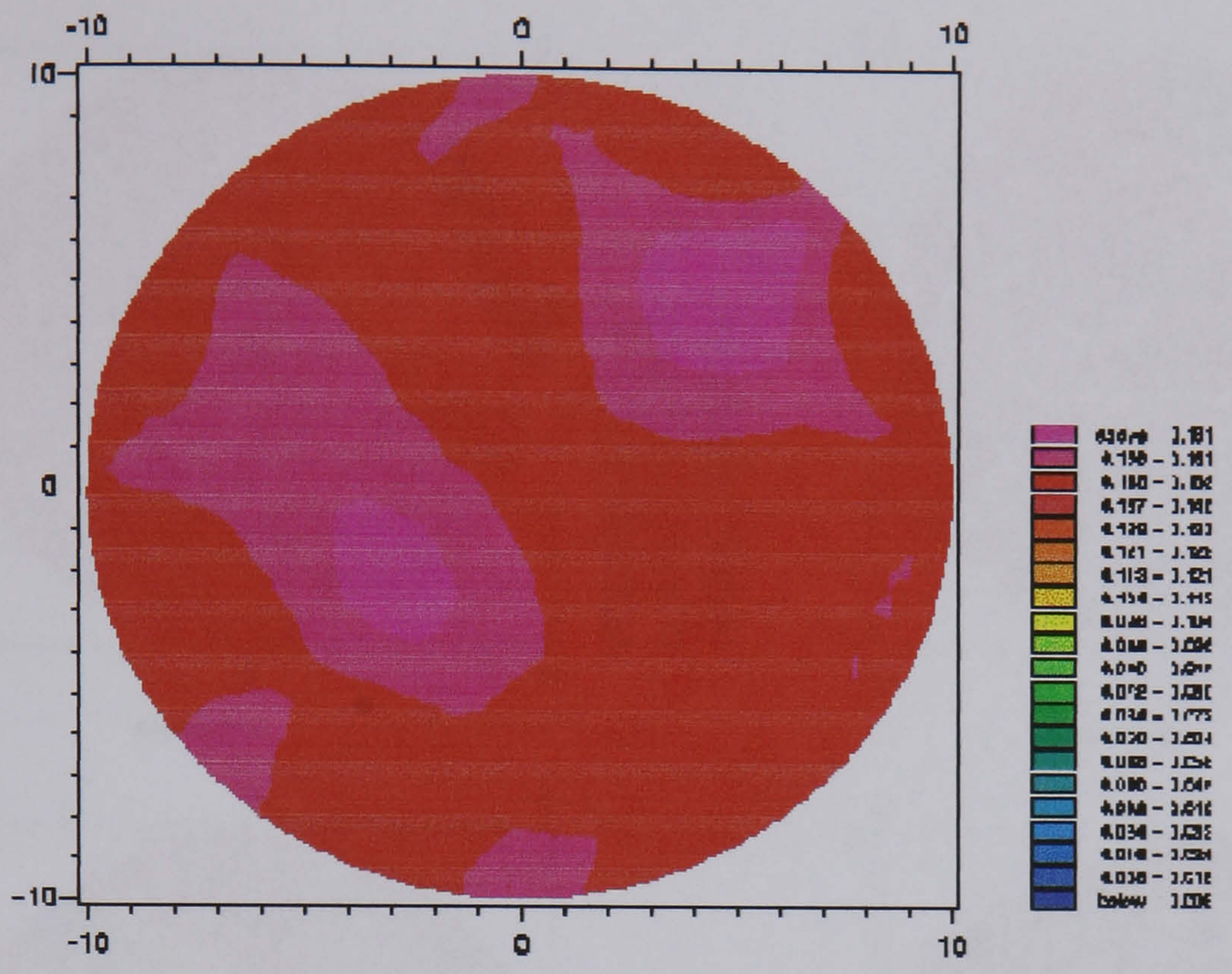
tering (g=0) was assumed in all regions. The Laplace transform was again applied and the transformed results were chosen for the value of s/c =0.1 to supply to the reconstruction algorithm, as in the previous problem. The reference medium for the inverse solution is the cylinder with the same mesh as given in Figure 5.2 and the same optical properties, $\mu_a = 0.15$ mm^{-1} and $\mu_s = 0.45$ mm^{-1}, as used the first reconstruction problem.

In Figure 5.5, the first iteration reconstruction of the image and the further improvement after 12 iterations are shown. As it can be seen two cylinders, 2 and 3, start to appear from the first iteration while the first cylinder, Cylinder 1, cannot be resolved even in the last iteration. This could be due to the small absorption coefficient of this cylinder as the value very near to that of the homogeneous cylinder using for the reconstruction. This results in the Cylinder 1 not being distinguished from the background medium. The absorption coefficient values of three regions obtained by the reconstruction algorithm for the two iterations are given in Table 5.1. It can be seen from the figure that although the two cylinders are resolved, the absorption coefficient of the cylinders is not representative of their true values.

Cylinders	**Absorption Coefficient Values**		
	Real	**Iteration Number: 1**	**Iteration Number: 14**
Background	0.05 mm^{-1}	0.121 - 0.153 mm^{-1}	0.093 - 0.187 mm^{-1}
Cylinder 2	0.12 mm^{-1}	0.153 - 0.161 mm^{-1}	0.187 - 0.374 mm^{-1}
Cylinder 3	0.15 mm^{-1}	0.153 - 0.161 mm^{-1}	0.187 - 0.318 mm^{-1}

Table 5.1: Reconstructed absorption coefficient values of the problem given in Figure 5.4.

The result for the weight function for μ_a, which basically quantifies the effect on the recovered values of μ_a [193], is plotted in Figure 5.6. The pictures provide a representation of the light bundle, which contains the majority of the photon paths from the source to 6 different detectors.



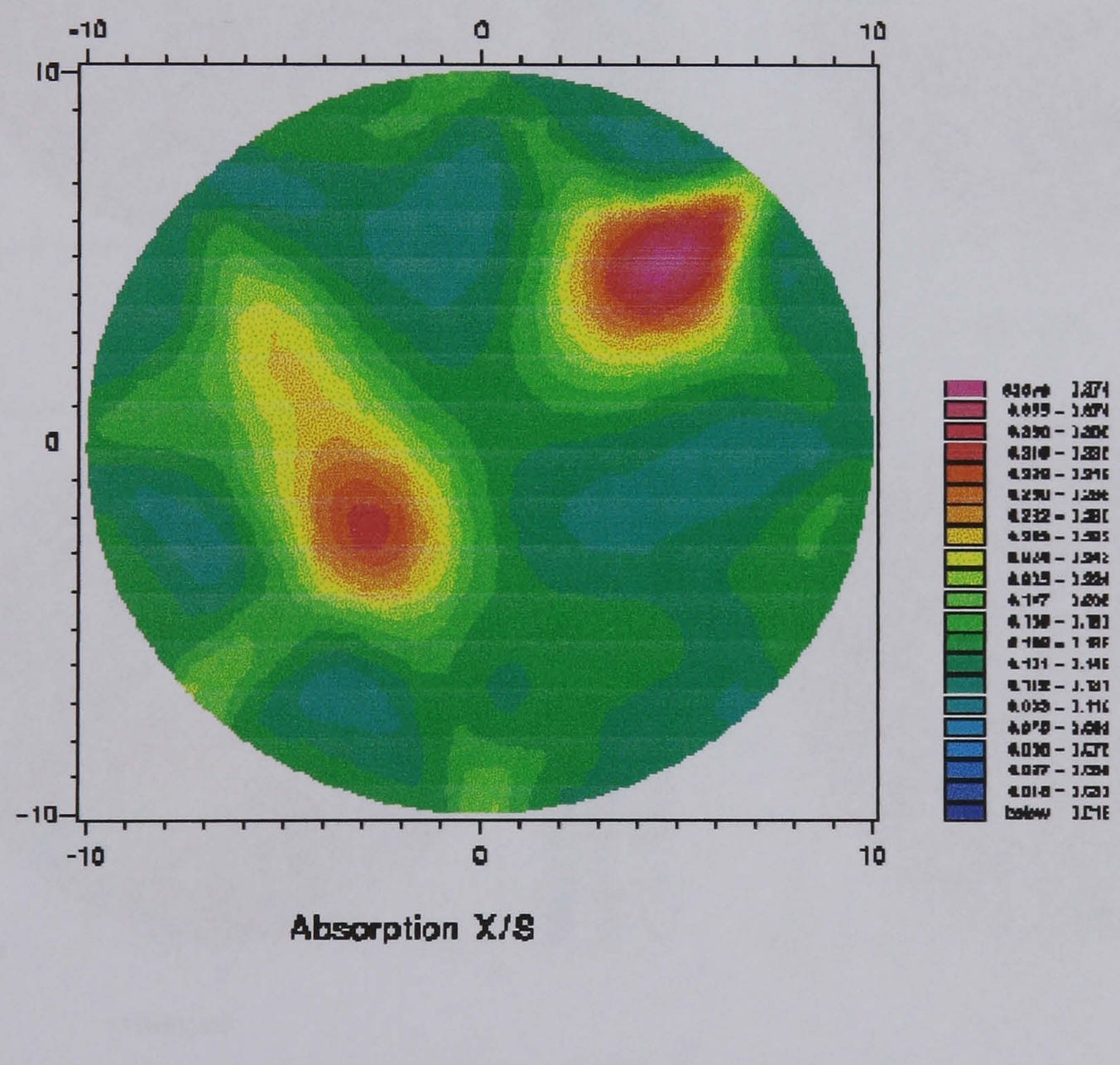


Figure 5.5: Reconstruction of Monte Carlo data of three cylindrical regions within a 20 mm cylinder. The upper illustration shows first iteration results and the lower gives the results for iteration number 12.

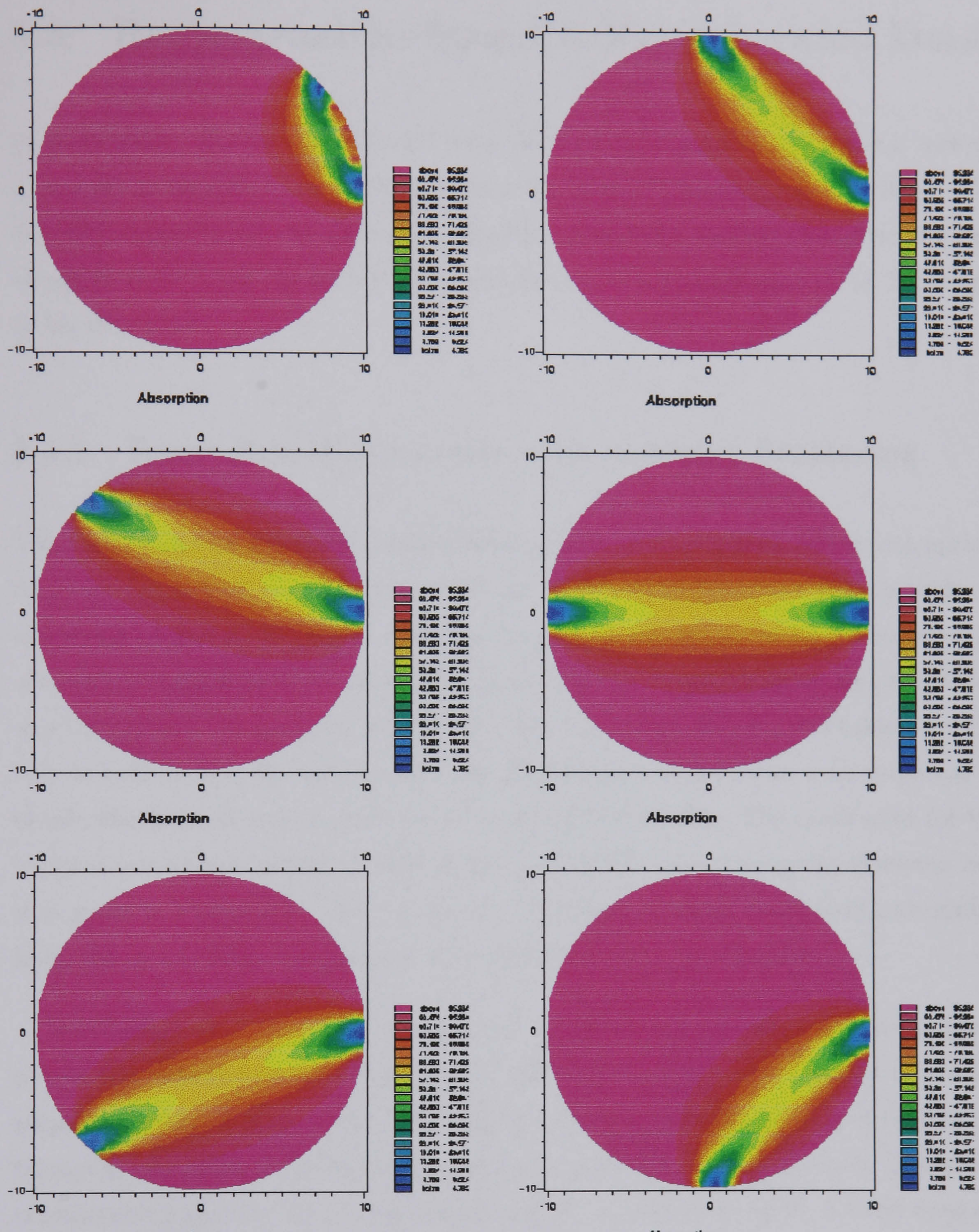


Figure 5.6: Weight functions for absorption coefficient of the problem given in Figure 5.4. The pictures shows the weights from the source 1 to the detectors 2, 3, 4, 5, 6 and 7 for the first iteration.

5.3 Reconstruction from FE-P_N-Generated Data

In this section, the results obtained with the data generated by the FE-P_N forward model are presented to show the performance of the reconstruction algorithm. The first two reconstruction results are obtained for geometries that were employed by Patterson et al. [42] and the second two problems were those addressed by M. Schweiger in his thesis [17].

5.3.1 Reconstruction Results with Isotropic Scattering

The first simulation geometry consisted of a cylinder of 50 mm in diameter with optical properties $\mu_a = 0.01$ mm^{-1} and $\mu_s = 1.0$ mm^{-1}. The inhomogeneity was a cylindrical absorbing object of 10 mm in diameter located at the centre of the cylinder. The absorption coefficient of the object was $\mu_a = 0.02$ mm^{-1} and the scattering coefficient was the same as the background medium. The anisotropy factor g was taken equal to zero in both media. 20 equi-spaced isotropic sources and detectors were employed to obtain the forward data and also the reconstruction results. The mesh used for the forward solution consisted of 5654 nodes and 11306 linear triangular elements and it is given in Figure 5.7. The P_3 angular approximation was employed in obtaining both the steady-state forward and inverse (reconstruction) solutions.

The background cylinder with the same diameter and optical properties as given above, but without the absorbing object, was used for the reconstruction of the absorption coefficient map. The cylindrical mesh consisted of 4231 nodes and 8460 linear triangular elements. Two iterations had been made with the algorithm to obtain the reconstructed picture. The reconstruction was done on a 15x15 grid. The forward solution took 3 cpu minutes and the reconstruction of two pictures took approximately 7 cpu minutes on a Dec Alpha 500/250 workstation.

The result of the second iteration is given in Figure 5.8. For this iteration the absorption coefficients of the object and the background were found to be as follows: the reconstructed absorption value of the background (basically the green colour



Figure 5.7: 2D finite element mesh with the absorbing object located at the centre.

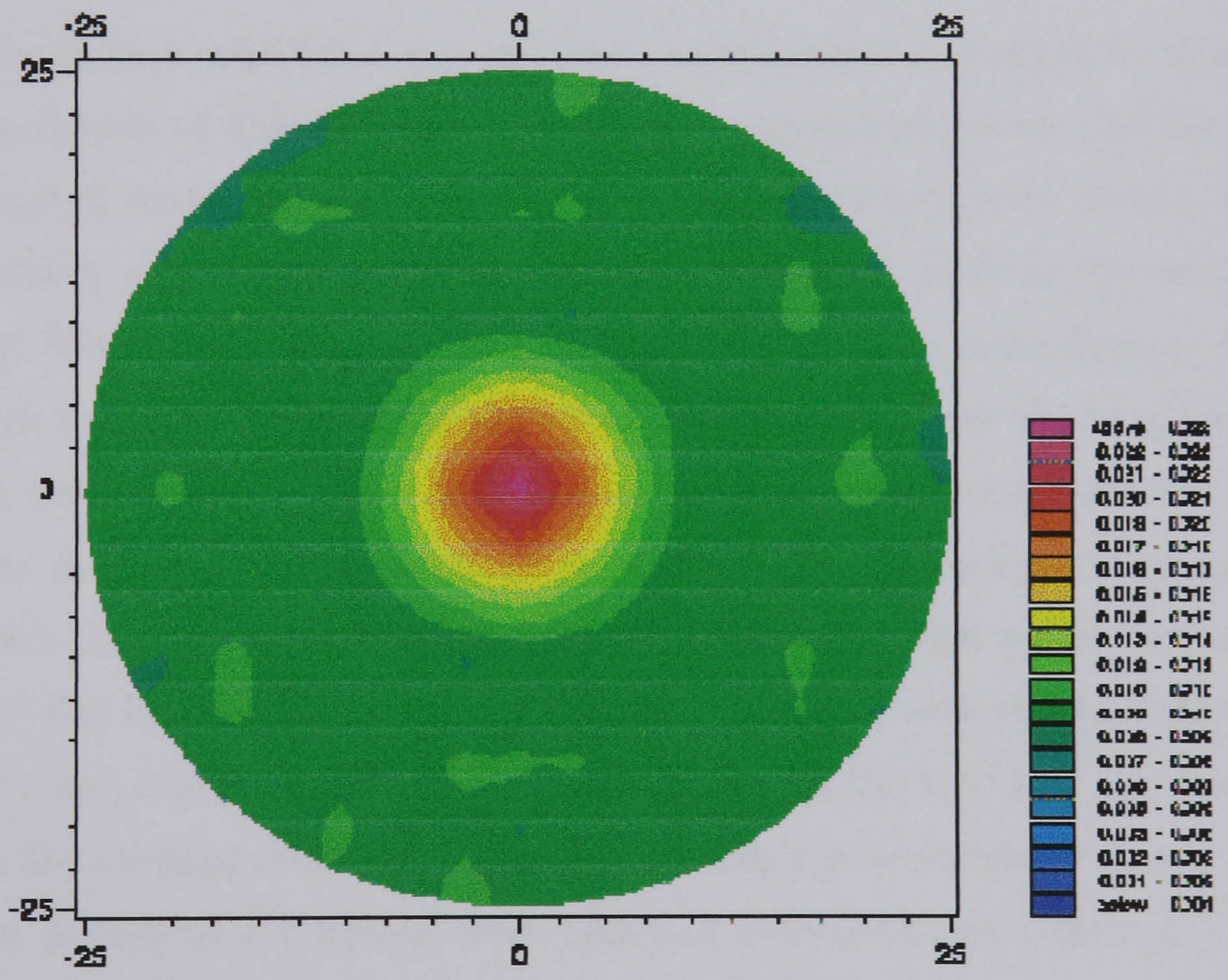


Figure 5.8: Reconstruction of the μ_a image for the problem having a centred absorbing inhomogeneity.

shown in the picture) is between 0.008 and 0.012 mm^{-1}. The absorption values of the small cylindrical regions around the absorbing object (starting from the mixed colours green and yellow to the mixed colours yellow and red) are in the scale between 0.012 and 0.015 mm^{-1}. The coefficients of the regions from this point to the centre of the object, which have the representative colours as starting from the mixed colours yellow and red to the pure red colour, were found to be between 0.015 and 0.02 mm^{-1}. The centre of the object has the colour pink with the absorption values between 0.02 and above 0.023 mm^{-1}. Real values of absorption coefficient for the background and inhomogeneity were as follows: Background: $\mu_a = 0.01$ mm^{-1}, inhomogeneity: $\mu_a = 0.02$ mm^{-1}. This result shows that even in the second iteration the absorbing object is identified successfully by the algorithm and the absorption values of the regions are basically representative of their true values except at the centre of the absorbing object.

The second case considered was another overall cylindrical region containing three absorbing objects of difference sizes. The outer region had double the diameter, 100 mm, compared with before and the diameters of the objects were chosen as: for the first absorbing object (lower left in Figure 5.9) 12 mm, and for the second (lower right) and third (the top) absorbing objects 10 mm. The mesh layout, containing 6326 nodes and 12650 triangular elements, and the locations of the objects can be seen from the Figure 5.9. The background had the same absorption and scattering coefficients as in the first problem given above. The scattering coefficient of three objects were the same as the background and their absorption coefficients were taken as follows: The largest one had $\mu_a = 0.04$ mm^{-1}, the first with the diameter of 10 mm (at the bottom) had $\mu_a = 0.03$ mm^{-1} and the last (at the top) had $\mu_a = 0.02$ mm^{-1}. To obtain the forward solution, a ring of 20 isotropic sources and detectors was used. The mean cosines of all regions were assumed zero (isotropic scattering). The P_3 angular approximation was used for the forward solution. The forward solution took 2.63 cpu minutes on a Dec Alpha 500/250.

Figure 5.10 shows the first and last (10th) iterations of the reconstruction of absorption images at a 32x32 resolution from the FE-P_N forward solution data. The reconstruction process used a cylinder of 100 mm in diameter with the starting value

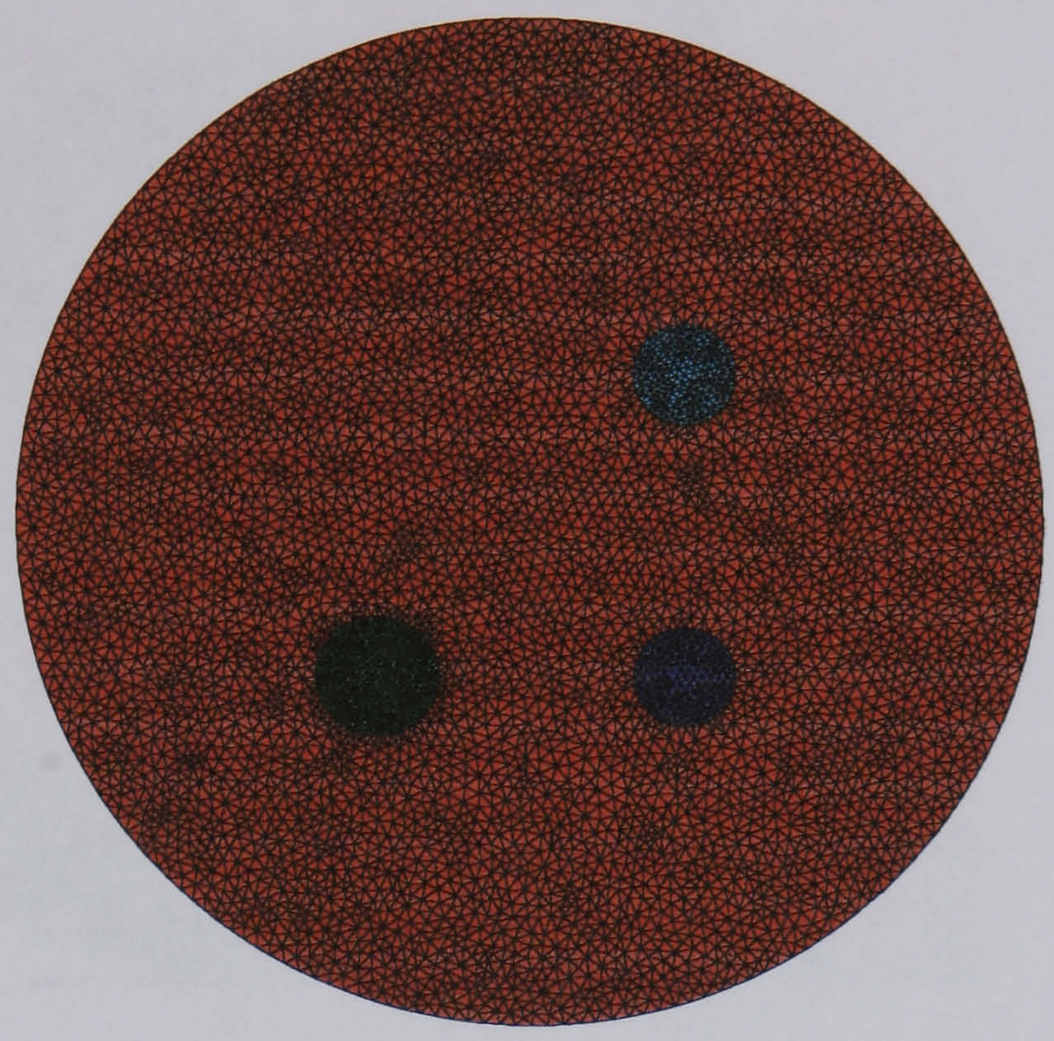
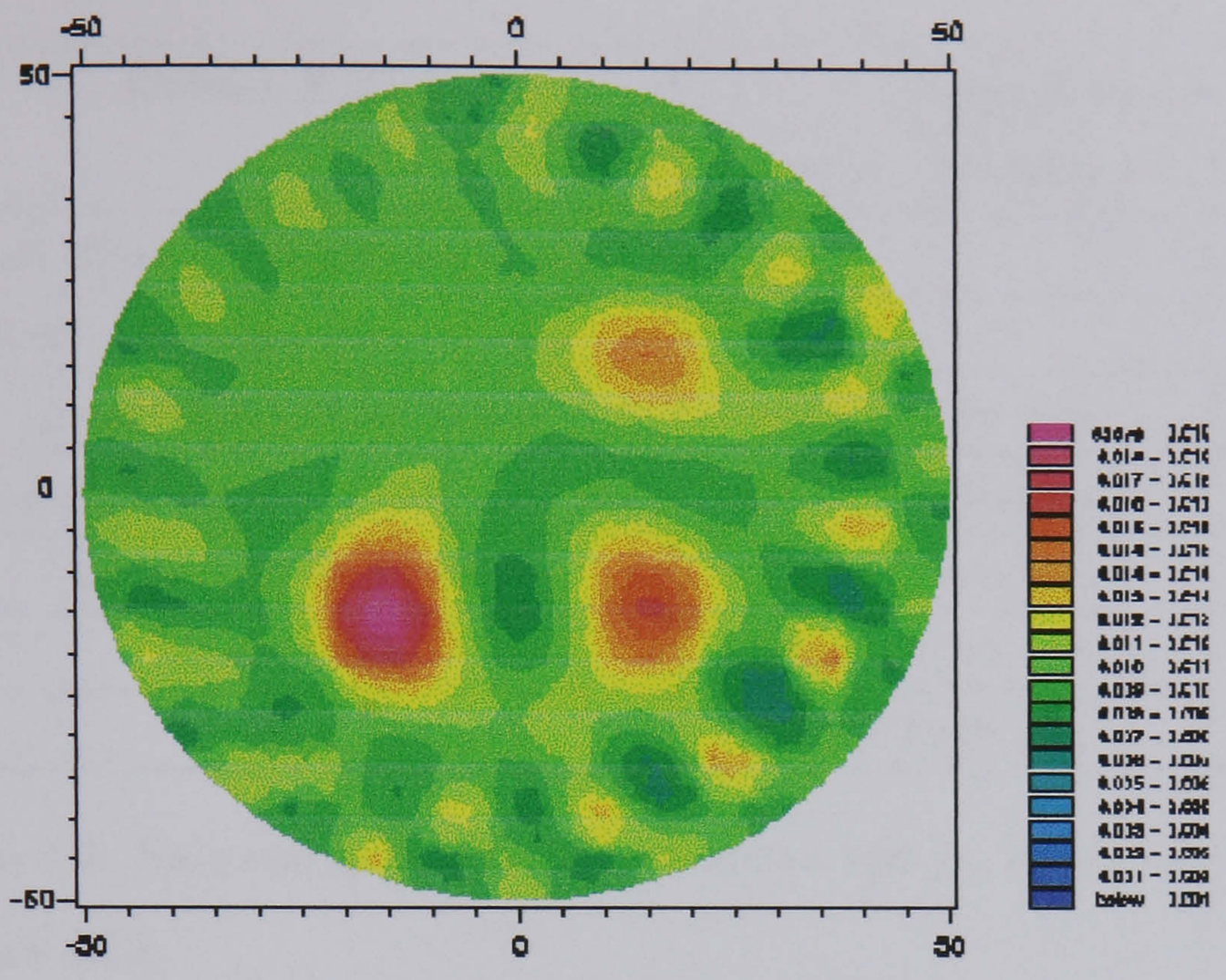


Figure 5.9: Locations of inhomogeneities for FE-P_N forward solution on 2D circular mesh (represents an infinite cylinder phantom).

for μ_a the same as the correct value (0.01 mm^{-1}). The inverse solution mesh consisted of 5138 nodes and 10274 linear triangular elements. The reconstruction results were obtained using the P_3 angular approximation. Ten iterations were performed and the completion of the reconstruction process took approximately 40 cpu minutes on a Dec Alpha 500/250.

It can be seen from the figure that by the first iteration three absorbing objects start to appear. The location and the approximate size of the objects are obtained correctly in both the first and the last (10) iteration step. The colour scales and the corresponding absorption coefficient values obtained with two iterations are given in Table 5.2. The reconstructed absorption value of the background on the first iteration result is remarkably close to the true value but, after ten iterations, the value for the background is overdetermined. Low absorption values are obtained in the first iteration for the inhomogeneities whereas for later iterations somewhat higher values are obtained in comparison to the original. This shows that the reconstruction algorithm tends to localise the inhomogeneities rather than obtain the absolute optical properties. This, however, may not be a big drawback, as contrasts may be sufficient for the expert eye of a clinician.



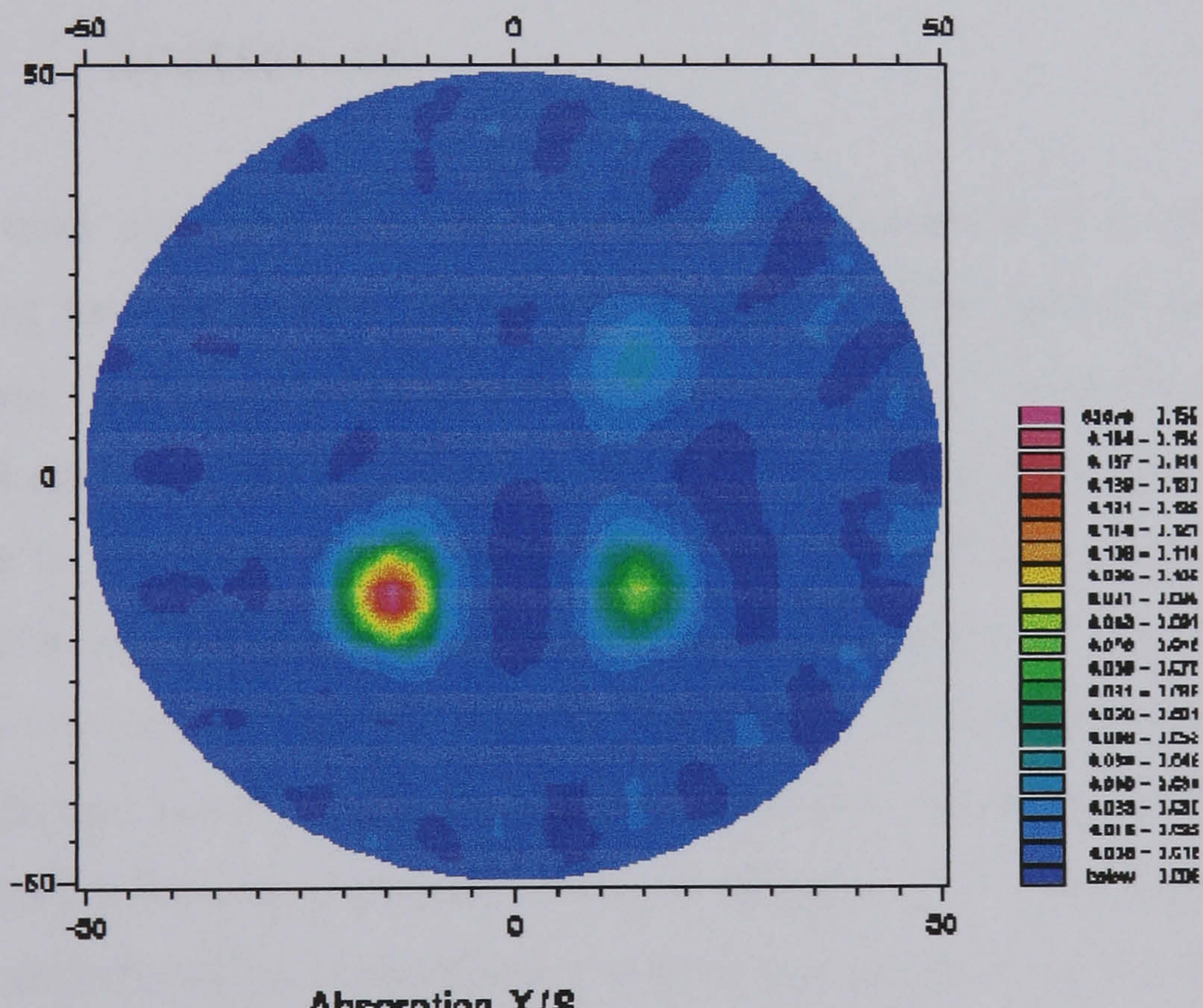


Figure 5.10: Reconstruction of the cylindrical region containing three absorbing objects. The upper illustration shows the result after the first iteration and the lower is for the 10th iteration.

Colour Scales	**Absorption Coefficient Values**	
	Iteration Number: 1	**Iteration Number: 10**
Dark Blue - Dark and Light Blue	—	0.008 - 0.03 mm^{-1}
Dark and Light Blue - Green	—	0.03 - 0.068 mm^{-1}
Green - Green and Yellow	0.008 - 0.012 mm^{-1}	0.068 - 0.099 mm^{-1}
Green and Yellow - Yellow and Red	0.012 - 0.015 mm^{-1}	0.099 - 0.121 mm^{-1}
Yellow and Red - Red	0.015 - 0.018 mm^{-1}	0.121 - 0.144 mm^{-1}
Red - Pink	0.018 - 0.019 mm^{-1}	0.144 - 0.152 mm^{-1}
Pink	above 0.019 mm^{-1}	above 0.152 mm^{-1}

Table 5.2: Side colour scales and reconstructed μ_a values of two illustrations given in Figure 5.10.

5.3.2 Reconstruction Results with Linearly Isotropic (P_1) Scattering

The next case used for the reconstruction consisted of a cylinder of radius 25 mm having two embedded cylindrical absorbers. The optical parameters for the background were $\mu_a = 0.025\ mm^{-1}$ and $\mu_s = 4.00\ mm^{-1}$ and the absorption values of the small cylinders were $\mu_a = 0.5\ mm^{-1}$. The radius of these inhomogeneities were taken equal to 2.5 mm. The problem geometry is illustrated in Figure 5.11. The central coordinates of the inhomogeneities were x=0 mm and y=-16 mm for the green one and x=8 mm and y=-10 mm for the purple. 16 sources and detectors located at 16 equidistant points along the external boundary, as shown in Figure 3.18, were utilised for both solutions. Linearly isotropic scattering, P_1 scattering, was assumed in this case and the value of the mean cosine g was taken to be 0.5 for all three regions. The FE-P_N forward solution was obtained with a mesh containing 10878 linear triangular elements - 5440 nodes and using P_5 angular approximation for approximately 3.7 cpu minutes on a Dec Alpha 500/250.

Figure 5.12 shows the reconstructed absorption coefficient throughout the problem domain for iterations 1 and 2. The mesh used for the optical property representation had 4780 nodes and 9558 triangular elements. Reconstruction of the images was

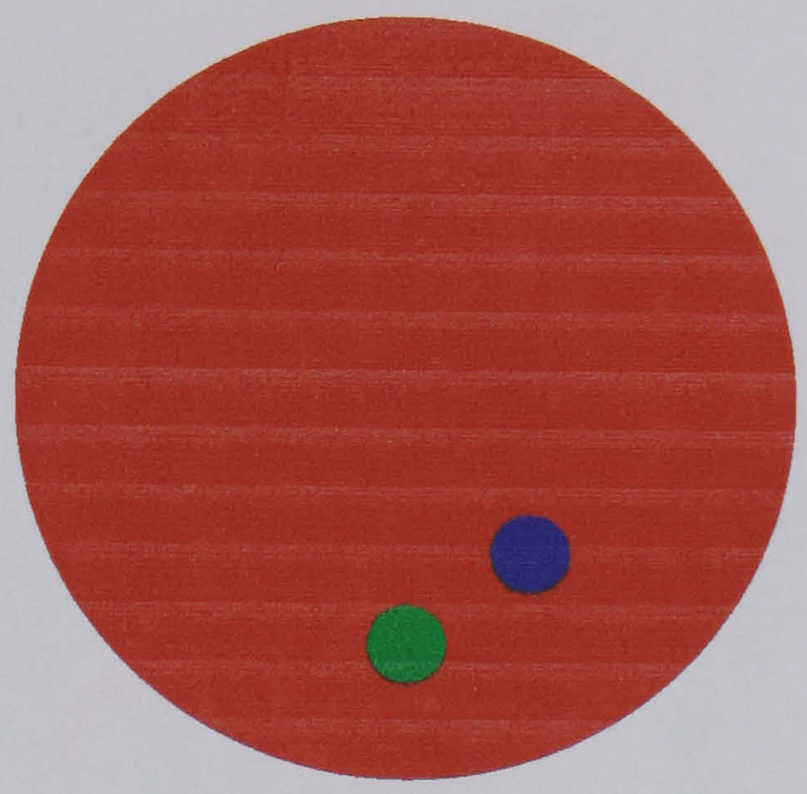


Figure 5.11: The positioning of the objects used for the reconstruction results given in Figure 5.12.

performed on a 32x32 grid using the same number of sources and detectors as in the previous problems. Table 5.3 shows the colour scales and the reconstructed absorption coefficients values for this case. In the first iteration result, the two absorbing objects are not resolved completely and the reconstructed absorption values of the objects are too low in comparison to their real values. In contrast, the second iteration image shows a better resolution for the locations and approximate sizes of the objects but the absorption values obtained are still underestimated for all three regions.

Colour Scales	**Absorption Coefficient Values**	
	Iteration Number: 1	**Iteration Number: 2**
Very Light Blue - Green	—	0.014 - 0.03 mm^{-1}
Green - Green and Yellow	0.02 - 0.03 mm^{-1}	0.03 - 0.041 mm^{-1}
Green and Yellow - Yellow and Red	0.03 - 0.039 mm^{-1}	0.041 - 0.054 mm^{-1}
Yellow and Red - Red	0.039 - 0.047 mm^{-1}	0.054 - 0.061 mm^{-1}
Red - Pink	0.047 - 0.049 mm^{-1}	0.061 - 0.068 mm^{-1}
Pink	above 0.049 mm^{-1}	above 0.068 mm^{-1}

Table 5.3: Colour scale of reconstruction results given in Figure 5.12.

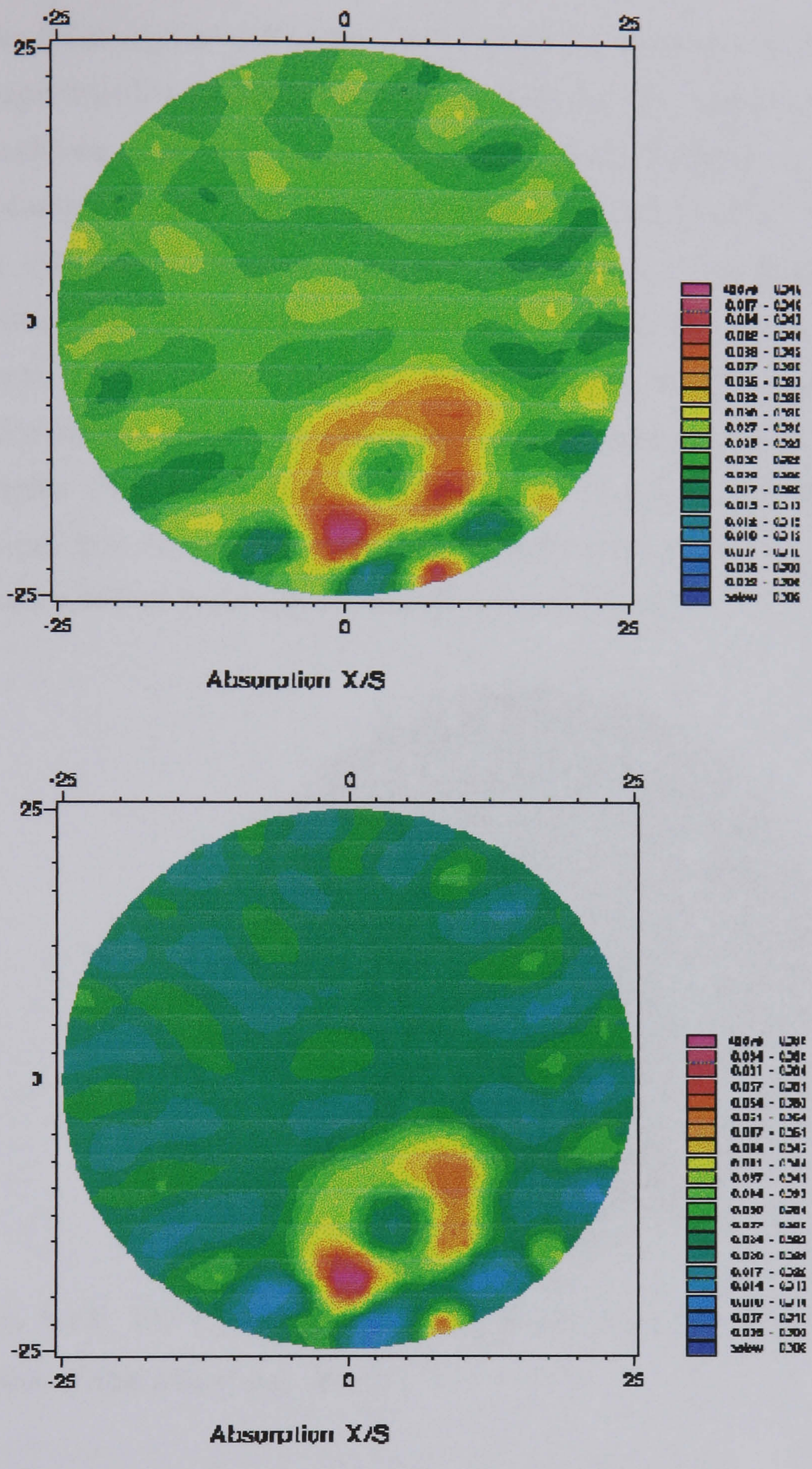


Figure 5.12: First two iterations obtained from the absorption coefficient reconstruction process for the problem given in Figure 5.11.

The following case illustrated in Figure 5.13, was solved before by Schweiger using the experimental phantom described in [17]. In our solution, the numerical phantom is a cylinder of 27 mm radius containing one cylindrical region of 2.5 mm radius. The absorption and scattering properties were (all in mm^{-1}): 0.02 and 3.12 for the outer cylinder; 0.1 and 3.12 for the small region. The central coordinates of the inhomogeneity were x=13.5 mm and y=-2.5 mm. The mean cosine g was taken 0.5 for both regions in both calculations. The steady-state forward calculation used a P_3 angular approximation, and the finite element mesh consisted of 3680 nodes and 7358 triangular elements as shown in Figure 5.13. 16 sources and detectors, located at the same position around the external boundary, were employed to obtain the data. The forward solution took approximately 54 cpu seconds.

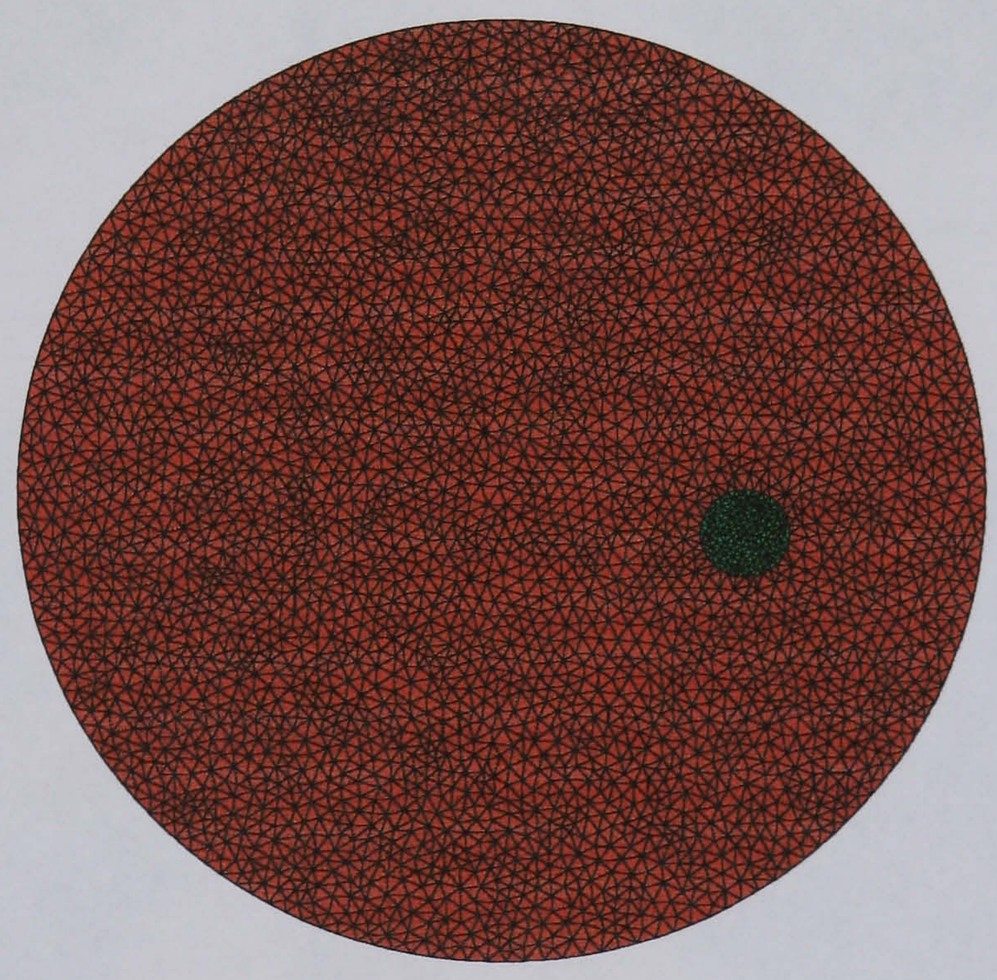


Figure 5.13: 2D circular mesh showing the mesh layout of the problem and the location of the absorbing object.

Figure 5.14 shows 4 iterations of the reconstruction of absorption images using a mesh consisting of 2245 nodes and 4488 triangular elements. A P_3 angular approximation and 32x32 pixel grids were used for reconstruction. Reconstruction time for four iterations was 8.3 cpu minutes on a Dec Alpha 500/250. Table 5.4 gives colours and the corresponding reconstructed μ_a values for Figure 5.14. As it can be seen from

the figure, the location and approximate size of the absorbing object are well detected at the first iteration. But the absorption value obtained by the reconstruction process does not represent the correct value of the object. As the iteration number increases, the absorption coefficient level of the object becomes more representative of its real value.

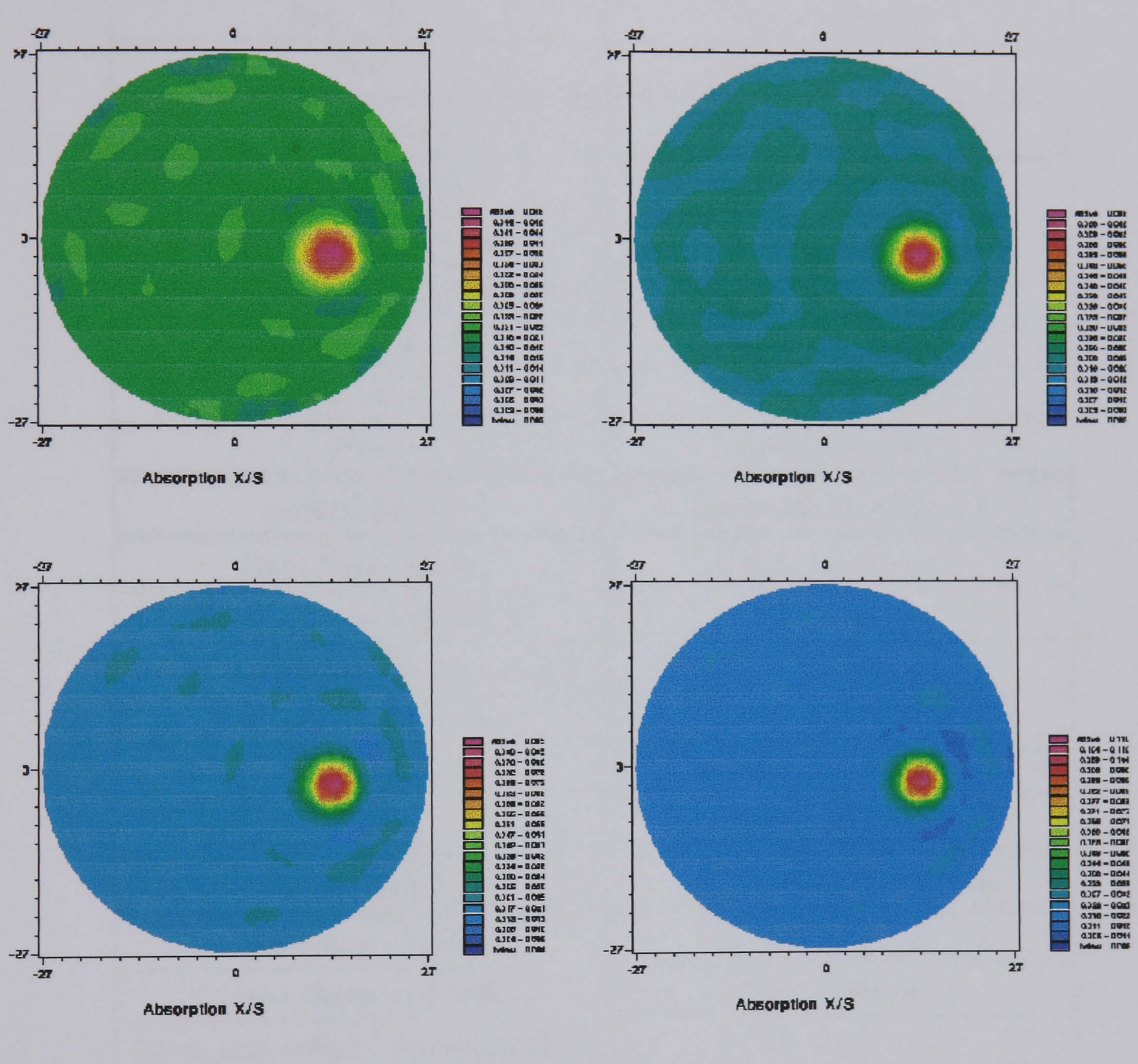


Figure 5.14: Results, for 4 iterations, of the reconstruction of the absorption coefficient image for the problem layout given in figure 5.13.

Colour Scales	**Absorption Coefficient Values**
	Iteration Number: 1
Green - Green and Yellow	0.018 - 0.028 mm^{-1}
Green and Yellow - Yellow and Red	0.028 - 0.039 mm^{-1}
Yellow and Red - Red	0.039 - 0.044 mm^{-1}
Red - Pink	0.044 - 0.046 mm^{-1}
Pink	above 0.046 mm^{-1}
Colour Scales	**Iteration Number: 2**
Light Blue - Green	0.013 - 0.026 mm^{-1}
Green - Green and Yellow	0.026 - 0.039 mm^{-1}
Green and Yellow - Yellow and Red	0.039 - 0.053 mm^{-1}
Yellow and Red - Red	0.053 - 0.059 mm^{-1}
Red - Pink	0.059 - 0.066 mm^{-1}
Pink	above 0.066 mm^{-1}
Colour Scales	**Iteration Number: 3**
Light Blue - Green	0.017 - 0.034 mm^{-1}
Green - Green and Yellow	0.034 - 0.051 mm^{-1}
Green and Yellow - Yellow and Red	0.051 - 0.068 mm^{-1}
Yellow and Red - Red	0.068 - 0.076 mm^{-1}
Red - Pink	0.076 - 0.085 mm^{-1}
Pink	above 0.085 mm^{-1}
Colour Scales	**Iteration Number: 4**
Light Blue - Green	0.022 - 0.038 mm^{-1}
Green - Green and Yellow	0.038 - 0.066 mm^{-1}
Green and Yellow - Yellow and Red	0.066 - 0.088 mm^{-1}
Yellow and Red - Red	0.088 - 0.099 mm^{-1}
Red - Pink	0.099 - 0.11 mm^{-1}
Pink	above 0.11 mm^{-1}

Table 5.4: Side colour scales of 4 iterations given in Figure 5.14.

5.3.3 Reconstruction Results with Highly Anisotropic Scattering

In the following two sections, some preliminary reconstruction results are presented for cylinders having two and three layered outer structures, with different values for μ_a and μ_s. The aim of using those numerical phantoms was to show the capability of the inverse solution model (described in Chapter 4) in reconstructing such layers, with some of the layers are having different scattering anisotropy factors. This represents a significant development for real time imagery as most organs in human body enclose such layers: for example when a tumour is present or for the example of the brain in human head.

Results for Symmetrical Layered Cylinder

The case considered here was a symmetrical layered cylinder (see Figure 5.15) representing in cross section a very simplistic approximation of a human head, with two layers and one inner inhomogeneity. The outer and second layers correspond to the skin/skull and bone, while the inhomogeneity may be correspond to a tumour. The diameter of the model was taken 40 mm. Optical parameters and the values of the anisotropy factor of each layer and the inhomogeneity are listed in Table 5.5. The skin/skull layer has a thickness of 3 mm. The diameter of the inhomogeneity was 4 mm and it was located at the position (x=4.0 mm;y=-5.0 mm). Steady-state forward solution results were obtained with the FE-P_N model using the P_9 angular approximation and a P_9 approximation for the expansion of the scattering kernel to model highly anisotropic scattering. 16 isotropic sources and 16 detectors were employed in both forward and inverse solutions. The FE mesh geometry is illustrated in Figure 5.15. The Legendre expansion coefficients for the scattering kernel were obtained using SAM phase function formula given by equation (2.19) in Chapter 2. 24 coefficients were calculated for the regions with g=0.92 and 18 coefficients for the inhomogeneity with g=0.9. Those coefficients were then truncated by the δ-M method to obtain the desired number of coefficients, 9 in this case, for the forward solution.

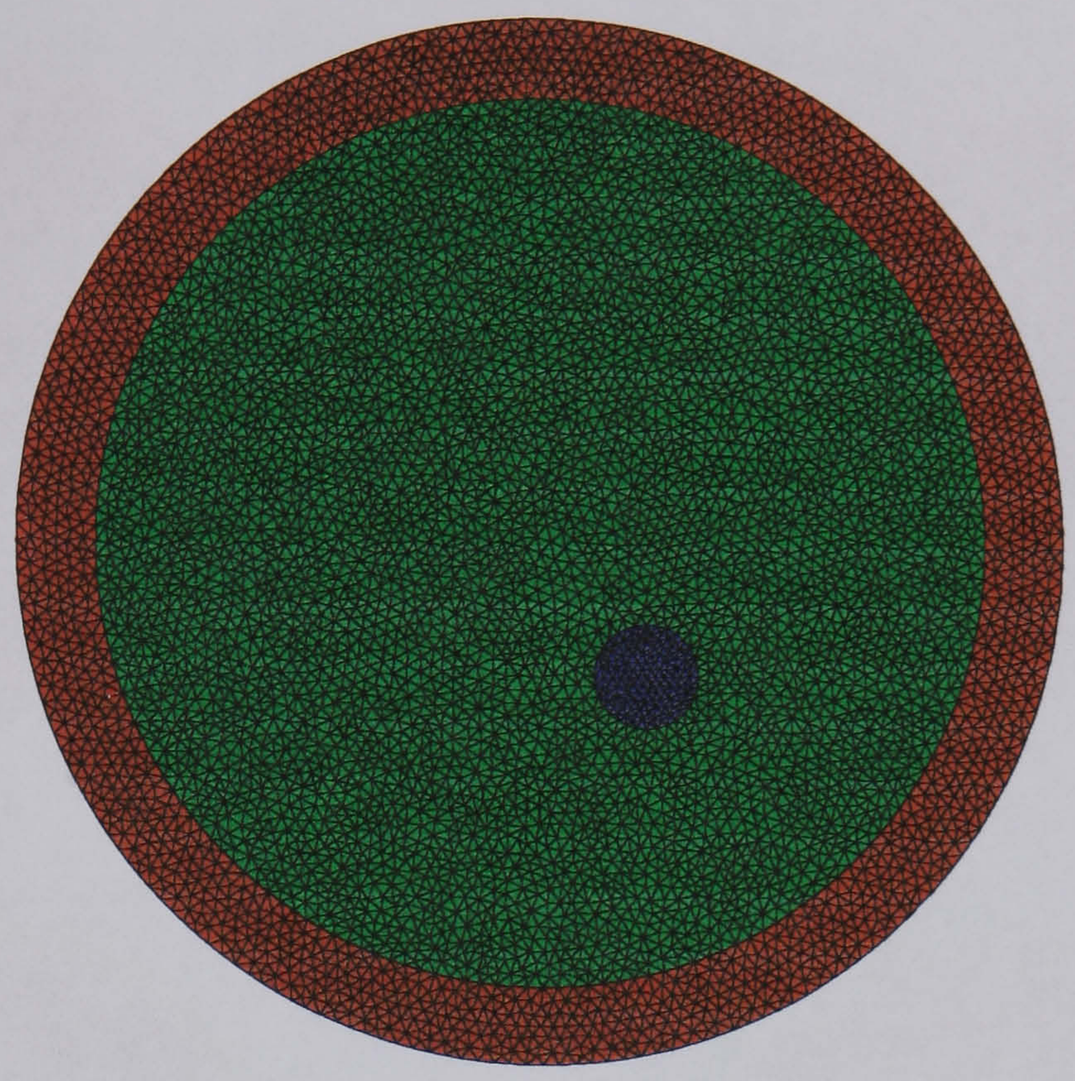


Figure 5.15: The layered FE mesh used to obtain data for the reconstruction algorithm. The number of nodes is 5919 and the number of triangular mesh elements is 11836. The forward solution took approximately 14 cpu minutes on a Dec Alpha 500/250 workstation.

Regions	$\mu_a(\text{mm}^{-1})$	$\mu_s(\text{mm}^{-1})$	$\mu'_s(\text{mm}^{-1})$	g
Skin/skull [150],[17]	0.025	18.75	1.500	0.92
Bone [17]	0.025	25.00	2	0.92
Inhomogeneity [150]	0.1	90.00	9.000	0.9

Table 5.5: Optical parameters for the symmetrical layered cylinder.

A cylindrical mesh consisting of 5142 nodes and 10282 linear triangular elements, together with the optical properties of the skin/skull layer, was employed for the reconstruction. The P_5 angular approximation with a P_5 approximation for the scattering kernel was employed for the inverse solution. Legendre coefficients of the scattering kernel were obtained using the same phase function formula as before, but truncated at 5 to enter 5 coefficients for the solution. Reconstruction of eight images took approximately 32 cpu minutes on a Dec Alpha 500/250 using a 32x32 sized grid.

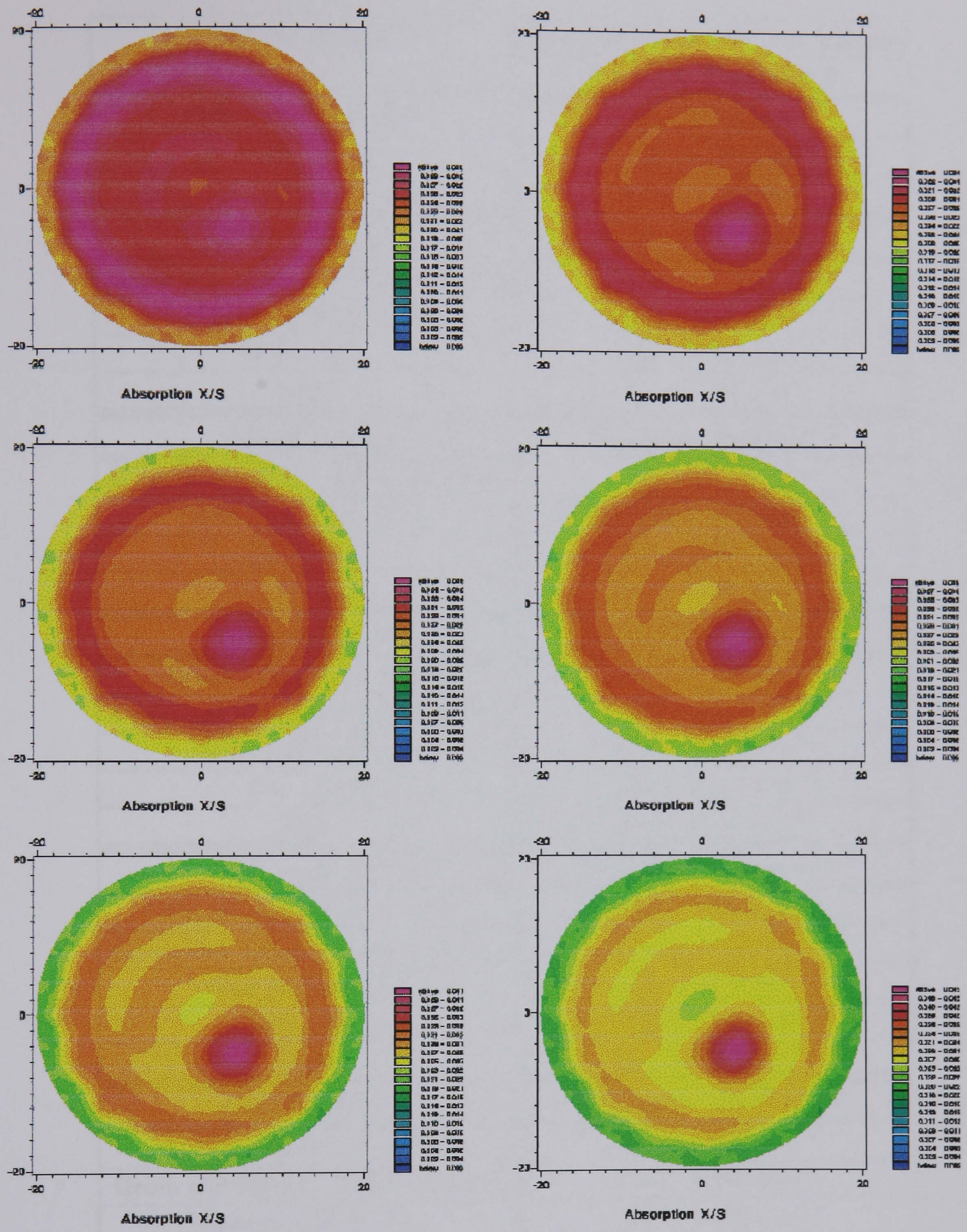


Figure 5.16: Absorption coefficient reconstruction of the symmetrical layered cylinder with embedded object. The images show the results for the iteration numbers 2, 4, 5, 6, 7, and 8 respectively.

Colour Scales	**Absorption Coefficient Values**
	Iteration Number: 2
Yellow and Red - Red	0.021 - 0.029 mm^{-1}
Red - Pink	0.029 - 0.030 mm^{-1}
Pink	above 0.030 mm^{-1}
Colour Scales	**Iteration Number: 4**
Green and Yellow - Yellow and Red	0.020 - 0.027 mm^{-1}
Yellow and Red - Red	0.027 - 0.031 mm^{-1}
Red - Pink	0.031 - 0.034 mm^{-1}
Pink	above 0.034 mm^{-1}
Colour Scales	**Iteration Number: 5**
Green and Yellow - Yellow and Red	0.020 - 0.029 mm^{-1}
Yellow and Red - Red	0.029 - 0.033 mm^{-1}
Red - Pink	0.033 - 0.036 mm^{-1}
Pink	above 0.036 mm^{-1}
Colour Scales	**Iteration Number: 6**
Green - Green and Yellow	0.017 - 0.023 mm^{-1}
Green and Yellow - Yellow and Red	0.023 - 0.031 mm^{-1}
Yellow and Red - Red	0.031 - 0.035 mm^{-1}
Red - Pink	0.035 - 0.039 mm^{-1}
Pink	above 0.039 mm^{-1}
Colour Scales	**Iteration Number: 7**
Green - Green and Yellow	0.017 - 0.025 mm^{-1}
Green and Yellow - Yellow and Red	0.025 - 0.033 mm^{-1}
Yellow and Red - Red	0.033 - 0.037 mm^{-1}
Red - Pink	0.037 - 0.041 mm^{-1}
Pink	above 0.041 mm^{-1}
Colour Scales	**Iteration Number: 8**
Green - Green and Yellow	0.018 - 0.027 mm^{-1}
Green and Yellow - Yellow and Red	0.027 - 0.036 mm^{-1}
Yellow and Red - Red	0.036 - 0.040 mm^{-1}
Red - Pink	0.040 - 0.045 mm^{-1}
Pink	above 0.045 mm^{-1}

Table 5.6: Colour scales and the corresponding μ_a values of 6 iterations given in Figure 5.16.

Figure 5.16 shows the reconstructed absorption coefficient images of the above layered cylinder. In the first picture, the approximate size and location of the tumour are resolved. Improvement in resolving the outer layer was obtained when the iteration number is increased and the layer become more apparent starting from 5th iteration. The colour scales and the reconstructed absorption coefficients values are documented in Table 5.6. It may be observed that the absorption values obtained from the reconstruction process especially for the main region and the outer layer, are close to the true values at all iterations. But, for later iterations, they become much more representative of their true values. For the inhomogeneity representing a tumour, the reconstructed absorption coefficient are too low in all images but, when the iteration number is increased, the values for the inhomogeneity also become closer to the true value.

Results for Asymmetrical Layered Cylinder

The second case resembling the human head layers consisted of a cylinder having a diameter of 40 mm with two layers arranged asymmetrically and the same small cylinder as above representing the tumour. This time three different tissue types, the skin/skull, bone and grey matter, representing the human brain, were chosen to test the reconstruction algorithm. The optical properties and the g values of the regions are given in Table 5.7. The skin/skull layer had a diameter of 40 mm, the bone layer has a diameter of 34 mm and the grey matter layer had a diameter of 30 mm. The tumour had the same location and the size as in the symmetrical problem. A finite element mesh with 5942 nodes and 11882 triangular elements was used for the forward solution. Figure 5.17 shows 2D finite element mesh and also the arrangement of the layers. To obtain the forward solution, the P_9 approximation was utilised for both the angle and scattering kernel. This time 16 non-isotropic (beam) sources and detectors located at 16 equidistant points along the external boundary were used.

Figure 5.18 shows 4 successive iterations of the reconstruction of absorption coefficient images. A cylindrical region with a mesh geometry consisting of 5142 nodes and 10282 triangular elements was used for the solution of inverse problem. The orig-

Regions	$\mu_a(\text{mm}^{-1})$	$\mu_s(\text{mm}^{-1})$	$\mu'_s(\text{mm}^{-1})$	g
Skin/skull [17]	0.022	12.50	1.00	0.92
Bone [17]	0.025	20.00	2.00	0.9
Grey matter [17]	0.04	5.50	2.00	0.9
Inhomogeneity [150]	0.1	90.00	9.00	0.9

Table 5.7: Optical parameters used in reconstruction for the asymmetrical layered cylinder.

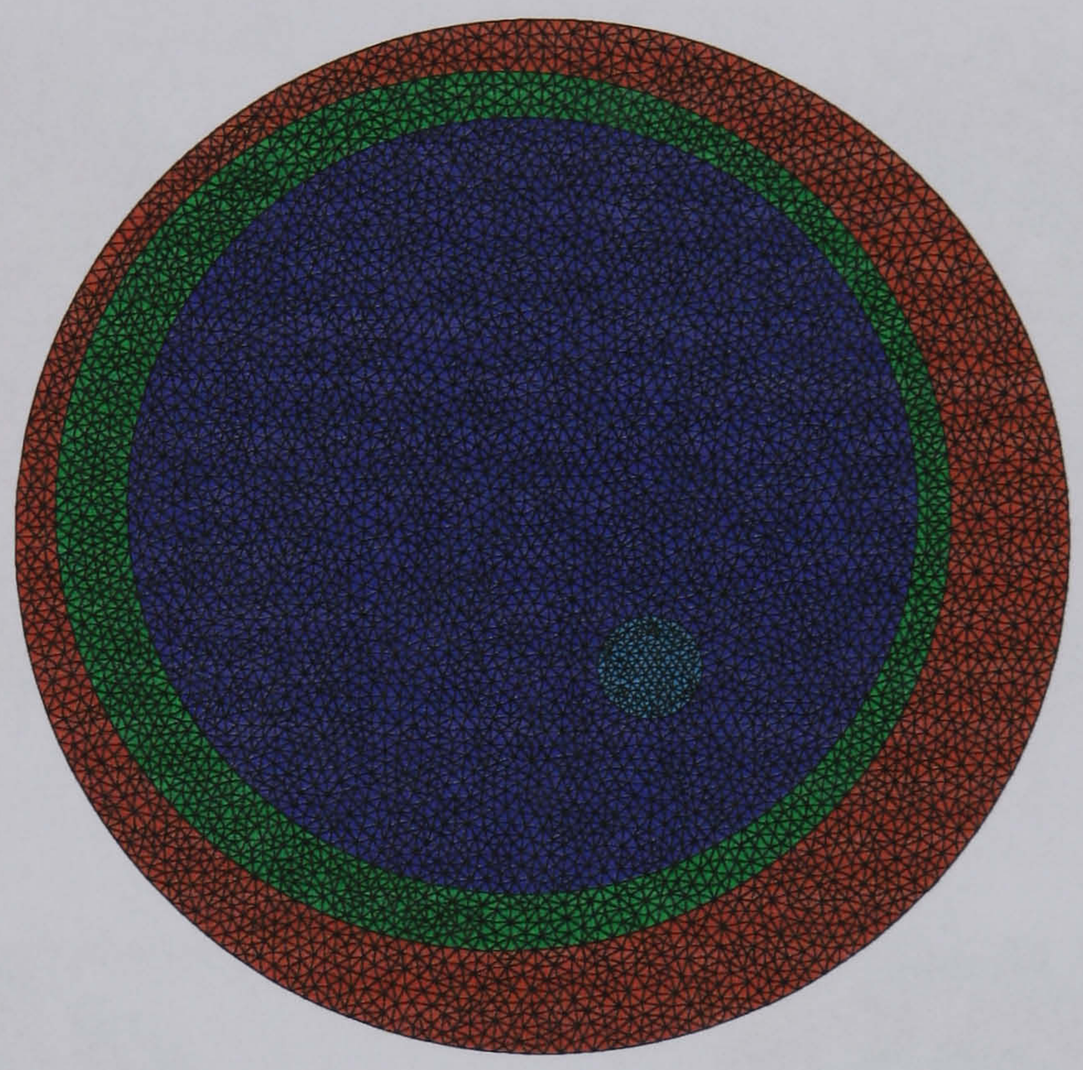


Figure 5.17: Mesh and layers/embedded object layout used for the solution of the asymmetrical layered problem.

inal complete distribution of parameters of the skin/skull layer were taken for this medium. Reconstruction was done on a 32x32 x-y grid using a P_5 angular approximation. 5 coefficients truncated using the δ-M method were entered for the scattering kernel. Seven iterations with 16 non-isotropic sources took approximately 70 cpu minutes on a Dec Alpha 500/250 workstation.

As can be seen from the results, there is an appearance of layer artifacts in the centre of the cylinder, especially in the first and second iterations. After around two

iterations the inhomogeneity begins to resolve from the background layer, but the artifacts still remain in the later iterations. The two outer layers are clearly identified from the first iteration. Although the reconstruction does not show any substantial alterations after the second iteration, the reconstructed absorption values are changing in each iteration. The μ_a values obtained with the reconstruction algorithm are given in Table 5.7. The reconstructed values for the first two layers are very close to the real values in the last iteration but the values for the rest of the regions are not representative of their true values.

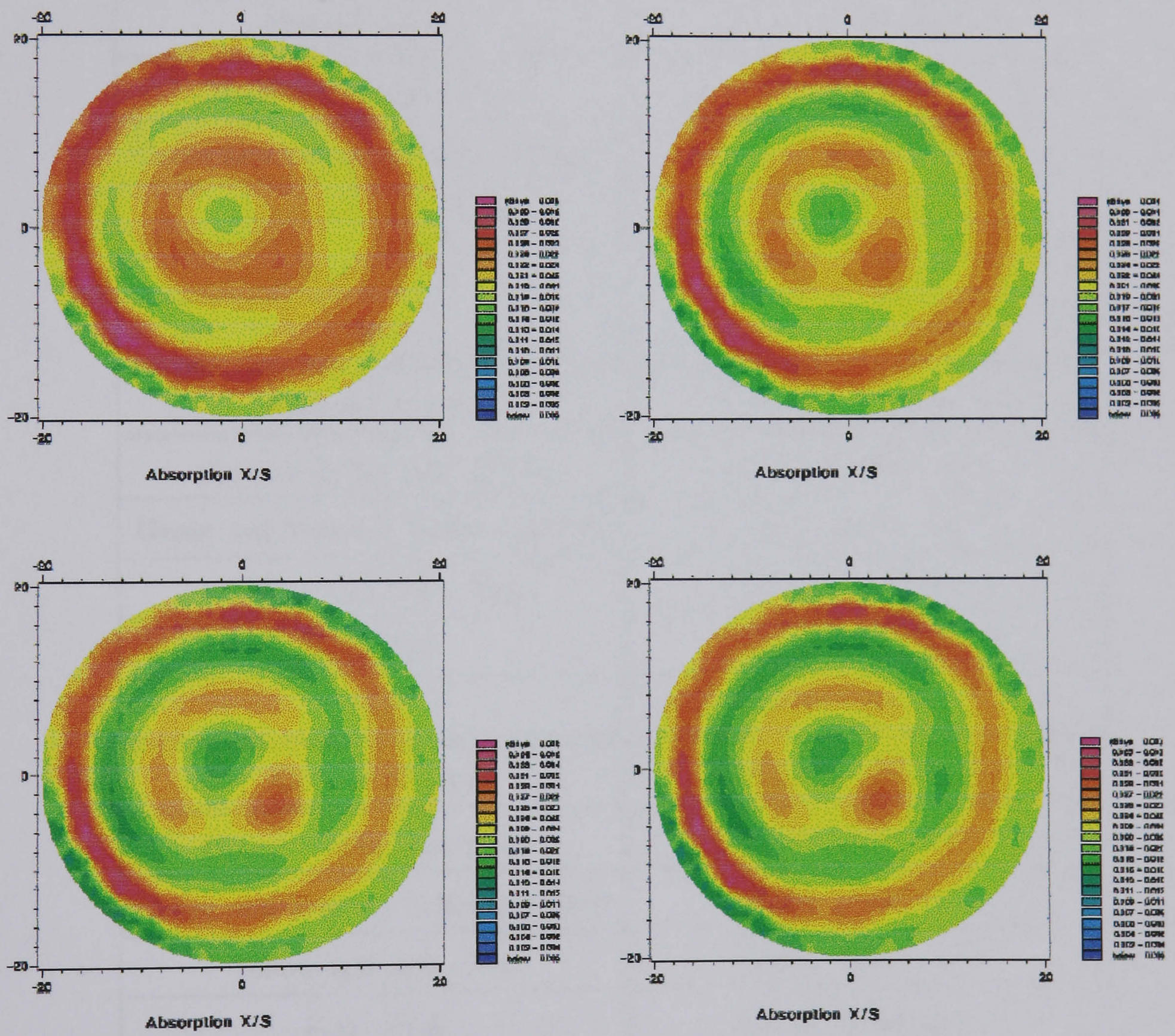


Figure 5.18: Absorption coefficient reconstruction results for the asymmetrical layered cylinder for four iterations. The first three images show the results of the first three iterations and the last image is the result of the 7th iteration. The bounding scales give dimensions in mm.

Colour Scales	**Absorption Coefficient Values**
	Iteration Number: 1
Green - Green and Yellow	0.013 - 0.019 mm^{-1}
Green and Yellow - Yellow and Red	0.019 - 0.026 mm^{-1}
Yellow and Red - Red	0.026 - 0.029 mm^{-1}
Red - Pink	0.029 - 0.032 mm^{-1}
Pink	above 0.032 mm^{-1}
Colour Scales	**Iteration Number: 2**
Green - Green and Yellow	0.014 - 0.021 mm^{-1}
Green and Yellow - Yellow and Red	0.021 - 0.028 mm^{-1}
Yellow and Red - Red	0.028 - 0.031 mm^{-1}
Red - Pink	0.031 - 0.034 mm^{-1}
Pink	above 0.034 mm^{-1}
Colour Scales	**Iteration Number: 3**
Green - Green and Yellow	0.013 - 0.022 mm^{-1}
Green and Yellow - Yellow and Red	0.022 - 0.029 mm^{-1}
Yellow and Red - Red	0.029 - 0.033 mm^{-1}
Red - Pink	0.033 - 0.036 mm^{-1}
Pink	above 0.036 mm^{-1}
Colour Scales	**Iteration Number: 7**
Green - Green and Yellow	0.013 - 0.022 mm^{-1}
Green and Yellow - Yellow and Red	0.022 - 0.029 mm^{-1}
Yellow and Red - Red	0.029 - 0.033 mm^{-1}
Red - Pink	0.033 - 0.037 mm^{-1}
Pink	above 0.037 mm^{-1}

Table 5.8: Side colour scales of Figure 5.18.

5.4 Summary

In this chapter, reconstructed images of absorption coefficient for a series of cases were presented in order to evaluate the capabilities of the reconstruction algorithm to detect the embedded and outer layered inhomogeneities. Simulated data generated by the MC program and the data obtained from the FE-P_N forward model were fed into the algorithm to reconstruct images of the various test problems. To test the algorithm in more realistic situations, two layered circular cases representing a simplistic approximation of human head layers having different scattering anisotropy factors were evaluated.

The results presented in this chapter indicated that a significant amount of useful information can be obtained from reconstructions based on the MC and FE-P_N forward data. Importantly, it shows that the transport theory-based reconstruction algorithm is capable of detecting the location, the size and the shape of the inhomogeneities within a target media. For the most part, the correct optical property values for the background were recovered. For the inhomogeneities although the image contrast is quite high, the correct parameter distribution cannot be obtained and lower or higher values (in comparison to the true values), were recovered with the current reconstruction method. This merits future investigation.

Chapter 6

Discussion of Results and Conclusions

This chapter reviews the research performed using the Finite Element-Spherical Harmonics method for the solution of forward and inverse photon propagation problems and discusses the results obtained. The conclusions from this research and suggestions for future applications are also included.

6.1 General Review of the Thesis

The aim of the work described in this thesis was to apply the FE-P_N radiation transport method to photon propagation problems in the context of optical tomography. For this purpose, the existing radiation transport code EVENT, which was developed originally for studies involving neutron (neutral particle) transport in nuclear systems, was adapted to photon tomography in tissues. The main contribution of the present study was to apply the transport theory with high-orders of angular approximation for modelling photon angular dependence and highly forward-peaked scattering phase functions in the solution of both forward and inverse photon transport problems. Previously only diffusion theory and Monte Carlo methods had been

applied to these problems.

Two classes of problems involving photon transport have been studied in this thesis. The first concerned the solution of forward problems, which may be defined as the prediction of the distribution of photons inside a medium by using the known optical properties. As a starting point for the solution of the forward photon transport problem, the Boltzmann transport equation was written in its linearised one-speed form. The scattering cross section was expanded in terms of Legendre polynomials to include anisotropic scattering. The second-order, even-parity form of the Boltzmann transport equation was derived and the K^+ variational principle of Ackroyd [140] was used to solve it. In this principle, a quadratic functional is defined and minimised by the application of the Ritz procedure. As a result, a set of simultaneous linear equations were obtained and solved by iterative methods. The FE-P_N approach used in this work is very similar to the Ritz numerical solution procedure differing only in choice of trial functions. An expansion of spherical harmonic functions in angle and finite elements in space was employed as the trial function to approximate the even-parity flux.

The second class of problems concerned the solution of inverse problems for the reconstruction of optical properties for selected idealised test cases. The inverse problem can be stated as the estimation of the optical properties of a medium, through which the particles have propagated, from a given set of measurements and the limited set of parameters describing the medium. In this thesis, a new model called the Reference Cross Section Model (RCSM)[190], which employs the one-speed Boltzmann transport equation directly, without making any simplification in the physical formulation, was used to solve the inverse problem. The unknown (real) and the known (reference) media were chosen and the Boltzmann transport equation was written for both media with the appropriate boundary conditions. The difference between these two equation sets led to a system of integral equations formed the non-reciprocal integral equation or the inverse Boltzmann equation. By applying this approach, the non-linear problem is reduced to one which is linear with respect to the difference between the real and reference medium. A variational formulation consistent with the non-reciprocal integral equation system was necessary for the implementation of

the numerical solution through the FE-P_N method. The resulting set of simultaneous equations were solved iteratively using a Newton-secant linearisation method for the recovery of the real cross section parameters followed by the application of a POCS (projection onto convex set).

6.2 Implementation of Anisotropic Scattering

High orders of angular approximation for modelling anisotropic scattering phase functions were investigated. The inclusion of anisotropic photon propagation is especially important in optical tomographic studies because of the highly forward scattering nature of biological tissues [17],[86].

The majority of researchers in this aspect of biomedical optical modelling have adopted the Henyey-Greenstein (H-G) phase function formulae due probably its simplicity in describing the average cosine of the scattering angle, which is the only parameter in the formula [122]. A more accurate phase function may be derived from Mie theory [194]. The H-G's formulae has shortcomings, the most serious being that it shows significant discrepancies compared with Mie theory, especially in the forward-peaked range (g>0.8). On the other hand, for the application of Mie theory, a detailed knowledge of the medium (such as the refractive index and radius of the spherical scatterers, the refractive index of the medium and the wavelength of the electromagnetic radiation incident to the medium) is necessary. The existence of a large number of randomly distributed scatterers and absorbers inside biomedical media makes, therefore, the use of Mie theory very complicated and impractical [194].

More recently, a new phase function that demonstrates much better agreement with Mie theory than H-G's phase function has been proposed [122]. A simplified form of this phase function formulae (called the Simplified Approximate Mie (SAM) scattering phase function), which depends only one variable, the mean cosine of the scattering angle g, has been mostly employed throughout this study for modelling scattering anisotropy.

A large number of Legendre expansion coefficients need to be calculated due to the fact that highly forward-peaked phase function cannot be represented by polynomials of low degree. For example, if an anisotropy factor of g=0.9 is assumed, over 80 expansion coefficients for the H-G phase function [195] and 18 coefficients for the SAM phase function are necessary to describe the phase function. The use of many Legendre orders can consume much computer time and slows the convergence of the method in question. In order to remedy this problem, Wiscombe's Delta-M (δ-M) approximation [196] has been employed in this work to truncate the phase function at a desired number of orders.

A FORTRAN program named Phasefun was developed to determine Legendre polynomial coefficients for expansion of three phase function formulas, Mie, H-G and SAM scattering phase function. The program Phasefun works in the following order: Firstly, the phase function is expanded in a series of Legendre polynomials, then the resulting integral for each coefficient is numerically calculated using Gauss-Legendre Quadrature. The δ-M method is then applied to the calculated coefficients to obtain the truncated values.

6.3 Forward Solution Results

While most optical tomographic modelling studies in the literature are devoted to modelling using diffusion theory, it is known that the applicability of this theory is limited and, in certain cases, invalid [61],[75]. Attempts have been made throughout Chapter 3 to demonstrate the validity and capabilities of the FE-P_N forward solution model.

6.3.1 Time-dependence

Firstly, two simple infinite cylindrical problems; homogeneous and inhomogeneous; were considered. Time-dependent P_N solutions were calculated at the detector lo-

cated diametrically opposite to the source for three absorption coefficients of increasing magnitude; zero, 0.1 and 0.2. For the homogeneous problem, although a good agreement among the P_N solutions and diffusion was obtained for non-absorbing case, maximum differences of $\sim$ 27% and $\sim$ 58% were found between P_7 and diffusion results when the absorption coefficients of 0.1 mm^{-1} and 0.2 mm^{-1} were incorporated into the non-absorbing cylinder. Similar observations have also been made for the inhomogeneous problem, but the discrepancies between P_7 and diffusion solutions were more apparent. For example, the difference was 63% for the inhomogeneous case with an absorption coefficient of 0.2 mm^{-1}.

Secondly, an independent Monte Carlo (MC) model has been used to confirm the P_N results. The radii of cases were kept smaller (between 6 and 10 mm) in order to reduce the calculation time for the MC program. It is shown that MC and P_N transport solutions are in good agreement in all cases. For the inhomogeneous, isotropic problem with three small inhomogeneities, a high degree of agreement with MC result and the FE-P_9 was obtained. The FE-P_N method is about 8 times faster than MC program when 5.0×10^9 source photons were sampled using a Dec Alpha 500/250 workstation. During these studies, the limitation of diffusion theory was highlighted in the case of the non-absorbing homogeneous cylinder. This was considered to be due to the closeness of the source and detector locations. The optical distance between source and detector was small and therefore the photons did not have time to undergo a large number of diffuse scattering events.

6.3.2 Steady-state

In this section, the limits of the diffusion approximation were analysed in relation to four different parameters by solving the steady-state form of the Boltzmann transport equation. Simple homogeneous, and various large and optically dense inhomogeneous media were chosen to simulate realistic geometries.

Influence of (μ_a/μ'_s)

It is well known that the diffusion approximation is only valid in scatter-dominated regions (and also remote from boundaries and strong-absorbers), which may be expressed as $\mu_a/\mu'_s \ll 1$. In this part of the research, a series of calculations using FE-P_N method were performed in order to show how and when diffusion theory fails to describe the propagation of photons in the case where μ_a/μ'_s approaches 1.

Diffusion and transport (with a P_{25} angular approximation) solutions were obtained for a homogeneous slab with an isotropic plane source. The reduced scattering coefficient was taken equal to 10 mm^{-1} (g=0) and vacuum boundary condition was applied to the other side of the slab. The absorption coefficient was varied from μ_a=0.1 mm^{-1} to μ_a=5.0 mm^{-1} to yield ratios of μ_a/μ'_s from 1/100 to 1/2. It was demonstrated that, when the absorption coefficient was very small (μ_a=0.1 mm^{-1}) in comparison to the reduced scattering coefficient, diffusion theory and transport theory yielded closely similar results. Diffusion theory, however, underestimated the photon flux even for μ_a=1.0 mm^{-1} (μ_a/μ'_s=1/10) and the difference between two approximations increased with increasing distance from the source.

Secondly, diffusion and transport theory results were compared to investigate again the effect of the ratio μ_a/μ'_s for a two-dimensional (infinite prismatic) inhomogeneous 100×100 mm box enclosing a cylindrical inhomogeneity of 20 mm in diameter located at the centre. This case was chosen in order to approximate a situation commonly encountered in, for example, blood vessels, hematoma (blood-filled region in the brain), organs with a high blood perfusion (such as liver), or a trauma situation where bleeding inside the brain occurs. As blood has an absorption coefficient that is comparable to the reduced scattering coefficient in the near-infrared wavelength region [151], diffusion calculations were expected to disagree with the transport calculations. The scattering coefficient was the same throughout the medium (g=0 and μ_s=μ'_s=1.0 mm^{-1}). Two calculations employed two different absorption values for the cylindrical inhomogeneity. In the first, a small absorption coefficient (in comparison to the reduced scattering coefficient, μ_a=0.1 mm^{-1}, μ_a/μ'_s=1/10) was employed inside the inhomogeneity, and in the second, the absorption of the cylinder was taken equal to

the reduced scattering coefficient (μ_a/μ'_s=1).

The results demonstrated that, for the first calculation, transport and diffusion results agreed well throughout the medium. However, when the absorption value of the cylinder was increased to equal μ'_s, large differences between the two approximations were observed inside the inhomogeneity; outside, the two theories agreed well. As was found earlier for the homogeneous media, diffusion theory again underestimated the photon flux by more than two orders of magnitude when the absorption equalled the reduced scattering coefficient. It can be concluded therefore that, in highly absorbing media of relevance to photon transport, diffusion theory overestimates the effect of strongly absorbing inhomogeneities.

Influence of g

The influence of high g-values on photon transport in tissues was investigated by comparing photon transport calculations in two 1D slab geometry media with the same reduced scattering coefficients, $\mu'_s=(1\text{-}g)\mu_s$, but different g-values. Because, in diffusion theory, only the parameter μ'_s appears but not g, employing diffusion theory in all media having the same μ'_s produces the same results. However, it was shown that this was not case when transport calculations were performed.

Photon flux distributions for media with high g-value and media with zero g-value were calculated for various values of the absorption coefficient and the ratio of them was compared. Two different scattering phase function formulas, H-G and SAM, were employed to model anisotropic scattering in the media with high g-value. Generally, it has been found that, for small values of absorption coefficient (in comparison to the reduced scattering coefficient), when diffusion approximation is valid, small difference between two media was observed. However, in the cases where the diffusion approximation is less applicable (with large absorption values), the choice of g becomes important. The larger g-value led to an increase in the photon flux distributions around 0.5-1 mfp from the source and a decrease with an increasing distance (around 4-6 mfp) from the source . For the comparison of the phase function formulas employed

it was observed that they both gave nearly the same results when the absorption coefficient had small values. But, when absorption was increased, higher flux values near to the source and bigger decreases further away were obtained with the SAM than H-G phase function. The use of SAM produces significantly large differences in the ratio of the photon distributions for cases where diffusion approximation does not hold in the medium.

Clear Regions with Low μ_a and μ'_s

Differences between diffusion and transport modelling were next examined for regions with very low-absorption and low-scattering coefficients. These regions are encountered within the body, for example, in the butterfly-like ventricles of the brain (located at the centre and filled with cerebrospinal fluid-CSF) and in the subarachnoid space, a layer of CSF, that forms a boundary between the skull and the brain. Influence of these void-like structures and of boundaries between these regions and the surrounding medium on the propagation of light were investigated in order to explore the failure of the diffusion approximation. The following simplified geometries were considered in both investigations: The first had a small cylindrical inhomogeneity centred a prismatic box and the second a 120×120 mm prism enclosing a small square prism of 40×40 mm located at the centre. The central regions in both geometries were assigned lower absorption and scattering coefficients than the surrounding medium and the coefficients were chosen in order to assure that the diffusion approximation held everywhere in the medium.

Photon flux distributions were calculated, for both geometries, with diffusion approximation and transport theory (with a P_{25} angular approximation). Two different comparisons were made using the results. Firstly, the ratio of the photon flux distributions (Diffusion/Transport) were compared. It was observed that, while diffusion theory was applicable everywhere, significant differences between two theories occurred near the boundaries of the inhomogeneities, where the optical properties changed dramatically. Diffusion theory failed to represent angular distributions of photons leaking from the surfaces of inhomogeneities. Secondly, the same results

discussed above were explored in order to study the spatial distribution of photon flux inside the void-like regions. In both configurations, the diffusion modelling resulted in almost constant photon flux distribution inside the void-like regions, while attenuation of the photon flux was predicted with transport theory. Because of geometrical effects, the flux should be attenuated even in void-like regions [153] and it was demonstrated that only transport theory can treat these structures.

Absorption- and Scattering-free Layers

As mentioned earlier, a void-like layer surrounds the brain. The effect of this thin CSF layer between the brain and skull was modelled using a simplified geometry. Inside a 100×100 mm square prism, a 4 mm thick box was taken as the void-like structure, which surrounded an 76×76 mm inner square prism. Diffusion and transport (with a P_{25} angular approximation) solutions were obtained using this geometry. Diffusion theory predicted channelling of photons within the low-absorbing and low-scattering layer, whereas the use of transport theory did not result in such channelling. In addition, a spatial reduction of the photon flux was only suggested by transport theory, within this void-like layer, to be expected due to the geometrical attenuation of photons, and which was not represented by diffusion theory.

The limits of the diffusion approximation, when applied to photon propagation in homogeneous and heterogeneous simulated biomedical media, were demonstrated and the results have also shown the necessity of employing transport theory in order to obtain relatively accurate solutions to the propagation of photons in large, optically dense and complex structured organs of the human body, such as the brain.

6.4 Inverse Solution Results

The intention here was to evaluate the performance and ability of an FE-P_N based reconstruction algorithm to detect inhomogeneities. Two different set of data generated by MC and by FE-P_N forward models were employed as input to the algorithm

for the recovery of the absorption coefficient.

To demonstrate reconstruction with data derived from an independent MC model, Laplace-transformed MC results were pre-calculated for two simple inhomogeneous cases and fed to the algorithm. One had a centred inhomogeneity and the other consisted of three small cylindrical regions. In the first case, although the centred inhomogeneity was localised even in the first iteration and became more apparent in the later iterations, the recovered absorption value of the inhomogeneity was not representative of its true value. In the second case, only two among the three small cylinders were significantly detected at the last iteration. This inhomogeneity had an absorption coefficient close to that of the reference medium. In this solution again, the true values of the absorption coefficient of two cylinders were not obtained. In general, the choice of the Laplace transform parameter s, statistical errors in the MC calculations and the choice of initial parameter distribution used in the reconstruction algorithm will influence image quality.

The MC program used in this work had a restriction that phase function values of only one g value could be entered for all regions and computation times were lengthly. As a variety of demanding large and optically dense cases having different angular approximation for the scattering kernel were considered in the second series of inverse calculations, data were obtained from FE-P_N forward modelling. The range of cases were chosen from simple geometries and material properties relevant to complex layered geometries representing human head in order to test further the performance and capabilities of the reconstruction algorithm.

In general, reconstruction studies have demonstrated that, using simulated data, the existing reconstruction algorithm can produce qualitatively correct results resolving the location, the size and the shape of inhomogeneities or layers. However, it was not possible, in majority of cases (except for the symmetrical layered problem), to obtain the correct absorption coefficient values for both the background and inhomogeneities/layers with the current reconstruction approach. However, this is not necessarily a serious drawback, as clinicians are often looking for contrasts which may indicate abnormalities. As stated earlier, initial parameter setting and the number

of sources and detectors chosen may have played a role in convergence and image quality.

6.5 Recommendations for Future Work

Various aspects need to be addressed and researched before the FE-P_N method can be used in real applications. We give here suggestions for further studies:

- In the present study, simple geometries were employed to show the differences between diffusion and transport theory modelling and for reconstruction of absorption coefficient images. For future studies, more complex and realistic geometries, e.g. the outline of a human head obtained from an NMR scan, should be considered in repeating forward calculations and in testing the reconstruction algorithm in more realistic situations. As has been indicated in the literature, an optical property map of the brain can be obtained by assigning different optical properties to different regions that appear in NMR images. This map could be used as an input to the FE-P_N radiation transport code to perform the calculations.

- The MC program used in this work to validate the FE-P_N method (by generating synthetic data) had a restriction that phase function values of only one g value could be entered. The program should be developed further in order to be able to model regions having differing g values. This is especially important in validating the FE-P_N transport method in realistic cases.

- Only one- and two-dimensional problems were modelled in this study of the solutions of forward and inverse problems. However, the FE-P_N model is capable of solving three-dimensional problems. 3D simulations should be considered as a next step in the research.

- Adaptive remeshing as refinement (adding new nodes to the current mesh in certain regions to enhance the quality of the solution) and coarsening (deleting nodes to remedy excessive resolution in other regions) of the mesh is an other aspect for fu-

ture work. The influence of employing adaptivity in the solutions of both forward and inverse problem should be further investigated, in particular how adaptive remeshing changes the resolution of the reconstructed images.

- Only one parameter, the absorption coefficient, has so far been reconstructed using the inverse solution method. The reconstruction model could be further improved in order to enable reconstruction of additional parameters such as the scattering coefficient.

- The choice of Laplace transform parameter s (or the factor s/c) becomes important in determining image quality. Further investigation into the influence of the choice of the s or s/c factor on the reconstructed image resolution is desirable.

- In addition to those aspects, systematic investigation is needed to quantify the limits of the reconstruction method. Factors affecting the limits of contrast and resolution of the method include: geometry, volume of the medium considered, the number and locations of both sources and detectors, the appropriate use of prior information to start the iterative solution procedure and its effect on convergence.

- Apart from using MC and FE-P_N data, real experimental data should also be considered to test the reconstruction algorithm.

Bibliography

[1] **S. Webb**

The Physics of Medical Imaging, Medical Science Series, IOP Publishing Ltd, (1988).

[2] **D. Walsh**

The Roentgen Rays in Medical Work, London:Bailliere, Tindall and Cox, (1897).

[3] **A. Macovski**

Medical Imaging Systems, Prentice-Hall Information and System Sciences Series, (1983).

[4] **E.E. Christensen, T.S. Curry III and J.E. Dowdey**

An Introduction to the Physics of Diagnostic Radiology, 2nd ed., Philadelphia: Lea and Febiger London: Kimpton, (1978).

[5] **K.S. Krane**

Introductory Nuclear Physics, John Wiley & Sons, Inc., (1987).

[6] **G.N. Hounsfield**

Computed Medical Imaging, Nobel Award Address, Med. Phys. **71**, pp. 283-290, (1980).

[7] **K.L. Garden**

An Overview of Computed Tomography, Ph.D. Dissertation, University of Canterbury, New Zealand, (1994).

[8] **D. Benaron, G. Muller and B. Chance**

Introduction: A Medical Perspective at The Threshold of Clinical Optical

Tomography, Medical Optical Tomography:Functional Imaging and Monitoring, SPIE Institute Series, Vol.**IS11**, pp. 3-9, (1993).

[9] **P.J. Early and E.R. Landa**
Use of Therapeutic Radionuclides in Medicine, Health Physics, **69(5)**, pp. 677-694, (1995).

[10] **J.A. Seibert**
One Hundred Years of Medical Diagnostic Imaging Technology, Health Physics, **69(5)**, pp. 695-720, (1995).

[11] **B. Lentle and J. Aldrich**
Radiological Sciences, past and present, The Lancet **350**, pp. 280-285, (1997).

[12] **R.J. Jaszczak**
Tomographic Radiopharmaceutical Imaging, Proc. IEEE, vol. 76, no. 9, pp. 1079-1094, (1988).

[13] **C.E. Floyd, R.J. Jaszczak, C.C. Harris and R.E. Coleman**
Energy and Spatial Distribution of Multiple Order Compton Scatter in SPECT: a Monte Carlo Investigation, Phys. Med. Biol., **29(10)**, pp. 1217-1230, (1984).

[14] **P.J. Early**
Use of Diagnostic Radionuclides in Medicine, Health Physics, **69(5)**, pp. 649-671, (1995).

[15] **P.M.W. French**
Biomedical Optics, **Physics**World, Vol.12, No.6, (1999).

[16] **G.A. Johnson, L. Hedlund and J. MacFall**
A New Window into the Lung, **Physics**World, Vol.11, No.11, pp. 35-38, (1998).

[17] **M. Schweiger**
Application of the Finite Element Method in Infrared Image Reconstruction of Scattering Media, PhD. Dissertation, University of London, (1994).

[18] **R.R. Alfano, P.P. Ho and K.M. Yoo**
Photons for Prompt Tumour Detection, **Physics**World, Vol.5, No.1, pp. 37, (1992).

[19] **M. Hiraoka, M. Firbank, M. Essenpreist, M. Cope, S.R. Arridge, P. van der Zee and D.T. Delpy**
A Monte Carlo Investigation of Optical Pathlength in Inhomogeneous Tissue and Its Application to Near-Infrared Spectroscopy, Phys. Med. Biol. **38**, pp. 1859-1876, (1993).

[20] **B. Chance and R.R. Alfano (eds)**
Photon Migration and Imaging in Random Media and Tissues, Proc. SPIE **1888**, (1993).

[21] **B. Chance and R.R. Alfano (eds)**
Optical Tomography, Photon Migration, and Spectroscopy of Tissue and Model Media:Theory, Human Studies, and Instrumentation, Proc. SPIE **2389**, (1995).

[22] **R.R. Alfano and J. Fujimoto**
Advances in Optical Imaging and Photon Migration TOPS-96, (OSA, Orlando), (1996).

[23] **A. Yodh and B. Chance**
Spectroscopy and Imaging with Diffusing Light, Physics Today, pp. 34, (1995).

[24] **J. Wu**
Photon Migration in Turbid Media:Time-Resolved Optical Imaging in Tissue-Like Phantom, Ph.D. Dissertation, MIT, Cambridge, USA, (1996).

[25] **J.C. Hebden, S.R. Arridge and D.T. Delpy**
Optical Imaging in Medicine: I. Experimental Techniques, Phys. Med. Biol. **42**, pp. 825-840, (1997).

[26] **D.T. Delpy and M. Cope**
Quantification in Tissue Near-infrared Spectroscopy, Phil. Trans. R. Soc. Lond. B **352**, pp. 649-659, (1997).

[27] **S.R. Arridge**

Optical Tomography in Medical Imaging, Inverse Problems **15**, pp. R41-R93, (1999).

[28] **B. Chance**

Time-resolved Spectroscopy and Imaging, SPIE **2389**, pp. 122, (1995),

[29] **S.A. Walker, A.E. Cerussi and E. Gratton**

Back-projection Image Reconstruction Using Photon Density Waves in Tissues, Optical Tomography, Photon Migration, and Spectroscopy of Tissue and Model Media:Theory, Human Studies, and Instrumentation, Proc. SPIE **2389**, pp. 350-357, (1995).

[30] **M. Cope and D.T. Delpy**

A System for Long Term Measurement of Cerebral Blood and Tissue Oxygenation in Newborn Infants by Near Infrared Transillumination, Med. Biol. Engng Comp. **26**, pp. 289-294, (1988).

[31] **J.C. Hebden, R.A. Kruger and K.S. Wong**

Time-resolved Imaging Through a Highly Scattering Medium, Appl. Opt., **30(7)**, pp. 788-794, (1991).

[32] **K. Wells, J.C. Hebden, F.E. Schmidt and D.T. Delpy**

UCL Multichannel Time-resolved System for Optical Tomography, Optical Tomography and Spectroscopy of Tissue: Theory,Instrumentation, Model, and Human Studies II, Proc. SPIE **2979**, pp. 599-607, (1997).

[33] **J.R. Lakowicz and K.W. Berndt**

Frequency Domain Measurements of Photon Migration in Tissues, Chem. Phys. Lett. **166**, pp. 246-252, (1990).

[34] **B.W. Pogue, M. Testorf, T. McBride, U. Osterberg and K.D. Paulsen**

Instrumentation and Design of a Frequency-domain Diffuse Optical Tomography Imager for Breast Cancer Detection, Optics Express 1, pp. 391-403, (1997).

[35] **M. Cutler**

Transillumination as an Aid in the Diagnosis of Breast Lesions, Surg. Gynecol. Obstet. **48**, pp. 721-728, (1929).

[36] **F.F. Jöbsis**

Non-invasive Infrared Monitoring of The Cerebral and Myocardial Oxygen Sufficiency and Circulatory Parameters, Science **198**, pp. 1264-1267, (1977).

[37] **A.D. Edwards et al.**

Cotside Measurement of Cerebral Blood Flow in Ill Preterm Infants by Near-Infrared Spectroscopy, Lancet II, pp. 770-771, (1988).

[38] **K.A. Kang, B. Chance, S. Zhao, S. Srinivasan, E. Patterson and R. Troupin**

Breast Tumor Characterization Using Near-Infrared Spectroscopy, Photon Migration and Imaging in Random Media and Tissues, Proc. SPIE **1888**, pp. 487-499, (1993).

[39] **D.A. Benaron et al.**

Imaging neonatal Brain Pathology Using Light, Ped Abstracts 33:369A, (1993).

[40] **B. Chance, D.T. Delpy, C.E. Cooper and E.O.R. Reynolds**

Near-infrared Spectroscopy and Imaging of Living Systems, Phil. Trans. R. Soc. B **352**, (1997).

[41] **J. Chang, R. Aronson, H.L. Graber and R.L. Barbour**

Imaging Diffusive Media Using Time-Independent and Time-Harmonic Sources:Dependence of Image Quality on Imaging Algorithms, Target Volume, Weight Matrix, and View Angle, Optical Tomography, Photon Migration, and Spectroscopy of Tissue and Model Media: Theory, Human Studies, and Instrumentation, Proc. SPIE **2389**, pp. 448-464, (1995).

[42] **B.W. Pogue, M.S. Patterson and T.J. Farrell**

Forward and Inverse Calculations for 3-D Frequency-Domain Diffuse Optical Tomography, Optical Tomography, Photon Migration, and Spectroscopy of Tis-

sue and Model Media:Theory, Human Studies, and Instrumentation, Proc. SPIE **2389**, pp. 328-339, (1995).

[43] **M. Schweiger, S.R. Arridge, D.T. Delpy**
Application of the Finite-Element Method for the Forward and Inverse Models in Optical Tomography, Journal of Mathematical Imaging and Vision **3**, pp. 263-283, (1993).

[44] **S.R. Arridge, M. Schweiger, M. Hiraoka and D.T. Delpy**
A Finite Element Approach for Modelling Photon Transport in Tissue, Med. Phys. **20(2)**, pp. 299-309, (1993).

[45] **J.J. Duderstadt and W.R. Martin**
Transport Theory, John Wiley & Sons, Inc., (1979).

[46] **A. Dubi**
Monte Carlo Calculations for Nuclear Reactors, Handbook of Nuclear Reactor Calculations, Vol.II, CRC Press LLC, (1987).

[47] **A.M. Mirza**
Discontinuous Finite Element Formulation of the Neutron Transport Equation, PhD Dissertation, University of London, Imperial College of Science, Technology and Medicine, (1994).

[48] **J. Briesmeister**
MCNP*: A General Monte Carlo N-Particle Transport Code*, Version 4A, Los Alamos National Laboratory Report, LA-12625-M, (1993).

[49] **E.D. Cashwell and C.J. Everett**
A Practical Manual on the MONTE CARLO METHOD *for Random Walk Problems*, Pergamon Press, (1959).

[50] **J. Spanier and E.M. Gelbard**
Monte Carlo Principles and Neutron Transport Problems, Addison Wesley, (1969).

[51] **G. Goertzel and M.H. Kalos**
Monte Carlo Methods in Transport Problems, Prog. Nucl. Physics, Vol.2, pp. 315-369, (1958).

[52] **M.S. Patterson, B.C. Wilson and D.R. Wyman**
The Propagation of Optical Radiation in Tissue I. Models of Radiation Transport and Their Application, Lasers in Medical Science Vol.6:155, pp. 155-168, (1991).

[53] **S.R. Arridge, M. Hiraoka and M. Schweiger**
Statistical Basis for the Determination of Optical Pathlength in Tissue, Phys. Med. Biol. **40**, pp. 1539-1558, (1995).

[54] **L.L. Carter and E.D. Cashwell**
Particle Transport Simulation with the Monte Carlo Method, Technical Information Center, Office of Public Affairs, U.S. Energy Research and Development Administration, (1975).

[55] **S.T. Flock, M.S. Patterson, B.S. Wilson and D.R. Wyman**
Monte Carlo Modelling of Light Propagation in Highly Scattering Tissues-I:model predictions and comparison with diffusion theory, IEEE Trans. Biomed. Eng. **BME-36**, pp. 1162-1168, (1989).

[56] **V.G. Peters, D.R. Wyman, M.S. Patterson and G.L. Frank**
Optical Properties of Normal and Diseased Human Breast Tissues in the Visible and Near Infrared, Phys. Med. Biol. **35**, pp. 1317-1334, (1990).

[57] **M. Essenpreis, P. van der Zee and T.N. Mills**
Monte Carlo Modelling of Light Transport in Tissue:the Effects of Laser Coagulation on Light Distributions, Bioptics: Optics in Biomedicine and Environmental Sciences, Proc. SPIE **1524**, pp. 122-137, (1992).

[58] **S.C. Feng, F.A. Zeng and B. Chance**
Monte Carlo Simulations of Photon Migration Path Distributions in Multiple Scattering Media, Photon Migration and Imaging in Random Media and Tissues, Proc. SPIE **1888**, pp. 78-89, (1993)

[59] **A.H. Hielscher, H. Liu, B. Chance, F.K. Tittel and S.L. Jacques**
Time-Resolved Photon Emission from Layered Turbid Media, Applied Optics, Vol.35, No.4, pp. 719-728, (1996).

[60] **E. Tinet, S. Avrillier and J.M. Tualle**
Fast Semianalytical Monte Carlo Simulation for Time-resolved Light Propagation in Turbid Media , Journal of the Optical Society of America A-Optics Image Science and Vision, Vol.13, No.9, pp. 1903-1915, (1996).

[61] **K.B. Tahir, C.R.E. de Oliveira, S. Katsimichas and J.C. Dainty**
A Comparison between Finite Element Transport and Monte Carlo Solutions for Photon Propagation, Proc. of Applied Optics and Optoelectronics, Reading University, UK, pp. 58-63, (1996).

[62] **K.M. Case and P.F. Zweifel**
Linear Transport Theory, New York: Addison-Wesley, (1967).

[63] **B. Davison**
Neutron Transport Theory, Oxford University Press, London, (1957).

[64] **A.R. Zolfaghari Daaryani**
Multidimensional Finite Element Modelling of Thermal Radiation in Participating Media, PhD Dissertation, University of London, Imperial College of Science, Technology and Medicine, (1998).

[65] **J.H. Jeans**
Mon. Not. R. Astr. Soc. **78**:28, (1917).

[66] **J.C. Mark**
The Spherical Harmonics Method I, National Research Council of Canada, Atomic Energy Project, MT-92, (1944).

[67] **J.C. Mark**
The Spherical Harmonics Method II, National Research Council of Canada, Atomic Energy Project, MT-92, (1945).

[68] **S. Chandrasekhar**

Radiative Transfer, Oxford:London, (1950), New York:Dover, (1960).

[69] **M.N. Ozisik**

Radiative Transfer and Interactions with Conduction and Convention, New York London: Wiley, (1973).

[70] **R. Siegel and J.R. Howell**

Thermal Radiation Heat Transfer, 3rd ed., Washington London: Hemisphere, (1992).

[71] **W.M. Star, J.P.A. Marijnissen and M.J.C. van Gemert**

Light Dosimetry in Optical Phantoms and in Tissues 1: Multiple Flux and Transport Theory, Phys. Med. Biol. **33**, pp. 437-454, (1988).

[72] **J.M. Kaltenbach and M. Kaschke**

Frequency- and Time-Domain Modelling of Light Transport in Random Media, Medical Optical Tomography:Functional Imaging and Monitoring, SPIE Institute Series, Vol.**IS11**, pp. 65-86, (1993).

[73] **H. Jiang and K.D. Paulsen**

Finite-Element-Based Higher Order Diffusion Approximation of Light Propagation in Tissues, Optical Tomography, Photon Migration, and Spectroscopy of Tissue and Model Media: Theory, Human Studies, and Instrumentation, Proc. SPIE **2389**, pp. 608-614, (1995).

[74] **W.M. Star**

Comparing the P_3-Approximation with Diffusion Theory and with Monte Carlo Calculations of Light Propagation in a Slab Geometry, SPIE Institute Series, Vol.**IS5**, pp. 146-154, (1989).

[75] **D.A. Boas, H. Liu, M.A. O'Leary, B. Chance and A.G. Yodh**

Photon Migration within the P_3 Approximation, Optical Tomography, Photon Migration, and Spectroscopy of Tissue and Model Media:Theory, Human Studies, and Instrumentation, Proc. SPIE **2389**, pp. 240-247, (1995).

[76] **C.R.E. de Oliveira**

An Arbitrary Geometry Finite Element Method for Multi-group Neutron Transport with Anisotropic Scattering, Progress in Nuclear Energy, Vol.18, No.1/2, pp. 227-236, (1986).

[77] **C.R.E. de Oliveira and A.J.H. Goddard**

EVENT - *A Multidimensional Finite Element-Spherical Harmonics Radiation Transport Code*, Proceedings of the OECD International Seminar on 3D Deterministic Radiation Transport Codes, Paris, December 01-02, (1996).

[78] **S.R. Arridge**

The Forward and Inverse Problem in Time Resolved Infra-Red Imaging, Medical Optical Tomography:Functional Imaging and Monitoring, SPIE Institute Series, Vol.**IS11**, pp. 35-64, (1993).

[79] **S.R. Arridge, M. Hiraoka and M. Schweiger**

Statistical Basis for the Determination of Optical Pathlength in Tissue, Phys. Med. Biol. **40**, pp. 1539-1558, (1995).

[80] **H.B. Jiang, K.D. Paulsen, U.L. Österberg, B.W. Pogue and M.S. Patterson**

Optical-Image Reconstruction Using Frequency-Domain Data - Simulations and Experiments, Journal of the Optical Society of America A- Optics Image Science and Vision, Vol.13, No.2, pp. 253-266, (1996).

[81] Optical Tomography, Photon Migration, and Spectroscopy of Tissue and Model Media:Theory, Human Studies, and Instrumentation, Part 1 and Part 2., B. Chance, R.R. Alfano, eds., Proc. SPIE **2389**, (1995).

[82] **R.A.J. Groenhuis, H.A. Ferwada and J.J. Ten Bosch**

Scattering and Absorption of Turbid Materials Determined From Reflection Measurements, (Parts 1 and 2), Appl. Opt **28**, pp. 2456-2467, (1983).

[83] **J.J. Duderstadt and L.J. Hamilton**

Nuclear Reactor Analysis, John Wiley & Sons, Inc., New York, (1976).

[84] **A.F. Henry**
Nuclear-Reactor Analysis, The MIT Press, (1975).

[85] **S.R. Arridge, M. Cope and D.T. Delpy**
The Theoretical Basis for The Determination of Optical Pathlengths in Tissue:Temporal and Frequency Analysis, Phys. Med. Biol., **37(7)**, pp. 1531-1560, (1992).

[86] **M. Firbank, S.R. Arridge, M. Schweiger and D.T. Delpy**
An Investigation of Light Transport Through Scattering Bodies with Non-Scattering Regions, Phys. Med. Biol. **41**, pp. 767-783, (1996).

[87] **A.H Hielscher and R.E. Alcouffe**
Non-diffusive Photon Migration in Homogeneous and Heterogeneous Tissues, Photon Propagation in Tissues II, Proc. SPIE **2925**, pp. 22-30, (1996).

[88] **M. Schweiger, S.R. Arridge, M. Hiraoka, M. Firbank and D.T. Delpy**
Comparison of a Finite Element Forward Model With Experimental Phantom Results:Application to Image Reconstruction, Photon Migration and Imaging in Random Media and Tissues, Proc. SPIE **1888**, pp. 179-190, (1993).

[89] **D.A. Boas**
Diffuse Photon Probes of Structural and Dynamical Properties of Turbid Media: Theory and Biomedical Applications, PhD Dissertation, University of Pennsylvania, (1996).

[90] **C.R.E. de Oliveira**
Finite Element Techniques for Multi-group Neutron Transport Calculations with Anisotropic Scattering, PhD Dissertation, University of London, Queen Mary College, (1987).

[91] **O.C. Zienkiewicz and R.L. Taylor**
The Finite Element Method, 4th revised ed., McGraw-Hill, London, (1989).

[92] **J.T. Oden and J.N. Reddy**
An Introduction to the Mathematical Theory of Finite Elements, John Wiley & Sons, Inc., New York, (1976).

[93] **T. Ohnishi**

The Application of Finite Element Solution Technique to Neutron Diffusion and Transport Equations, Proc. Conf. New Development in Reactor Mathematics in Applications, Idaho Falls, Idaho, (1971).

[94] **W.R. Martin, C.E. Yehnert, L. Lorenze and J.J. Duderstadt**

Phase Space Finite Element Methods Applied to The First Order Form of The Transport Equation, Annals of Nuclear Energy, Vol.8, pp. 633-646, (1981).

[95] **J.K. Fletcher**

A Solution of Multi-group Transport Equation Using a Weighted Residual Technique, Annals of Nuclear Energy, Vol.8, pp. 647-656, (1981).

[96] **S.H. Crandall**

A Survey of Numerical Procedures, Engineering Analysis, McGraw-Hill Inc., (1956).

[97] **O.C. Zienkiewicz and K. Morgan**

Finite Elements and Approximation, John Wiley & Sons Inc., (1983).

[98] **L. Collatz**

The Numerical Treatment of Differential Equations, New York, (1960).

[99] **J.A.C. Fletcher**

Computational Galerkin Methods, Springer-Verlag N Y Inc., (1960).

[100] **R.T. Ackroyd**

A Finite Element Method for Neutron Transport - VII. Completely Boundary Free Maximum Principles for the First-Order Boltzmann Equation, Annals of Nuclear Energy, Vol.10, pp. 243-261, (1983).

[101] **G.R. Buchanan**

Theory and Problems of Finite Element Analysis, Schaum's Outline Series, McGraw-Hill, Inc., (1995).

[102] **S. Kaplan and J.A. Davis**

Canonical and Involutory Transformation of The Variational Problems of Transport Theory, Nuclear Science and Engineering, Vol.28, pp. 166-176, (1967).

[103] **E.E. Lewis and W.F. Miller**

Computational Methods of Neutron Transport, John Wiley & Sons, Inc., New York, (1984).

[104] **R.T. Ackroyd**

A Finite Element Method for Neutron Transport - I. Some Theoretical Considerations, Annals of Nuclear Energy, Vol.5, pp. 75-94, (1978).

[105] **J. Galliara and M.M.R. Williams**

A Finite Element Method for Neutron Transport - II. Some Theoretical Considerations, Annals of Nuclear Energy, Vol.6, pp. 205-223, (1979).

[106] **R.T. Ackroyd and D.T. Grenfell**

A Finite Element Method for Neutron Transport - III. Two Dimensional One Group Test Problems, Annals of Nuclear Energy, Vol 6, pp. 563-577, (1979).

[107] **R.T. Ackroyd and B.A. Splawski**

A Finite Element Method for Neutron Transport - VI. Upper and Lower Bound Bounds for Local Characteristics of Solutions, Annals of Nuclear Energy, Vol.9, pp. 315-330, (1982).

[108] **V.S. Vladimirov**

Mathematical Problems in the One-Velocity Theory of Particle Transport, Atomic Energy of Canada, Ltd., Ontario (1963), translated from Trans. V.A. Steclov Mathematical Institute **61**, (1961).

[109] **R.T. Ackroyd**

Least-squares Derivation of Extremum and Weighted-residual Methods for Equations of Reactor Physics - I, Annals of Nuclear Energy, Vol.10, pp. 65-99, (1983).

[110] **R.T. Ackroyd**

Generalised Least Squares As A Generator of Variational Principles and

Weighted Residual Methods for FEM Transport Problems, Progress in Nuclear Energy, Vol.18, No.1/2, pp. 45-62, (1986).

[111] **R.T. Ackroyd and W.E. Wilson**
Composite Finite Element Solutions for Neutron Transport-VII. Completely Boundary Free Maximum Principles for the First-Order Boltzmann Equation, Annals of Nuclear Energy, Vol.15, pp. 397-419, (1986).

[112] **R.T. Ackroyd**
Least Squares Formulation of Extremum Principles and Weighted Residual Methods Used in Finite Element Codes for Solving Boltzmann Equation for Neutron Transport, The Mathematics of Finite Elements and Applications V, Academic Press, (1985).

[113] **R.T. Ackroyd and M.M. Nanneh**
Upper and Lower Bounds for Disadvantage Factors as a Test of an Algorithm Used in a Synthesis Method, Annals of Nuclear Energy, Vol.15, pp. 241-259, (1988).

[114] **R. Sanchez and N.J. McCormick**
A Review of Neutron Transport Approximations, Nucl. Sci. Eng. **80**, pp. 481-535, (1982).

[115] **W-F Cheong, S.A. Prahl and A.J. Welch**
A Review of the Optical Properties of Biological Tissues, IEEE Journal of Quantum Electronics, Vol.26, No.12, pp. 2166-2185, (1990).

[116] **A. Ishimaru**
Wave Propagation in Random Media, Academic Press, New York, (1978).

[117] **C.F. Bohren and D.R. Huffman**
Absorption and Scattering of Light by Small Particles, John Wiley & Sons, Inc., (1983).

[118] **R.L. Fante**
Relationship Between Radiative Transport Theory and Maxwell's Equations in Dielectric Media, J. Opt. Soc. Am. A **71**, pp. 460-468, (1981).

[119] **J.F. de Boer**

Optical Fluctuations on the Transmission and Reflection of Mesoscopic Systems, PhD Dissertation, University of Amsterdam, (1995).

[120] **B.C. Wilson and S.T. Jacques**

Optical Reflectance and Transmittance of Tissues:Principles and Applications, IEEE Journal of Quantum Electronics, Vol.26, No.12, pp. 2186-2199, (1990).

[121] **J.R. Mourant, J. Boyer, A.H. Hielscher and I.J. Bigio**

Influence of the Scattering Phase Function on Light Transport Measurements in Turbid Media Performed with Small Source-Detector Separations, Optics Letters, Vol.21, No.7, pp. 546-348, (1996).

[122] **P. Liu**

A new Phase Function Approximating to Mie Scattering for Radiative Transport Equations, Phys. Med. Biol. **39**, pp. 1025-1036, (1994).

[123] **G. Mie**

Considerations on the Optics of Turbid Media, Especially Colloidal Metal Sols, Ann. Phys. Lpz. **25**, pp. 337, (1908).

[124] **M. Kerker**

The Scattering of Light and Other Electromagnetic Radiation, New York: Academic Press, (1969).

[125] **A. Stratton**

Electromagnetic Theory, McGraw-Hill, New York, (1941).

[126] **L.G. Henyey and J.L. Greenstein**

Diffuse Radiation in the Galaxy, Astrophys. J. **93**, pp. 70-83, (1941).

[127] **H.C. van de Hulst**

Multiple Light Scattering: Tables, Formulas and Applications, New York London: Academic Press, (1980).

[128] **L.O. Reynolds and N.J. McCormick**

Approximate Two-Parameter Phase Function for Light Scattering, Journal of the Optical Society of America **70**, pp. 1206-1212, (1980).

[129] **K.M. Case, F. de Hoffmann and G. Placzek**

Introduction to the Theory of Neutron Diffusion, U.S. Government Printing Office, Washington, D.C., (1953).

[130] **M.M.R. Williams**

Mathematical Methods in Particle Transport Theory, Butterworths, London, (1971).

[131] **C. Cercignani**

Mathematical Methods in Kinetic Theory, Plenum Publishing Company, New York, (1969).

[132] **G.I. Bell and S. Glasstone**

Nuclear Reactor Theory, Van Nostrand-Reinhold, New York, (1970).

[133] **S. Katsimichas**

Particle Transport Solutions for Problems Involving Transparent Media, PhD Dissertation, University of London, Imperial College of Science, Technology and Medicine, (1998).

[134] **Jr. W.F. Miller, E.E. Lewis and E.C. Rossow**

The Application of Phase-Space Finite Elements to the One-Dimensional Neutron Transport Equation, Nucl. Sci. Eng. **51**, pp. 148-156, (1973).

[135] **Jr. W.F. Miller, E.E. Lewis and E.C. Rossow**

The Application of Phase-Space Finite Elements to the Two-Dimensional Neutron Transport Equation in X-Y Geometry, Nucl. Sci. Eng. **52**, pp. 12-22, (1973).

[136] **J. Pitkäranta and P. Silnennoinen**

Finite Element Analysis of some Critical Fast Assemblies, Nucl. Sci. Eng. **52**, pp. 447, (1973).

[137] **H.G. Kaper, G.K. Leaf and A.J. Lindeman**
Applications of Finite Element Methods in Reactor Mathematics. Numerical Solution of the Neutron Transport Equation, ANL-8126, Argonne National Laboratory, (1974) **52**, pp. 447, (1973).

[138] **B.A. Splawski**
Finite Element Methods for Neutron Transport Calculations, PhD Dissertation, University of London, (1981)

[139] **A.K. Ziver**
Solution of the Boltzmann Transport Equation by Finite Elements, PhD Dissertation, University of London, (1981)

[140] **R.T. Ackroyd**
Finite Element Methods for Particle Transport Applications to Reactor and Radiation Physics, Research Studies Press:England, Wiley:New York, (1997).

[141] **E.E. Lewis**
Finite Element Approximation to the Even-Parity Transport Equation, Adv. in. Nucl. Sci. Tech. **13**, Plenum Press, NY., pp. 155-225, (1981).

[142] **J. Pitkäranta**
A Non-Self-Adjoint Variational Procedure for the Finite-Element Approximation of the Transport Equation, Transport Theory and Statistical Physics **4(1)**, pp. 1-24, (1975).

[143] **A.R. Mitchell and R. Wait**
The Finite Element Method in Partial Differential Equations, John Wiley & Sons, Inc., (1977).

[144] **C.R.E. de Oliveira**
EVENT - A Multigroup, Finite Element-Spherical Harmonics Program for the Solution of Steady-State and Time-Dependent Radiation Transport Problems in Arbitrary Geometry, User Notes, (1996).

[145] **C.R.E. de Oliveira**
Multidimensional Deterministic Radiation Transport Review and Status, Frédéric Joliot Summer School CEA, Cadarache, France, (1997).

[146] **S.J. Madsen, B.C. Wilson, M.S. Patterson, Y.D. Park, S.L. Jacques and Y. Hefetz**
Experimental Tests of Simple Diffusion Model for the Determination of Scattering and Absorption-Coefficients of Turbid Media from Time-Resolved Diffuse Reflectance Measurements, Appl. Opt. **31**, pp. 3509-3517, (1992).

[147] **A.H Hielscher, H. Liu, B. Chance, F.K. Tittel and S.L. Jacques**
The Influence of Boundary Conditions on the Accuracy of Diffusion Theory in Time-Resolved Reflectance Spectroscopy of Biological Tissue, Pyhs. Med. Biol. **40**, pp. 1957-1975, (1995).

[148] **E. Okada, M. Schweiger, S.R. Arridge, M. Firbank and D.T. Delpy**
Experimental Validation of Monte-Carlo and Finite-Element Methods for the Estimation of the Optical Path-length in Homogeneous Tissues, Appl. Opt. **35**, pp. 3362-3371, (1996).

[149] **S. Katsimichas**
MCMCYL, Energy Systems Section, Mechanical Engineering, Imperial College, March, (1996).

[150] **C.R.E. de Oliveira and K.B. Tahir**
Higher-order Transport Approximations for Optical Tomography Applications, Photon Propagation in Tissues III, Proc. SPIE **3194**, pp. 212-218, (1997).

[151] **A.H Hielscher, R.E. Alcouffe and R.L. Barbour**
Comparison of Finite-Difference Transport and Diffusion Calculations for Photon Migration in Homogeneous and Heterogeneous Tissues, Phys. Med. Biol. **43**, pp. 1285-1302, (1998).

[152] **A.M. Nilsson, G.W. Lucassen, W. Verkruysse, S. Andersson-Engels and M.J.C. Van Gemert**

Changes in Optical Properties of Human Whole Blood in Vitro Due to Slow Heating, Photochem. Photobiol. **65**, pp. 366-373, (1997).

[153] **A.H Hielscher, R.E. Alcouffe and R.L. Barbour**
Transport and Diffusion Calculations on MRI-generated data, Optical Tomography and Spectroscopy of Tissue:Theory, Instrumentation, Model, and Human Studies II, Proc. SPIE **2979**, pp. 500-508, (1997).

[154] **S.R. Arridge and M. Kaschke**
Modelling of Light Propagation and Image Formation, Medical Optical Tomography:Functional Imaging and Monitoring, SPIE Institute Series, Vol.**IS11**, pp. 31-33, (1993).

[155] **R.L. Barbour, H.L. Graber, Y. Wang, J.Chang and R. Aronson**
A Perturbation Approach for Optical Diffusion Tomography Using Continuous-Wave and Time-Resolved Data, Medical Optical Tomography:Functional Imaging and Monitoring, SPIE Institute Series, Vol.**IS11**, pp. 87-120, (1993).

[156] **N.C. Roberty and C.R.E.de Oliveira**
Transport Models for Tomography:Theoretical and Practical Considerations, Proceedings of 10th ENFIR Aguas de Lindoia, S.P. Brazil, (1995).

[157] **S.R. Arridge and J.C. Hebden**
Optical Imaging in Medicine: II. Modelling and Reconstruction, Phys. Med. Biol. **42**, pp. 841-853, (1997).

[158] **S.A. Walker, A.E. Cerussi and E. Gratton**
Back-projection Image Reconstruction Using Photon Density Waves in Tissue, Optical Tomography, Photon Migration, and Spectroscopy of Tissue and Model Media:Theory, Human Studies, and Instrumentation, Proc. SPIE **2389**, pp. 350-357, (1995).

[159] **S. Walker, S. Fantini and E. Gratton**
Image Reconstruction by Backprojection from Frequency-Domain Optical Measurements in Highly Scattering Media, Appl. Opt. **36**, pp. 170-179, (1997).

[160] **D.A. Benaron, D.C. Ho, S.D. Spilman, J.P. Van Hounten and D.K. Stevenson**

Non-recursive Linear Algorithms for Optical Imaging in Diffusive Media, Advances in Experimental Medical Biology. Oxygen Transport to Tissue XVI., New York:Plenum Press., (1994).

[161] **S.R. Arridge and M. Schweiger**

Image Reconstruction in Optical Tomography, Philos. Trans. R. Soc. London Ser. B. **352**, pp. 717-726, (1997).

[162] **W. H. Press, B.P. Flannery, S.A. Teukolsky and W. T. Vetterling**

Numerical Recipes in FORTRAN: The Art of Scientific Computing, 2nd ed. Cambridge, England: Cambridge University Press, (1992).

[163] **S.R. Arridge, M. Schweiger and D.T. Delpy**

Iterative Reconstruction of Near Infrared Absorption Images, Inverse Problems in Scattering and Imaging, Proc. SPIE **1767**, pp. 372-383, (1992).

[164] **S.R. Arridge, M. Schweiger, M. Hiraoka and D.T. Delpy**

Performance of an Iterative Reconstruction Algorithm for Near Infrared Absorption Imaging, Photon Migration and Imaging in Random Media and Tissues, Proc. SPIE **1888**, pp. 360-371, (1993).

[165] **H. Jiang, K.D. Paulsen, U.L. Osterberg, B.W. Pogue and M.S. Patterson**

Simultaneous Reconstruction of Optical Absorption and Scattering Maps in Turbid Media from Near-Infrared Frequency-Domain Data, Optic Letters **20**, pp. 2128-2130, (1995).

[166] **B.W. Pogue, M. Testorf, T. McBride, U. Osterberg and K. Paulsen**

Instrumentation and Design of a Frequency-Domain Diffuse Optical Tomography Imager for Breast Cancer Detection, Optics Express, Vol.1, No.13, pp. 391-403, (1997).

[167] **H.B Jiang, K.D. Paulsen, U.L. Österberg and M.S. Patterson**

Frequency-Domain Near-Infrared Photo Diffusion Imaging:Initial Evaluation in

Multi-target Tissuelike Phantoms, Medical Physics, Vol.25, No.2, pp. 183-193. (1998).

[168] **K.D. Paulsen and H.B Jiang**
Spatially Varying Optical Property Reconstruction Using a Finite-Element Diffusion Equation Approximation, Medical Physics, Vol.22, No.6, pp. 691-701. (1995).

[169] **K.D. Paulsen and H.B Jiang**
Enhanced Frequency-Domain Optical Image Reconstruction in Tissues Through Total-Variation Minimisation, Applied Optics, Vol.35, No.19, pp. 3447-3458. (1996).

[170] **D.C. Youla and H. Webb**
Image Restoration by the Method of Convex Projection onto Convex Sets - Part I, IEEE Trans. Med. Imaging, Vol.MI-1, pp. 81-94, (1982).

[171] **D.C. Youla**
Mathematical Theory of Image Reconstruction by the Method of Convex Projection, Image Recovery:Theory and Application, ed. Henry Stark, Academic Press, New York, (1987).

[172] **P. Oskoui-Fard and H. Stark**
Tomographic Image Reconstruction Using the Theory of Convex Projections, IEEE Trans. Med. Imaging, Vol.MI-7, pp. 45-58, (1988).

[173] **P.E. Gill, W. Murray and M.H. Wright**
Practical Optimisation, Academic Press, New York, (1981).

[174] **G. Strang**
Introduction to Applied Mathematics, Wellesley-Cambridge Press,MA, (1986).

[175] **A.C. Kak and M. Slaney**
Principles of Computerised Tomographic Imaging, IEEE Press, New York, (1988).

[176] **A.H. Anderson and A.C. Kak**
Simultaneous Algebraic Reconstruction Technique (SART): A Superior Implementation of the ART Algorithm, Ultrasonic Imaging **6**, pp. 81-94, (1984).

[177] **T.S. Pan and A.E. Yagle**
Numerical Study of Multi-grid Implementation of Some Iterative Reconstruction Algorithms, IEEE Trans. Med. Imaging, Vol.MI-10, pp. 572-588, (1991).

[178] **J.H. Chang, W.W. Zhu, Y. Wang, H.L. Graber and R.L. Barbour**
Regularized Progressive Expansion Algorithm for Recovery of Scattering Media from Time-resolved Data, Journal of the Optical Society of America A-Optics Image Science and Vision, Vol.14, No.1, pp. 306-312, (1997).

[179] **F.H. Schlereth, J.M. Fossaceca and R. Barbour**
Imaging of Diffusion Media with a Neural Net Formulation: A Problem in Large Scale Computation, Physiological Monitoring and Early Detection Diagnostic Methods, Proc. SPIE **1641**, pp. 46-57, (1992).

[180] **J.R. Singer, F.A. Grünbaum, P. Kohn and J. Zubelli**
Image Reconstruction of the Interior of Bodies that Diffuse Radiation, Science **248**, pp. 990-993, (1990).

[181] **F.A. Grünbaum, P. Kohn, G. Latham, J.R. Singer and J.P. Zubelli**
Diffuse Tomography, Time-Resolved Spectroscopy and Imaging of Tissues, SPIE **1431**, pp. 232-238, (1991).

[182] **H.L. Graber, R. Aronson and R.L. Barbour**
Nonlinear Effects of Localised Absorption Perturbations on the Light Distribution in a Turbid Medium, Journal of the Optical Society of America A-Optics Image Science and Vision, Vol.15, No.4, pp. 834-848, (1998).

[183] **H.L. Graber, J. Chang, R. Aronson and R.L. Barbour**
A Perturbation Model for Imaging in Dense Scattering Media: Derivation and Evaluation of Imaging Operators, Medical Optical Tomography: Functional Imaging and Monitoring, SPIE Institute Series, Vol.**IS11**, pp. 121-143, (1993).

[184] **B.B. Das, J. Dolne, R.L. Barbour, H.L. Graber, J. Chang, M. Zevallos, F. Liu and R.R. Alfano**
Analysis of Time-Resolved Data for Tomographical Image Reconstruction of Opaque Phantoms and Finite Absorbers in Diffusive Media, Optical Tomography, Photon Migration, and Spectroscopy of Tissue and Model Media: Theory, Human Studies, and Instrumentation, Proc. SPIE **2389**, pp. 16-28, (1995).

[185] **H.L. Graber, R.L. Barbour and J. Chang**
Algebraic Reconstruction of Images of a Diffusive Medium Containing Strong Absorbers: Comparative Study of Different Illumination Schemes and the Effect of Restricted View Angle, Optical Tomography, Photon Migration, and Spectroscopy of Tissue and Model Media:Theory, Human Studies, and Instrumentation, Proc. SPIE **2389**, pp. 431-447, (1995).

[186] **J.H. Chang, H.L. Graber, R.L. Barbour and R. Aronson**
Recovery of Optical-Cross-Section Perturbations in Dense- Scattering Media by Transport-Theory-Based Imaging Operators and Steady-state Simulated Data, Applied Optics, Vol.35, No.20, pp. 3963-3978, (1996).

[187] **J.W. Chang, H.L. Graber, P.C. Koo, R. Aronson, S.L.S. Barbour and R.L. Barbour**
Optical Imaging of Anatomical Maps Derived from Magnetic Resonance Images Using Time-independent Optical Sources, IEEE Transactions on Medical Imaging, Vol.16, No.1, pp. 68-77, (1997).

[188] **W.W. Zhu, Y. Wang, Y.N. Deng, Y.Q. Yao and R.L. Barbour**
A Wavelet-based Multi-resolution Regularized Least Squares Reconstruction Approach for Optical Tomography, IEEE Transactions on Medical Imaging, Vol.16, No.2, pp. 210-217, (1997).

[189] **S.R. Arridge, P. van der Zee and D.T. Delpy**
Reconstruction Methods for Infra-red Absorption Imaging, Time-Resolved Spectroscopy and Imaging of Tissues, Proc. SPIE **1431**, pp. 204-217, (1991).

[190] **N.C. Roberty**

Methodology for the Solution of the Inverse Boltzmann Transport Equation, Internal Report, (1996).

[191] **C.R.E. de Oliveira**

Private Communication, (1996).

[192] **J.R. Lamarsh**

Introduction to Nuclear Reactor Theory, Addison-Wesley, Reading, MA, (1966).

[193] **S. Fantini, M.A. Franceschini, S.A. Walker, J.S. Maier and E. Gratton**

Photon Path Distributions in Turbid Media: Applications for Imaging, Optical Tomography, Photon Migration, and Spectroscopy of Tissue and Model Media:Theory, Human Studies, and Instrumentation, Proc. SPIE **2389**, pp. 340-349, (1995).

[194] **P. Liu and R.A. Kruger**

Semianalytical Approach to Pulsed Light Propagation in Scattering and Absorbing Media, Optical Engineering, Vol.33, No.8, pp. 2783-2799, (1994).

[195] **A.H Hielscher and R.E. Alcouffe**

Discrete-Ordinate Transport Simulation of Light Transport in Highly Forward Scattering Heterogeneous Media, Advances in Optical Imaging and Photon Migration TOPS-98, (OSA, Orlando),(1998).

[196] **W.J. Wiscombe**

The Delta-M Method: Rapid Yet Accurate Radiative Flux Calculations for Strongly Asymmetric Phase Functions, Journal of Atmospheric Sciences, Vol.34, pp. 1408-1422, (1977).

[197] **M. Abramowitz and I.A. Stegun**

Handbook of Mathematical Functions with Formulas, Graphs, and Mathematical Tables, 9th printing. New York: Dover, (1972).

[198] **C.R.E. de Oliveira, C.C Pain and A.J.H. Goddard**
Parallel Domain Decomposition Methods for Large-Scale Finite Element Transport Modelling, Proc. of the ANS International Conference on Mathematics and Computation, Portland, Oregon, (1995).

[199] **R.S. Birnbaum, C.R.E. de Oliveira and A.J.H. Goddard**
A Parallel Solution of Multidimensional Finite Element-Spherical Harmonics Radiation Transport Equations, Reactor Physics and Reactor Computations, 415, Negev Press, (1994).

[200] **B. Karaoglu**
Fizik ve Muhendislikte Matematik Yontemler, BilgiTek Yayincilik, Istanbul, (1994).

[201] **E.W. Weisstein**
CRC concise encyclopedia of mathematics, Boca Raton, Fla. London: CRC Press, (1999).

[202] **G. Arfken**
Mathematical Methods for Physicists, 3rd ed. Orlando, FL: Academic Press, (1985).

[203] **R.D. Schafer**
An Introduction to Nonassociative Algebras, New York: Dover, (1996).

Appendix A

Anisotropic Scattering

Following is the listing of the FORTRAN program developed to calculate the Legendre expansion coefficients of the scattering kernel. The coefficients can be obtained using three different scattering phase functions: Mie Theory, Henyey-Greenstein and Simplified Approximate Mie theory.

The expansion of the scattering phase function as a series in Legendre polynomials was considered (equation (2.26)) and the resulting integral for each coefficient (equation (2.27)) was numerically calculated with Gauss-Legendre integration. The value of the integral in equation (2.27) becomes the sum of the product of weights and the values of the scattering phase function at key points (abscissas) as

$$a_n = \left[\frac{2(i-1)+1}{2}\right] \sum_{i=1}^{n+1} w_i f(x_i) P_{i-1}(x_i) dx, \tag{A.1}$$

where x_i are the abscissas, and w_i the associated weights for Gaussian Quadrature on [-1,1]. The delta-M method was then applied within the program internally in order to truncate the calculated coefficients at a desired number.

A.1 Program PHASEFUN

```
      implicit none
      integer maxcof
      parameter( maxcof = 1000 )
      real*8 pn(maxcof), anfacg
      integer nopt, ncoeff, nmat
c
c delta-m part variables:
c
      real*8 sigma, sabs, fiss, scatt, scateff
c
c local variables:
c
      integer imat, knopt, m, n1, m1
c
      print *
      write(*,*)' Please choose an option for phase function: '
c
      print *
      write(*,*)' 1-) H-G Phase Function; '
      write(*,*)' 2-) Simp. App. Mie Theory Phase Function '
      write(*,*)' 3-) Mie Theory Phase Function '
      print *
c
      read(*,*) nopt
c
      open(unit=7,file='phasefun.out',status='unknown')
c
      if ( nopt .eq. 1 ) then
c
C *************** H-G PHASE FUNCTION ***************
c
         call henyey( pn, ncoeff, anfacg )
c
      else if( nopt .eq. 2 ) then
c
C *************** SIMPLIFIED MIE PHASE FUNCTION ****
c
        call simpmie( pn, ncoeff, anfacg )
c
      else if( nopt .eq.3 ) then
c
C *************** MIE PHASE FUNCTION ***************
c
        call mie( pn, ncoeff, anfacg )
c
      end if
c
      print *
c
c *************** DELTA-M TRUNCATION ***************
c
      write(*,*)' Do you want to truncate the coeffs. (Y->1,N->2) '
      read(*,*) knopt
c
      if( knopt .eq. 1 ) then
         write(*,*)' Please enter number of materials : '
         read(*,*) nmat
         write(*,*)' At which number you want to truncate the coeffs.: '
         read(*,*) m
c
         sabs = 0.
         fiss = 0.
```

```
C
          if( nopt .eq. 1 ) then
             m1 = m + 1
             n1 = ncoeff + 1
          else if( nopt .eq. 2 ) then
             m1 = m + 1
             n1 = ncoeff + 1
          else if( nopt .eq. 3 ) then
             m1 = 2*m
             n1 = 2*ncoeff-1
          end if
c
          do imat = 1, nmat
C
            write(*,*)' Please enter total,absorption and scattering '
            write(*,*)' cross sections for each material: '
            read(*,*) sigma, sabs, scatt
c
            call deltam( pn,ncoeff,m,m1,n1,imat,sigma,sabs,scatt )
c
          end do
c
       end if
c
       stop
       end
C
C*********************************************************************
C
       SUBROUTINE bhmie(a1,a2,xsize,refrel,n,s1,s2,
      :                 qsca,gsca,rs,cgh)
C
C Declare parameters:
C Note: important that mxn be consistent with dimension of s1 and s2
C       in calling routine!
c
       integer mxn,nmxx
       parameter(mxn=1000,nmxx=15000)
real*8 a1,a2,rs(100),cgh(100)
C Arguments:
c
       integer n
       real*8 gsca,qsca,xsize
       complex refrel,s1(2*mxn-1),s2(2*mxn-1)
c
C Local variables:
C
       integer j,jj,l,nstop,nmx,nn
       real apsi,apsi1,chi,chi0,chi1,fn,p,pii,rn,
      :                 xstop,ymod,amu(mxn),pi(mxn),
      :                 pi0(mxn),pi1(mxn),tau(mxn)
       real*8 psi0,psi1,psi,dn,dx
       complex an,an1,bn,bn1,xi,xi1,y
       complex d(nmxx)

C*********************************************************************
C Subroutine BHMIE is the Bohren-Huffman Mie scattering subroutine
C    to calculate scattering and absorption by a homogeneous isotropic
C    sphere.
C Given:
C    xsize  = 2*pi*a/lambda
C    refrel = (complex refr. index of sphere)/(real index of medium)
C    n      = number of coefficients between 0 and 90 degrees
C             (will calculate 2*n-1 directions from 0 to 180 deg.)
C             if called with n<2, will set n=2 and will compute
C             scattering for theta=0,90,180.
C Returns:
```

```
C     s1(1 - 2*n-1) = -i*f_22 (incid. E perp. to scatt. plane,
C                                   scatt. E perp. to scatt. plane)
C     s2(1 - 2*n-1) = -i*f_11 (incid. E parr. to scatt. plane,
C                                   scatt. E parr. to scatt. plane)
C     qsca = C_sca/pi*a**2 = efficiency factor for scattering
C     gsca = <cos(theta)> for scattering
C
C     cos(theta) = gauss points
C*********************************************************************
C
C*** Safety checks
      if( n .gt. mxn ) stop'***Error: n > mxn in bhmie'
      if( n .lt. 2 ) n=2
C*** Obtain pi:
      pii=4.d0*datan(1.d0)
c
      dx=xsize
C
      y=xsize*refrel
      ymod=abs(y)
C
C*** Series expansion terminated after nstop terms
C     Logarithmic derivatives calculated from nmx on down
      xstop=xsize+4.e0*xsize**0.3333+2.0
C*** Experimental code:
      nmx=1.0*amax1(xstop,ymod)+15
      nstop=1.0*xstop
C
      if ( nmx .gt. nmxx) then
         write(0,*)'Error: nmx > nmxx=',nmxx,' for |m|x=',ymod
         stop
      endif
C
      call gauleg(a1,a2,rs,cgh,(2*n-1))
c
      do 1000 j=1,2*n-1
         amu(j) = rs(j)
 1000 continue
c
      do 1100 j=1,n
          pi0(j)=0.e0
          pi1(j)=1.e0
 1100 continue
c
      nn = 2*n-1
c
      do 1200 j=1,nn
          s1(j)=(0.e0,0.e0)
          s2(j)=(0.e0,0.e0)
 1200 continue
C
C*** Logarithmic derivative d(j) calculated by downward recurrence
C     beginning with initial value (0.,0.) at j=nmx
C
      d(nmx)=(0.e0,0.e0)
      nn=nmx-1
      do 2000 l=1,nn
          rn=nmx-l+1
          d(nmx-l)=(rn/y)-(1.e0/(d(nmx-l+1)+rn/y))
 2000 continue
C
C*** Riccati-Bessel functions with real argument X
C     calculated by upward recurrence
C
      psi0=dcos(dx)
      psi1=dsin(dx)
      chi0=-sin(xsize)
```

```
      chi1=cos(xsize)
c
      apsi1=psi1
c
      xi1=cmplx(apsi1,-chi1)
      qsca=0.e0
      gsca=0.e0
      p=-1.
      do 3000 l=1,nstop
          dn=l
          rn=l
          fn=(2.e0*rn+1.e0)/(rn*(rn+1.e0))
          psi=(2.e0*dn-1.e0)*psi1/dx-psi0
          apsi=psi
          chi=(2.e0*rn-1.e0)*chi1/xsize-chi0
          xi=cmplx(apsi,-chi)
C
C*** Store previous values of an and bn for use
C    in computation of g=<cos(theta)>
c
          if( l .gt. 1 ) then
             an1=an
             bn1=bn
          endif
C
C*** Compute an and bn:
c
          an=(d(l)/refrel+rn/xsize)*apsi-apsi1
          an=an/((d(l)/refrel+rn/xsize)*xi-xi1)
          bn=(refrel*d(l)+rn/xsize)*apsi-apsi1
          bn=bn/((refrel*d(l)+rn/xsize)*xi-xi1)
C
C*** Augment sums for qsca and g=<cos(theta)>
c
          qsca=qsca+(2.*rn+1.)*(cabs(an)**2+cabs(bn)**2)
          gsca=gsca+((2.*rn+1.)/(rn*(rn+1.)))*
     :         (real(an)*real(bn)+aimag(an)*aimag(bn))
c
          if( l .gt. 1 ) then
              gsca=gsca+((rn-1.)*(rn+1.)/rn)*
     :         (real(an1)*real(an)+aimag(an1)*aimag(an)+
     :          real(bn1)*real(bn)+aimag(bn1)*aimag(bn))
          endif
C
C*** Now calculate scattering intensity pattern
C    First do angles from 0 to 90
          do 2500 j=1,n
              jj=2*(n)-j
              pi(j)=pi1(j)
              tau(j)=rn*amu(j)*pi(j)-(rn+1.e0)*pi0(j)
              s1(j)=s1(j)+fn*(an*pi(j)+bn*tau(j))
              s2(j)=s2(j)+fn*(an*tau(j)+bn*pi(j))
 2500     continue
C
C*** Now do angles greater than 90 using PI and tau from
C    angles less than 90.
C    p=1 for N=1,3,...; P=-1 for N=2,4,...
          p=-p
          do 2600 j=1,n-1
              jj=(2*n)-j
              s1(jj)=s1(jj)+fn*p*(an*pi(j)-bn*tau(j))
              s2(jj)=s2(jj)+fn*p*(bn*pi(j)-an*tau(j))
 2600     continue
          psi0=psi1
          psi1=psi
          apsi1=psi1
          chi0=chi1
```

```
          chi1=chi
          xi1=cmplx(apsi1,-chi1)
C
C*** Compute pi_n for next value of n
C    For each angle j, compute pi_n+1
C    from PI = pi_n , PI0 = pi_n-1
c
          do 2800 j=1,n
              pi1(j)=((2.*rn+1.)*amu(j)*pi(j)-(rn+1.)*pi0(j))/rn
              pi0(j)=pi(j)
 2800     continue
 3000 continue
C
C*** Have summed sufficient terms.
C    Now compute qsca and gsca
      gsca=2.*gsca/qsca
      qsca=(2.e0/(xsize*xsize))*qsca
      return
      end
C
C ***********************************************************************
C
      SUBROUTINE gauleg(x1,x2,x,w,n)
c     ----------------------------------
c     Given the lower and upper limits of integration x1 and x2,
c     and given n, this routine return (x:n) and (w:n) of length
c     n, containing the abscissas and weights of the Gauss-Legendre
c     n-point quadrature formula.
c
      integer n,i,j,m
      real*8 x(n),w(n),EPS,x1,x2,p1,p2,p3,pp,
     :                 xl,xm,z,z1
      parameter (EPS=3.d-15)
c
      m=(n+1)/2
      xm=0.5d0*(x2+x1)
      xl=0.5d0*(x2-x1)
      do 12 i=1,m
         z=dcos(3.141592653589793d0*(i-.25d0)/(n+.5d0))
1       continue
         p1=1.d0
         p2=0.d0
          do 11 j=1,n
            p3=p2
            p2=p1
            p1=((2.d0*j-1.d0)*z*p2-(j-1.d0)*p3)/j
11        continue
         pp=n*(z*p1-p2)/(z*z-1.d0)
         z1=z
C
         z=z1-p1/pp
         if(abs(z-z1).gt.EPS)goto 1
         x(i)=xm-xl*z
         x(n+1-i)=xm+xl*z
         w(i)=2.d0*xl/((1.d0-z*z)*pp*pp)
            w(n+1-i)=w(i)
12    continue
      return
      end
c
c***********************************************************************
C
      SUBROUTINE fleg(x,pl,nl)
c     ----------------------------------
c     Fitting routine for an expansion with nl Legendre polynomials
c     pl, evaluated using the recurrence relation.
c
```

```
      integer nl,j
      real*8 pl(nl),x,d,f1,f2,twox
c
      pl(1)=1.
      pl(2)=x
      if(nl.gt.2) then
      twox=2.*x
      f2=x
      d=1.
       do 11 j=3,nl
         f1=d
         f2=f2+twox
         d=d+1.
         pl(j)=(f2*pl(j-1)-f1*pl(j-2))/d
11     continue
      endif
      return
      end
c
c*********************************************************************
C
      SUBROUTINE henyey( pn, ncoeff, anfacg )
c     ---------------------------------
c     This routine calculates the expansion coefficients
c     using Henyey-Greenstein phase function formula
c
      real*8 pn(1000), anfacg
      integer ncoeff
c
c - local
c
      integer k
      real*8 hn(1000)
      real*8  fourpi
c
      print *
      write(*,*)' Please enter g and the number of coefficients: '
      read(*,*) anfacg, ncoeff
      write(*,*) 'g :', anfacg, ' no. of coeff :', ncoeff
      print *
c
      fourpi = 16.0*atan( 1.0 )
c
      do k = 1,ncoeff+1
C
         hn(k) = (2*(k-1) + 1)*(anfacg)**(k-1)
         pn(k) = hn(k)/fourpi
         write( *, * ) k-1, pn(k)
C
      end do
c
      return
      end
c
c*********************************************************************
C
      SUBROUTINE deltam( pn,ncoeff,m,m1,n1,imat,sigma,sabs,scatt )
c     ------------------------------------------------------------
c     This subroutine adjusts the Pn coefficients according to the
c     delta-m method
c
      real*8 pn(1000), sigma, sabs, scatt
      integer ncoeff, m, m1, n1, imat
c
c - local
c
      integer in
```

```
c
      sabs = 0.
      fiss = 0.
C
C ******************************************************
C * The calculation of the single scattering albedo: *
C *                scattering/total                    *
C ******************************************************
C
       scateff = scatt / sigma
C
C ********************************************************************
C * f is the optimum expansion coefficient of the approximate        *
C * or truncated phase function or the fractional scattering         *
C * into the forward peak and equal to last expansion coefficient of *
C * the original phase function.                                     *
C ********************************************************************
C
       fdelta = pn(m1+1)/((2*m1+1)*scatt)
C
       scatti = scatt
C
C ************************************************************
C * calculation of the new transformed scattering, total and *
C * absorption cross section values by using the following   *
C * formula: new value = (1 - albedo*f)*old value            *
C ************************************************************
C
       print *
       sigma = ( 1. - scateff*fdelta ) * sigma
       scatt = ( 1. - scateff*fdelta ) * scatti
       sabs = sigma - scatt
C
       write(*,3) imat, sigma, sabs, fiss
C
       sigs0 = pn(1)
c
c
C ****************************************************************
C * Calculation of the new coefficients using the original phase *
C * function coefficients in the formula:                        *
C * new coeff. = (original coeff. - f)/(1 - f)                   *
C ****************************************************************
C
      do i = 0, m
c
          xm = pn(i+1)/((2.*float(i)+1.)*sigs0)
          pn(i+1) = scatt * ( xm - fdelta ) / ( 1 - fdelta )
          write(*,2) imat, pn(i+1)
C
      end do
C
 2        format('ma',i1,'          ',E13.7,' ^')
 3        format('ma',i1,'          ',3(E13.7,2x),' ^')
C
      return
      end
c
c*******************************************************************
C
      SUBROUTINE simpmie( pn, n, anfacg )
c     ---------------------------------
c     this subroutine calculates the phase function values and the expansion
c     coefficients according to the Simplified Approximate Mie theory phase
c     function formula
c
      real*8 pn(1000), anfacg
```

```
      integer ncoeff
      real*8 rs(100),a(100),pol(100),
     :                 f(100),cgh(100),pi,b,c,a1,a2,g,
     :                 fww(200),y(100)
c
c Parameters:
c
      integer mxn
      parameter(mxn=1000)
c
c Variables:
c
      real*8 gsca,qsca,s11,rad,refmed,wavel,
     :                 xsize,wavenum
      complex refrel,cxeps,s1(2*mxn-1),s2(2*mxn-1)
c
       write(*,*)' Please enter g value :'
       read(*,*) anfacg
       write(*,*) anfacg
c
      print *
c
c calculate np-number of coefficients
c
      pi = 4.0*atan( 1.0 )
      a1 = -1.0
      a2 = +1.0
c
      n = (2.*anfacg) / (1. - anfacg)
c
      if ( mod(n,2) .eq. 0 ) then
         n = n
c
      else
         n = n + 1
c
      endif
c
      write(*,*) n
      write(*,*) 'Number of coefficients included 0 :', n+1
      print *
c
c calculate constant Ks(=b)
c
      b=(n+1.)/(pi*2.**(n+2.))
c
c calculate n+1 gauss points (rs) and weights (cgh)
c
      call gauleg(a1,a2,rs,cgh,n+1)
c
      write(7,609)
c
      do i=1,n+1
c
        y(i) = b*(1.+rs(i))**n
c
        write(*,607)acos(rs(i))*180/pi,y(i)
        write(7,607) acos(rs(i))*180/pi,y(i)
  609   format(2x,'angle',3X,'Phase Func.')
  607   format(1X,F6.2,2X,2(1PE12.5))

c
      enddo
c
      write(7,*)
      print *
c
```

```
      do k=1,n+1
c
c initilaze pol(k)
c
        pol(k)=0.
c
        do i=1,n+1
           g = rs(i)
           f(i) = b*((1+g)**n)
c
c calculate (n+1) Legendre pol. at each gauss point
c
      call fleg (g,pol,k)
c
           c = (2.*(k-1) + 1.)/2.
           a(k) = a(k) + (c*cgh(i)*pol(k)*f(i))
c
           pn(k) = a(k)
c
        enddo
c
        write(*,*) k-1, pn(k)
        write(7,*) k-1, pn(k)
c
      enddo
c
      return
      end
c
c**********************************************************************
C
      SUBROUTINE Mie( pn, n, anfacg )
c     ------------------------------
c     This subroutine calculates the phase function values and
c     the coefficients using Mie theory
c
      real*8 pn(1000), anfacg
      integer n
      real*8 rs(100),a(100),pol(100),
     :                f(100),cgh(100),pi,b,c,a1,a2,g,
     :                fww(200),y(100)
c
c Parameters:
c
      integer mxn
      parameter(mxn=1000)
c
c Variables:
c
      real*8 gsca,qsca,s11,rad,refmed,wavel,
     :                xsize,wavenum
      complex refrel,cxeps,s1(2*mxn-1),s2(2*mxn-1)
c
      pi = 4.0*atan( 1.0 )
      a1 = -1.0
      a2 = +1.0
c
      write(*,*)'Wish to enter refr.index(m)-size parameter(x) OR '
      write(*,*)'real refr. index of surrounding medium '
      write(*,*)'complex refr. index of sphere '
      write(*,*)'radius, wavelength? (1 or 2)'
      print *
      read (*,*) nnopt
c
      if( nnopt .le. 1 ) then
c
        write(*,*)'Enter refractive index m '
```

```
        read(*,*) refrel
        write(*,*) 'Refractive index m =', refrel
        write(7,*) 'Refractive index m =', refrel
c
        write(*,*)'Enter size parameter x '
        read(*,*) xsize
        write(*,*) 'Size parameter x =', xsize
        write(7,*) 'Size parameter x  =', xsize
c
      else
c
        write(*,*)'Enter (real) refractive index of surrounding medium'
        read(*,*) refmed
        write(7,*) 'Real refr. index of surrounding medium =', refmed

C
        write(*,*)'Wish to enter refr.index or epsilon? (0 or 1)'
        read(*,*) ireadep
C
 1000 if( ireadep .le. 0 ) then
c
        write(*,*)'Enter complex refractive index of sphere'
        read(*,*) refrel
        write(7,*) 'Complex refr. index of sphere =', refrel
c
      else
c
          write(*,*)'Enter complex epsilon of sphere'
          read(*,*) cxeps
c
          refrel = sqrt(cxeps)
c
      endif
C
C  Calculation of the relative refractive index (m = k1/k = N1/N)
C
      refrel = refrel / refmed
C
       write(7,6012) refrel
c
 6012 format(' Complex refractive index=',1P2E10.3)
C
      write(*,*)' Enter radius'
      read(*,*) rad
      write(7,*) 'Radius=', rad
C
      write(*,*)' Enter wavelength'
      read(*,*) wavel
      write(7,*) 'Wavelength=', wavel
C
C Calculation of the size parameter (x = k*a = 2*pi*N*a/Lambda) and
C wave number k
C
      xsize = 2.e0*pi*rad*refmed / wavel
c
       wavenum = xsize / rad
C
       write(*,6013) rad,wavel,xsize,wavenum
       write(7,*) 'Size parameter=', xsize
       write(7,*) 'Wave number=',wavenum
6013   format (' radius=',1PE11.4,' lambda=',E11.4,' x=',E11.4,
     &' wavenum=',E11.4)
c
       endif
c
       print *
c
```

```
      write(*,*)' (2*n-1) coefficients will be calculated so please '
      write(*,*)' enter the number of coefficients: '
      read(*,*) n
C
      if( n .gt. mxn ) stop'***Error: n > mxn'
      n = n
c
      if( n .lt. 2 ) n = 2
C
C*********************************************************************
C n=number of coefficients between 0 and 90 degrees (incl. 0 and 90)
C 2*n-1 is the total calculated coefficients
C*********************************************************************
c
call bhmie(a1,a2,xsize,refrel,n,s1,s2,qsca,gsca,rs,cgh)
C
      write(*,6065) qsca,gsca
      write(7,*) 'Single scatt. efficiency=',qsca
      write(7,*) 'Mean cosine of the scatt. angle g=',gsca
      write(7,*)
c
 6065 format(/,'Qsca=',E11.4,' <cos>=',E11.4)
c
      print *
c
      if( n .gt. 1 ) then
c
         s11nor = 0.5*(cabs(s2(1))**2+cabs(s1(1))**2)
         nan=2*n-1
         write(7,906)
c
           do 455 j=1,nan
           theta = acos(rs(j))
           s11=0.5e0*cabs(s2(j))*cabs(s2(j))
           s11=s11+0.5e0*cabs(s1(j))*cabs(s1(j))
           fww(j) = s11/(xsize*xsize*qsca)*pi*0.1
           s11=s11/s11nor
           write(*,6075)theta*180/pi,fww(j)
           write(7,6075)theta*180/pi,fww(j)
  906      format(2x,'angle',3X,'Phase Func.')
 6075      format(1X,F6.2,2X,2(1PE12.5))
 455     continue
c
         write(7,*)
         print *
c
          do 355 j=1,nan
            s11=0.5e0*cabs(s2(j))*cabs(s2(j))
            s11=s11+0.5e0*cabs(s1(j))*cabs(s1(j))
            fww(j) = s11/(xsize*xsize*qsca)*pi*0.1
c
            s11=s11/s11nor
C
  355      continue
      endif
C
      do k=1,2*n-1
        pol(k)=0.
c
        do i=1,2*n-1
           g= rs(i)
C
C calculate (n+1) Legendre pol. at each gauss point
c
      call fleg (g,pol,k)
c
           c = (2.*(k-1) + 1.)/2.
```

```
            a(k) = a(k) + (c*cgh(i)*pol(k)*fww(i))
c
            pn(k) = a(k)
c
          enddo
c
          write(*,*) k-1, pn(k)
          write(7,*) k-1, pn(k)
c
        enddo
c
        return
        end
```

Appendix B

Definitions of $S_1(\theta)$ and $S_2(\theta)$ for Mie Theory Approximation

The amplitude functions $S_1(\theta)$ and $S_2(\theta)$ are given as [116],[117]

$$S_1(\theta) = \sum_{n=0}^{\infty} \frac{2n+1}{n(n+1)} (a_n \pi_n(\cos\theta) + + b_n \tau_n(\cos\theta)) \tag{B.1}$$

and

$$S_2(\theta) = \sum_{n=0}^{\infty} \frac{2n+1}{n(n+1)} (b_n \pi_n(\cos\theta) + a_n \tau_n(\cos\theta)) \tag{B.2}$$

where $\pi_n(\cos\theta)$ and $\tau_n(\cos\theta)$ are the angular coefficients given by

$$\pi_n(\cos\theta) = \frac{P_n^1(\cos\theta)}{\sin\theta}, \qquad \tau_n(\cos\theta) = \frac{dP_n^1(\cos\theta)}{d\theta}. \tag{B.3}$$

Here, $P_n^1 = P_n^1(\cos\theta)$ is a special case of the associated Legendre functions $P_n^m(\cos\theta)$ with m = 1 [197]; a_n and b_n are defined by

$$a_n = \frac{m\psi_n(Mka)\psi_n'(mka) - M\psi_n(mka)\psi_n'(Mka)}{-m\xi_n(Mka)\psi_n'(mka) - M\psi_n(mka)\xi_n'(Mka)} \tag{B.4}$$

and

$$b_n = \frac{m\psi_n'(Mka)\psi_n(mka) - M\psi_n'(mka)\psi_n(Mka)}{-m\xi_n'(Mka)\psi_n(mka) - M\psi_n'(mka)\xi_n(Mka)} \tag{B.5}$$

where ψ_n and ξ_n are the Ricatti-Bessel functions of order n with definitions

$$\psi_n(x) = xj_n(x) \qquad and \qquad \xi_n(x) = xh_n^{(1)}(x)$$

where $j_n(x)$ is the spherical Bessel function of order n, and $h_n^{(1)}(x)$ is the nth order spherical Hankel function of the first kind [197]. ψ_n' and ξ_n' are the derivatives of the Ricatti-Bessel functions, ψ_n and ξ_n, with respect to their argument, x, respectively. k appearing in arguments Mka and mka of functions ψ_n and ξ_n is the *in vacuo* wavenumber which is defined by

$$k = \frac{2\pi}{\lambda} \tag{B.6}$$

Appendix C

Radiation Transport Code EVENT

C.1 Specification of the Program

Even though it is strictly not a finished product, EVENT is a good vehicle for publicising the radiation finite element method and representing the state-of-the-art of the spherical harmonics-finite element solution of transport problems.

EVENT is a flexible computer program capable of solving the anisotropic even-parity multi-group or multi-frequency problem by two possible solution modes, direct and/or adjoint solutions, for steady-state (fixed-source), steady-state eigenvalue and time-dependent photon and neutron problem types. Solution of the problems is possible in the six geometries and three dimensions of general interest: slab, sphere, or cylinder in 1D; (x,y) and (r,z) in 2D; (x,y,z) in 3D. The following boundary conditions may be imposed on external boundaries of the problem domain: zero flux (diffusion): vacuum or bare surface; reflection; incoming surface source; white albedo; symmetry and beams.

Odd-order spherical harmonics functions, P_N, are used in order to approximate the angular dependence of the even-parity flux and there is no restriction on the

order of angular expansion (arbitrary) as also on the order of the P_L expansion of the scattering kernel. Energy dependence is discretised by employing the conventional multi-group approximation for arbitrary number of groups. The multi-group equations are solved as a sequence of one-groups problems with the group-to-group (coherent) scattering contribution providing the coupling between the groups and problems can involve down-scatter only or up-scatter as well. A number of implicit and explicit time-integrating schemes are obtained for time discretisation via the integration of the parity equations over time and using *Padé* approximants. The schemes implemented in EVENT are: Implicit (Backward-Euler), Crank-Nicolson, Galerkin: Explicit (Forward-Euler). Features of the numerical implementation are the splitting of the time domain into time zones which can have different materials, sources etc. and automatic time-step control. For the spatial discretisation local polynomial basis functions of up to fifth order are used in various isoparametric finite elements shapes such as lines, triangles, quadrilaterals, tetrahedra, hexahedra and prisms.

C.2 Solution Strategies

The coefficient matrix **A** in equation (2.72) is symmetric and positive definite in addition to this due to the compact support of the finite element shape functions it is sparse and, if the nodes are numbered in an orderly fashion, also banded. This means that all the non-zero elements are grouped in a band around the main diagonal of the coefficient matrix. Because of the importance of the storage reduction as always requiring while working with the computers, this symmetric and banded nature of **A** becomes very attractive computational feature. This provides storing only the elements in the main diagonal and those above or below the diagonal but within the band instead of having to store a full $MN \times MN$ matrix.

Success of the above method is highly dependent on the expedient solution of the system of linear equations given by equation (2.72). The solution of this equation

system can be obtained by using either direct methods, such as Gaussian elimination or Cholesky factorisation, or iterative methods, such as the Preconditioned Conjugate Gradient Method (**PCG**) or the other iterative procedures.

A highly efficient Gaussian elimination frontal solver has been devised for the direct solution of system of equation (2.72) and its application is largely restricted to 2D cases. Another economical and more general moment-by-moment (**MBM**) solution scheme, which is based on a preconditioned symmetric conjugate gradient (**PCG**) iterative procedure, has been developed for the solution of 3D problems. The main feature of this scheme is that there is no need to explicitly calculate and store both the global and preconditioning matrix. Extension of the **MBM** solution algorithm to parallel processing has been achieved via domain decomposition methods and these are used as acceleration techniques or preconditioners for the **MBM** procedure. Two strategies have been implemented in EVENT at present. One of them is based on an iterative multi-block explicit procedure [198] and the other on a direct nested dissection procedure [199]. The numerical implementation of the procedure is based on the **PVM** message passing library.

Appendix D

Legendre Polynomials and Spherical Harmonics

D.1 Legendre Polynomials

The Legendre Polynomials $P_l(x)$ are solutions to the Legendre Differential Equation,

$$(1-x^2)y'' - 2xy' + l(l+1)y = 0 \tag{D.1}$$

and they are defined by Rodrigues formula as

$$P_l(x) = \frac{1}{2^l l!}\frac{d^l}{dx^l}[(x^2-1)^l], \quad for \;\; l = 1, 2, ... \tag{D.2}$$

They may also be defined as the unique (except for normalisation) set of polynomials orthogonal on the interval -1 $\leq$ x $\leq$ 1, such that l is the highest power of x in $P_l(x)$. They satisfy the orthogonality relation

$$\int_{-1}^{+1} P_m(x)P_l(x)dx = \frac{2\delta_{ml}}{2l+1} \tag{D.3}$$

where δ_{ml}, the Kronecker delta, is unity if $m = l$ and zero otherwise. The first few Legendre polynomials are

$$P_0(x) = 1$$

$$P_1(x) = x$$

$$P_2(x) = \frac{1}{2}(3x^2 - 1)$$

$$P_3(x) = \frac{1}{2}(5x^3 - 3x)$$

$$P_4(x) = \frac{1}{8}(35x^4 - 30x^2 + 3)$$

$$P_5(x) = \frac{1}{8}(65x^5 - 70x^3 + 15x)$$

$$P_6(x) = \frac{1}{16}(231x^6 - 315x^4 + 105x^2 - 5)$$

The Legendre Polynomials satisfy the following recurrence relations

$$xP_l(x) = \frac{1}{2l+1}[(l+1)P_{l+1}(x) + lP_{l-1}(x)]$$

$$(1-x^2)\frac{dP_l(x)}{dx} = l(xP_l(x) - P_{l-1}(x)] \tag{D.4}$$

The Legendre polynomials form a complete set of orthogonal functions [200],[201] for the expansion of a continuous function, f(x), defined on the interval -1 $\leq$ x $\leq$ 1. Therefore, f(x) can be expanded in terms of Legendre polynomials,

$$f(x) = \sum_{l=0}^{\infty} a_l P_l(x) \tag{D.5}$$

The coefficients a_l are obtained by multiplying (A.5) by $P_m(x)$ and integrating over the range -1 $\leq$ x $\leq$ 1. This gives

$$\int_{-1}^{+1} P_m(x)f(x)dx = \sum_{l=0}^{\infty} a_l \int_{-1}^{+1} P_m(x)P_l(x)dx$$

which by (A.3) equals $2a_m/(2m + 1)$. Hence the coefficients in (A.5) are given by

$$a_m = \frac{2m+1}{2}\int_{-1}^{+1} f(x)P_m(x)dx \tag{D.6}$$

D.1.1 Associated Legendre Polynomials

The associated Legendre polynomials $\mathrm{P}_l^m(x)$ are solutions to the following second-order differential equation

$$(1-x^2)y'' - 2xy' + \left[l(l+1) - \frac{m^2}{1-x^2}\right] y = 0 \tag{D.7}$$

where l is a positive integer and m = 0,1,...l. They can be given in terms of the Legendre polynomials by [201]

$$\begin{aligned} P_l^m(x) &= (-1)^m (1-x^2)^{(m/2)} \frac{d^m}{dx^m} P_l(x) \\ &= \frac{(-1)^m}{2^l l!} (1-x^2)^{(m/2)} \frac{d^{(l+m)}}{dx^{(l+m)}} (x^2-1)^l. \end{aligned} \tag{D.8}$$

Note that some authors [202] omit the Condon-Shortley Phase $(-1)^m$, while others include it [197],[162]. From this it is seen that if m = 0, the associated Legendre polynomials reduce to the Legendre polynomials, $\mathrm{P}_l^0(x) = \mathrm{P}_l(x)$. Equation (A.8) can be used to extend the definition of $\mathrm{P}_l^m(x)$ to negative values of m and $\mathrm{P}_l^m(x)$ and $\mathrm{P}_l^{-m}(x)$ can be related by

$$P_l^{-m}(x) = (-1)^m \frac{(l-m)!}{(l+m)!} P_l^m(x) \tag{D.9}$$

The associated Legendre functions are part of the Spherical Harmonics, which are the solution of Laplace's Equation in Spherical Coordinates [202]. They satisfy the orthogonality relation

$$\int_{-1}^{+1} P_l^m(x) P_{l'}^m(x) dx = \left(\frac{2}{2l+1}\right) \frac{(l+m)!}{(l-m)!} \ \delta_{ll'} \tag{D.10}$$

and the recurrence relations

$$x P_l^m(x) = \frac{1}{2l+1} \left[(l-m+1) P_{l+1}^m(x) + (l+m) P_{l-1}^m(x)\right] \tag{D.11}$$

$$(l-m) P_l^m(x) = x(2l-1) P_{l-1}^m(x) - (l+m-1) P_{l-2}^m(x) \tag{D.12}$$

Written in terms of x and using the convention without a leading factor of $(-1)^m$ [202], the first few associated Legendre polynomials are [201]

$$P_0^0(x) = 1$$

$$P_1^0(x) = x$$

$$P_1^1(x) = -(1-x^2)^{1/2}$$

$$P_2^0(x) = \frac{1}{2}(3x^2-1)$$

$$P_2^1(x) = -3x(1-x^2)^{1/2}$$

$$P_2^2(x) = 3(1-x^2)$$

$$P_3^0(x) = \frac{1}{2}x(5x^2-3)$$

$$P_3^1(x) = \frac{3}{2}(1-5x^2)(1-x^2)^{1/2}$$

$$P_3^2(x) = 15x(1-x^2)$$

$$P_3^3(x) = -15(1-x^2)^{3/2}$$

$$P_4^0(x) = \frac{1}{8}(35x^4-30x^2+3)$$

$$P_4^1(x) = \frac{5}{2}x(3-7x^2)(1-x^2)^{1/2}$$

$$P_4^2(x) = \frac{15}{2}x(7x^2-1)(1-x^2)$$

$$P_4^3(x) = -105x(1-x^2)^{3/2}$$

$$P_4^4(x) = 105x(1-x^2)^2$$

$$P_5^0(x) = \frac{1}{8}x(63x^4-70x^2+15)$$

Written in terms $x \equiv \cos\theta$

$$P_0^0(\cos\theta) = 1$$

$$P_1^0(\cos\theta) = \cos\theta = \mu$$

$$P_1^1(\cos\theta) = \sin\theta$$

$$P_2^0(\cos\theta) = \frac{1}{2}(3\cos^2\theta - 1)$$

$$P_2^1(\cos\theta) = 3\sin\theta\cos\theta = \frac{3}{2}\sin^2\theta$$

$$P_2^2(\cos\theta) = 3\sin^2\theta = \frac{3}{2}(1-\cos^2\theta)$$

$$P_3^0(\cos\theta) = \frac{1}{2}\cos\theta(5\cos^2\theta - 3) = \frac{1}{2}\cos\theta(2-5\sin^2\theta)$$

$$P_3^1(\cos\theta) = \frac{3}{2}(5\cos^2\theta - 1)\sin\theta = \frac{3}{8}(\sin\theta + 5\sin^3\theta)$$

D.2 Spherical Harmonics

The spherical harmonics $Y_l^m(\theta, \phi)$ are the angular portion of the solution to Laplace's Equation in Spherical Coordinates where azimuthal symmetry is not present [202],[197]. They are defined by

$$Y_l^m(\theta, \phi) = \sqrt{\frac{2l+1}{4\pi}\frac{(l-m)!}{(l+m)!}} P_l^m(\cos\theta) e^{im\phi} \tag{D.13}$$

which is valid for m$\geq$ 0, while the eigenfunctions corresponding to negative values of m are obtained from

$$Y_l^{-m}(\theta, \phi) = (-1)^m Y_l^{m*}(\theta, \phi) \tag{D.14}$$

where Y_l^{m*} is the complex conjugate of Y_l^m. The first few spherical harmonics are [200]

$$Y_0^0(\theta, \phi) = \frac{1}{2}\frac{1}{\sqrt{\pi}}$$

$$Y_1^0(\theta, \phi) = \frac{1}{2}\sqrt{\frac{3}{\pi}}\cos\theta$$

$$Y_1^1(\theta, \phi) = -\frac{1}{2}\sqrt{\frac{3}{2\pi}}\sin\theta e^{i\phi}$$

$$Y_1^{-1}(\theta, \phi) = \frac{1}{2}\sqrt{\frac{3}{2\pi}}\sin\theta e^{-i\phi}$$

$$Y_2^0(\theta, \phi) = \frac{1}{4}\sqrt{\frac{5}{\pi}}(3\cos^2\theta - 1)$$

$$Y_2^1(\theta, \phi) = -\frac{1}{2}\sqrt{\frac{15}{2\pi}}\sin\theta\cos\theta e^{i\phi}$$

$$Y_2^{-1}(\theta, \phi) = \frac{1}{2}\sqrt{\frac{15}{2\pi}}\sin\theta\cos\theta e^{-i\phi}$$

$$Y_2^2(\theta, \phi) = \frac{1}{4}\sqrt{\frac{15}{2\pi}}\sin^2\theta e^{2i\phi}$$

The spherical harmonics form a complete set of orthonormal functions [201], i.e.

$$\int_{\phi=0}^{2\pi}\int_{\theta=0}^{\pi} Y_l^m(\theta, \phi) Y_{l'}^{m'*}(\theta, \phi)\sin\theta d\theta d\phi \;=\; \int_0^{2\pi}\int_{-1}^{1} Y_l^m(\theta, \phi) Y_{l'}^{m'*}(\theta, \phi) d(\cos\theta) d\phi$$

$$= \delta_{ll'} \ \delta_{mm'}. \tag{D.15}$$

Thus, any function of θ and ϕ can be expanded in terms of spherical harmonics.

$$f(\theta,\phi) = \sum_{l=0}^{\infty} \sum_{m=-l}^{l} f_{lm} Y_l^m(\theta,\phi) \tag{D.16}$$

where the coefficients f_{lm} are given by

$$f_{lm} = \int_0^{2\pi} \int_{-1}^{1} f(\theta,\phi) Y_l^{m*}(\theta,\phi) d(\cos\theta) d\phi \tag{D.17}$$

One of the important properties of spherical harmonics is the addition theorem. For two direction vectors $\mathbf{\Omega}' = (\theta',\phi')$ and $\mathbf{\Omega} = (\theta,\phi)$, the addition theorem can be written as [201]

$$P_l(\mathbf{\Omega}' \cdot \mathbf{\Omega}) = \frac{4\pi}{(2l+1)} \sum_{m=-l}^{l} Y_l^{m*}(\theta,\phi) Y_l^m(\theta',\phi'). \tag{D.18}$$

This property is very useful for representing the scattering process for particles in which a particle originally moving in direction $\mathbf{\Omega}'$ is scattered off by another particle in direction $\mathbf{\Omega}$.

Appendix E

The Tensor Product of Matrices

Given an $(m \times n)$ matrix A having elements (a_{ij}, $i = 1,...,m$; $j = 1,...,n$) and a $(p \times q)$ matrix B having elements (b_{kl}, $k = 1,...,p$; $l = 1,...,q$), their tensor or direct product $\mathbf{C} = \mathbf{A} \otimes \mathbf{B}$ is an (mp) $\times$ (nq) matrix defined as [203],

$$\mathbf{A} \otimes \mathbf{B} = \begin{bmatrix} a_{11}\mathbf{B} & a_{12}\mathbf{B} & a_{13}\mathbf{B} & \dots & a_{1n}\mathbf{B} \\ a_{21}\mathbf{B} & a_{22}\mathbf{B} & a_{23}\mathbf{B} & \dots & a_{2n}\mathbf{B} \\ a_{31}\mathbf{B} & a_{32}\mathbf{B} & a_{33}\mathbf{B} & \dots & a_{3n}\mathbf{B} \\ \vdots & \vdots & \vdots & \ddots & \vdots \\ a_{m1}\mathbf{B} & a_{m2}\mathbf{B} & a_{m3}\mathbf{B} & \dots & a_{mn}\mathbf{B} \end{bmatrix} \tag{E.1}$$

The resulting matrix $\mathbf{C}$ can be written with elements as

$$\mathbf{C}_{\alpha\beta} = \mathbf{A}_{ij}\mathbf{B}_{kl}, \tag{E.2}$$

where

$$\alpha \equiv p(i-1) + k \tag{E.3}$$

$$\beta \equiv q(j-1) + l \tag{E.4}$$

For example, the matrix direct product of a 2×2 matrix $\mathbf{A}$ and a 3×2 matrix $\mathbf{B}$ is given by the following 6×4 matrix,

$$\mathbf{A} \otimes \mathbf{B} = \begin{bmatrix} a_{11}\mathbf{B} & a_{12}\mathbf{B} \\ a_{21}\mathbf{B} & a_{22}\mathbf{B} \end{bmatrix} = \begin{bmatrix} a_{11}b_{11} & a_{11}b_{12} & a_{12}b_{11} & a_{12}b_{12} \\ a_{11}b_{21} & a_{11}b_{22} & a_{12}b_{21} & a_{12}b_{22} \\ a_{11}b_{31} & a_{11}b_{32} & a_{12}b_{31} & a_{12}b_{32} \\ a_{21}b_{11} & a_{21}b_{12} & a_{22}b_{11} & a_{22}b_{12} \\ a_{21}b_{21} & a_{21}b_{22} & a_{22}b_{21} & a_{22}b_{22} \\ a_{21}b_{31} & a_{21}b_{32} & a_{22}b_{31} & a_{22}b_{32} \end{bmatrix} \tag{E.5}$$

The tensor product of matrices has various properties and some of these are given below [202],

- Associative Property:

$$\mathbf{A} \otimes (\mathbf{B} \otimes \mathbf{C}) = (\mathbf{A} \otimes \mathbf{B}) \otimes \mathbf{C} \tag{E.6}$$

- Inverse of a Tensor Product:

$$(\mathbf{A} \otimes \mathbf{B})^{-1} = \mathbf{A}^{-1} \otimes \mathbf{B}^{-1} \tag{E.7}$$

- Transpose of a Tensor Product:

$$(\mathbf{A} \otimes \mathbf{B})^{T} = \mathbf{A}^{T} \otimes \mathbf{B}^{T} \tag{E.8}$$

- Left and Right Distributive Property over Addition:

$$\begin{aligned} \mathbf{A} \otimes (\mathbf{B} + \mathbf{C}) &= (\mathbf{A} \otimes \mathbf{B}) + (\mathbf{A} \otimes \mathbf{C}) \\ (\mathbf{B} + \mathbf{C}) \otimes \mathbf{A} &= (\mathbf{B} \otimes \mathbf{A}) + (\mathbf{C} \otimes \mathbf{A}) \end{aligned} \tag{E.9}$$

- Scalar Multiplicative Property: For a scalar α,

$$\mathbf{A} \otimes (\alpha\mathbf{B}) = (\alpha\mathbf{A}) \otimes \mathbf{B} \tag{E.10}$$

- Matrix Multiplication:

$$(\mathbf{A} \otimes \mathbf{B})(\mathbf{C} \otimes \mathbf{D}) = \mathbf{AC} \otimes \mathbf{BD} \tag{E.11}$$